Tiny, mighty machine learning for the Global South p. 818

Mice help unconscious peers pp. 827, 842, & 843

Robot collectives with dynamic strength and shape p. 880

Science

$15
21 FEBRUARY 2025
science.org

AAAS

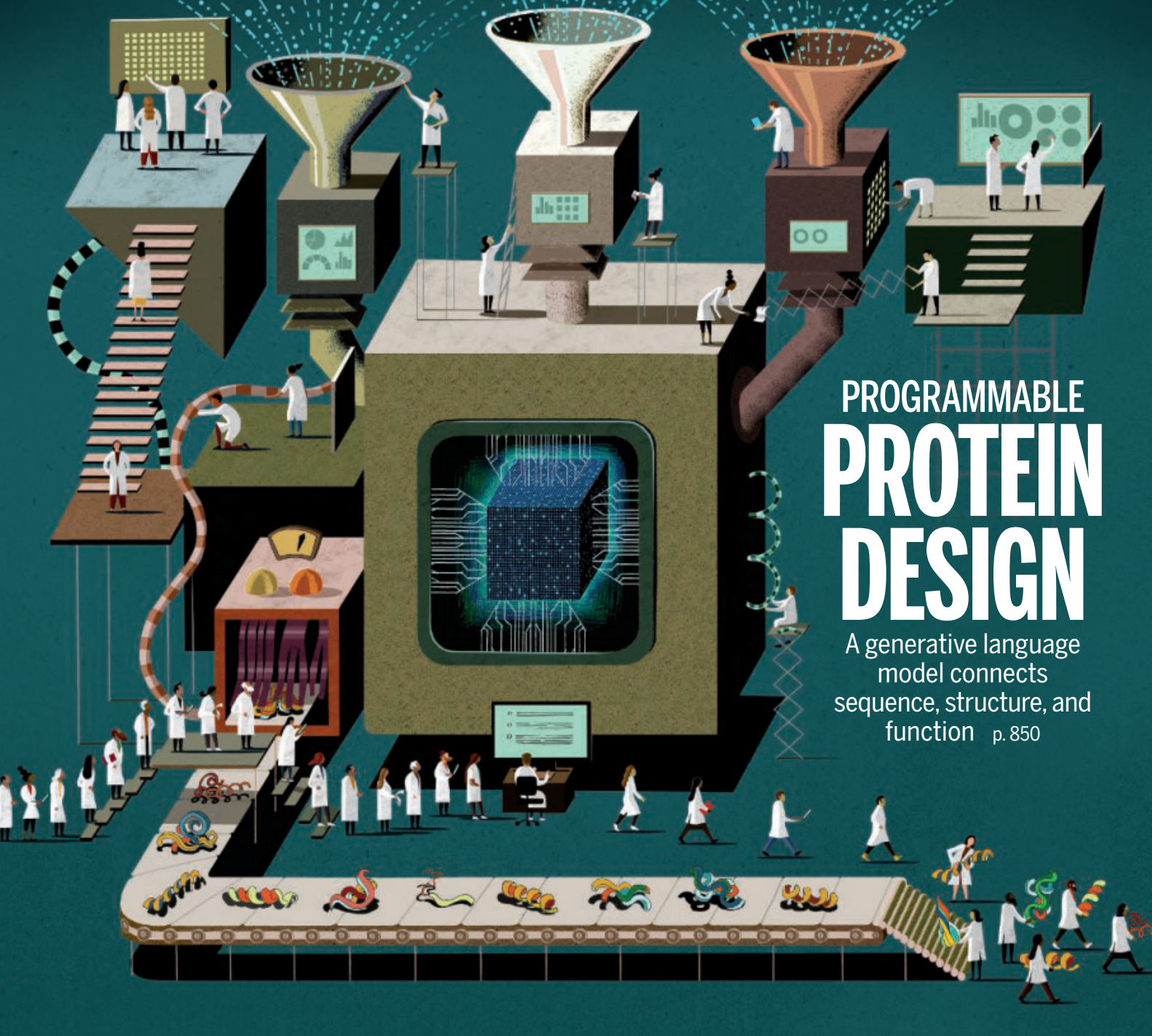

PROGRAMMABLE PROTEIN DESIGN

A generative language model connects sequence, structure, and function p. 850

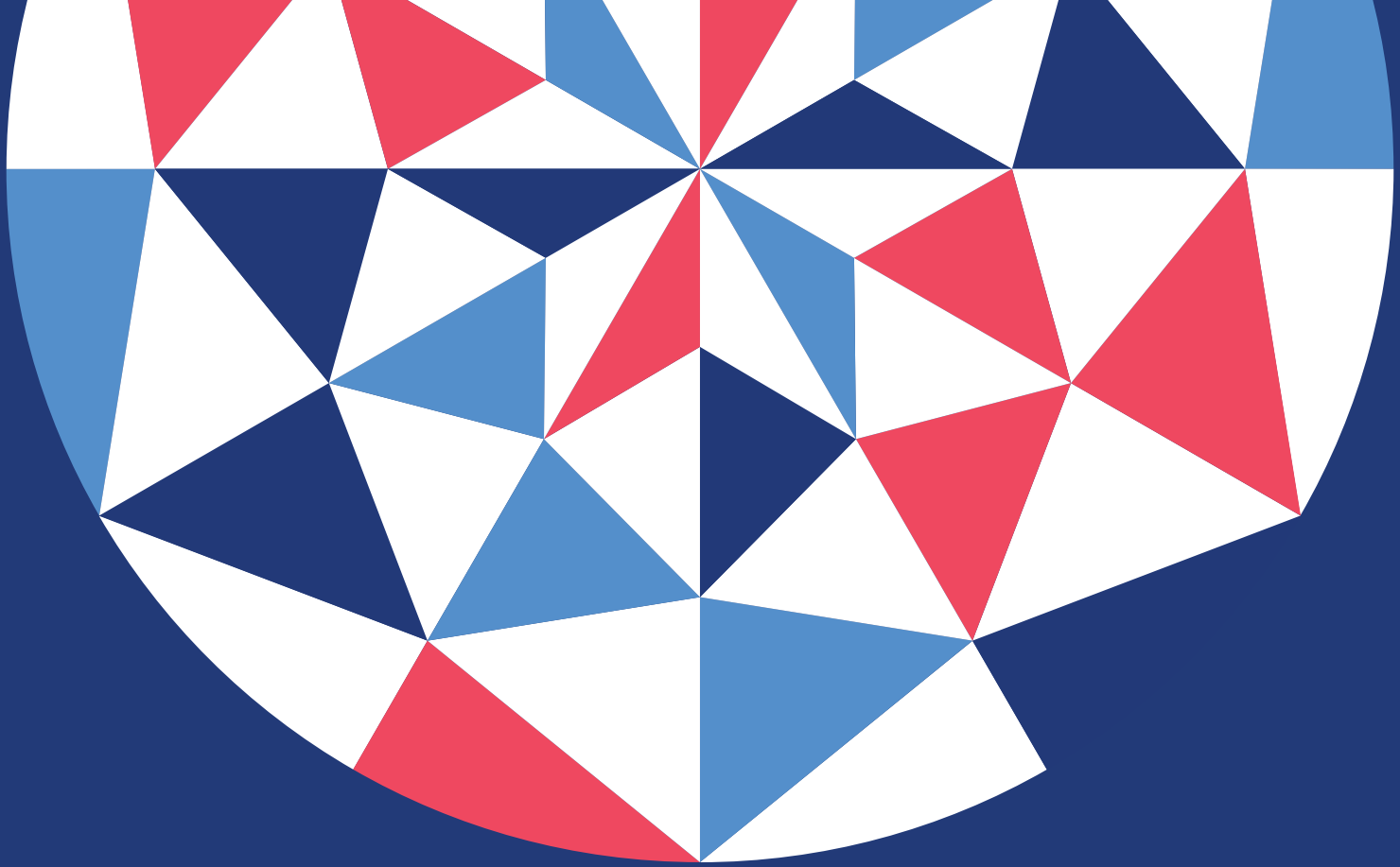

SCIENCE @SCALE

AAAS | ANNUAL MEETING
Phoenix, AZ | February 12–14, 2026

Science is at a pivotal moment in which we are reexamining how basic research is funded by the public and private sectors; seeking alternative ways for science to inform policy in the wake of the Chevron Doctrine being overturned; and exploring how science must be implemented at scale for meaningful impact in different contexts at the local, regional, national, and global levels.

Propose a session or workshop for the 2026 AAAS Annual Meeting!
Visit aaas.org/meetings for more information.

CONTENTS

21 FEBRUARY 2025
VOLUME 387 • ISSUE 6736

822

NEWS

IN BRIEF

IN DEPTH

FEATURES

INSIGHTS

PERSPECTIVES

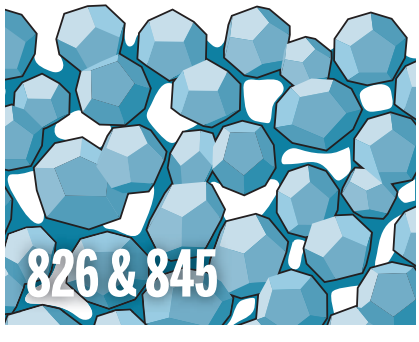

POLICY FORUM

BOOKS *ET AL.*

LETTERS

YOUR RESEARCH HAS ITS REWARDS.

Submit an essay by 3/15/25 to enter to win $25K.

The *Science* & PINS Prize seeks to recognize researchers who ask fundamental questions in the field of neuromodulation. It is awarded to scientists who conduct research at the intersection between engineering and clinical neurology to develop innovative neuromodulation approaches to advance our understanding of human health and disease or to guide therapeutic interventions.

To enter, just write a 1000-word essay about your research performed in the last three years. The Grand Prize winner will be presented a US$25,000 award, as well as have their essay published in *Science* magazine and online. A runner-up will have their essay published online.

For additional inquiries,
email SciencePINSPrize@aaas.org.

SCIENCE-PINS PRIZE FOR NEUROMODULATION
SCIENCE-PINS

SCIENCE.ORG/PINS

RESEARCH

IN BRIEF

RESEARCH ARTICLES

DEPARTMENTS

ON THE COVER

Researchers have developed a deep learning protein language model, ESM3, that enables programmable protein design. This illustration depicts users lining up to input prompts at a console attached to a machine that represents the language model. Three large funnels represent inputs from public databases of protein sequences, structures, and functional annotations. See page 850. *Image: Adam Simpson/Heart Agency*

PHOTO: SUN *ET AL.*

SCIENCE (ISSN 0036-8075) is published weekly on Friday, except last week in December, by the American Association for the Advancement of Science, 1200 New York Avenue, NW, Washington, DC 20005. Periodicals mail postage (publication No. 484460) paid at Washington, DC, and additional mailing offices. The title SCIENCE is a registered trademark of the AAAS. Domestic individual membership, including subscription (12 months): $165 ($74 allocated to subscription). Domestic institutional subscription (51 issues): $2865; Foreign postage extra: Air assist delivery: $135. First class, airmail, student, and emeritus rates on request. Canadian rates with GST available upon request, GST #125488122. Publications Mail Agreement Number 1069624. **Printed in the U.S.A.**
Change of address: Allow 4 weeks, giving old and new addresses and 8-digit account number. **Postmaster:** Send change of address to AAAS, P.O. Box 96178, Washington, DC 20090–6178. **Single-copy sales:** $15 each plus shipping and handling available from backissues.science.org; bulk rate on request. **Authorization to reproduce** material for internal or personal use under circumstances not falling within the fair use provisions of the Copyright Act can be obtained through the Copyright Clearance Center (CCC), www.copyright.com. The identification code for *Science* is 0036-8075. *Science* is indexed in the *Reader's Guide to Periodical Literature* and in several specialized indexes.

Science AAAS

Editor-in-Chief Holden Thorp, hthorp@aaas.org

Executive Editor Valda Vinson

Editor, Research Jake S. Yeston **Editor, Insights** Lisa D. Chong **Deputy Executive Editor** Lauren Kmec

DEPUTY EDITORS Stella M. Hurtley (UK), Phillip D. Szuromi, Sacha Vignieri **SR. EDITORS** Caroline Ash (UK), Michael A. Funk, Angela Hessler, Di Jiang, Priscilla N. Kelly, Marc S. Lavine (Canada), Sarah Lempriere (UK), Mattia Maroso, Yevgeniya Nusinovich, Ian S. Osborne (UK), L. Bryan Ray, H. Jesse Smith, Keith T. Smith (UK), Jelena Stajic, Peter Stern (UK), Yury V. Suleymanov, Valerie B. Thompson, Brad Wible **ASSOCIATE EDITORS** Jack Huang, Sumin Jin, Bianca Lopez, Sarah Ross (UK), Madeleine Seale (UK), Corinne Simonti, Ekeoma Uzogara **SENIOR LETTERS EDITOR** Jennifer Sills **NEWSLETTER EDITOR** Christie Wilcox **RESEARCH & DATA ANALYST** Jessica L. Slater **LEAD CONTENT PRODUCTION EDITORS** Chris Filiatreau, Harry Jach **SR. CONTENT PRODUCTION EDITOR** Amelia Beyna **CONTENT PRODUCTION EDITORS** Anne Abraham, Robert French, Julia Haber-Katris, Nida Masiulis, Abigail Shashikanth, Suzanne M. White **SR. EDITORIAL MANAGERS** Carolyn Kyle, Beverly Shields **SR. PROGRAM ASSOCIATE** Maryrose Madrid **EDITORIAL ASSOCIATES** Aneera Dobbins, Joi S. Granger, Lisa Johnson, Anita Wynn **SR. EDITORIAL COORDINATORS** Jeffrey Hearn, Alexander Kief, Ronmel Navas, Jerry Richardson, Isabel Schnaidt, Alice Whaley (UK), Brian White **EDITORIAL COORDINATORS** Clair Goodhead (UK), Kat Kirkman, Samantha Price **ADMINISTRATIVE COORDINATOR** Karalee P. Rogers **ASI DIRECTOR, OPERATIONS** Janet Clements (UK) **ASI OFFICE MANAGER** Victoria Smith **ASI SR. OFFICE ADMINISTRATORS** Dawn Titheridge (UK), Jessica Waldock (UK) **COMMUNICATIONS DIRECTOR** Meagan Phelan **DEPUTY DIRECTOR** Matthew Wright **SENIOR WRITERS** Walter Beckwith, Joseph Cariz **WRITERS** Abigail Eisenstadt, Mahathi Ramaswamy **SENIOR COMMUNICATIONS ASSOCIATES** Zachary Graber, Sarah Woods **COMMUNICATIONS ASSOCIATES** Kiara Brooks, Haley Riley, Mackenzie Williams

News Editor Tim Appenzeller

NEWS MANAGING EDITOR John Travis **INTERNATIONAL EDITOR** David Malakoff **DEPUTY NEWS EDITORS** Rachel Bernstein, Shraddha Chakradhar, Elizabeth Culotta, Martin Enserink, David Grimm, Eric Hand, Kelly Servick, Matt Warren (Europe) **SR. CORRESPONDENTS** Daniel Clery (UK), Jon Cohen, Jeffrey Mervis, Elizabeth Pennisi **ASSOCIATE EDITORS** Jeffrey Brainard, Michael Price **NEWS REPORTERS** Adrian Cho, Jennifer Couzin-Frankel, Phie Jacobs, Jocelyn Kaiser, Rodrigo Pérez Ortega (Mexico City), Robert F. Service, Erik Stokstad, Paul Voosen, Meredith Wadman **CONTRIBUTING CORRESPONDENTS** Vaishnavi Chandrashekhar, Dan Charles, Warren Cornwall, Andrew Curry (Berlin), Ann Gibbons, Sam Kean, Eli Kintisch, Kai Kupferschmidt (Berlin), Andrew Lawler, Mitch Leslie, Virginia Morell, Dennis Normile (Tokyo), Cathleen O'Grady, Elisabeth Pain (Careers), Charles Piller, Richard Stone (Senior Asia Correspondent), Gretchen Vogel (Berlin), Lizzie Wade (Mexico City) **CAREERS** Katie Langin (Associate Editor) **INTERNS** Hannah Richter **COPY EDITORS** Julia Cole (Senior Copy Editor), Hannah Knighton, Cyra Master (Copy Chief) **ADMINISTRATIVE SUPPORT** Meagan Weiland

Creative Director Beth Rakouskas

DESIGN MANAGING EDITOR Chrystal Smith **GRAPHICS MANAGING EDITOR** Chris Bickel **PHOTOGRAPHY MANAGING EDITOR** Emily Petersen **MULTIMEDIA MANAGING PRODUCER** Kevin McLean **DIGITAL DIRECTOR** Kara Estelle-Powers **DESIGN EDITOR** Marcy Atarod **DESIGNER** Noelle Jessup **SENIOR SCIENTIFIC ILLUSTRATOR** Noelle Burgess **SCIENTIFIC ILLUSTRATORS** Austin Fisher, Kellie Holoski, Ashley Mastin **SENIOR GRAPHICS EDITOR** Monica Hersher **GRAPHICS EDITOR** Veronica Penney **SENIOR GRAPHICS SPECIALISTS** Holly Bishop, Nathalie Cary **SENIOR PHOTO EDITOR** Charles Borst **PHOTO EDITOR** Elizabeth Billman **SENIOR PODCAST PRODUCER** Sarah Crespi **SENIOR VIDEO PRODUCER** Meagan Cantwell **SOCIAL MEDIA STRATEGIST** Jessica Hubbard **SOCIAL MEDIA PRODUCER** Sabrina Jenkins **WEB DESIGNER** Jennie Pajerowski

Chief Executive Officer and Executive Publisher Sudip Parikh

Publisher, Science Family of Journals Bill Moran

DIRECTOR, BUSINESS SYSTEMS AND FINANCIAL ANALYSIS Randy Yi **DIRECTOR, BUSINESS OPERATIONS & ANALYSIS** Eric Knott **MANAGER, BUSINESS OPERATIONS** Jessica Tierney **MANAGER, BUSINESS ANALYSIS** Cory Lipman **BUSINESS ANALYSTS** Kurt Ennis, Maggie Clark, Isacco Fusi **BUSINESS OPERATIONS ADMINISTRATOR** Taylor Fisher **DIGITAL SPECIALIST** Marissa Zuckerman **SENIOR PRODUCTION MANAGER** Jason Hillman **SENIOR MANAGER, PUBLISHING AND CONTENT SYSTEMS** Marcus Spiegler **CONTENT OPERATIONS MANAGER** Rebecca Doshi **SENIOR CONTENT & PUBLISHING SYSTEMS SPECIALIST** Jacob Hedrick **SENIOR PRODUCTION SPECIALIST** Kristin Wowk **PRODUCTION SPECIALISTS** Kelsey Cartelli, Audrey Diggs **DIGITAL PRODUCTION MANAGER** Lisa Stanford **ADVERTISING PRODUCTION OPERATIONS MANAGER** Deborah Tompkins **DESIGNER, CUSTOM PUBLISHING** Jeremy Huntsinger **SR. TRAFFIC ASSOCIATE** Christine Hall **SPECIAL PROJECTS ASSOCIATE** Shantel Agnew

MARKETING DIRECTOR Sharice Collins **ASSOCIATE DIRECTOR, BUSINESS DEVELOPMENT** Justin Sawyers **GLOBAL MARKETING MANAGER** Allison Pritchard **ASSOCIATE DIRECTOR, MARKETING SYSTEMS & STRATEGY** Aimee Aponte **JOURNALS MARKETING MANAGER** Shawana Arnold **MARKETING ASSOCIATES** Ashley Hylton, Lorena Chirinos Rodriguez, Jenna Voris **SENIOR DESIGNER** Kim Huynh

DIRECTOR AND SENIOR EDITOR, CUSTOM PUBLISHING Erika Gebel Berg

DIRECTOR, PRODUCT & PUBLISHING DEVELOPMENT Chris Reid **DIRECTOR, PRODUCT MANAGEMENT** Kris Bishop **PRODUCT DEVELOPMENT MANAGER** Scott Chernoff **PUBLISHING PLATFORM MANAGER** Jessica Loayza **SR. PRODUCT ASSOCIATE** Robert Koepke **PRODUCT ASSOCIATES** Caroline Breul, Anne Mason

ASSOCIATE DIRECTOR, INSTITUTIONAL LICENSING MARKETING Kess Knight **BUSINESS DEVELOPMENT MANAGER** Rasmus Andersen **ASSOCIATE DIRECTOR, INSTITUTIONAL LICENSING SALES** Ryan Rexroth **INSTITUTIONAL LICENSING MANAGER** Nazim Mohammedi, Claudia Paulsen-Young **SENIOR MANAGER, INSTITUTIONAL LICENSING OPERATIONS** Judy Lillibridge **MANAGER, RENEWAL & RETENTION** Lana Guz **SYSTEMS & OPERATIONS ANALYST** Ben Teincuff **FULFILLMENT ANALYST** Aminta Reyes

ASSOCIATE DIRECTOR, US ADVERTISING Stephanie O'Connor **US MID WEST, MID ATLANTIC AND SOUTH EAST SALES** Chris Hoag **US WEST COAST SALES** Lynne Stickrod **ASSOCIATE DIRECTOR, INTERNATIONAL** Roger Goncalves **SALES REP, ROW** Sarah Lelarge **SALES ADMIN ASSISTANT, ROW** Victoria Glasbey **DIRECTOR OF GLOBAL COLLABORATION AND ACADEMIC PUBLISHING RELATIONS, ASIA** Xiaoying Chu **ASSOCIATE DIRECTOR, INTERNATIONAL COLLABORATION** Grace Yao **SALES MANAGER** Danny Zhao **MARKETING MANAGER** Kilo Lan **ASCA CORPORATION, JAPAN** Rie Rambelli (Tokyo), Miyuki Tani (Osaka)

DIRECTOR, COPYRIGHT, LICENSING AND SPECIAL PROJECTS Emilie David **RIGHTS AND PERMISSIONS ASSOCIATE** Elizabeth Sandler **LICENSING ASSOCIATE** Virginia Warren **RIGHTS AND LICENSING COORDINATOR** Dana James **CONTRACT SUPPORT SPECIALIST** Michael Wheeler

EDITORIAL
science_editors@aaas.org

NEWS
science_news@aaas.org

INFORMATION FOR AUTHORS
science.org/authors/science-information-authors

REPRINTS AND PERMISSIONS
science.org/help/reprints-and-permissions

MULTIMEDIA CONTACTS
SciencePodcast@aaas.org
ScienceVideo@aaas.org

MEDIA CONTACTS
scipak@aaas.org

PRODUCT ADVERTISING & CUSTOM PUBLISHING
advertising.science.org/products-services
science_advertising@aaas.org

CLASSIFIED ADVERTISING
advertising.science.org/science-careers
advertise@sciencecareers.org

JOB POSTING CUSTOMER SERVICE
employers.sciencecareers.org
support@sciencecareers.org

MEMBERSHIP AND INDIVIDUAL SUBSCRIPTIONS
science.org/subscriptions

MEMBER BENEFITS
aaas.org/membership/benefits

INSTITUTIONAL SALES AND SITE LICENSES
science.org/librarian

AAAS BOARD OF DIRECTORS
CHAIR Gilda A. Barabino
PRESIDENT Keith R. Yamamoto
PRESIDENT-ELECT Willie E. May
TREASURER Carolyn N. Ainslie
CHIEF EXECUTIVE OFFICER Sudip Parikh
BOARD Cynthia M. Beall, Janine Austin Clayton, Kaye Husbands Fealing, Kathleen Hall Jamieson, Jane Maienschein, Robert B. Millard, Babak Parviz, William D. Provine, Juan S. Ramírez Lugo, Susan M. Rosenberg, Vassiliki Betty Smocovitis

Science serves as a forum for discussion of important issues related to the advancement of science by publishing material on which a consensus has been reached as well as including the presentation of minority or conflicting points of view. Accordingly, all articles published in *Science*—including editorials, news and comment, and book reviews—are signed and reflect the individual views of the authors and not official points of view adopted by AAAS or the institutions with which the authors are affiliated.

EDITORIAL

A direct hit

H. Holden Thorp
Editor-in-Chief,
Science journals.
hthorp@aaas.org

Earlier this month, the Trump administration set off a frenzy in the US scientific community when the National Institutes of Health (NIH) announced that indirect cost reimbursement for federally funded research would be capped at 15%, a drastic cut from a usual range of 50 to 70%. In the American system, a federal research grant comes with one component that pays the direct costs of research—covering salaries of the researchers and supplies and equipment they use—and a so-called indirect component that represents the government's contribution to facilities and administration—the overhead necessary to do the work. The indirect contribution does not cover everything needed to support the research; the remainder is provided by the university. This agreement between higher education and the government has been a hallmark of the funding system for 70 years. The scientific community must unite in speaking out against this betrayal of a partnership that has enabled American innovation and progress.

In rough terms, for every dollar spent on the planning and execution of research, another dollar is needed for not only the laboratory facility costs but also the support staff (including not just financial administrators but also people who handle radiation and chemical safety) and systems to administer the grants and ensure that the research follows government guidelines and expenditures are accounted for. The support staff has grown over the years, but that is because the government has increased the number and complexity of requirements that ensure that the money is properly spent.

The cost of overhead has typically been split about equally between the government and the institutions. Thus, if the indirect rate was 50%, then for every dollar of direct research expense, an additional 50 cents in indirect support would come from the government and 50 cents from the institution. Lowering the indirect rate to 15% would cut the overall federal support budget by 35 percentage points, leaving the university to cover the rest. For example, if an institution has $200 million in NIH support for direct costs, then at a 50% indirect cost rate, the indirect support from the government and the institution would each be $100 million. Thus, the total federal funding would be $300 million. Abruptly cutting the indirect rate to 15% would decrease the government's contribution to support costs to $30 million. That's a removal of $70 million from the total federal investment.

> **"...cuts to federal funding threaten to cause enormous economic damage..."**

Such an unforeseen and immediate hit to the budget doesn't leave the institutions with many options to make up the difference. They likely will have to cut other academic programs as well as raise revenue by increasing tuition fees and squeezing philanthropy for more donations. These two sources are unlikely to provide enough to fill the hole quickly, if at all. And it will be difficult to lose support staff while remaining in compliance with federal regulations. Violations can lead to sanctions that could further endanger federal funds or at least lead to public shaming. Perhaps, universities will have to walk away from federally funded programs altogether to lower the administrative burden. Either way, these cuts to federal funding threaten to cause enormous economic damage as well, especially in the states where these universities are located. In many states, including Alabama, Pennsylvania, and Missouri, an academic medical research center is the largest employer.

It is a misnomer to call these funds indirect costs. They are essential to the safe and ethical performance of research. The environment in which research is conducted is highly specialized and costly. The government's share is not a giveaway. Rather, it is an investment in the research infrastructure of the country. That partnership is now being broken and will lead to a further erosion in American leadership in science and technology at the very time it is needed most to compete worldwide.

These cuts should be a rallying cry for higher education to come together to make the case for the American system of research and teaching. Leaders have an opportunity to step forward and marshal their campuses in the effort. Conflicts between faculty and administrators, no matter how justifiable, should be set aside to focus attention on this ruthless takedown of academia. All disciplines will be affected by these cuts, not just science. This is a moment to unite.

–H. Holden Thorp

PHOTO: CAMERON DAVIDSON

Published online 11 February 2025; 10.1126/science.adw6467

NEWS

IN BRIEF

Edited by
Jeffrey Brainard

Robert F. Kennedy Jr. (right) was sworn in last week in the Oval Office as the top U.S. health official.

PHOTO: ALEX BRANDON/AP

TRUMP TRACKER

Judges, critics push back against a whirlwind of science actions

As President Donald Trump's administration fired numerous researchers at U.S. agencies (see story, p. 810), other White House efforts to overhaul government spending and policy drew criticism from scientists and some restrictions from federal judges. (Follow breaking news about the administration's decisions affecting research at https://scim.ag/TrumpAdmin.)

CHRONIC DISEASE PUSH After the U.S. Senate narrowly confirmed Robert F. Kennedy Jr. as secretary of the Department of Health and Human Services (HHS) on 13 February on a mostly party-line vote, Trump created a new commission to advance one of Kennedy's key priorities: preventing chronic diseases. Trump directed the Make America Healthy Again Commission to deliver a strategy focused on childhood chronic diseases within 180 days. Skeptics worry the panel, composed of Cabinet secretaries and other high-ranking administration officials, will serve as a vehicle for amplifying Kennedy's views on the dangers posed by vaccines and other treatments, views many scientists say are not supported by evidence. Kennedy has also called for investigating conflicts of interest between officials at federal health agencies and pharmaceutical companies.

AID FREEZE REVERSED A judge issued a temporary injunction on 13 February blocking the Trump administration's blanket freeze on foreign aid, which has halted the distribution of food and medicines and interrupted clinical trials and other types of research in many countries. In a lawsuit brought by government contractors and others, U.S. District Court Judge Amir Ali ruled that the freeze has caused "irreparable harm" and lacked adequate justification. But as *Science* went to press, groups supported by the U.S. Agency for International Development and other federal agencies said they were still having difficulty accessing promised funds. And in some cases, they said, the funding thaw does not matter because it is impossible to restart research projects.

NIH GRANTS THAW The U.S. National Institutes of Health (NIH), the nation's largest single source of nondefense research funding, last week lifted a freeze on issuing new grants and funding continuing ones. The agency started the pause early this month to review the awards, checking for compliance with Trump's orders barring federal funds for diversity, equity, and inclusion, and other topics. But in a 12 February memo, NIH acknowledged the stoppage violated two court orders suspending Trump's order in January that froze all federal funding, according to the news site Popular Information. Some NIH grantees say they are still unclear whether their award money will arrive.

GENDER CRITICISM The administration has directed the U.S. Centers for Disease Control and Prevention (CDC) and the Food and Drug Administration (FDA) to place a notice condemning "gender ideology" on web pages the White House says "inculcate or promote" that ideology. The pages were taken offline on 31 January in response to an administration memo, but on 11 February a federal judge ordered they be restored. Some of the web pages include data sets, such as CDC's Youth Risk Behavior Surveillance System, widely used by public health researchers. The required notice—which was reported by *The Washington Post* and appears on several restored CDC and FDA pages—states that any information "promoting gender ideology is extremely inaccurate and disconnected from the immutable biological reality that there are two sexes, male and female." That statement is scientifically inaccurate, many researchers say.

Last month, Trump ordered agencies to replace the word "gender" with "sex" throughout federal documents.

EDUCATION SURVEYS The administration last week said it had canceled $881 million in government contracts to collect information on the state of U.S. education. Researchers warn the move will blind the government to important trends from preschool to college and beyond. The cuts at the National Center for Education Statistics, orchestrated by the Department of Government Efficiency, led by Elon Musk, include projects studying problems in U.S. schools such as declining student mental health, the growing gap between low- and high-achieving students, and rising chronic absenteeism.

MARCHES PLANNED A group called Stand Up for Science is organizing rallies on 7 March in Washington, D.C., and in state capitals to support research. Without referring directly to Trump, the group is calling for stopping interference with and censorship of science; it also opposes attacks on diversity, equity, and inclusion in research. The organizers are different from those who spurred the March for Science in 2017, shortly after the first Trump administration began.

GEOLOGY HEAD In other news, Trump nominated geologist Ned Mamula to lead the U.S. Geological Survey (USGS). He has called for the United States to increase mining of uranium and improve its access to other minerals needed for manufacturing and other purposes, a view in sync with Trump's foreign policy. Mamula worked as a staff scientist at USGS before directing the Department of Energy's critical minerals program during the first Trump administration and former President Joe Biden's administration. In 2023, he become chief geologist of GreenMet, a company that promotes the U.S. critical minerals industry. He holds a Ph.D. in geological and earth sciences from Texas A&M University.

PHOTO: DAVID TIPLING PHOTO LIBRARY/ALAMY

Threats to peatlands mapped

CONSERVATION | In their soggy, acidic soil, Earth's peatlands store an estimated 600 gigatons of carbon, more than the world's forests—despite taking up just 3% of land. Nearly one-quarter of this habitat is under intense threat from human activities, such as farming, deliberately set management fires, and mining, according to a new global survey. Just 17% of the 4 million square kilometers is protected, far less than other carbon-rich habitats such as tropical forests or mangroves. And half of protected peatlands areas are under moderate to high levels of threat, the team reported last week in *Conservation Letters*. When peatlands are disturbed, they release their carbon as greenhouse gases. One bright spot: More than 1 million square kilometers of peatlands lie on the land of Indigenous peoples, where they may be managed more sustainably than elsewhere.

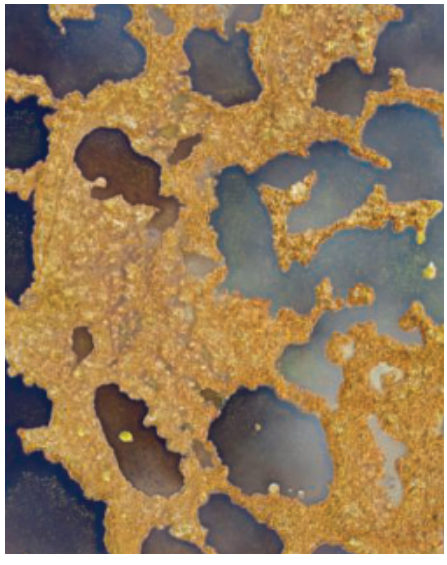

Peatlands, such as a blanket bog in Scotland shown in this aerial view, store vast amounts of carbon.

Sleuth endows integrity grants

SCIENTIFIC FRAUD | Elisabeth Bik, a microbiologist and prominent independent scientific integrity consultant, has donated $200,000 to establish a grants program to help expand investigations of research fraud. The money is the entire sum of Bik's 2024 Einstein Foundation Award for Promoting Quality in Research that honored her work. The Elisabeth Bik Science Integrity Fund will be administered through the nonprofit Center for Scientific Integrity, which operates the Retraction Watch news website, and Bik will choose the grantees, she and the center announced last week. Bik says the grants will likely be modest—typically several hundred dollars each—to cover expenses such as relevant courses and training, buying software, writing educational resources to aid other sleuths, or travel to conferences on research integrity. Independent sleuths, most of whom are volunteers, have few sources of funding for their work, such as rooting out manipulated images, fabricated text, cooked data, and paper mills.

More U.S. universities join elite

RANKINGS | Forty-one universities have ascended into the top tier of U.S. research powerhouses, a status viewed as aiding the recruitment of top faculty and students. The number of R1 institutions in the latest Carnegie Classification of Institutions of Higher Education, released last week, now stands at 187, a 28% increase over the total in the 2021 rankings. The increase reflects new criteria. An R1 university must award 70 doctoral degrees annually and have $50 million a year in research activity, but the previous formula required institutions to award those degrees across many fields, a standard some called arbitrary. The new one helped elevate Howard University, making it the only historically Black college or university in the R1 category. Other newcomers include five flagship universities in states that previously had no R1 institutions: Idaho, North Dakota, Rhode Island, Vermont, and Wyoming.

Flu shot for chickens advances

INFECTIOUS DISEASES | With egg prices at an all-time high in the United States as H5N1 influenza viruses devastate poultry flocks, a vaccine to protect the birds moved one step closer to the market. The U.S. Department of Agriculture on 13 February issued a "conditional approval" to the manufacturer Zoetis to market its poultry vaccine. The agency still must give a final green light for its use because of special regulations surrounding so-called highly pathogenic avian influenza viruses. China, Egypt, France, and Mexico already use vaccines to protect poultry against such viruses; the U.S. has relied on culling flocks of infected birds to control them. The H5N1 viruses now in circulation occasionally sicken humans as well and have jumped to U.S. dairy cattle, causing significant losses in that industry.

PHOTO: MARK SCHIEFELBEIN/AP

SCIENCE POLICY

Mass firings decimate U.S. science agencies

White House's sweeping, chaotic dismissals shatter careers and threaten research efforts

By **John Travis**, **Katie Langin**, **Jocelyn Kaiser**, *and* **Meredith Wadman**

On 13 February, a research entomologist at the U.S. Department of Agriculture (USDA) was among the first, receiving an email after the close of business hours saying they were being "removed" from what they describe as a dream job, studying a key problem in agriculture science. The change had gone into effect 14 minutes before the email arrived. "The letter said I was being let go due to poor performance, which is nonsensical since they invited me to apply for a promotion just the other month," the stunned researcher says.

Thousands of other federal scientists were similarly shocked over subsequent days as President Donald Trump's administration unleashed a massive, unprecedented, and chaotic wave of firings across the U.S. government. The job losses—guided by the White House's semiofficial Department of Government Efficiency (DOGE) run by billionaire entrepreneur Elon Musk—struck tens of thousands of workers. Most were among some 200,000 probationary workers in the 2.4 million person federal workforce—people who had recently been hired or transferred to a new position, and enjoyed fewer job protections. The layoffs decimated the foot soldiers of many health and science agencies, sweeping up early-career scientists as well as old hands in new positions. Scores of scientists working as federal contractors received termination notices as well.

The total tally of dismissed scientists remains unclear. The Department of Health and Human Services (HHS)—which includes the National Institutes of Health, the Centers for Disease Control and Prevention (CDC), and the Food and Drug Administration (FDA)—planned to cut "~5200" employees, according to a 14 February internal NIH memo, but some got eleventh hour reprieves.

At NIH, where institute directors were alerted to the imminent firings at a hastily called Friday morning meeting, about 1500 employees were initially scheduled to be cut, but the list dropped below 1200 after some got designated as essential; at CDC an early list targeted almost 1300 but later shrank to 750. On 18 February, the National Science Foundation dismissed 168 employees, roughly 10% of its workforce. After broad firings at FDA, its deputy commissioner for human food resigned over the 89 people cut from his division. Other science agencies expect dismissals as DOGE marches on.

Senior members of U.S. scientific leadership were also axed last week. Lawrence Tabak, former acting director of NIH who still held the second highest role there, was forced to retire. HHS also fired bioengineer Renee Wegrzyn, director of the Advanced Research Projects Agency for Health, a $1.5 billion agency created 3 years ago to fund high-risk, high-payoff biomedical research.

Although the final toll on science agencies may not exceed the number of staff who retire, resign, or otherwise leave government each year, observers fear the abrupt and seemingly indiscriminate firings could hamper vital research and waste money. "This is truly a national tragedy and one that is being executed by people who do not understand the value of scientific research," says molecular biologist Shirley Tilghman, former president of Princeton University and longtime adviser to NIH directors.

Administration statements and sources defended the cuts as strategic measures to increase efficiency, saying they are well-planned and affect less important employees. But crit-

Epidemic Intelligence Service disease detectives like these were fired but given a quick reprieve.

ics note the probationary firings swept away recently promoted veteran federal scientists and experienced researchers who had just been lured to government service. They also say the chaotic rollout, which included last-minute scrambles to remove employees from to-be-fired lists and rehire needed people, reflected hastiness.

For example, dozens of physicians in subspecialty training, research nurses, and other essential staff at NIH's massive Clinical Center were short-listed to be fired, according to sources. But hours before notification they were removed from the list; their absence could have closed the facility, jeopardizing hundreds of often deeply ill patients and ruining biomedical studies.

Members of CDC's famed disease outbreak training program, the Epidemic Intelligence Services were told last week that their positions had been eliminated. But the decision was reversed over the weekend after an uproar. Those in an equally prestigious but less visible CDC program, the Laboratory Leadership Service, were not spared. And despite the stated intent of the new HHS secretary, Robert F. Kennedy Jr., to focus on combating chronic diseases, CDC eliminated contractors at its National Center for Chronic Disease Prevention and Health Promotion.

One, who worked on cardiovascular disease, messaged on Signal: "Half of my team (we work on epidemiology and surveillance) is contractors and we have all been terminated within a few short hours."

At the National Nuclear Security Administration, a part of the Department of Energy that manages nuclear weapons, officials reportedly scrambled to rehire key technical staff—but couldn't reach them because their government emails had been disconnected.

Some science leaders argued the Trump administration is not specifically targeting research. "Science seems to be collateral damage to these [downsizing] efforts that are almost random, by date of hire or date of promotion," says Sudip Parikh, CEO of AAAS, the world's largest science society. "It's not strategic. It's not based on the needs of the future, the needs of science." (AAAS publishes *Science* but the News team operates independently.)

Much remained uncertain as *Science* went to press, including whether some firings will withstand legal challenges. Congress may also eventually push back; NIH, for example, has strong bipartisan support.

Parikh and others said this year's funding levels for the science agencies, due to be decided in Congress over the next few weeks, will determine the fate of many more federal scientists and the research they oversee. "The next month is probably one of the most important months in the history of science and technology in the United States—and I'm not one to tend to hyperbole," Parikh told attendees at the AAAS annual meeting in Boston last weekend.

Since the firings began, *Science* has communicated with dozens of current and former federal scientists, who often asked to remain anonymous. They have described tear-filled meetings and critical work being interrupted. "It's pretty horrific," one said. "The abrupt way this was implemented prevented us from even being able to prioritize what data needed to be collected or to transfer that data in an orderly way to collaborators," another wrote.

Dismissed federal scientists expressed fear over finances and lamented the destruction of a long-running bargain where they provide applied research or services for the U.S. government in exchange for a secure career. One fired U.S. Geological Survey (USGS) postdoc was working on an invasive species problem with "huge economic implications" and had wanted to mirror his mom who worked for a federal agency for 20 years. After his termination notice, the shocked postdoc still hoped to salvage work before losing computer access. "I'm trying to quickly share code and files with people who are still going to be at the research center … I don't know who's going to be able to pick up this," he said on the day of his firing.

"It's a national tragedy."
Shirley Tilghman, Princeton University

At NIH, some newly hired or promoted division directors had to call junior staff to inform them of their impending firings while knowing they, too, were targeted for termination. And one U.S. Fish and Wildlife Service (FWS) employee who serves in a manager role described a colleague who is living in government housing and had 7 days to move out. "It's insane," the manager says. "We lost about 40% of the staff" at that office, they add.

Many of the fired workers worry about finding another job in a private or academic market flooded with government scientists. "My wife is 6 months pregnant and we are scrambling to make sure we stay insured through the birth and beyond," one former USDA researcher told *Science*. "[I feel] betrayed, gutted, lost, anxious, and furious," says one biologist who received a termination notice from FWS. "I have a mortgage, a car payment, prescriptions, and other bills to pay and not much savings to fall back on."

Beyond the personal toll, the firings threaten ongoing science, including key agricultural and health surveillance efforts. One USDA bird flu scientist kept a job but had to say goodbye to several colleagues. "We all work on high pathogenicity avian influenza—seems like an absolutely reckless time to fire qualified scientists who are directly involved in monitoring and responding to this virus right now," the scientist wrote.

Many of the termination notices seen by or described to *Science* cite inadequate performance as justification. For example, letters emailed to multiple USDA researchers reference a 2005 report by the U.S. Merit Systems Protection Board that stated that until an employee's probationary period is over, they have "the burden to demonstrate why it is in the public interest for the Government to finalize an appointment to the civil service." The letters then go on to say: "The Agency finds, based on your performance, that you have not demonstrated that your further employment at the Agency would be in the public interest."

But some employees had never even had a manager's review. "The claim this is performance based is objectively false," one USDA scientist says. "To argue that I'm not adequate in my job is asinine, delinquent, delirious," vented a fired USGS scientist.

Risa Lieberwitz, a labor and employment law expert at Cornell University, says the way the mass firings were implemented contradicts regulations written by the U.S. Office of Personnel Management. She notes that the purpose of the probationary period is to thoroughly evaluate a person's performance before they're given a permanent government post. "The regulations are not written in a way to simply give carte blanche to the government to decide to terminate an employee … for any reason."

Some of the fired employees have formed chat groups outside official channels. One former USGS biologist is part of a Signal group that is discussing "how and if we can file for unemployment, how to make a formal complaint to our supervisors about our firing if we believe it was illegal, [how] and what class action lawsuits that are popping up might be applicable." Last week five unions representing federal workers filed a class action lawsuit to stop the firings; the first emergency court hearing on the matter was scheduled for this week.

Many scientists also plan to appeal their termination directly. One fired worker, who spoke to *Science* a few minutes after taking a call from an attorney's office, said, "It's bad, but I'm not gonna lay down and roll over. I'm going to do my due diligence. … Got to stay positive." ■

With reporting by Jeffrey Mervis.

This young adolescent chimp, Virginia, is working on her social skills in the Kibale Forest of Uganda.

PHOTO: KEVIN LEE

ANIMAL BEHAVIOR

Researchers seek lessons from animals' growing pains

Studies reveal common patterns of adolescence in chimps, elephants, and dolphins

By **Ann Gibbons**, *in Bethesda, Maryland*

On a humid morning in May 2024, two young male chimpanzees in the Kibale Forest of Uganda sat sponging up water from a puddle with a leaf and languidly dribbling it into their mouths. Suddenly, an adolescent female chimp named Virginia threw a large branch at one of them. Her bottom was pink and swollen, signaling that at age 10, she was beginning to mature sexually. But the object of her attention, a 9-year-old male named Sufjan, ignored her, and eventually she gave up, making a dramatic exit on a liana vine.

Virginia was just being a teen. She "was saying, 'Pay attention to me,' whether to play or antagonize," says graduate student Isabelle Clark at the University of Texas (UT) at Austin, who narrated the video last month to a working group on adaptive social learning in adolescence. Virginia was "learning how to attract the interest of males," says Clark, who filmed the video at the Ngogo Chimpanzee Project in Uganda as part of her research on how territorial behavior develops in juvenile and adolescent chimps.

The group's discussion brought together primatologists, anthropologists, animal behavioral biologists, and psychologists to look at the growing pains of adolescence across species of mammals, including chimpanzees, bonobos, dolphins, elephants, and dogs, as well as humans. The researchers aim to identify milestones in social learning that determine animals' success as adults—and trace how behavior and temperament in adolescence can predict problems later in life.

They have already made common findings across species, such as the shift from social learning primarily focused on parents to learning from peers or other adults. Such observations could "have clinical and policy implications" for supporting human adolescents, says pediatrician Ron Dahl, founding director of the University of California, Los Angeles's Center for the Developing Adolescent and director of the Institute of Human Development at UC Berkeley.

As any parent of a teenager knows, humans take a long time to grow up. Their adolescence lasts nearly a decade, typically starting with a dramatic growth spurt and surging hormones, which initiate changes in emotion, cognition, and behavior. Evolutionary biologists have theorized that humans and some other highly social mammals evolved this long period between puberty and adulthood to allow more time and energy for learning how to adapt to complex social interactions and environments. Mammals that invest more time to grow up have offspring that are more likely to survive, says primatologist Aaron Sandel of UT Austin.

But which other species go through adolescence? How is their social learning adaptive, and what similarities does it bear to ours? These were the questions researchers asked at the informal gathering, which was to be held as a workshop at the U.S. National Institutes of Mental Health but was canceled at the last minute because of President Donald Trump's freeze on communication at the National Institutes of Health. Instead, some researchers who had traveled here for the workshop gathered in their hotel to talk about their work. It focused on chimps, dolphins, and other animals that live in complex fission/fusion social groups, where individuals shift between different social clusters over time, similar to humans.

Adolescent female chimps face especially difficult social tests because most have to leave their birth group to join a new troop. Adolescents like Virginia seem to be testing not just their ability to attract mates, but also their ability to handle aggression, says primatologist Anne Pusey of Duke University, who has studied adolescent female chimps at Gombe National Park in Tanzania.

The stakes are high because young chimps can be seriously injured, and even killed, when they change groups. How adults respond to a young female's social cues on the day she arrives also determines her social rank, which influences the quality of her mates, and how she and her offspring fare, adds Rachna Reddy, a biological anthropologist at the University of Utah, co-director of the Ngogo Chimpanzee Project. "What you do on Day 1 when you're 14 determines what your baby will eat 40 years later."

She and other researchers shared recent videos, photos, and other observations of social learning in adolescent chimps. Much of it involves peering intently at adults. Adolescents are particularly interested in adults gathering food, having sex, and treating wounds with leaves or insects. Adolescent males, who remain in their birth group, spend a lot of time grooming high-ranking males and studying their habits, especially their aggressive behavior, like disciples learning at the foot of a master, Reddy says.

Behavioral ecologist Kate Evans of the Gothenburg Global Biodiversity Centre and Elephants for Africa described a similar need for older male examples among elephants. Evans recounted a notorious episode in-

volving a gang of young male elephants at Pilanesberg National Park in South Africa in the 1990s. The park had been stocked with young male and female elephants, but not large bull elephants, which were challenging to transport. Without the company of older males, the young males went into a state known as musth and were flooded with reproductive hormones years earlier than normal. They tried to mate with the park's rhinos and ended up killing 50 of them. In the end, hormonal and behavioral cues from six older males trucked in during the crisis modulated the young males' hormones and they became far less aggressive.

Some of the most mesmerizing videos showed social play among young male dolphins in Australia's Shark Bay. As juveniles, males spend many hours practicing synchronized leaps and turns, sometimes rolling each other and goosing other males' genitals. This seems to be preparation for behavior after puberty, when most males form alliances with one or two other males to herd females for mating, says behavioral biologist Kathryn Holmes of the Brookfield Zoo Chicago's Sarasota Dolphin Research Program, who presented the video, taken during her Ph.D. with Shark Bay Dolphin Research.

The cost of missing out on such teamwork can be high. Male dolphins that didn't join pods had fewer offspring, Holmes says.

For humans, too, finding older mentors and forming alliances with peers can be a key to social success. But in our species, the hormones that drive teens to find new friends and mates can also backfire in risk-taking behavior and hypersensitivity to peers' reactions and to social rejection. Overall morbidity and mortality increase dramatically worldwide during adolescence, and 75% of lifetime mental disorders begin by age 25, Dahl says.

By identifying skills and learning processes essential for adolescents across species, researchers in the working group hope to develop a general model of this tumultuous life stage. It would include testable hypotheses about key behaviors teens need to learn during pivotal points in development that might indicate the best times and targets for intervention in young humans struggling with the transition. For example, the onset of puberty represents a "window of opportunity for adaptive social learning," Dahl says, especially if teens can learn to overcome anxieties and develop key relational skills.

The study of other species might also suggest how and when it's most critical to provide mentorship, encourage creative risk taking, and foster social interactions with peers, Dahl says. The research holds an overarching lesson, he adds: "Adolescents have the capacity to learn how to change their identities in deep ways." ■

PHOTO: JIM WEST/REPORT DIGITAL-REA VIA REDUX

ENERGY TECHNOLOGY

Sodium batteries power up

Batteries based on sodium could aid a future green energy economy—if they can match lithium batteries' performance

By **Robert F. Service**

Lithium-ion batteries are ubiquitous, not just in earbuds, phones, and cars, but also in massive facilities that store renewable energy for when the Sun doesn't shine or the wind dies down. But lithium itself is relatively scarce and available from just a few countries. A world that runs on renewable energy would need 200 times more battery capacity than exists today—and that probably means a different kind of battery. "I don't know if we can get there with just lithium-ion," says Y. Shirley Meng, a battery chemist at the University of Chicago.

A decades-old technology may be rising to the challenge: batteries that use sodium rather than lithium ions to carry and store charge. Sodium is everywhere, in seawater and salt mines, so supply and cost aren't a problem. But the metal isn't as good at storing charge as lithium because its ions are three times bigger, hampering their ability to slip in and out of existing battery electrodes. Labs worldwide are developing new electrode materials to address that shortcoming, and in the past 6 months, several groups have announced sodium batteries that hold as much energy as low-end lithium cells. "The progress has been amazing," says Dan Steingart, a battery chemist at Columbia University. Meanwhile, commercial sodium-ion batteries are starting to roll off the assembly lines for electric vehicles, scooters, and grid power storage.

Researchers caution, though, that sodium batteries are not ready for widespread deployment. "We're not there yet," says Jean-Marie Tarascon, a solid-state chemist at the College of France. The batteries are still far from matching the performance of the best lithium-ion cells. And the economic incentive for a shift is lacking for now: Lithium shortages remain a theoretical concern, and the price of the metal actually dropped 70% in the past 3 years because of an oversupply.

Like lithium batteries, those based on sodium work by passing positively charged ions between a pair of electrodes separated by an ion-conducting electrolyte. During charging, electrons are fed to the negatively charged anode, attracting metal ions to flow through the electrolyte from the positively charged cathode. During discharge, electrons are drawn out of the battery, causing the ions to travel back from anode to cathode.

Because sodium ions are larger than lithium ions, fewer of them can squeeze into the anode to store charge. The need for larger cells to hold the same amount of power adds cost and bulk. Sodium batteries have struggled to reach even half the storage capacity of the best lithium batteries, which hold more than 300 watt-hours of energy per kilogram (Wh/kg). But Gui-Liang Xu, a battery chemist at Argonne National Laboratory, says, "There are multiple avenues to go down" to address the challenge.

There's no shortage of sodium, as salt piles at a facility in Oklahoma attest.

One is changing the composition of the anode. Most lithium-ion cells use graphite, a form of carbon whose tightly layered structure tends to exclude sodium ions. Many researchers have turned to an alternative form of carbon, called hard carbon, made up of a jumble of carbon particles that leaves pores into which sodium ions can wiggle.

Unfortunately, all those pores also reduce an anode's energy-storing volume. But researchers have found that adding tin to the anode can help. When stabilized on a carbon support, each tin atom can bind up to 3.75 sodium ions, boosting an anode's ability to hold sodium, and thus energy. For example, batteries developed at the San Diego–based startup UNIGRID hold 170 Wh/kg. Although this remains less than the 200 Wh/kg of a low-end lithium battery, "it looks very exciting," says Yan Yao, a sodium-ion battery expert at the University of Houston.

Another improvement comes from tweaking the composition of the positively charged cathode, typically made of metal oxides, for better sodium storage and flow. One of the most popular new materials is a mixture of sodium, vanadium, phosphorus, and oxygen (NaVPO), which tends to form a layered structure that allows sodium atoms to readily enter and exit.

For now, NaVPO's energy density is moderate compared with that of cathodes in lithium cells. But researchers led by Pieremanuele Canepa, a chemist at the University of Houston, recently used computer modeling and x-ray diffraction to identify a promising tweak to NaVPO's crystalline structure. In a reported posted online on 23 October 2024 in *Nature Materials*, Canepa and his colleagues reported not only synthesizing the new material, but incorporating it into a sodium-ion battery cathode that could hold 15% more energy than previous NaVPO designs.

A more radical approach is to make cathodes out of organic compounds, which can also form layered structures able to hold and release sodium ions. Many organics decompose in the presence of a battery's electrolytes, but in the 5 February issue of the *Journal of the American Chemical Society*, researchers led by Mircea Dincă at the Massachusetts Institute of Technology reported creating a more durable layered organic cathode, called TAQ. The material not only proved stable for thousands of charge and discharge cycles, but TAQ's energy density was among the highest of any sodium-ion cathodes ever made. Canepa calls it "a beautiful piece of chemistry."

As a result of these and other advances, "Industry's interest is really high right now," says Laurence Croguennec, a chemist and managing director of the Institute of Condensed Matter Chemistry of Bordeaux. In November 2024, CATL, the world's largest batterymaker in China, unveiled its second-generation sodium-ion battery, which it claims holds 200 Wh/kg, up from 160 Wh/kg in its first-generation cells. Meanwhile, BYD, one of CATL's rivals, says it is building a factory to produce 30 gigawatt-hours' worth of sodium-ion batteries per year by 2027, in part for renewable-energy storage. At least a half-dozen other startups around the world are also jumping in with their own tweaks to battery chemistry.

Still, many battery experts remain both cautious about sodium's future and skeptical of some company announcements. "There's a lack of transparency" about the details of battery design and performance, says UNIGRID CEO Darren Tan.

The hurdles aren't just technical. For now, the low cost of lithium undercuts sodium's chief selling point, Steingart says. Sodium-ion battery manufacturers also remain too small to benefit from economies of scale. In November 2024, such challenges upended one of the field's pioneers when the Swedish sodium-ion battery firm Northvolt filed for bankruptcy.

> **"The progress [in sodium battery storage capacity] has been amazing."**
> **Dan Steingart**
> Columbia University

Politics is another wild card. When U.S. President Donald Trump swept into office last month, he immediately announced a halt to federal support for wind and solar power projects, a step that could shelve plans to deploy large-scale backup battery systems. (In a move that perhaps cuts the other way, in January China announced new export restrictions on graphite, a key component of lithium-ion batteries, in response to new 10% tariffs on Chinese goods announced by the Trump administration.)

But William Chueh, a materials scientist at Stanford University, says it's technological advances that will decide how cost effective sodium-ion batteries become. On 13 January, he and his colleagues published a paper online in *Nature Energy* evaluating more than 6000 road maps for producing them, and concluded that to be fully competitive with low-cost lithium-ion batteries, researchers will need several breakthroughs, including eliminating all of the expensive materials sodium batteries currently require, such as nickel and vanadium.

Steingart believes those advances are coming. When it comes to understanding the basic chemistry of sodium-ion batteries, he says, "we're still in the early days." ■

ASTROPHYSICS

A new origin story for the highest energy cosmic rays

Curious similarity among space particles points to neutron star mergers

By **Adrian Cho**

Earth is constantly pelleted with subatomic bullets. Every few seconds, a single, infinitesimal atomic nucleus traveling at near–light speed crashes into the atmosphere packing as much energy as a golf ball midflight. Physicists have struggled for decades to explain how and where the particles acquire such stupendous energy, invoking, for example, supermassive black holes at the cores of galaxies. But one theorist now argues that a subtle similarity among the highest energy rays points to a more modest source: the mergers of neutron stars. Proposed in a paper in press at *Physical Review Letters*, the idea has piqued the interest of astrophysicists, who now aim to test it.

"I totally agree that a neutron star merger is a promising candidate," says Toshihiro Fujii, a particle astrophysicist at Osaka Metropolitan University who works with the Telescope Array, a huge cosmic ray detector in Dugway, Utah. Markus Roth, a particle astrophysicist at the Karlsruhe Institute of Technology who works on the Pierre Auger Observatory, an even bigger detector in Argentina, says, "I do not see any argument that would contradict [the] proposal."

Scientists can't spot an ultra–high energy cosmic ray directly. Rather, they study the kilometers-wide avalanche of electrons and other charged particles like positrons and pions created when one strikes the atmosphere. For example, Auger consists of 1600 particle detectors spread over 3000 square kilometers of the Pampa Amarilla, an area more than four times the size of New York City. By counting charged particles and precisely timing when they hit its detectors, researchers can deduce the direction and energy of the original cosmic ray. From the periphery, telescopes in four

stations peer into the sky and, on moonless nights, detect the faint glow produced when the shower make the air fluoresce as it waxes and wanes.

Auger started taking data in 2005, and the Telescope Array—which deployed 507 detectors over 762 square kilometers until it was recently enlarged—began 2 years later. The arrays have detected more than 1 million cosmic rays with energies above 1 exa-electron volt (EeV), 100,000 times higher than reached by the protons at the world's biggest atom smasher, Europe's Large Hadron Collider (LHC).

Whatever it is, the cosmic accelerator that creates those rays has to have a magnetic field strong enough and a volume large enough to contain protons and atomic nuclei as they whirl in ever-bigger circles to gain the requisite energy. Many physicists favored so-called active galactic nuclei (AGNs), in which matter swirls around a giant black hole. In 2007, Auger reported that rays above 57 EeV appeared to emerge from nearby AGNs. But that correlation faded with more data.

Theorists have suggested other possible sources, such as a tidal disruption, in which a star is sheared apart as it swirls into a black hole, or a long gamma ray burst, a massive explosion triggered when the core of huge young star collapses to form a black hole. But none seems capable of producing as many ultra–high energy cosmic rays as are observed, or explaining their spectrum of energies. And none accounts for the most energetic cosmic rays, such as a 240-EeV marvel reported by the telescope array in 2023.

Merging neutron stars are a more promising source, argues Glennys Farrar, a theorist at New York University. In 2017, physicists and astronomers spotted the first such merger by detecting ripples in space called gravitational waves, churned out as two neutron stars swirled into each other. Telescopes of all kinds watched the resulting "kilonova" explosion spew gold and other newly forged heavy elements into space. Such a gyrating merger could serve as a dynamo, converting gravitational energy into a roiling magnetic field strong enough to produce the highest energy cosmic rays, Farrar argues in the new paper. It could also explain a surprising regularity among the highest energy rays.

Twenty years ago, physicists thought that, like lower energy cosmic rays, the highest energy ones were protons. But details of the air showers detected by Auger suggest the most energetic cosmic rays are actually heavier nuclei, ranging up to iron. More important, Auger data suggest that at the highest energies, whatever the number of protons in a nucleus, the energy per proton—a measure called the rigidity—is roughly constant.

Sources as variable in size as AGNs, tidal disruptions, and long gamma ray bursts shouldn't produce that striking regularity. But neutron star mergers could, Farrar says, as they're all nearly the same. A neutron star—the corpse of a middle-weight star that has exploded—is essentially an atomic nucleus 20 kilometers wide with a mass between 1.3 and 2.0 times that of the Sun. That narrow mass range implies every neutron star merger produces a similar dynamo that, like a humanmade accelerator of a fixed size, should boost any nucleus to the same energy per proton, says Francis Halzen, a physicist at the University of Wisconsin–Madison. Each merger, he says, is "like an LHC in the sky."

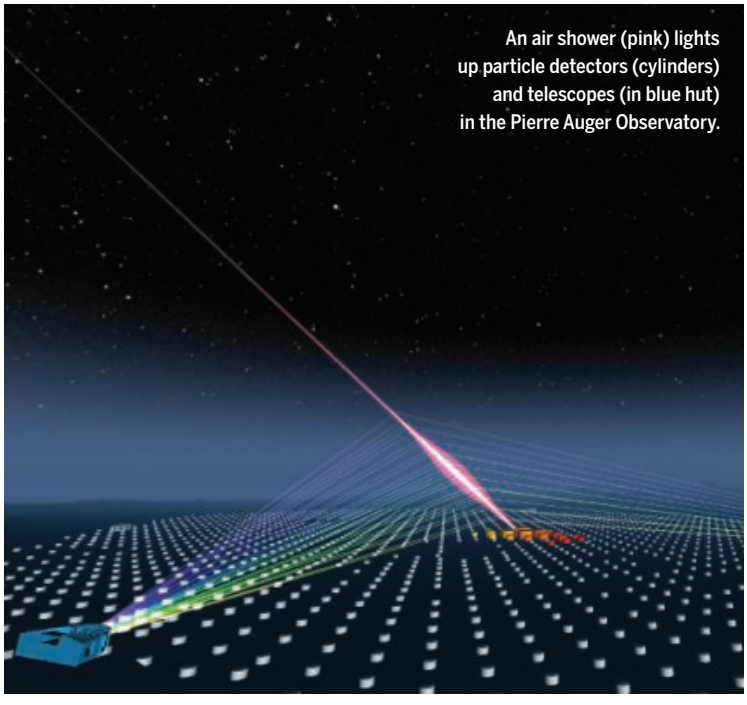

An air shower (pink) lights up particle detectors (cylinders) and telescopes (in blue hut) in the Pierre Auger Observatory.

IMAGE: PIERRE AUGER OBSERVATORY

Neutron star pairs seem common enough to produce the right flux of ultra–high energy rays, Farrar says. They also might neatly explain the highest energy events, which are particularly mysterious. Theorists assume they are iron nuclei, but the usual candidates for the cosmic accelerator would struggle to accelerate iron to such high energies. Neutron star mergers, however, are factories of rare, heavier, more highly charged nuclei such a tellurium. So the highest energy cosmic rays could merely be some of those nuclei accelerated to the same rigidity as lighter nuclei. The scenario "just automatically explains this handful of ultra, ultra–high energy events," Farrar says. "It's so nice when it just falls out like that."

The model can be tested in several ways, she and others say. First, in a neutron star merger, high energy nuclei should interact with photons to produce, ultimately, neutrinos with an energy of about 20 peta-electron volts. IceCube, an enormous detector of cosmic neutrinos built into the ice at the South Pole, and other instruments have seen a few such events. Halzen, who founded IceCube, says its researchers are trawling their data with new machine learning tools to search for more.

Similarly, when future neutron star mergers are detected from their gravitational waves, an ultra–high energy neutrino or two coming from the same direction would indicate that particles are being accelerated to ultrahigh energies there, confirming the model. But such tests will have to wait for an expansion of IceCube and a new generation of gravitational wave detectors, Farrar says.

Auger itself might soon be able to test Farrar's scenario. Researchers there have installed additional detectors designed to be better at identifying particles called muons—fleeting, heavier versions of electrons. The muons in a shower carry clues to the mass of an incident cosmic ray, says Denise Boncioli, a particle astrophysicist at the University of L'Aquila who works on Auger. Spotting nuclei heavier than iron would clinch the case for the neutron-merger scenario, Boncioli says, and "if you do not see nuclei heavier than iron, then you couldn't have these sources."

One tack won't work: the original idea of tracing the particles back to their origins. That approach was already looking difficult because magnetic fields deflect charged particles, and if the highest energy rays are heavy nuclei and not protons, galactic magnetic fields should scramble their paths more drastically. If the new theory is correct, source tracing would lose its relevance, physicists say, as neutron-star mergers can occur in any galaxy. ■

AGRICULTURE

Crop research hit by U.S. foreign aid freezes

A court ruling may temporarily ease funding problems, but long-term outlook is uncertain

By **Dan Charles** *and* **Erik Stokstad**

Researchers at Peru's National Agrarian University La Molina have spent years developing a fast-growing cultivar of passion fruit and introducing it to farmers. The U.S.-funded effort, called PERU-Hub, is intended to diversify agricultural options in an area once known for the production of plants used to make cocaine. But the project's staff stopped getting paid in late January after President Donald Trump's administration ordered that most work funded by the U.S. Agency for International Development (USAID) be shut down. A judge issued a temporary injunction last week ordering USAID to honor existing funding commitments, but the future of this project—and many others like it around the world—remains uncertain.

USAID is known by many for its work in global health and famine relief. But the agency has also spent considerable sums on agricultural research intended to reduce poverty, hunger, and malnutrition, and the January funding freeze sent shock waves that hit agricultural scientists around the world. Workers stopped collecting data in test plots of sorghum, peanuts, and other crops at experimental stations in Africa. Payments ceased to small companies that produce seeds for crop trials. And research coordinators at more than a dozen U.S. universities stopped work, laid off staff, and even ceased communicating with global partners.

Receiving the stop work order felt "unreal," says David Tschirley, an agricultural economist at Michigan State University who chairs a council of USAID-funded researchers. Project leaders are now "trying to figure out" which activities could resume in light of the court injunction, he says.

USAID funds agricultural research through multiple pathways. The agency is one of the top donors to the Consultative Group on International Agricultural Research, a global nonprofit that runs a network of scientific centers. It also funds research through the Feed the Future Innovation Labs, an effort led by researchers at 13 U.S. universities.

Some of the university labs help develop locally suitable varieties of crops such as soybean and tomatoes, as well as fish and poultry. Other labs focus on irrigation efficiency, technical training for farmers, and developing markets for new crops. The labs—funding for which was authorized by the Global Food Security Act of 2016, signed by Trump—have received more than $60 million in federal contracts annually from USAID to support research in the United States and 40 other countries.

The U.S. Agency for International Development has funded agricultural research in dozens of countries, including Cambodia.

PHOTO: MAKARA OUCH/DOCUMENTATION CENTER OF CAMBODIA VIA USAID

When USAID issued stop work orders in late January, the universities had no choice but to lay off workers. Peter Goldsmith, an agricultural economist and head of the Soybean Innovation Lab at the University of Illinois Urbana-Champaign, says he held a "very tearful" meeting last week, where he laid off 30 scientists and other Illinois-based staff. It's not clear whether they will be rehired.

Similar layoffs happened abroad. Timothy Dalton, director of the innovation lab at Kansas State University, says his group had to stop paying workers who tend research plots of sorghum and millet in Ethiopia, Niger, and Senegal. Trials of peanut varieties that the University of Georgia set up in Malawi met a similar fate, according to a researcher who's familiar with the work there. "It's kind of bonkers. The amount of money it took to get those varieties in the ground is a lot more than just the pennies for labor to keep them going and collect the data," they said.

The orders also shut down several nutrition studies after researchers had recruited participants and begun to collect data. The studies included one on ways to improve access to more nutrient-rich fruits and vegetables in Nepal. "These are projects that have such immense value," said Shibani Ghosh, director of the innovation lab on nutrition at Tufts University, which funded the work through its USAID contract.

"Everybody's on edge," one scientist said of the mood among USAID-funded researchers. As they look ahead to secure the future of their projects, some are banking on the argument that the research delivers benefits to farmers in the U.S., not just those abroad. Dalton points to work in Africa and Haiti that identified varieties of sorghum that were resistant to a pest called the sugarcane aphid. When that insect, and a related species called the greenbug aphid, arrived in the U.S., plant breeders were able to incorporate the protective trait into U.S. crop varieties, saving farmers hundreds of millions of dollars. Similar work on peanut varieties in Africa, which are afflicted by the groundnut rosette virus, could someday be used to aid U.S. farmers as well, another researcher says.

The federal court's temporary injunction may start funds flowing again, at least temporarily. For the longer term, Tschirley says he's optimistic that at least some of the work can continue, despite the Trump administration's desire to completely shutter USAID. He notes that agricultural research has enjoyed long-standing support from both Democrats and Republicans in Congress and politically influential U.S. farm groups. "I think there are enough people that see the value [of the labs] that this work is going to continue in one form or another," Tschirley says. ■

With reporting by Roberto González.

eppendorf & Science

PRIZE FOR NEURO BIOLOGY

2024 Winner
Laura Seeholzer, Ph.D.
University of California San Francisco, School of Medicine, USA

For research on airway neuroendocrine cells responding to external threats

Application Deadline
June 15, 2025

Call for Entries 2025

Eppendorf & Science Prize for Neurobiology
The annual Eppendorf & Science Prize for Neurobiology is an international prize which honors young scientists for outstanding neurobiological research based on methods of molecular, cellular, systems, or organismic biology. If you are 35 years of age or younger and doing great research, now is the time to submit an entry for this prize.
It's easy to apply! Write a 1,000-word essay and tell the world about your work.

eppendorf.com/prize

As the winner, you could be next to receive
> Prize money of US$25,000
> Publication of your work in *Science*
> Full support to attend the Prize Ceremony held in conjunction with the Annual Meeting of the Society for Neuroscience in the USA
> 10-year AAAS membership and online subscription to *Science*
> Complimentary products worth US$1,000 from Eppendorf
> An invitation to visit Eppendorf in Hamburg, Germany

eppendorf

Science AAAS

CUTTING AI DOWN TO SIZE

A $14 chip incorporating tinyML AI models, actual size shown.

Many artificial intelligence models are power hungry and expensive. Researchers in the Global South are increasingly embracing low-cost, low-power alternatives

By **Sandeep Ravindran**

The small drone circles the cashew tree, its rotor arms splayed out from its compact body like a water strider's. As it rises, its camera captures a bird's-eye view of the foliage, which shades from a dark glossy green at the tree's bottom to a purplish green at the top. Meanwhile an artificial intelligence (AI) model built into the drone determines whether the leaves are diseased—based on telltale black or brown splotches—or healthy. If needed, the system can one day direct other drones toward individual sick plants to treat their disease with a spritz of pesticide.

This system is the handiwork of Bala Murugan, a computer scientist at the Vellore Institute of Technology in Chennai, India. Murugan comes from a family of cashew farmers, including his father and uncle. "They apply a lot of pesticides on the cashew," he says. "I wanted to build a so-

PHOTO: SEEED STUDIO

lution to minimize the application of pesticides." But he needed a solution that didn't require internet connectivity, which is often hard to come by in rural India.

Murugan drew on his technical expertise. During his Ph.D., he had worked on small, cheap processors. Now, he realized AI models running on such small devices could help farmers like those in his family quickly identify and treat cashew disease. "That is when I ended up using tinyML," he says.

TinyML (the ML stands for machine learning) is a low-cost, low-power implementation of AI that is being increasingly adopted in resource-poor regions, especially in the Global South. In contrast to the large language models (LLMs) that have dominated the news with their versatility and uncanny knack for humanlike expression, tinyML devices currently have modest, specialized capabilities. Yet they can be transformative. Murugan's tinyML-equipped drones, for example, have been able to identify cashew leaves with the fungal disease Anthracnose with 95% to 99% accuracy. They should save farmers time they would otherwise spend looking for signs of disease themselves. And their ability to target treatments to diseased plants removes the need to indiscriminately spray pesticides on all the plants, which is both expensive and damaging to health and the environment.

Murugan is one of many researchers in the Global South finding uses for tinyML. The devices can serve as low-cost aids for teaching AI skills, but they are also providing homegrown solutions to problems that are not being sufficiently addressed by tech companies in the Global North, from detecting plant diseases to tracking wildlife. About 15 million tinyML devices were shipped in 2020, and that number, according to one estimate, could grow to 2.5 billion by 2030.

Part of the appeal for Murugan and others is that once the AI model is trained on a personal computer, it can often run for weeks on low-power tinyML devices powered by everyday batteries, sipping as little electricity as a typical laser pointer. The devices don't need internet connectivity, which can be scarce in resource-poor regions of the world looking to embrace AI solutions. Despite its limited capabilities, "I think [tinyML] is the future," says Marcelo Jose Rovai, a data scientist at the Federal University of Itajubá (UNIFEI). "It's fantastic for developing countries."

IN AI, "THE TREND HAS BEEN THE BIGGER, the better," says Thomas Basikolo, program officer in the Telecommunication Standardization Policy Department of the United Nations's International Telecommunication Union. The trend has culminated in current state-of-the-art generative AI models—those, including LLMs such as ChatGPT, that create new content. But the rise of these models "has so many issues," Basikolo says.

As LLMs are fed more and more training data and parameters to fine-tune and expand their ability to answer queries, the models have also grown dramatically in cost. The latest AI hardware chips can cost about $40,000 each, and ChatGPT alone uses tens of thousands of such chips.

Small but mighty

Tiny machine learning (tinyML) devices are orders of magnitude cheaper and less power hungry than the chips used to run artificial intelligence (AI) like large language models.

TinyML

$2–$60
Cost per device (including sensors)

≤1–100 milliwatts
Average power consumption per device

LLMs

$25K–$70K
Average cost per AI chip, requires tens of thousands of chips

700–1200 watts
Average power consumption per chip

Generative AI models are also hungry for power, which means more water usage and greenhouse gas emissions. Some estimates have ChatGPT sucking up almost 600 megawatt-hours of energy every day—more than 50 times what an average U.S. household consumes in a year. (And it took considerably more energy than that to initially train ChatGPT.)

These models typically run remotely on huge data centers accessed through the internet—or "in the cloud"—which means users need internet connectivity. The estimated tens of billions of liters of potable water needed every year to cool data centers leave a profound environmental impact, especially in areas where drinking water is already scarce. "Every time that you ask [ChatGPT] a question several liters of water are used cooling the big machines that are running big data centers in the cloud," Rovai says.

In 2019, former Google engineer Pete Warden explored a far less resource-intensive approach. He and his colleagues pared down traditional machine learning models by tweaking the numerical values that define how a model learns. They could cut unnecessary values and also reduce the precision of others without losing much overall accuracy. The result: models that could run on computer chips with limited memory and processing power.

TinyML models now rely on microcontroller chips similar to those found in everything from washing machines to car airbags. Warden and others first envisioned tinyML consuming so little power—less than 1 milliwatt—that devices could run for a year or more on coin-cell batteries and virtually forever using solar power. "There's some magic stuff that happens once you get below 1 milliwatt," Warden says. They haven't reached that threshold widely yet, but tinyML devices can run for weeks or sometimes months on AA batteries.

The chips themselves are cheap and commercially available from several different manufacturers. As a result, most tinyML devices now cost from a few dollars to tens of dollars, depending on how powerful they are. They often include not just the chip, but also cameras and sensors to detect images and sounds for the AI models to interpret. Much of the software, hardware, and data sets that researchers need to get started with tinyML are open source, which means they can freely access and modify them.

TinyML models typically use less data than larger varieties, ingesting thousands of images or sounds instead of the millions that LLMs often require. Murugan, for instance, says he used 20,000 images of cashew Anthracnose disease collected from various public domain sources to train his model, although he is supplementing that data set with his own photos to improve the model's accuracy. Once trained, the model does all its computation on the device, so tinyML systems can provide results within milliseconds with no need to go to the cloud and back. With no need to connect to the internet, tinyML uses less power and also tends to be a boon for privacy and security.

An artificial intelligence model running on tiny machine learning devices is helping cleanup efforts in Malaysia quickly classify types of trash hampering the growth of mangroves, including plastic food containers (●), plastic bags (●), food wrappers (●), clear plastic water bottles (●), or other kinds of bottles (●).

João Yamashita first came across tinyML in 2020 while completing his undergraduate degree remotely because of the COVID-19 pandemic. An electronics engineer at UNIFEI, Yamashita spent this time at his home in Mogiana Paulista, a coffee-growing region in the southeastern part of Brazil.

Yamashita realized that many small farmers were struggling to diagnose diseases in their coffee plants. Specialists to do this diagnosis didn't come cheap and wouldn't travel during the pandemic. Yamashita turned to tinyML for a possible solution.

After using public data sets to train a generic AI model, Yamashita went to the farmers to find out about coffee diseases specific to Brazil. "At first they were very skeptical," he says. "A lot of them don't even have cellphones," so an AI model to autodetect disease was very new, he says.

To fine-tune his model, which runs on a tinyML device about the size of a pack of cards, Yamashita took photos of healthy and diseased coffee leaves from rows of coffee plants growing on hillside plantations in his home region. He also collected samples and photographed them later under more controlled light and background conditions. The resulting model could identify a variety of coffee diseases with 96% to 98% accuracy, including fungal diseases such as Phoma, sooty mold, and rust, as well as the leaf miner moth. A farmer could point the device's camera at a leaf and its screen would show the disease name and a score indicating the model's confidence. "When I showed [farmers] the device working … they looked like they were amazed," says Yamashita, who is now working on tinyML devices for other uses.

The device is practical for poor farmers, Yamashita says. It doesn't need internet access, lasts a week or more without needing to charge its battery, and costs less than $20. It's just the sort of bespoke, homegrown solution tinyML is good for, and explains why agriculture has been a popular use for the technology.

Beyond agriculture, researchers are also developing tinyML devices for health care applications, from detecting atrial fibrillation—a type of abnormal heart rhythm—in Brazil to anemia in Peru. And multiple groups have used the technology to distinguish mosquito species by the buzzing of their wings, making it unnecessary to collect mosquitoes in traps and manually identify each one. The result is speedier alerts that could help with control of species that spread disease.

Rovai, for example, trained an AI model to identify two species of *Aedes* mosquitoes—which can transmit dengue, Zika, and chikungunya viruses—with an accuracy of 98% on a proof-of-concept device whose battery can last for up to 4 days in the field. He envisions the device being of great use in Brazil, where dengue affects more than 1 million people each year. In Kenya, similar projects are using tinyML to automatically classify mosquitoes that carry malaria. "Being able to categorize that in an automatic way is a huge advantage for people working in the field," says Marco Zennaro, a computer scientist at the Abdus Salam International Centre for Theoretical Physics (ICTP) who worked with Rovai on the *Aedes* mosquito detection project.

Similar devices are also finding their way into environmental applications. Researchers have tacked tinyML devices to the back of tortoise shells in Argentina to track how and where the animals move. And in Malaysia, Rosdiadee Nordin, an engineer at Sunway University, is using tinyML devices to monitor rivers for plastic trash that might hinder the growth of delicate young mangroves. He and a team of volunteers gathered 9000 images of plastic trash to train AI models until they could classify it, distinguishing clusters of plastic bottles from clumps of plastic bags. They plan to make the data publicly accessible to help track the location, quantity, and types of plastic waste. "This will help not only [those who pick up the trash], but also local council or environmental agencies to further plan their waste collection activities," Nordin says.

Nordin's work extends to Tasik Chini Lake in eastern Malaysia, which supplies the local Indigenous community with both drinking water and fish. Nordin deployed solar-powered water quality sensors to de-

IMAGE: SITI ZULAIKHA; ROBOFLOW

tect pollution in the lake and send that information to tinyML devices, where AI models use it to make predictions about water quality. "If we make the water quality data accessible [to] the community, they will be able to understand whether the water is safe for them to consume," Nordin says.

The lake lacks the internet and cellular connectivity needed to broadcast data to the researchers. To avoid having to travel to each device and manually download the data, Nordin had to improvise. He turned to LoRa, a long range wireless transmission protocol that uses relatively little power and bandwidth compared with Wi-Fi and can work over tens of kilometers.

Other tinyML researchers are eyeing the same system to send data from tinyML devices used in agriculture to farmers' computers or phones. Without a way to download the data remotely, "the farmer will have to go through all these devices; it is time consuming, and it is tedious," says James Adeola, a Ph.D. student in computer science at the University of Abomey-Calavi who is developing tinyML devices that can detect diseases in cotton and reduce the need for pesticide use. Farmers "will be very happy if this solution can be implemented," he says.

SIMPLE AS TINYML DEVICES appear, developing them can be a challenge. For one, it requires expertise in multiple skill sets. "It's combining hardware, software, and machine learning," Basikolo says. "Very few people can do all these, so combining all these skills also takes time."

Researchers are trying to disseminate that expertise by running tinyML courses and workshops in Morocco, Brazil, Nigeria, South Africa, Rwanda, Malaysia, and other countries in the Global South. In 2021, for example, Harvard University and ICTP launched the tinyML for development academic network, which now encompasses 50 academic institutions across the Global South. The organizers, including Zennaro and Vijay Janapa Reddi, a computer scientist at Harvard University, began by donating tinyML kits to partner institutions. "When we started this initiative, we saw that the main issue was getting the hardware in the hands of people," because low-cost in the United States can still be expensive elsewhere, Zennaro says.

The resulting kits have been used to train students at universities in Malaysia, Saudi Arabia, and elsewhere. In just an hour or two, students were able to train tinyML devices to recognize words and phrases in their own local languages, "which is … empowering for communities," Zennaro says.

By nature, tinyML's capabilities are limited. "I think tinyML is very good at tiny problems," Yamashita says. The microcontrollers that run the devices have extremely limited memory and computing power, which makes them more suited for highly specific tasks than as generalizable commercial products. A device could be great at identifying words in one language or identifying diseases of one plant species, but it's less likely to serve as a universal translator or identify diseases across all plants.

Yet the appeal of smaller models that run directly on devices is dawning on many tech companies in the Global North, including Apple and Microsoft. For some applications, such as taking an order at a McDonald's, specialized tinyML models that can run on local devices rather than in the cloud, at lower cost and power use, may be preferable to running an expensive general LLM. "Sometimes these large language models are doing way more than you might need," says Jean Louis, a computer science Ph.D. student at the University of Florida; they might be the equivalent of using a sledgehammer to crack a nut.

Meanwhile, tinyML devices themselves are rapidly becoming more powerful. Just a few years ago it was considered "ridiculous" to be able to run advanced machine learning models on microcontrollers, says Peter Ing, an electronics engineer and member of the TinyML Open Education Initiative. Warden has already gotten a simple LLM to run on a device that is only slightly more expensive and power hungry than tinyML devices. He envisions more large AI models migrating to these smaller, power-efficient devices rather than relying solely on data centers.

At the same time, the simplest tinyML devices are likely to become more prevalent as microcontrollers continue to become cheaper and more powerful, with some already being developed specifically to run AI. "It's just reached a maturity point where we are now seeing solutions and technology that can be commercialized," says Reddi, who runs a free, massively online course on tinyML and has written an open-source book about it. And even though each tinyML device may be relatively small and specialized, many such devices talking to each other could help tackle bigger and more complex tasks.

As Yamashita puts it, "[TinyML] will enable AI to, in fact, go everywhere." ■

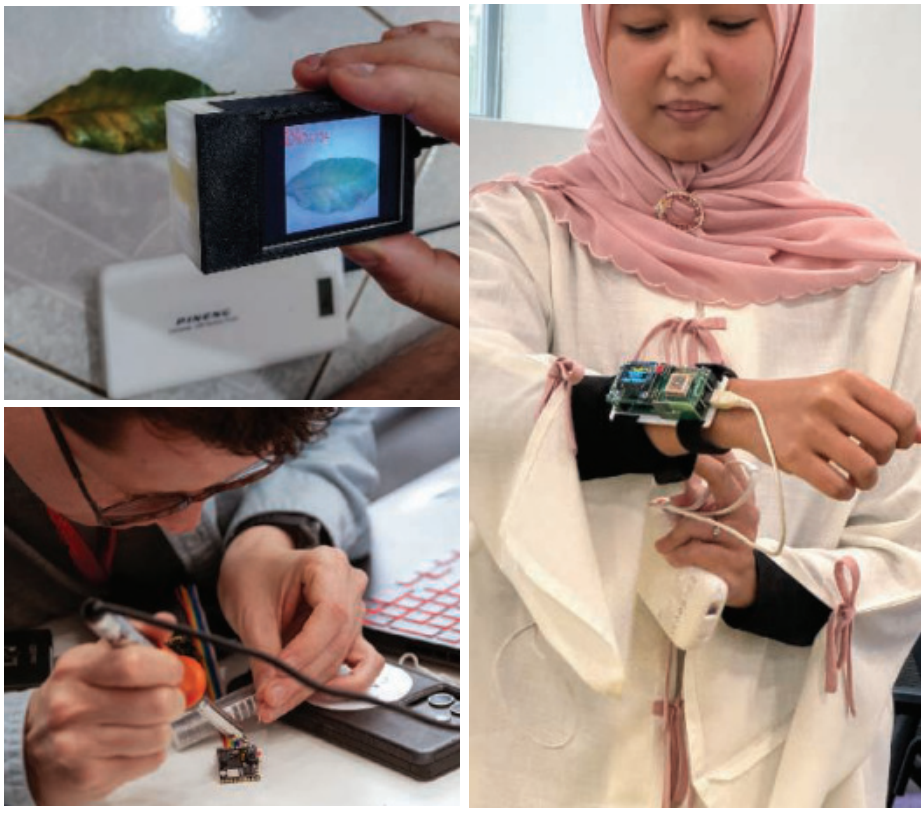

Tiny machine learning (tinyML) projects around the world aim to tackle challenges in the Global South, including identifying diseases such as rust in coffee leaves in Brazil (top left). TinyML devices to detect mosquitoes in the field (bottom left) and heart rate and other physiological readings (right) are also being developed in workshops.

PHOTOS: (CLOCKWISE FROM TOP LEFT) JOÃO YAMASHITA; SERGE STINCKWICH; RODRIGO NEUMANN

Sandeep Ravindran is a science journalist near Washington, D.C.

INSIGHTS

PERSPECTIVES

NEUROSCIENCE

Evaluating animal consciousness

An emerging field shows how animal feelings can be studied scientifically

By **Kristin Andrews[1], Jonathan Birch[2], Jeff Sebo[3]**

Honeybees becoming "pessimistic" after stressful experiences (*1*); cuttlefish remembering the past and planning for the future (*2*); and cleaner wrasse fish seemingly recognizing themselves in a mirror (*3*): If scientific reports like these were accepted as evidence of consciousness, then the implications would be substantial. The neuroscience of consciousness would need to expand its focus beyond humans and other primates and include a much wider range of model species. Animal welfare policies likely would need to expand as well. The outstanding question is whether such reports serve as evidence of consciousness. If so, what conclusions can be drawn about animals that display some consciousness indicators but not others?

Assessing animal consciousness would be easier if there were a widely accepted theory of consciousness and a precise definition of consciousness tied to that theory. Unfortunately, theories of consciousness abound, with 22 theories identified in a recent study (*4*). Although some ideas enjoy more empirical support than others, most researchers agree that all current theories are insecure.

In the absence of a secure theory or a precise definition, consciousness science instead starts with sensible examples that involve felt experience in humans. These include sensory experiences such as color perception, affective experiences such as bodily pleasure, and vivid imagery during dreams, memories, imagination, or plan-

[1]Department of Philosophy, York University, Toronto, ON, Canada. [2]London School of Economics and Political Science, London, UK. [3]Department of Environmental Studies, New York University, New York, NY, USA. Email: andrewsk@yorku.ca; j.birch2@lse.ac.uk; jeffsebo@nyu.edu

PHOTO: MAMETRAHARDI/ALAMY STOCK

What if markers of consciousness in humans are identified in other animals, from vertebrates to invertebrates?

ning. These examples provide an initial characterization of consciousness that allows researchers to investigate dimensions of conscious experience.

A challenge in studying animal consciousness is the "problem of other minds," a concept widely recognized across world philosophies. In 1889, the British philosopher John Stuart Mill described the problem when he pondered, "By what evidence do I know…that the walking and speaking figures which I see and hear, have sensations and thoughts, or in other words, possess Minds?" (*5*). He answered this question with an analogical argument, identifying similarities between himself and other humans and then inferring that conscious experience is a further similarity: "First, they have bodies like me, which I know in my own case to be the antecedent condition of feelings; and because, secondly, they exhibit the acts, and outward signs, which in my own case I know by experience to be caused by feelings" (*5*).

Although reasoning by analogy never delivers certainty, especially when applied across species, it can still be a valid approach for studying animal consciousness when viewed as a kind of inference to the best explanation—that is, the best rationale for the available observations and data. When humans and other animals perform similar behaviors, and when the best explanation for these behaviors in humans involves conscious experience, then that could be considered evidence—albeit tentative, inconclusive evidence—of conscious experience in other animals, too. Such an analysis might provide evidence for or against a claim without definitively proving or refuting the claim.

Philosophers call this kind of reasoning an "abductive" inference, and it is at the core of the scientific method—a process of inquiry and investigation that identifies the most likely conclusion from a set of observations. Of course, abductive inference can deliver stronger evidence for some "other minds" than for others. When the question is whether other (awake, adult) humans are conscious, this method delivers virtual certainty. However, when the question is whether nonhuman animals are conscious, it delivers less certainty. For animals such as chimpanzees that are closely related to humans, abductive inference can establish a high level of confidence that consciousness is present. For animals that are farther away on the phylogenetic tree, such as ants, this method might at best establish only a "realistic possibility" that consciousness is present—yet even this finding can still be important.

How does the science of animal consciousness determine which continuities between humans and other animals are relevant without a secure theory of consciousness in hand? Over the past decade, researchers have developed frameworks for conceptualizing the many forms that subjective experiences might take and have used these frameworks to investigate specific dimensions of consciousness (*6*). This approach starts with identifying a particular dimension of consciousness, such as pain experience, visual experience, or a sense of self. It then requires identifying observable markers of that dimension and seeking evidence that such markers are present or absent in the target species. Taking these steps can produce evidence for or against that dimension of consciousness in the species of study.

The degree to which a particular marker can increase or decrease confidence in particular dimensions of animal consciousness depends on context. For instance, linguistic behavior is a marker of specific kinds of conscious thought and emotion in humans. But as demonstrated by large language models that simulate human conversation, linguistic behavior alone is not strong evidence of consciousness in nonhuman systems. Awake, adult humans display many interconnected behavioral and neurobiological markers of conscious thought and emotion. When humans face danger, they do not merely report "Danger!" but they may freeze and tense their muscles, and they may demonstrate increased heart rate and respiration, as both the brain's amygdala and cerebral cortex regions increase activity. When a system only demonstrates one type of marker, such as verbal behavior, it provides at best very weak evidence of consciousness. But when many types of markers are present together, they can jointly provide strong evidence.

When some markers of consciousness are present and others are absent, careful interpretation is required. For example, when behavioral markers of consciousness are absent in humans—as with fetuses, infants, and humans who are unresponsive after brain injuries—researchers can give more weight to neurophysiological markers, such as the perturbational complexity index and the P3b wave (both of which measure responses to specific kinds of external stimuli). Alternatively, when human neurophysiological markers are absent—as with animals that have very different brain structures, such as octopuses or bees—behavioral markers become more important.

A key challenge with assessing behavioral markers is that some behaviors can be caused by conscious as well as unconscious processing of a stimulus. For instance, aversive behavior can be caused by pain, a negatively valenced conscious experience. But aversive behavior can also be caused by nociception, the detection of a noxious stimulus (mechanical, thermal, or chemical) that can occur unconsciously—that is, the body can detect such a stimulus and activate neural pathways without causing a conscious experience of the stimulus. To serve as evidence for consciousness, then, aversive behavior must go beyond mere sensitivity,

by, for example, implicating mechanisms of learning and memory to enable flexible, adaptive, and lasting behavioral change.

To make progress on defining behavioral markers, it is necessary to distinguish conscious and unconscious neural processing related to a specific situation (such as tissue damage). Researchers can then identify markers of the conscious version in humans (such as behaviors that occur when tissue damage feels bad) and can search for species-appropriate versions of these markers in other animals. Clearly, this approach leaves room for doubt about whether these markers correspond to conscious experience in animals—and room for improvement regarding both the choice of markers and the search for markers. However, these kinds of markers have face validity and warrant further investigation.

Behavioral markers of pain have been observed in many different taxa, from vertebrates to invertebrates. In a conditioned place preference test conducted on rodents, the animal chooses between two chambers. The initially favored chamber is then paired with a noxious stimulus, whereas the initially disfavored chamber is paired with an analgesic or local anesthetic. If a human subject were to switch the preferred chamber choice in this context, then the best explanation would be that the noxious stimulus felt bad and that the subject was attempting to remove this unpleasant experience. This is the best explanation of the data in rodents, too (*7*).

Markers of pain have been reported in birds as well. Lame broiler chickens demonstrate a greater ability to walk when administered carprofen, an anti-inflammatory drug with analgesic properties. When offered a choice between a normal feed and a feed laced with carprofen, these birds learn to selectively self-administer the analgesic when experiencing leg problems (*8*). Self-administration of this kind of analgesic indicates that the animal values the kind of pain relief that the analgesic provides. When humans take ibuprofen after fracturing a rib, they are evidently seeking to alleviate a negative experience. When a bird performs a similar behavior in a similar situation, they are plausibly seeking to do the same.

What about other vertebrates—reptiles, amphibians, and fishes? Behavioral and neurophysiological markers of experiencing pain have been found in all three. For instance, reptiles such as pythons show a range of pain-related behaviors in response to capsaicin injection, such as reduced feeding and raising the wound site off the ground (*9*). Amphibians such as frogs share anatomical and physiological features associated with pain in mammals, including neuronal Aδ and C fibers and ascending spinal cord projections that reach the brain stem and thalamus (*10*). And fishes not only sense negative stimuli such as shocks but also quickly learn to avoid them in the future (*11*).

What about invertebrates? Cephalopod mollusks such as octopuses have demonstrated conditioned place preference. A single trial was enough to produce a shift in preferences, suggesting that acetic acid causes a strongly aversive experience that lidocaine relieves (*12*). Pain markers have been reported in decapod crustaceans as well. Crabs and shrimps exhibit wound-tending and rubbing in response to electric shocks. When hermit crabs receive electric shocks within a shell, they are less likely to abandon a higher-quality shell than a lower-quality shell, suggesting that the shock elicits an unpleasant state that can be weighed against other motivations (*13*). Similar markers have recently been found in some insects, indicating that there might be conscious experiences in this vast taxon as well. For example, bees can remember the heat experienced on a heat pad and can trade this off, in their future decision-making, with the sweetness of a sugar reward experienced when on the pad—behavior that goes well beyond nociceptive reflexes (*14*).

It is arguable that behavioral markers of pain pertain to perception, learning, memory, and other such forms of cognition and that it is possible for an animal to have these capacities in a purely unconscious sense, without having any feelings. However, by distinguishing between conscious and unconscious versions of these capacities in humans, identifying markers for the conscious versions in humans, and finding relevantly similar markers in other animals, researchers can increase confidence that these animals may well have feelings associated with these processes.

The "New York Declaration on Animal Consciousness," released in April 2024 and signed by over 500 experts, captures a changing understanding of consciousness while acknowledging uncertainty (www.nydeclaration.com). What should the future hold for this emerging field? Research on animal consciousness is overly reliant on pain markers, yet there is more to consciousness than pain. For example, when rats are laughing and bees are playing, is this behavior evidence of a felt emotion of joy? Attempts to develop markers for joy are currently underway (*15*). New and better methods for disentangling conscious and unconscious neural processing in animals are also needed. In humans and other primates, the study of blindsight, in which individuals with lesions in the primary visual cortex who report blindness still respond adaptively to visual stimuli, is one way to accomplish this goal. Noninvasive techniques such as backward masking, in which a stimulus is followed quickly by a "white noise" stimulus that renders it subliminal, have been influential as well. Future work should investigate translating noninvasive methods to a wider range of animals.

As the science of animal consciousness evolves, evidence in different taxa will evolve as well, supporting higher or lower degrees of confidence that this state of awareness exists beyond humans. The idea that there is a "realistic possibility" of consciousness in all vertebrates and many invertebrates may eventually be replaced by more confident language. But for as long as the evidence remains limited and mixed, it is important to keep an open mind and strive to learn more. At this early stage, it is also important to accept the absence (for now) of a secure theory or a precise definition of consciousness, along with a lack of proof or certainty. Although definitive proof or certainty are not achievable goals, strong evidence of the different dimensions of consciousness across species should help the field construct better theories of consciousness—and a better understanding of the tree of life. ■

REFERENCES AND NOTES

1. M. Bateson, S. Desire, S. E. Gartside, G. A. Wright, *Curr. Biol.* **21**, 1070 (2011).
2. A. K. Schnell, M. Boeckle, M. Rivera, N. S. Clayton, R. T. Hanlon, *Proc. Biol. Sci.* **288**, 20203161 (2021).
3. M. Kohda *et al.*, *Proc. Natl. Acad. Sci. U.S.A.* **120**, e2208420120 (2023).
4. A. K. Seth, T. Bayne, *Nat. Rev. Neurosci.* **23**, 439 (2022).
5. J. S. Mill, *An Examination of Sir William Hamilton's Philosophy*, ed. 6, 1889), pp. 243–244.
6. J. Birch, A. K. Schnell, N. S. Clayton, *Trends Cogn. Sci.* **24**, 789 (2020).
7. E. Navratilova, J. Y. Xie, T. King, F. Porreca, *Ann. N. Y. Acad. Sci.* **1282**, 1 (2013).
8. T. C. Danbury, C. A. Weeks, J. P. Chambers, A. E. Waterman-Pearson, S. C. Kestin, *Vet. Rec.* **146**, 307 (2000).
9. L. E. James, C. J. Williams, M. F. Bertelsen, T. Wang, *J. Zoo Wildl. Med.* **48**, 196 (2017).
10. S. A. Guénette, M. C. Giroux, P. Vachon, *Exp. Anim.* **62**, 87 (2013).
11. C. Brown, C. Dorey, *Anim. Stud. J.* **8**, 175 (2019).
12. R. J. Crook, *iScience* **24**, 102229 (2021).
13. M. Appel, R. W. Elwood, *Appl. Anim. Behav. Sci.* **119**, 120 (2009).
14. M. Gibbons *et al.*, *Adv. Insect Physiol.* **63**, 155 (2022).
15. X. J. Nelson *et al.*, *Biol. Rev. Camb. Philos. Soc.* **98**, 1548 (2023).

ACKNOWLEDGMENTS

Thanks to T. Sims for research support, to S. Fogel for project support, and to the initial signatories of the 2024 New York Declaration on Animal Consciousness for useful feedback and discussion on a draft. K.A. acknowledges funding from the Social Sciences and Humanities Research Council (grant 435-2022-0749), Canadian Institute for Advanced Research Future Flourishing program, and York University. J.B. acknowledges funding from the European Research Council Horizon 2020 programme (grant 85145). J.S. acknowledges funding from Longview Philanthropy, Open Philanthropy, Polaris Ventures, and The Navigation Fund.

10.1126/science.adp4990

EVOLUTIONARY BIOLOGY

Enabling evolvability to evolve

A multilevel population architecture enables bacteria to evolve increased adaptability

By **Edo Kussell**[1,2]

Evolvability, or the capacity to generate adaptive phenotypic variation, can itself evolve in response to selection (*1*). Species that evolve too slowly may be unable to adapt to environmental change and are more likely to go extinct than faster-evolving species. Yet what it takes to get evolvability to evolve, in nature or in the lab, has remained puzzling. For example, many generations might be needed for natural selection to change a species' ability to adapt. Higher evolvability can result in lower heritability, a cornerstone of natural selection's ability to act, and the same degree of evolvability might not suit all traits equally. On page 840 of this issue, Barnett *et al.* (*2*) describe how experimental evolution can yield increased evolvability by localized hypermutation in populations of bacteria exposed to an alternating selection regime, akin to the regularly fluctuating conditions that pathogenic bacteria experience moving from one host to another.

Barnett *et al.* sought to evolve evolvability using the soil-dwelling bacterium *Pseudomonas fluorescens*. In a static culture, *P. fluorescens* rapidly depletes oxygen dissolved in a liquid medium, which leads it to form a "mat" of cells at the air-liquid interface (*3*), allowing cells to directly access oxygen from the air. To form a mat, cells must produce large amounts of the extracellular matrix structural component cellulose (*4*), a behavior known as a CEL^+ phenotype. Once the mat has formed, it can be colonized by cells that do not produce cellulose, a CEL^- phenotype. These cells take advantage of easy access to oxygen while avoiding the metabolic cost of cellulose production. Switching between CEL phenotypes is associated with mutations in the genome, and the rate at which switching occurs corresponds to the evolvability of the CEL phenotype.

The approach of Barnett *et al.* involved an alternating selection regime with eight parallel cultures of *P. fluorescens* propagated over many rounds (see the figure). Although each culture contained a single population with billions of cells, collectively the eight cultures constituted a multilevel structure, known as a metapopulation, which was key to the experiment's success. Each time a population failed to produce cells of the alternative phenotype, that population was declared extinct. In its place, the authors seeded a new population using cells of the required phenotype from another randomly chosen population, effectively allowing interpopulation competition within the metapopulation.

Mutations in the *pflu0185* gene accounted for many CEL phenotype switching events observed by Barnett *et al.* This gene negatively regulates amounts of cyclic-di–guanosine monophosphate (cyclic-di-GMP), a signaling molecule that activates cellulose production. During the experiment, *pflu0185* gained a seven-nucleotide-repeat sequence motif near the beginning of the gene, which is prone to insertions and deletions during DNA replication. Formation of the repeat causes a frameshift in the coding sequence that yields a nonfunctional protein, which elevates cyclic-di-GMP levels and activates cellulose production, resulting in a CEL^+ phenotype. Repeat contraction reverses this behavior, yielding a CEL^- phenotype. In this way, the heptanucleotide repeat motif increases evolvability at the genomic locus that controls the specific trait under fluctuating selection.

Barnett et al. traced the motif's first appearance to a specific round of selection in a single population. Tracking this lineage backward in time, they found that a series of mutations in the pflu0185 gene and its upstream regulatory region gradually increased its transcription rate. These pflu0185 alleles also caused successive increases in the rate of frameshift mutations within the gene. When another wild-type copy of pflu0185 was inserted elsewhere in the genome, it did not exhibit increased frameshifting, confirming that hypermutability was localized around the pflu0185 locus. Thus, a molecular mechanism involving transcription-associated mutagenesis (*5*) could explain the local increase in frameshift mutations that first enabled the repeat motif to occur.

The phenotypic switching that evolved de novo in these experiments uses the same molecular mechanism that exists in contingency loci found in many pathogenic bacteria (*6*). Contingency loci genes encode proteins that modify bacterial cell-surface structures that are recognized by the host immune system. These genes also contain repeat motifs that enable a population to rapidly diversify its cell-surface repertoire to evade the immune system, which itself varies from host to

[1]Department of Biology, New York University, New York, NY, USA. [2]Department of Physics, New York University, New York, NY, USA. Email: edo.kussell@nyu.edu

Multilevel population architecture for evolution of lineage traits

A metapopulation consists of *N* populations of individuals with different phenotypes (orange and blue dots). Individuals are selected to continue to the next round on the basis of their phenotype. Populations that fail to produce the alternate phenotype go extinct and are reseeded from a different population. Each population corresponds to a single ancestral lineage traced backward through its phylogenetic tree (bolded line). The metapopulation maintains a diverse collection of lineages that compete, allowing selection to act on traits such as evolvability.

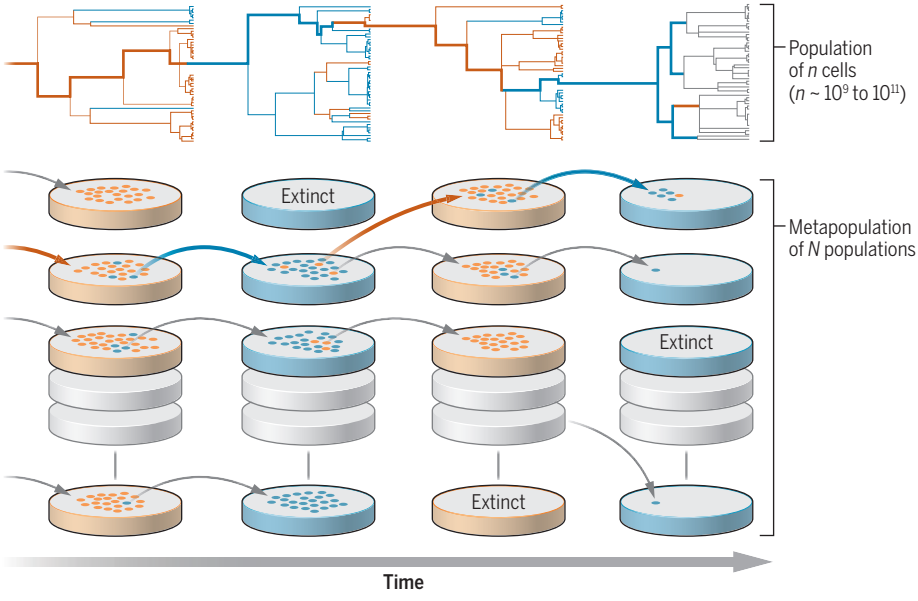

GRAPHIC: A. MASTIN/*SCIENCE*, BASED ON E. KUSSELL

host. There is a strong parallel between the metapopulation structure with alternating selection of Barnett *et al.* and real-world environments that pathogens encounter. Each infected host carries a single pathogen population, and the collection of all hosts constitutes a metapopulation of pathogen lineages. Phenotypes that are successful in one host may be deleterious in a subsequent host (*7*), and different pathogen lineages must compete for a large but limited number of hosts.

The ability of a metapopulation with fluctuating selection to promote the evolution of evolvability may explain why contingency loci are prevalent in pathogenic bacteria. More broadly, it is possible that using a multilevel "architecture" for evolution experiments could enable the evolution of many other adaptive modalities. The evolution of any trait requires heritability, diversity, and differences in fitness. However, some traits, such as evolvability, do not correspond to properties of an individual, but control statistical properties of all lineages that can be generated. Gene regulation, including stochastic and responsive switching, is a lineage-level trait that determines the ensemble of lineages that will be generated in a fluctuating environment (*8*). Evolving such traits efficiently requires competition among a diverse set of lineages. Yet within a single population, selection causes lineages to rapidly coalesce, making it difficult to maintain more than one lineage for a substantial number of generations. A multilevel population structure increases lineage diversity while enabling interlineage competition to act on differences in lineage fitness. Accordingly, the ability of selection to act on lineage traits will be limited by the size of the metapopulation. It is striking that the emergence of a new contingency locus could be observed with a metapopulation size of only eight lineages. The evolutionary potential of this architecture has powerful implications, given the huge metapopulations with billions of parallel lineages that exist in nature. Understanding how to design architectures that bridge the gap between what can be observed in the lab and what takes place in nature is a key goal for future research. ■

REFERENCES AND NOTES

1. J. L. Payne, A. Wagner, *Nat. Rev. Genet.* **20**, 24 (2019).
2. M. Barnett *et al.*, *Science* **387**, eadr2756 (2025).
3. P. B. Rainey, M. Travisano, *Nature* **394**, 69 (1998).
4. A. J. Spiers *et al.*, *Mol. Microbiol.* **50**, 15 (2003).
5. S. Jinks-Robertson, A. S. Bhagwat, *Annu. Rev. Genet.* **48**, 341 (2014).
6. R. Moxon *et al.*, *Annu. Rev. Genet.* **40**, 307 (2006).
7. R. Moxon, E. Kussell, *Evolution* **71**, 2803 (2017).
8. S. Leibler, E. Kussell, *Proc. Natl. Acad. Sci. U.S.A.* **107**, 13183 (2010).

ACKNOWLEDGMENTS

E.K. acknowledges support from National Institutes of Health grant R01-GM097356.

10.1126/science.adv4087

ADDITIVE MANUFACTURING

Connecting the dots for cooling

Semiconductor particles are fused to make a thermoelectric cooler

By **Lara Perren** *and* **Maksym Yarema**

Additive manufacturing, also known as three-dimensional (3D) printing, has swiftly become a go-to fabrication approach for a wide span of applications, such as automotive, aerospace, biomedical, and construction (*1*). For energy technologies such as thermoelectric cooling, however, 3D printing is notably less integrated because of the intricate specifications required of functional semiconductors. Characteristics of a material, such as charge carrier mobility, level of impurities (dopants), and microstructural defects, as well as surface and interfacial properties, must be precisely engineered to achieve desired performance. 3D printed semiconductor devices often demonstrate lesser performance compared to their thin-film counterparts because of imperfections in the functional layer that are introduced during printing (*2*, *3*). On page 845 of this issue, Xu *et al.* (*4*) report additive manufacturing of a thermoelectric cooler with a cooling efficiency surpassing that of existing devices. This demonstrates potential use of 3D printing for large-scale production of semiconductor devices.

A thermoelectric cooler is a solid-state device that uses electrical current to transfer heat from one side to another. This modern method of thermal management avoids the use of harmful refrigerants in conventional vapor compression systems. However, implementing thermoelectric cooling for large-scale applications is primarily limited by low cooling efficiency and high manufacturing cost. Extrusion-based 3D printing (*5*) that deposits materials in a form of ink could be an alternative to expensive microfabrication—the process of creating micrometer-scale semiconductor devices using photolithography, etching, and deposi-

3D printing a thermoelectric cooler

Formulating an ink with a reactive component and polymer binder enables precise engineering of a material's microstructure during three-dimensional (3D) printing. A thermoelectric device with a better cooling efficiency than its thin-film counterparts was fabricated, which shows the potential of 3D printing for large-scale production of semiconductor devices.

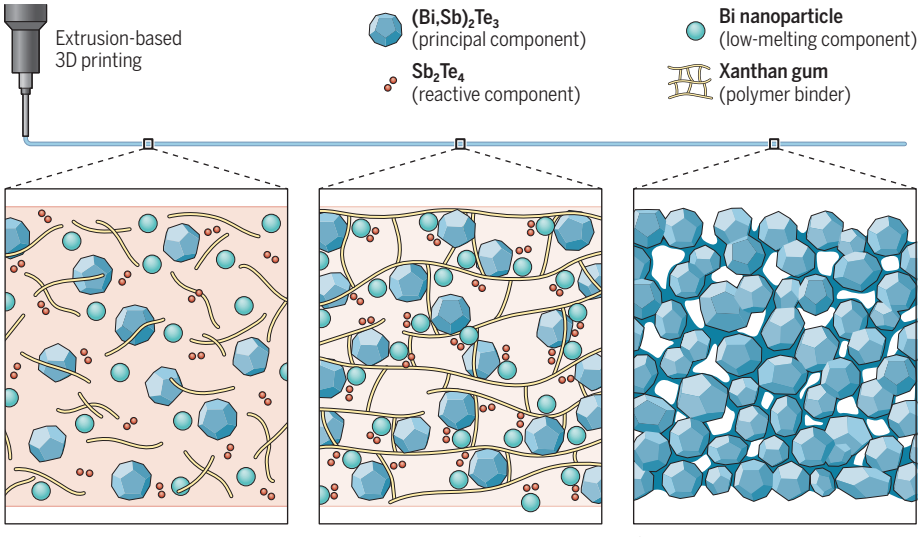

Bi, bismuth; Sb, antimony; Te, tellurium.

GRAPHIC: K. HOLOSKI/*SCIENCE*

tion of thin films. The main challenge of implementing additive manufacturing to such devices is formulating an ink that promotes sufficient bonding between its constituents upon drying. Additionally, it is highly unconventional to fine tune the functional properties of semiconductors after printing.

For an efficient thermoelectric cooler, achieving high electrical and low thermal conductivity are required. Both these properties are dictated by a material's microstructure—the atomic arrangement that consists of crystalline grains, interfaces, and defects. Length scale of individual grains and spatial dimension of defects within a crystal affect the mobilities of charge carriers and phonons (quasiparticles associated with atomic vibration). Good interfacial bonding between grains is needed to maximize electrical conductivity, whereas a certain density of defects is required to scatter phonons to reduce thermal conductivity (*6, 7*). Although these two conditions are seemingly incompatible, charge carriers and phonons generally have a different mean free path—the average distance a particle travels without a collision. Thus, engineering a material's microstructure could decouple the two conditions to achieve desired functionality of a thermoelectric cooler (*8*). Extrusion-based 3D printing inevitably results in porous structures because of the inherent gap between the deposited components. Such material has air pockets that scatter phonons, resulting in low thermal conductivity (*4*). By contrast, achieving adequate electrical conductivity is challenging because of the reduced interfacial areas between the grains. Thus, coherent networks of semiconductor grains should be formed by carefully controlling the microstructure of porous thermoelectric coolers, which has not been obtained using 3D printing methods.

Xu *et al.* report additively manufactured components of a thermoelectric device with a record-high cooling temperature gradient of 50°C in an ambient environment. The authors demonstrate judicious microstructure engineering of 3D printed parts using a material's inherent properties and additives in the ink formulation (see the figure). The two leading n-type (negative) and p-type (positive) semiconductors used for thermoelectric cooling—silver selenide (Ag_2Se) and bismuth antimony telluride [$(Bi,Sb)_2Te_3$], respectively—were successfully printed. Colloidal suspensions were used as inks to promote interparticle bonding at low temperatures without an applied pressure. The printed materials exhibited a porous structure with micrometer-sized grains and abundant defects.

Engineering the microstructure of n-type silver selenide is elegant in its simplicity. Xu *et al.* exploited a phase transition at 130°C to a superionic phase that consists of more freely moving atoms within a solid lattice. The increased mobility of silver atoms formed coherent interfaces between grains with a large density of defects, which is ideal for low thermal conductivity and high electrical conductivity. In the case of bismuth antimony selenide, the low melting temperature of bismuth nanoparticles acted as a solder to enable a solid network within the 3D printed components during the mild heat treatment. Liquid bismuth also accelerated the reaction with the molecular antimony telluride additive (Sb_2Te_4), such that the composition of the interfaces matches closely that of bismuth antimony selenide grains. This reaction produced a high density of defects to scatter phonons. Further, Xu *et al.* included the xanthan gum binder in the ink to reinforce mechanical properties of as-printed semiconductors.

The findings of Xu *et al.* highlights how microstructure engineering by carefully formulating printer ink can make a high-performance functional material. Optimizing constituents of the ink and deposition parameters could potentially print materials that are close to the benchmark quality of crystalline layers with precise arrangement of atoms. This would enable fabrication of high-quality semiconductors with the benefits of 3D printing for simplicity, fast production speed, and efficiency.

The work of Xu *et al.* demonstrates that a highly porous thermoelectric cooler can perform as well as its dense thin-film counterparts. The economic cost of 3D printing makes it desirable for fabricating semiconductor devices beyond thermoelectric cooling. The ability to precisely control porous microstructure could be advantageous to other energy applications that can tolerate or require high surface areas. These include electrocatalysts, fuel cells, batteries, and supercapacitors, from liquid-borne materials, such as molecular complexes and colloidal nanoparticles (*9*). ■

REFERENCES AND NOTES

1. T. D. Ngo *et al.*, *Compos. Compos. B Eng.* **143**, 172 (2018).
2. F. Kim *et al.*, *Nat. Electron.* **4**, 579 (2021).
3. S. Jo, S. Choo, F. Kim, S. H. Heo, J. S. Son, *Adv. Mater.* **31**, 1804930 (2019).
4. S. Xu *et al.*, *Science* **387**, 845 (2025).
5. M. P. Browne, E. Redondo, M. Pumera, *Chem. Rev.* **120**, 2783 (2020).
6. S. I. Kim *et al.*, *Science* **348**, 109 (2015).
7. Y. Zheng *et al.*, *Chem. Soc. Rev.* **50**, 9022 (2021).
8. X. Meng *et al.*, *Adv. Energy Mater.* **7**, 1602582 (2017).
9. F. Li *et al.*, *Science* **381**, 1468 (2023).

Institute for Electronics, Department of Information Technology and Electrical Engineering, ETH Zürich, Zürich, Switzerland. Email: yaremam@ethz.ch

10.1126/science.adv7126

NEUROSCIENCE

An innate drive to save a life

In mice, two brain regions drive the impulse to revive an unconscious companion

By **William M. Sheeran**[1,2] *and* **Zoe R. Donaldson**[1,3]

People who witness someone collapse and who subsequently perform cardiopulmonary resuscitation (CPR) report that they intervene because they intuitively understand that the person would otherwise die (*1*). Humans are not alone in this instinct. Animals as diverse as elephants [*Loxodonta africana* and *Loxodonta cyclotis* (*2*)], chimpanzees [*Pan troglodytes* (*3*)], and dolphins [*Tursiops truncatus* (*4*)] can recognize and intervene by touching, nudging, and even carrying an incapacitated individual. On pages 843 and 842 of this issue, Sun *et al.* (*5*) and Sun *et al.* (*6*), respectively, provide information on the neurobiology underlying this impulse. They report that mice (*Mus musculus*) have an instinct to revive an unresponsive mouse and identify two distinct brain regions that are crucial for this behavior. These findings add to the evidence that an impulse to help others in states of extreme distress is shared by many species and highlight neural mechanisms that drive instinctive rescue.

Innately driven social behaviors are those that are not explicitly taught but instead seem to preexist in the brain, ready to be triggered by the right circumstance (*7*). For example, a newly hatched duckling or gosling will exclusively follow the first moving entity it sees, a form of social bonding critical for offspring survival. This process, called imprinting, is mediated by *N*-methyl-D-aspartate (NMDA) receptors in the intermediate and medial mesopallium of the brain and is so strong and immutable that once imprinting has occurred, the baby bird is unable to imprint on anyone else (*8*).

Sun *et al.* and Sun *et al.* addressed whether such innate predisposition for specific social actions extends to how an animal responds to another's apparent distress. Both groups

[1]Department of Molecular, Cellular and Developmental Biology, University of Colorado Boulder, Boulder, CO, USA. [2]Medical Scientist Training Program, University of Colorado School of Medicine, Aurora, CO, USA. [3]Department of Psychology and Neuroscience, University of Colorado Boulder, Boulder, CO, USA. Email: zoe.donaldson@colorado.edu

A bystander mouse bites an incapacitated mouse's face and tongue, pulling the tongue out of the mouth and enlarging the unconscious animal's airway. This behavior often facilitated recovery.

found that mice increased the time they spent investigating and grooming another mouse if it was rendered unresponsive by either a sedative (*5*) or an anesthetic (*6*). As the drugged animal fell deeper into an unresponsive state, the bystander transitioned from more passive social investigation, such as sniffing, to increasingly intense grooming directed at the face. These bystander mice rarely groomed the faces of awake mice or asleep (but not drugged) controls.

Sun *et al.* (*6*) showed that facial grooming was particularly focused on pulling and biting at the incapacitated animal's tongue. Approximately half the time, the bystander animal was able to pull the other animal's tongue out of its mouth, successfully enlarging the unconscious animal's airway (see the photo). Furthermore, when a foreign object was placed in the incapacitated animal's mouth, the bystander mouse removed it before continuing to manipulate the tongue. These behaviors are reminiscent of how humans are taught to clear the airway of an unconscious individual during CPR (*9*).

It is easy to anthropomorphize these resuscitation-like behaviors as a rodent's approximation of CPR, but do they facilitate recovery? Sun *et al.* (*5*) found that incapacitated animals that received face-directed grooming from a bystander twitched more often and, critically, both Sun *et al.* and Sun *et al.* found that they regained consciousness more quickly than incapacitated animals that were alone. Furthermore, a separate, recent study reported that tongue biting and dragging promotes arousal in anesthetized mice through a direct tongue-brain circuit (*10*). Notably, in the studies by Sun *et al.* and Sun *et al.*, the bystander animals reduced the amount of face-directed grooming as the drugged animals regained consciousness, ultimately reverting to sniffing and other interactive behaviors that are typical of awake animal pairs. Therefore, face-directed grooming behaviors seem to aid recovery of the incapacitated mouse and to be implemented only when bystander animals sense that their intervention is needed.

To investigate the neuronal mechanisms underlying the observed resuscitation-like response, Sun *et al.* (*6*) screened candidate regions in the brains of bystander mice for increased expression of the immediate early gene *Fos*, which is a marker for neuronal activation. This screen identified the paraventricular nucleus (PVN) of the hypothalamus and the medial amygdala as regions of interest. *Fos* expression was particularly high in the subpopulation of PVN neurons that produce oxytocin, a neurohormone that is important for social behavior in organisms ranging from worms to humans (*11*). In rodents, oxytocin promotes consolation and empathy-like behaviors, which prompted Sun *et al.* (*6*) to focus on the potential role of these neurons in mediating resuscitation-like behaviors. By contrast, Sun *et al.* (*5*) focused their efforts on the medial amygdala, which is a part of the brain critical for a range of innate social behaviors. These behaviors include allogrooming, a form of comforting, gentle touch directed toward a distressed animal (*12*).

Despite examining two distinct brain regions, Sun *et al.* and Sun *et al.* obtained very similar results. In bystander mice, subsets of medial amygdala and oxytocinergic PVN neurons showed patterns of activity that discriminated between incapacitated and awake individuals. This discrimination was also evident in the collective activity of all recorded neurons in either region, implying that the brain might encode information about incapacitated states by using strategies that range from the output of individual, stimulus-responsive neurons to the summated output of entire populations of neurons. Furthermore, experimental inhibition of neurons in the medial amygdala or oxytocinergic neurons in the PVN diminished resuscitation-like behaviors, whereas activation of either enhanced them. This indicates that both brain regions are critical for promoting rescue responses.

Why might neurons in two distinct regions contribute to the same behavior? Oxytocinergic neurons in the PVN have diffuse projections throughout the brain, including a direct connection with neurons in the medial amygdala (*13*). The release of oxytocin from such projections might increase the signal-to-noise ratio of neuronal activity relating to specific social cues and in turn modify the perceived importance of those cues (*13*). For example, oxytocin release in female mice who have recently given birth heightens their focus on distressed pups, promoting the retrieval of those pups to the nest. This occurs because oxytocin enhances neural responses to pup calls in the left auditory cortex (*14*). Through mechanisms such as this, oxytocin and other neuromodulators such as dopamine and norepinephrine have been proposed to shape information processing in the brain in a dynamic way to promote distinct cognitive and behavioral functions (*15*).

In the context of behavioral responses to an unresponsive mouse, a specific neuromodulatory state, generated in part by PVN oxytocinergic neurons, might enable optimal information processing in key regions, including the medial amygdala, to enhance recognition of incapacitation and/or promote a rescue response. Experimental manipulation of oxytocin release specifically in the medial amygdala and other target regions will be required to test this hypothesis. ■

REFERENCES AND NOTES

1. J. Mausz, P. Snobelen, W. Tavares, *Circ. Cardiovasc. Qual. Outcomes* **11**, e004035 (2018).
2. I. Douglas-Hamilton, S. Bhalla, G. Wittemyer, F. Vollrath, *Appl. Anim. Behav. Sci.* **100**, 87 (2006).
3. M. Shimada, W. Yano, *Sci. Rep.* **13**, 16661 (2023).
4. S. A. Kuczaj 2nd *et al.*, *Learn. Behav.* **43**, 289 (2015).
5. F. Sun *et al.*, *Science* **387**, 843 (2025).
6. W. Sun *et al.*, *Science* **387**, 842 (2025).
7. D. Wei, V. Talwar, D. Lin, *Neuron* **109**, 1600 (2021).
8. B. J. McCabe, *Front. Physiol.* **10**, 658 (2019).
9. T. M. Olasveengen *et al.*, *Circulation* **142**, S41 (2020).
10. P. Cao *et al.*, *Sci. Adv.* **11**, eadq3874 (2025).
11. Z. R. Donaldson, L. J. Young, *Science* **322**, 900 (2008).
12. Y. E. Wu *et al.*, *Nature* **599**, 262 (2021).
13. R. C. Froemke, L. J. Young, *Annu. Rev. Neurosci.* **44**, 359 (2021).
14. B. J. Marlin, M. Mitre, J. A. D'amour, M. V. Chao, R. C. Froemke, *Nature* **520**, 499 (2015).
15. D. A. McCormick, D. B. Nestvogel, B. J. He, *Annu. Rev. Neurosci.* **43**, 391 (2020).

10.1126/science.adv3731

PHOTO: SUN *ET AL.*

POLICY FORUM

COMPUTING

High-performance computing at a crossroads

Long-term plans and comprehensive vision are needed

By **Ewa Deelman[1], Jack Dongarra[2,3,4], Bruce Hendrickson[5], Amanda Randles[6], Daniel Reed[7], Edward Seidel[8], Katherine Yelick[9]**

Over the past four decades, high-performance computing (HPC) has enabled considerable advances in scientific discovery and engineering, spurring technological development across the globe. However, with the demand for precision and fidelity of computational models continuing to grow, HPC faces bottlenecks in data handling, algorithm efficiency, and the scalability of new architectures, especially in fields such as chemistry and biology, where molecular simulations increasingly strain hardware and software limits. Governments worldwide are heavily investing in HPC infrastructure to support research, industrial innovation, and national security, each adopting distinct approaches shaped by national interests and regulatory landscapes. Conversely, in the US, there is no long-term plan or comprehensive vision for the next era of HPC advancements, leaving the future trajectory of US HPC and scientific and technological leadership uncertain.

HPC systems are advanced computing ensembles that harness the power of tens of thousands of tightly coupled processors and high-performance storage to deliver massive processing power, parallelism, and scalability. They enable faster computations, high-throughput exploration of ideas, more detailed models, and real-time decision-making in time-critical scenarios. They provide the ability to search massive key spaces for cryptography, conduct biomedical simulations for patient-specific treatments, and analyze petabyte-scale datasets generated by high-energy particle accelerators. Large-scale partial differential equation solvers are being used in a wide spectrum of simulations, from severe weather forecasting and seismic hazard modeling through aircraft and automotive design to managing oil and gas extraction. These solvers and applications require high fidelity and numerical precision because they often involve solving complex, nonlinear systems over millions or even billions of degrees of freedom. The computational intensity and memory demands of these applications also require HPC's massive parallel processing capabilities, high memory bandwidth, and efficient interconnection networks to handle the needed scale and resolution.

The rise of generative artificial intelligence (AI) has intensified the demands on HPC, transforming it from a resource primarily focused on physics-based simulations and large-scale scientific data analyses into a critical foundation for massive neural network training and inference. With AI's ubiquitous applicability to science, commerce, and global competitiveness, HPC's role has expanded, driving unprecedented demand and introducing new computational, economic, and energy requirements.

The 2024 Nobel Prizes awarded in physics, chemistry, and economics all underscored the pivotal role of computing in advancing scientific discovery and economic competitiveness. These achievements are enabled by AI method development and applications that rely on powerful HPC systems to accelerate AI model training, enable advanced AI research through model exploration, and support the large-scale data processing and data generation. However, although these successes capture global attention, they represent only a fraction of the broader ecosystem needed to maintain leadership in computing-driven innovation. Simply put, continued technical advances in HPC are needed for both traditional simulations and to advance the power and reach of AI.

TECHNICAL CHALLENGES

Today, HPC is in a state of transition, shaped by both technology constraints and market forces. As processor floating point operations per second (FLOPS) have grown exponentially, owing to advancements in transistor density, parallelism, and specialized accelerators, the memory bandwidth—which dictates the amount of data that can be moved to the processors per second—has improved much more modestly because of physical constraints, such as latency and power consumption, leading to an increasing FLOPS-to–memory bandwidth ratio. This means that systems can be inefficient, with processors incurring idle time while waiting for data. Along with fast-paced changes in computing hardware and software, the rise of generative AI, the market dominance of large-scale cloud service providers (hyperscalers), and the growth of international competition in innovation and workforce development are all reshaping the computing ecosystem.

Moore's law (*1*) predicted that the number of transistors on a microchip would double approximately every 2 years, leading to exponential increases in processing power and performance at steady-to-declining price points. Over nearly 60 years, this extraordinary, sustained progress has reshaped the modern world, but no exponential lasts forever. With transistor sizes approaching atomic scales, this rate of progress is no longer attainable.

State-of-the-art microchip fabrication facilities are technological marvels that now cost in excess of $10 billion. These costs can only be justified by products with very high market demand, and unfortunately, the HPC community is too small to drive markets on its own. Since the mid-1990s, the scientific community has leveraged "commodity" processors designed for other markets. This approach has worked well as central processing units (CPUs) and, more recently, graphics processing units (GPUs) have proved suitable for computational science. However, today's dominant market is AI, which does not require the high-precision arithmetic long common in computational modeling and is leading the design of chips with lower-precision arithmetic (16-bit floating point or 8-bit integer precision, as opposed to the 64-bit floating point precision of traditional processors). This trend raises a very real risk that future commodity hardware will not be appropriate for traditional modeling

[1]Information Sciences Institute, University of Southern California, Marina del Rey, CA, USA. [2]Department of Electrical Engineering and Computer Science, University of Tennessee, Knoxville, TN, USA. [3]Oak Ridge National Laboratory, Oak Ridge, TN, USA. [4]Department of Mathematics, University of Manchester, Manchester, UK. [5]Computing Directorate, Lawrence Livermore National Laboratory, Livermore, CA, USA. [6]Department of Biomedical Engineering, Duke University, Durham, NC, USA. [7]Scientific Computing and Imaging Institute, University of Utah, Salt Lake City, UT, USA. [8]Office of the President, University of Wyoming, Laramie, WY, USA. [9]Department of Electical Engineering and Computer Sciences, University of California Berkeley, Berkeley, CA, USA. Email: deelman@isi.edu

and simulation applications that continue to be important for science, engineering, and defense.

To mitigate these risks, algorithm researchers and numerical analysts are exploring ideas for effectively using the low-precision arithmetic that future chips will provide. On the hardware side, new design and fabrication models will allow the different functional units of a chip to be fabricated separately (so-called "chiplets") and then joined together. This should lower the cost of semicustom devices, perhaps allowing specialized HPC chips to be affordable. And, of course, the rapid advances in AI that are driving these trends will create new ways to use computing to advance science. At the same time, AI can also improve chip and HPC system design, reliability, scalability, and performance. Still, it remains to be seen whether these approaches will bear fruit for physics-based simulations.

Another major challenge for HPC is the power consumption of current machines, which is on the order of tens of megawatts. In 1974, Robert Dennard observed that the shrinkage from Moore's law came with a corresponding shrinkage in transistor energy consumption (*2*). For the subsequent three decades, microprocessors grew in performance with minimal increases in energy consumption. Dennard scaling ended in the mid-2000s, and the energy consumption of HPC platforms has been steadily rising ever since. There are ways to reduce power by changing programming models and architectures (for example, GPUs are notably more energy efficient than CPUs). However, sustained progress in energy efficiency will require a dedicated research program involving codesign of hardware and software. The results will potentially not only affect HPC but also improve the sustainability of power-hungry AI.

GEOPOLITICAL CONTEXT

In the second half of the 20th century, HPC was a tool for solving problems, often using simulations, that were not solvable using analytical methods. From early scientific and military applications, HPC was also adopted by the industrial sector, and more recently, it became a core driver for AI research and applications. Over time, the global HPC landscape has evolved, placing HPC in a geopolitical arena where nations compete for technological sovereignty and leadership, recognizing the strategic importance of computing leadership in advancing economic, scientific, and military capabilities. Governments worldwide are heavily investing in HPC infrastructure to support research, industrial innovation, and national security, each adopting distinct approaches shaped by national interests and regulatory landscapes. For example, EuroHPC (*3*), a European Union initiative, is Europe's response to concerns over data sovereignty and technological dependency. By building some of the world's fastest supercomputers in locations such as Finland, Italy, and Slovenia, EuroHPC aims to reduce reliance on external technologies, prioritize privacy-centric design, and establish Europe as a leader in fields requiring immense computational power, including climate modeling, personalized medicine, and AI. In Japan, the Fugaku supercomputer (*4*) developed by RIKEN and Fujitsu exemplifies a hybrid approach that balances academic and commercial use cases. This model reflects Japan's commitment to pushing computational boundaries for both fundamental research and industrial applications. Meanwhile, China has rapidly advanced its HPC capabilities, leveraging domestically developed infrastructure and processor technologies, such as those underpinning the Sunway TaihuLight and Tianhe-3 supercomputers (*5*). China's HPC strategy underscores a broader national goal of technological self-sufficiency, aiming to reduce dependence on foreign technology amid trade restrictions. These initiatives reveal deep-seated policy and technical tensions around national security, international collaboration, and market independence, highlighting the essential role of computational power in shaping geopolitical influence and sustaining global competitiveness.

Lawrence Livermore National Laboratory's El Capitan exascale system is the first supercomputer to use Advanced Micro Device (AMD)'s MI300A accelerated processing units.

PHOTO: GARRY MCLEOD/LLNL

US-CENTRIC CONCERNS

In 2024, the US celebrated the success of its Exascale Computing Project (ECP) (*6*), a $1.8 billion project launched by the Department of Energy (DOE) in 2016. This effort culminated in deploying the first US exascale supercomputers (capable of 10^{18} operations per second) at Oak Ridge, Argonne, and Lawrence Livermore National Laboratories. The ECP was a collaborative, multiyear effort that brought together national laboratories, academia, and industry to develop more than 20 new applications running on these exascale systems along with the underlying software stack and advanced hardware features. Today, the US lacks a strategic roadmap and a broad and coordinated federal HPC investment strategy, which puts the US at a crossroads, especially as other global players—notably China, Japan, and the European Union—aggressively pursue ambitious plans to develop their own advanced computing ecosystems.

In the past 2 years, we have coauthored multiple papers (*7*–*10*) that reviewed the state of the art in HPC, examined US leadership in this area, and explored potential future research and development (R&D). These reports have also called for a coordinated national R&D and funding strategy to advance HPC hardware designs, algorithms, software, and their applications. Such a strategy should be sustained over at least the next decade and across multiple federal agencies and should involve companies, including hyperscalers, universities, national laboratories, and strategic international partners. Because the technology and application landscapes are changing extremely rapidly, we advocated for developing prototype systems that would allow exploration of new hardware and software solutions. We also advocated for a holistic codesign to integrate hardware and software systems to optimize performance and efficiency across the computing ecosystem to support a new era of applications that will use AI, simulation, and their combination.

Given the importance of HPC to future economic competitiveness and national security, we are dismayed by the lack of coordinated action to address the recommendations in these reports, and we foresee long-term adverse outcomes for the US. With this Policy Forum, we aim to bring attention to the totality of challenges and opportuni-

ties in HPC and advocate for a multiagency, "whole-nation," and internationally collaborative effort to reenergize HPC R&D.

A key area of focus should be high-end computational science and engineering, where the US has a deep foundation in applied mathematics, particularly in scientific machine learning, optimization, and numerical algorithm development. These fields are essential in building applications and software for future national priorities and for harnessing the potential of emerging computing architectures. Moreover, sustained investment in core computer science disciplines—such as programming models, algorithmic complexity, AI, data management, system architectures, and network research—will be critical to drive future HPC innovations. There is also exciting research into new computing models, in particular quantum computing, which will require deep interdisciplinary efforts to realize. This should be seen as a promising future technology with the potential to transform the feasibility of computational solutions for important applications, such as cryptography, drug discovery, and molecular modeling, but not as a replacement for the breadth and ubiquity of traditional computing in the near term.

The 2022 CHIPS and Science Act (*11*) was a step in the right direction, bolstering semiconductor manufacturing (for example providing almost $8 billion to expand semiconductor facilities across Arizona, New Mexico, Ohio, and Oregon) and creating a new Directorate for Technology, Innovation and Partnerships within the US National Science Foundation geared toward transitioning research into practice and tighter engagement with industry (for example, funding regional microelectronics hubs). Another key advance is a renewed focus on data life cycles and data ecosystems. More recently, the creation of the new Vision for American Science & Technology (VAST) task force to advise decision-makers in the federal government is also another positive development (*12*) because charting the course of US science and technology will undoubtably require investments in HPC computing to solve complex problems. The US Congress has also made recommendations that would help maintain US leadership in AI research, industry adoption, and private sector innovation (*13*), noting that responsible AI innovation requires HPC support to ensure ethical guardrails and sustainable development. Meanwhile, the private sector is investing hundreds of billions of dollars in AI data center infrastructure.

Although laudable, these steps have yet to bear fruit, and more importantly, they do not address the central challenge of federal support for HPC-specific R&D that would result in innovative HPC solutions to the outlined technical challenges. Lack of progress in HPC puts US competitiveness at risk in the race against countries with integrated public-private strategies. The US must urgently pursue meaningful collaborations with industry, including deeper research in computing hardware, software systems, algorithm development, and applications, to capitalize fully on progress in microelectronics.

To navigate HPC's future, we urge the US federal government to organize a task force charged with creating a national, 10-year roadmap for HPC in the post-exascale, post-ECP era. The roadmap should encompass the entire HPC ecosystem, which in addition to hardware acquisition, includes application and system software as well as a well-trained workforce. The task force should include participation from academia, national laboratories, industry, and government. The needed roadmap should include investment at the federal level in computational science and engineering, integrated with AI advancements, and exploration of customized HPC systems tailored to address the distinct demands of multidisciplinary scientific and engineering simulations as well as their commercial and national security applications. Such efforts include creating real hardware and software prototypes at scale, incorporating custom silicon designs to test emerging ideas, and education and training of future researchers and engineers that can contribute to the HPC-AI ecosystem. To realize the roadmap, it is essential to move beyond planning to deliberate implementation. The enactment should promote broad participation, building on ideas developed in programs such as the National Artificial Intelligence Research Resource (NAIRR) (*14*), which aims to broaden access to AI research resources (computational systems, datasets, and educational materials) and to address key barriers that limit participation. Because technologies are evolving at a rapid pace, such a roadmap would need to be a living document. The roadmap and associated actions would need to be periodically revisited and adapted both to the national needs and priorities and to the changing technosocial landscape.

CONCLUSIONS

Recently, the Council on Competitiveness and its National Commission on Innovation and Competitiveness Frontiers have called on the new administration and the new Congress to "act strategically and boldly toward a transformative goal for US competitiveness: boosting U.S. innovation tenfold" (*15*) and to specifically pursue a whole-nation approach to drive technological innovation. There are many lessons to learn from previous efforts and many existing programmatic elements to build upon. With international competition for leadership in computing intensifying, without a renewed commitment, we fear that the US will soon lose scientific computing leadership and technological independence, which will have deeply worrying implications for the US economy, national security, and the international science community. ■

REFERENCES AND NOTES

1. G. E. Moore, *Electronics* **38**, 114 (1965).
2. R. H. Dennard *et al*., *IEEE J. Solid-State Circuits* **9**, 256 (1974).
3. The European High Performance Computing Joint Undertaking (EuroHPC JU); https://eurohpc-ju.europa.eu/about/discover-eurohpc-ju_en.
4. S. Matsuoka, "Fugaku and A64FX: The first exascale supercomputer and its innovative arm CPU" in *2021 Symposium on VLSI Circuits* (IEEE, 2021), pp. 1–3.
5. Z. Chen, "The progress of high performance computing in China and the development trend of international high performance computing" in *China's E-Science Blue Book 2020*, Chinese Academy of Sciences *et al*., Eds. (Springer, 2021), pp. 43–60.
6. P. Messina, *Comput. Sci. Eng.* **19**, 63 (2017).
7. J. Dongarra *et al*., "Can the United States Maintain Its Leadership in High-Performance Computing? - A report from the ASCAC Subcommittee on American Competitiveness and Innovation to the ASCR Office" (US DOE Office of Science, 2023); https://www.osti.gov/biblio/1989107.
8. E. Seidel *et al*., "2024 Advanced Scientific Computing Advisory Committee (ASCR): Facilities Subcommittee Recommendations" (US DOE, 2024); https://www.osti.gov/biblio/2370379.
9. E. Alhajjar, T. Islam, "SIAM Task Force Anticipates Future Directions of Computational Science" (Society for Industrial and Applied Mathematics, 2024); https://www.siam.org/publications/siam-news/articles/siam-task-force-anticipates-future-directions-of-computational-science/.
10. National Academies of Sciences, Engineering, and Medicine, *Charting a Path in a Shifting Technical and Geopolitical Landscape: Post-Exascale Computing for the National Nuclear Security Administration* (National Academies Press, 2023).
11. T. Ryan [D-OH-13], CHIPS and Science Act (117th Congress, 2022); https://www.congress.gov/bill/117th-congress/house-bill/4346.
12. S. S. Parikh, M. K. McNutt, D. Gil, *Science* **386**, 947 (2024).
13. 118th Congress, "Bipartisan House Task Force Report on Artificial Intelligence" (2024); https://www.speaker.gov/wp-content/uploads/2024/12/AI-Task-Force-Report-FINAL.pdf.
14. National Artificial Intelligence Research Resource Task Force, "Strengthening and Democratizing the U.S. Artificial Intelligence Innovation Ecosystem: An Implementation Plan for a National Artificial Intelligence Research Resource" (2023); https://www.ai.gov/wp-content/uploads/2023/01/NAIRR-TF-Final-Report-2023.pdf.
15. National Commission on Innovation & Competitiveness Frontiers, "Competing in the Next Economy: Innovating in the Age of Disruption and Discontinuity" (2024); https://compete.org/wp-content/uploads/coc-disruption_discontinuity-call-to-action-final_12.13.24.pdf.

ACKNOWLEDGMENTS

B.H. leads the Computing Directorate at Lawrence Livermore National Security, LLC, under contract no. DE-AC52-07NA2 7344 with the US DOE. D.R. is a Microsoft stockholder. E.S. is a member of the DOE Advanced Scientific Computing Advisory Committee and a member of the Scientific Advisory Board to the president of the Helmholtz Association.

10.1126/science.adu0801

Shannon Alonzo's *Washerwoman* (2018) honors the labors of the artist's Caribbean ancestors.

PUBLIC HEALTH

The perils of labor

A new exhibition probes the health consequences of work

By **Caitjan Gainty**

The Wellcome Collection's exhibition *Hard Graft: Work, Health and Rights* locates its inspiration in the labor inequalities that the COVID-19 pandemic revealed, between "people in lower paid, public-facing jobs and those who were able to isolate." In its bid to illuminate undervalued work, the exhibition moves peripatetically across space and time, beginning with "the Plantation."

This first section's exploration of the global intensification and exploitation of both land and people begins in the 19th century. A photograph that sets viewers amid workers on a hillside coffee farm in 19th-century Brazil and a print that brings viewers to a tea plantation in the same period in China make clear the grueling nature of plantation work. They hint too at the power structures that define it, a theme neatly encapsulated in a nearby description of "drapetomania"—the 19th-century "mental health condition" that described the desire of enslaved individuals to escape. You would have to be crazy to want freedom: a convenient thought for plantation owners whose pocketbooks were the beneficiaries of such medical convolutions.

Hard Graft: Work, Health and Rights
Cindy Sissokho, curator
Wellcome Collection, London, UK; through 27 April 2025.

A series of photos by Md Fazla Rabbi Fatiq brings visitors to the present, with depictions of the gnarly physical effects suffered by those working today on tea plantations in Bangladesh. And a compelling video by the investigative agency Forensic Architecture powerfully connects the spatial continuity of inequality in Louisiana's Death Alley, where toxic air, the petrochemical behemoths that produce it, and the Black communities that breathe it map onto the historical boundaries of antebellum plantations with ruthless precision. The film is a highlight, not just for what it has to say about the racial politics of work in the United States but also for its stark reminder that such exploitation is all too often a generational affair.

In comparison to the Plantation, the other two sections of the exhibition feel a bit thinner. "The Street," which covers a range of work from sanitation to prostitution, is dominated by an enormous altar by the artist Lindsey Mendick and a film by the author and actor Mendez, both commissioned for the exhibition. The altar references the ecclesiastical setting of sex worker protests during the 1970s and 1980s, when taking refuge in the church offered protection from rampant discrimination and criminalization. It is impressive but slightly opaque, as is Mendez's film at the center, which commands the space but requires a transcript to make sense of.

"The Home" too lacks the impressiveness of the Plantation, but it has its own gems, particularly a set of blueprints and photographs lifted from architectural magazines. Originally published to showcase the massive modern residences designed by top architectural firms for the Peruvian one percent, they are here recurated to highlight the minimal spaces set aside for the live-in help, which are artfully hidden in the far reaches of the home, like a clever storage hack.

At the far end of this space, a film movingly personalizes this architectural abstraction. Made in cooperation with migrant domestic workers in the UK, it documents the often-degrading experience associated with "caring" for those who do not "care" for you. The film focuses on personal journeys and the psychological and physical toll of this work. But it also implicates the British state for its failure to put in place basic protections for all those working within its borders.

Then there is Shannon Alonzo's beautiful, terrible sculpture of a life-size "washerwoman." Headless and made of materials (beeswax and resin) that evoke bodily decay, her twisted and swollen hands challenge the viewer as much as any bust of Apollo. One important theme of *Hard Graft* is the "impact of physical work on health," and here it is powerfully expressed.

Elsewhere, the relationship between labor and health is more conceptually reductive in its depiction. Charmaine Watkiss's series of images connecting herbal remedies to women's bodies is beautiful, as is Maria Floriza Veríssimo's "Book of Landscapes." But both are folded into a view of 19th-century herbal remedies as significant only as resistance to Western medical practice. Yet, these remedies often became Western medicine, appropriated (because they worked) into the bedrock of the conventional medical practice we use today.

That there is more of a story to tell here, about the health care we enjoy and the uncredited labor that made it, is no inconsequential complaint. Here, as elsewhere, the exhibition prefers examples that leave implicit the fact that everything that makes our lives possible, safe, and comfortable—from the medicine we use, to the food we eat, to the things we buy—is entangled in this story of exploitation. For all of the visibility it brings, the exhibition mostly shies away from asking us to do the work to confront our own role in keeping hard graft so inhumanly hard. ■

10.1126/science.adu6588

The reviewer is at the Centre for the History of Science, Technology and Medicine, King's College London, London, UK. Email: caitjan.gainty@kcl.ac.uk

SCIENCE AND SOCIETY

Morality in a more-than-human world

Two authors probe the metrics by which we determine who, and what, matters

By **Joshua C. Gellers**

The dawn of the more-than-human world is upon us, and scholars have begun tackling relevant moral and legal questions in ways that cut across entities rather than focusing exclusively on any one kind of being. Two new books, philosopher Jeff Sebo's *The Moral Circle* and anthropologist Webb Keane's *Animals, Robots, Gods*, make meaningful contributions to this fraught but fascinating discourse.

As evidenced by its subtitle ("Who Matters, What Matters, and Why"), *The Moral Circle* takes on a heady task. Drawing on the utilitarian tradition, Sebo articulates a moral calculus that broadly observes the importance of traits such as agency, consciousness, and sentience: "If a being has at least a *one in a thousand* chance of mattering, given the evidence, then they merit at least *some* consideration, even if only a tiny amount." This seemingly simple framework is actually quite novel. Recognizing that the possession of morally important attributes by nonhumans is rife with uncertainty, he counsels that the optimal approach should be one of caution and humility.

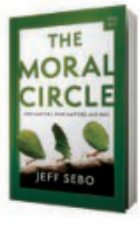

The Moral Circle: Who Matters, What Matters, and Why
Jeff Sebo
Norton, 2025. 192 pp.

Animals, Robots, Gods: Adventures in the Moral Imagination
Webb Keane
Princeton University Press, 2025. 192 pp.

Sebo is nothing if not cautious and humble. He is cognizant of the risk that inheres in mistreating animals, robots, and even future nonhumans—actions that might cause major moral harms. But underlying this tentative prescription are some contradictions and unaddressed weaknesses. For instance, his reliance on ontological properties neglects consideration of scholars' serious disagreements about their utility and empirical basis. Sebo accepts these properties as valid without fully contemplating the potential of relational approaches to moral status, which are often found in non-Western and Indigenous cultures, thus not quite fulfilling his stated objective of being "pluralistic." In addition, some may find his "probabilistic" approach to assessing moral concern uncomfortably technocratic and thus divorced from the more emotive and phenomenological dimensions of our moral intuitions. These shortcomings aside, *The Moral Circle* is a thoroughly digestible and wonderfully approachable example of popular philosophy at its very best, as curious as it is careful.

In *Animals, Robots, Gods*, Keane embarks on a global journey across our messy moral terrains. Right from the outset, he prepares the reader to accept that identifying an always-applicable law might not be possible, as moral traditions are complex, contingent, and culturally specific. This imbues the discourse on the moral status of nonhumans with just the kind of cross-cultural sensitivity that only anthropology can offer. Keane also seeks to draw a contrast between his work and "the mainstream philosophical tradition," which, he notes, tends to reflect the views of a "Western, Educated, Industrialized, Rich and Democratic" (i.e., "WEIRD") global minority.

Organized in terms of cultural encounters with humans, near-humans, quasi-humans, and superhumans, *Animals, Robots, Gods* covers substantial ground. From autonomous vehicles and grandmothers on ventilators to sacrificial buffalo and Mayan shamans, Keane touches on more kinds of morally relevant beings than perhaps any other scholar has to date. And despite the impossibility of drawing universal conclusions about what qualifies an entity for moral concern, his sprawling but tightly managed effort does sketch out several pervasive trends: that humans "have always lived with ethically significant others," that every culture throughout history abides by a code of ethics, and that moral differences between societies are inevitable.

Given its disciplinary perspective, *Animals, Robots, Gods* unsurprisingly engages with academic concepts in a way that will be intelligible to anthropologists. But occasionally, Keane's lack of familiarity with how key constructs are treated within other fields comes to the fore. He writes, for instance, about moral subjects without discriminating between moral agents and moral patients, a bright line for many moral philosophers. The book is also at least descriptively anthropocentric, expertly telling stories of how various cultures treat nonhumans without working to destabilize the human-centered thinking that dominates the WEIRD world. Still, *Animals, Robots, Gods* lands as a narratively rich circumnavigation of how we treat others.

While these two new works share a common ambition to expand our moral thinking beyond our own species, they also differ in important ways. Whereas Sebo is meticulous and deliberate in his attempt to outline a program capable of helping us make moral decisions, Keane devotes more energy to merely walking readers through alternative views without making a case for what should matter and how. Keane also revels in a kind of moral agnosticism that Sebo actively seeks to overcome, going as far as to claim that the "dream of a single calculus" is simply "unrealistic." Overall, however, both authors deliver fresh, accessible entrants to the burgeoning literature on the more-than-human world and our obligations toward it. ■

New frameworks probe the moral status of nonhumans, such as robots and animals.

PHOTO: SASCHA SCHUERMANN/GETTY IMAGES FOR THE INVICTUS GAMES FOUNDATION

The reviewer is at the Department of Political Science and Public Administration, University of North Florida, Jacksonville, FL, USA, and the author of *Rights for Robots: Artificial Intelligence, Animal and Environmental Law* (Routledge, 2020). Email: josh.gellers@unf.edu

10.1126/science.adu4642

LETTERS

A US military base could harm fragile Galápagos species, such as this marine iguana (*Amblyrhynchus cristatus*).

Edited by **Jennifer Sills**

Military base threatens Galápagos Islands

In December 2024, the Ecuadorian government, led by President Daniel Noboa, authorized the establishment of a US military base on the Galápagos Islands, a Natural World Heritage Site. This decision risks violating Articles 10, 71, 72, and 258 of the Ecuadorian Constitution, which recognize nature's rights and prohibit activities that harm fragile ecosystems, such as the Galápagos (*1*). Moreover, the project undermines the sovereignty of the Ecuadorian people and sets a dangerous precedent for violating international treaties that safeguard protected areas and World Heritage Sites. To prioritize the preservation of this irreplaceable natural heritage and the rights of the Ecuadorian people, decision-makers should reconsider their approval of the base.

US military bases on islands have often left irreversible scars on fragile ecosystems (*2*, *3*). The installations require extensive land modification, infrastructure, and resource consumption, exacerbating overpopulation and resource depletion (*4*, *5*). Hazardous waste, pollution, and unsustainable practices are common, as seen in Okinawa and Hawai'i (*2*, *3*). The Galápagos have already suffered similar consequences. In 1941, a US base on Baltra Island caused habitat destruction, resource overexploitation, and increased risk of invasive species because of heightened travel, which resulted in substantial ecological disruption (*4*–*6*).

Beyond environmental harm, the proposed military base poses economic and political concerns. Minister of National Defense Gian Carlo Loffredo claimed that the base would strengthen maritime security and combat illegal fishing and drug trafficking (*7*). Although these goals may appear legitimate, they prompt questions about whether US geopolitical ambitions could undermine Ecuador's sovereignty. Additionally, the Status of Forces Agreement between the US and Ecuador (*8*) grants immunity to US personnel, jeopardizing accountability. The Galápagos Islands must not become a casualty of political or strategic agendas.

With US ships and crews already entering the islands, governments, academic institutions, scientists, and conservationists worldwide must take immediate action. In addition to its constitutional obligations, Ecuador must uphold its commitments to several international treaties, including the Convention on Biological Diversity (CBD) (*9*), the United Nations Framework Convention on Climate Change (UNFCCC) (*10*), the Law of the Sea (*11*), and the United Nations Educational, Scientific and Cultural Organization (UNESCO) World Heritage Convention (*12*). National and international stakeholders should urge Ecuador to adhere to these agreements. In addition, scientists, conservationists, and academic institutions must unite to expose the harm that a military base could inflict on the Galápagos and to safeguard this distinctive and fragile environment.

María José Navarrete Méndez[1]*, Gabriela Mena González[2], Leticia M. Ochoa Ochoa[1,3]
[1]Department of Integrative Biology and Museum of Vertebrate Zoology, University of California Berkeley, Berkeley, CA, USA. [2]Maestría en Ecología Tropical y Conservación, Universidad San Francisco de Quito, Quito, Ecuador. [3]Museo de Zoología Alfonso L. Herrera, Facultad de Ciencias, Universidad Nacional Autónoma de México, Mexico City, Mexico.
*Corresponding author.
Email: mnavarrete@berkeley.edu

REFERENCES AND NOTES

1. Asamblea Constituyente, Constitución de la República del Ecuador (Quito, 2008).
2. A. Oshiro, *Sociol. Compass* **18**, e13099 (2024).
3. K. Niheu, L. M. Turbin, S. Yamada, *Pac. Public Health* **13**, 172 (2006).
4. M. J. Barragan-Paladines, R. Chuenpagdee, *Coast. Manag.* **45**, 339 (2017).
5. M. Becker, *Dipl. Hist.* **41**, 518 (2017).
6. E. Hennessy, *Soc. Stud. Sci.* **48**, 483 (2018).
7. Ministry of National Defense of Ecuador, "Informe sobre el conflicto armado interno," YouTube (18 December 2024); https://www.youtube.com/watch?v=-vBs_xesOCI.
8. US Department of State, Status of Forces Agreement between the United States of America and Ecuador (24-223.1) (signed at Quito 6 October 2023, entered into force 23 February 2024); https://www.state.gov/ecuador-24-223.1.
9. United Nations, Convention on Biological Diversity (1992); www.cbd.int/doc/legal/cbd-en.pdf.
10. United Nations, Framework Convention on Climate Change (1992); https://unfccc.int/sites/default/files/resource/02_0.pdf.
11. United Nations, United Nations Convention on the Law of the Sea (1982); www.un.org/depts/los/convention_agreements/texts/unclos/unclos_e.pdf.
12. United Nations, United Nations Educational, Scientific and Cultural Organization: Convention Concerning the Protection of the World Cultural and Natural Heritage (1972); https://whc.unesco.org/archive/convention-en.pdf.

10.1126/science.adv5791

Airport plan imperils South Korea's tidal flat

Sura, a tidal flat in the Mangyeong estuary in South Korea, has survived one of the world's largest coastal reclamation projects. Now, a proposed airport threatens this critical refuge (*1*). The airport's construction, planned to take place between 2025 and 2029, would lead to an irreversible loss of the biodiversity and sociocultural activities that Sura supports (*1*, *2*).

The reclamation site in which Sura is located, Saemangeum, was once a vast estuarine ecosystem (*3*, *4*). Saemangeum served as a key stopover along the East Asian–Australasian Flyway, supporting at least 330,000 shorebirds annually (*5*). However, the construction related to the reclamation project disrupted its biodiversity and ecosystem services (*3*, *4*, *6*). Amid this environmental upheaval, Sura still supports endangered flora and fauna, especially migratory birds, including 59 nationally protected species and 27 globally threatened species (*1*).

PHOTO: GABRIELA MENA-GONZÁLEZ

The airport proposal claims socioeconomic benefits, but the plan was exempted from the preliminary feasibility assessment, so no evidence is available to demonstrate that the anticipated benefits outweigh the environmental risks (*7*). Gunsan Airport is located about 1.3 km from the proposed site and is underused, putting the need for a new airport in question. Moreover, environmental impact assessments confirm the conservation value of Sura and indicate that bird strikes would pose substantial aviation safety risks, as they do at other airports near bird habitats (*1*, *8*).

This development would undercut the South Korean government's efforts to convince the international community of the outstanding universal value of their tidal flats, half of which were designated as United Nations Educational, Scientific and Cultural Organization (UNESCO) World Heritage sites in 2021 (*9*). Sura is only 7 km away from the heritage site location. The country was also among the 188 nations at the 2022 UN Biodiversity Conference (COP15) that committed to halt global biodiversity loss by 2030 and to take urgent actions to prevent the extinction of endangered species (*10*). Sacrificing Sura to create another unjustifiable airport would put the country's commitment to environmental goals in question.

To resolve this controversy, the South Korean government must pause the airport project until a thorough and independent feasibility and environmental impact review has been conducted. UNESCO and the International Union for Conservation of Nature should assess the impact of the airport on the integrity of heritage properties. Scientific experts should provide alternatives that promote conservation and demonstrate the irreplaceable socioeconomic and ecological value of Sura. Organizations such as the Convention on Biological Diversity should develop international legal mechanisms to stop ecologically destructive and risky projects of this kind. The dire situation in Sura challenges mainstream conservation paradigms that rely on government goodwill, which is often compromised by competing development priorities, and highlights the fate of countless tidal flats lost in South Korea and globally in recent decades (*2*, *11*, *12*).

Taejin Park[1]*, Young Rae Choi[2], Yekang Ko[3], Nahee Kim[4], Dongpil Oh[5], Nial Moores[6]
[1]Bay Area Environmental Research Institute, Moffett Field, CA, USA. [2]Florida International University, Miami, FL, USA. [3]University of Oregon, Eugene, OR, USA. [4]Joint Action for Cancellation of Saemangeum New Airport, Jeonju, Jeollabuk-do, Republic of Korea. [5]Saemangeum Citizen Ecological Investigation Team, Gunsan, Jeollabuk-do, Republic of Korea. [6]Birds Korea, Busan, Republic of Korea.
*Corresponding author. Email: tpark@baeri.org

REFERENCES AND NOTES

1. Ministry of Land, Infrastructure, and Transport, "Saemangeum International Airport construction project strategic environmental impact assessment report" [in Korean] (2021); https://doi.org/10.5281/zenodo.14799451.
2. Y. R. Choi, *J. Hist. Geog.* **82**, 23 (2023).
3. N. Moores, D. I. Rogers, K. Rogers, P. M. Hansbro, *Emu* **116**, 136 (2016).
4. J. Ryu *et al.*, *Ocean Coast. Manag.* **102**, 559 (2014).
5. M. Barter, "Shorebirds of the Yellow Sea: Importance, threats, and conservation status," Wetlands 461 International Global Series 9, International Wader Studies 12 (Environment Australia, 2002).
6. J. K. Lee *et al.*, *Bird Conserv. Intl.* **28**, 238 (2018).
7. Ministry of Land, Infrastructure, and Transport, "Saemangeum new airport prefeasibility study" [in Korean] (2019); https://doi.org/10.5281/zenodo.14799463.
8. I. C. Metz, J. Ellerbroek, T. Mühlhausen, D. Kügler, J. M. Hoekstra, *Aerospace* **7**, 26 (2020).
9. UNESCO, "Decision 44 COM 8B.6 Getbol, Korean Tidal Flats" (Republic of Korea) (2021); https://whc.unesco.org/en/decisions/7925.
10. Convention on Biological Diversity, *The Kunming-Montreal Global Biodiversity Framework* (2022); https://www.cbd.int/doc/c/e6d3/cd1d/daf663719a03902a9b116c34/cop-15-l-25-en.pdf.
11. N. J. Murray *et al.*, *Nature* **565**, 222 (2019).
12. D. Sengupta *et al.*, *Earth Futur.* **11**, e2022EF002927 (2023).

COMPETING INTERESTS

N.K. and D.O. are members of the Joint Action for the Cancellation of Saemangeum New Airport, an organization leading a litigation case to halt the airport plan. Y.R.C., Y.K., and N.M. have participated in the case as expert witnesses.

10.1126/science.adv5597

COP30's hypocritical cruise ship lodging plan

The 2025 United Nations Climate Change Conference (COP30) will convene in November in Belém, Brazil. The location, often referred to as the gateway to the Amazon (*1*, *2*), represents a historic opportunity to position the Amazon as central in global climate negotiations. Hosting the conference in a region that faces critical challenges such as deforestation (*3*), illegal mining (*4*), and extreme climatic events (*5*, *6*) underscores the importance of the discussions. However, the Brazilian government's proposed use of luxury cruise ships for conference accommodations (*2*) is at odds with the meeting's goals.

Although cruise ships can meet the demand for temporary accommodation, their operations are notoriously polluting (*7*–*9*), with substantial emissions of greenhouse gases, including carbon dioxide, nitrogen oxides, sulfur oxides, and particulate matter (*7*, *9*). About 88.5% of gas and particle pollutants from diesel-powered cruise ships are generated during the hoteling phase, during which they use auxiliary engines (*7*, *9*).

Cruise ship passengers are associated with 0.42 tonnes of carbon dioxide emissions per day, compared with 0.05 tonnes for land-based tourists (*10*). For COP30, between 7000 and 12,000 people are expected to stay in the floating lodges for 11 days (*2*, *11*). For the minimum number of guests, the difference between ship and land-based lodging (0.37 tonnes per person per day) will total about 28,450 tonnes of carbon dioxide. The production of such substantial emissions conflicts with global commitments to climate mitigation. At a conference focused on climate goals, logistics should align with values such as sustainability and climate justice.

If Brazil proceeds with the plan to use cruise ships, organizers should implement mitigation measures and take ethical considerations into account. Shore power systems (cold ironing) could substantially reduce the environmental burden by allowing ships to connect to the electrical grid instead of relying on diesel-powered auxiliary engines (*7*). In addition, organizers should prioritize investments in local infrastructure to benefit host communities and nearby areas such as Outeiro district, where 57% of residents live in precarious conditions and 16% lack access to basic sanitation (*2*). Transforming the conference into a model of sustainable planning is not only a responsibility but also a reaffirmation of the values COP30 seeks to promote.

Diego S. Campos[1,2], Rafael F. Oliveira[2]*, Lucas O. Vieira[1,2], Felipe P. Ottoni[1,2]
[1]Programa de Pós-Graduação em Biodiversidade e Biotecnologia da Amazônia Legal—Rede BIONORTE, Universidade Federal do Maranhão, São Luís, MA, Brazil. [2]Laboratório de Sistemática e Ecologia de Organismos Aquáticos, Universidade Federal do Maranhão, Chapadinha, MA, Brazil.
*Corresponding author.
Email: raphaelmais12@gmail.com

REFERENCES AND NOTES

1. "Rumo à COP30," *gov.br* (2024) [in Portuguese]; https://www.gov.br/planalto/pt-br/agenda-internacional/missoes-internacionais/cop28/cop-30-no-brasil.
2. V. Sassine, "Governo quer transatlânticos da COP30 em área onde casas dependem de fossas e enfrentam erosão," *Folha de São Paulo* (2025) [in Portuguese]; https://archive.ph/8qZsF.
3. E. A. Haddad *et al.*, *Nat. Sustain.* **7**, 1141 (2024).
4. L. C. Ferreira Neto *et al.*, *Nat. Commun.* **15**, 9847 (2024).
5. F. P. Ottoni *et al.*, *Science* **382**, 1253 (2023).
6. J. A. Marengo *et al.*, *Acta Amaz.* **54**, e54es22098 (2024).
7. S. Virgili, U. Rizza, M. Tommasi, S. Di Nisio, G. Passerini, *WIT Trans. Ecol. Environ.* **263**, 221 (2024).
8. S. Papaefthimiou, A. Maragkogianni, K. Andriosopoulos, *Int. J. Sustain. Transp.* **10**, 985 (2016).
9. F. Murena, L. Mocerino, F. Quaranta, D. Toscano, *Atmos. Environ.* **187**, 70 (2018).
10. Friends of the Earth, "Cruising versus land vacationing: An analysis of vacation carbon footprints in Seattle" (2024); https://foe.org/resources/cruising-vs-land-vacationing-an-analysis/.
11. J. Gabriel, "Pará aposta em Airbnb, vila provisória e cruzeiros para tentar vencer falta de mais de 30 mil quartos para COP30," *Folha de São Paulo* (2024) [in Portuguese]; https://archive.ph/wip/0wohg.

10.1126/science.adv7134

RESEARCH

IN *SCIENCE* JOURNALS

Edited by **Michael Funk**

PHOTO: DEVLIN *ET AL.*

ROBOTICS

Collectives acting as solids or fluids

One vision for robotics is to design groups of simple robots that work together, for example, like a colony of ants that can move like a flowing fluid but can also form a solid structure such as a bridge for an unpassable span. Devlin *et al*. designed a robot collective that can switch between a "fluidizing" state and a solid state based on the rotational state of the robot. Drawing from embryonic morphogenesis, the authors identified three important components of the biological process, interunit force, polarization, and adhesion, and developed their robotic counterparts. These elements enable locally tunable mechanical properties that can be exploited to change the collective's shape and strength. —Marc S. Lavine *Science* p. 880, 10.1126/science.ads7942

Motorized gears, magnets, and photodiodes enable collective action of robots based on principles from cell biology.

PROTEIN DESIGN

Leveling up a protein language model

A protein sequence encodes the information needed to determine the three-dimensional structure and cellular function of said protein. Advances in machine learning and the availability of large public repositories of sequence, structural, and functional data are enabling researchers to understand this code and build on it. Hayes *et al*. now present ESM3, a protein language model that enables the programmed generation of protein structure and sequence in response to user prompts. The authors demonstrate versatility across a range of motif scaffolding and key word–prompted generation tasks. As an example of the functional sensitivity of ESM3, they produced highly diverged variants of green fluorescent protein that retain the ability to fold and produce the protein-derived chromophore. —Michael A. Funk

Science p. 850, 10.1126/science.ads0018

POLYMER CHEMISTRY

Breaking down methacrylates

Most current plastic-recycling methods rely on macroscopic mechanical shredding, cleaning, and reprocessing. As a result, the properties of the recycled material degrade relative to the virgin polymer. Chemical decomposition to the original monomer would enable more thorough purification and then repolymerization to restore ideal performance. Wang *et al*. report the surprising discovery that in dichlorobenzene solvent, violet light irradiation can cleanly break down polymethacrylates such as plexiglass to their original monomers. The process appears to involve hydrogen abstraction from the backbone by small quantities of chlorine radicals liberated from the solvent. —Jake S. Yeston

Science p. 874, 10.1126/science.adr1637

NEUROSCIENCE

Targeting α-synuclein internalization

One of the major causes of neurodegeneration in patients with Parkinson's disease (PD) is the intracellular accumulation of α-synuclein in neurons. Wu *et al*. investigated the mechanisms mediating the uptake of α-synuclein in neurons using in vitro and in vivo models. The product of the recently identified PD-risk gene *FAM171A2* was found to be the neuronal receptor for α-synuclein fibrils, mediating their internalization through endocytosis. In silico screening identified an

approved drug, bemcentinib, that is able to inhibit α-synuclein internalization in vitro and in vivo by blocking its binding to FAM171A2. The results provide insights into PD pathogenesis and identify a potential therapeutic target. —Mattia Maroso

Science p. 892, 10.1126/science.adp3645

METALLURGY

Managing metals with magnetics

Laser-based additive manufacturing of metals is a complex process that often leads to the introduction of voids through what are called keyhole instabilities. Fan *et al*. sought to understand how this pore-forming process is modified with magnetic fields using high-speed x-ray imaging. They found that a flow driven by the thermoelectric effect can either improve or degrade keyhole formation depending on the direction of the field. These observations reveal one way to modulate the formation of pores, which is important for controlling the mechanical properties of the alloy. —Marc S. Lavine

Science p. 864, 10.1126/science.ado8554

GPCR SIGNALING

A sticky ligand sustains GPCR signaling

The vasopressin type 2 receptor (V_2R) is a G protein–coupled receptor (GPCR) that regulates fluid balance and can be activated by the ligands oxytocin and arginine vasopressin. Teixeira *et al.* found that sustained V_2R signaling depended on the activating ligand but was independent of receptor internalization by the scaffolding protein β-arrestin. V_2R-induced signaling occurred primarily at the plasma membrane, and its duration depended on the residence time of the ligand on the receptor, which was longer after activation with arginine vasopressin than with oxytocin. V_2R internalization into endosomes induced by β-arrestin helped to terminate V_2R signaling due to ligand dissociation from V_2R caused by acidified endosomal pH. These results show that the overall duration of V_2R signaling is determined by ligand residence time on the receptor. —Wei Wong

Sci. Signal. (2025) 10.1126/scisignal.adf6206

ICE SHEETS

Shake and break

How ice streams flow, an essential element of understanding how ice sheets lose mass, is incompletely known, making it difficult to project sea level and ice sheet size change as accurately as desired. Using measurements made with fiber-optic cables, Fichtner *et al*. report observations of brittle deformation in the Greenland Ice Sheet that reveal a nonviscous flow mechanism caused by englacial ice quake cascades. This effect should help to reconcile results from current ice sheet models and observations. —Jesse Smith

Science p. 858, 10.1126/science.adp8094

T CELLS

TRAF3 coordinates T_{FH} specification

The generation and maintenance of germinal centers require CD4 T follicular helper (T_{FH}) cells; however, the cell-intrinsic signals that specify early T_{FH} cell differentiation are not fully defined. Using a mouse model of *Plasmodium* infection, Shao *et al.* found that the adaptor protein TRAF3 promoted T_{FH} cell lineage commitment by transcriptional and epigenetic reprogramming of CD4 T cells and coordination of cytokine receptor signaling. TRAF3-deficient human CD4 T cells exhibited impaired T_{FH} polarization. These data reveal a conserved mechanism through which TRAF3 regulates T_{FH} cell specification commitment and function. —Hannah M. Isles

Sci. Immunol. (2025) 10.1126/sciimmunol.adr0517

IN OTHER JOURNALS

Edited by **Corinne Simonti** *and* **Jesse Smith**

Sequencing bloodmeals from tsetse flies reveals population dynamics of animals such as the African bush elephant (*Loxodonta africana*).

PHOTO: SEBASTIAN KENNERKNECHT/MINDEN PICTURES

STEM WORKFORCE

Support beyond the stipend

Increased pay for graduate assistants (GAs) is a hot policy topic, and most would agree that GAs need more resources than those currently provided. Christiaens *et al.* explored how US GAs perceive their working conditions and experience challenges. The team reviewed 493 open-ended responses from GAs regarding their institutional experiences. Although findings were mostly indicative of institutional ecological systems failing to support GAs, data also led to the creation of a concept map on GA working conditions. This map includes three main components, contextual factors, stress and well-being, and competing tensions, with subthemes related to social identity, funding, campus climate, and assistantship structure and support. As institutions work toward increased GA pay, these findings can help in designing ways to improve the GA experience. —Melissa McCartney

Stud. Grad. Postdr. Educ. (2025) 10.1108/SGPE-06-2023-0051

WILDLIFE POLICY

Unintended consequences of trade bans

Trade of wildlife for pets, medicines, and other uses is a multibillion-dollar industry. Banning trade of rare or threatened species can be effective for reducing harvest and population declines, but banning the harvest of one species can increase the demand for others. Kubo *et al.* assessed the spillover effects of trade bans in Japan, focusing on giant water bugs (*Kirkaldyia deyrolli*), Tokyo salamanders (*Hynobius tokyoensis*), and the golden venus chub

ENVIRONMENTAL DNA

Finding elephants in a blood meal

Advances in next-generation sequencing have opened up new possibilities for wildlife studies using DNA from unconventional sources. Working with samples from Kenya and Tanzania, Khan *et al.* explored whether blood-feeding insects, specifically tsetse flies, could serve as noninvasive samplers for mammalian population genomics. By comparing short-read sequencing and adaptive sampling of long-read data, the authors successfully recovered genomic information from various host species, including elephants, warthogs, and giraffes. Remarkably, they identified over 300,000 unfiltered single-nucleotide polymorphisms for elephants, enabling estimation of allele frequencies and expected heterozygosity. This approach demonstrates the potential of using biting insects to obtain genome-wide data for wild mammals, offering a promising tool for conservation genetics and population studies of elusive species. —Di Jiang *Mol. Ecol.* (2025) 10.1111/mec.17661

(*Hemigrammocypris neglectus*), a freshwater fish. Other species labeled with the same trade name as those that had been banned showed an increase in sales after the bans, but only for water bugs did this trend last longer than a year. —Bianca Lopez

Conserv. Lett. (2025)
10.1111/conl.13077

NEURODEGENERATION

Parkinson's disease in the kidneys

Lewy body diseases (LBDs) such as Parkinson's disease are neurodegenerative diseases characterized by the pathological aggregation of α-synuclein in the brain, but they can begin in peripheral organs such as the gut. The incidence of LBDs is increased in individuals with chronic renal failure, but the mechanism underlying this is unknown. Yuan *et al*. found α-synuclein deposits in the kidneys of patients with LBDs. In mice, they found that renal failure caused α-synuclein deposition in the kidney, which subsequently spread to the brain. These findings identify a mechanism by which impaired kidney function could contribute to the onset of LBDs, providing a new direction for research into possible therapies. —Sarah Lemprière

Nat. Neurosci. (2025)
10.1038/s41593-024-01866-2

OPTICAL MODULATORS

Converting photons to phonons

Quantum information processing requires quantum bits of information to be stored locally in a memory for manipulation and then passed along to another node in the network. The storage of localized vibrations, phonons, in high-quality mechanical resonators could be an ideal method to store information carried by photons. However, the frequency difference between microwave phonons (gigahertz) and visible-to-infrared photons (terahertz) creates a substantial challenge for conversion. Sonar *et al.* have designed an optomechanical phonon-optical transducer comprising a two-dimensional silicon optomechanical cavity resonator that is side-coupled to a mechanically detached optical wave guide, which minimizes the thermal noise of its millikelvin environment and optimizes the optical coupling. With a phonon-photon conversion efficiency of around 93%, this approach presents a promising platform for quantum technologies. —Ian S. Osborne

Optica (2025)
10.1364/OPTICA.538557

IMMUNOLOGY

Repopulating inflamed airways

Although immune-related inflammatory diseases may be subdued temporarily, inflammation typically reoccurs. Lan *et al.* analyzed CD8 T cells within nasal polyps taken from individuals requiring repeated surgery for chronic rhinosinusitis. Recurrent polyps were infiltrated by memory-like CD8 T cells of the same antigen specificity. These cells were characterized by the expression of the protease granzyme K and clustered around blood vessels, alongside other immune cells, in areas enriched with markers of inflammation. The proteins cleaved by granzyme K in vitro implied that it could promote inflammation. In mice, granzyme K exacerbated airway inflammation, and a peptide inhibitor of granzyme K alleviated asthma. —Sarah H. Ross

Nature (2025)
10.1038/s41586-024-08395-9

SULFUR CATHODES

An organosulfur polymer microcage cathode

Sulfur cathodes used in sodium-sulfur and potassium-sulfur batteries, cost-effective alternatives to traditional lithium-ion batteries, face challenges such as low sulfur utilization and poor cycling performance. These issues are primarily attributed to significant volume changes during cycling and the high solubility of polysulfide discharge products. Zeng *et al.* addressed these limitations by fabricating a conductive organosulfur polymer microcage derived from microbial and elemental sulfur. This structure effectively mitigates volume deformation during electrochemical cycling, delivering excellent capacity, cyclability, and efficiency. The conductive polymer matrix with covalent bonds between short-chain sulfur species is crucial in suppressing polysulfide dissolution and enhancing reaction kinetics. —Jack Huang

J. Am. Chem. Soc. (2025)
10.1021/jacs.4c11845

RESEARCH ARTICLE SUMMARY

EVOLUTION

Experimental evolution of evolvability

Michael Barnett*, **Lena Meister**, **Paul B. Rainey***

INTRODUCTION: The capacity to generate adaptive variation is critical for long-term evolutionary success. However, the extent to which natural selection directly favors enhanced evolvability remains debated. Although studies with microbes show that mutants with elevated genome-wide mutation rates can be selected, a deeper question persists: Can natural selection structure genetic and developmental systems to bias mutations toward adaptive outcomes? This hypothesis challenges the traditional view of evolution as a "blind" process fueled by random variation, which amplifies traits beneficial in the present without regard for future contingencies.

RATIONALE: Mutation being biased toward adaptive outcomes challenges conventional perspectives but aligns with the logic of natural selection acting on lineages. Across changing environments, lineages capable of rapid adaptation are more likely to survive and replace those less able. If competing lineages, because of their varying genetic architecture, tend to generate phenotypic variation in different ways, then those with tendencies that are more conducive to an adaptive response in a given environment will be favored. Provided the same environmental challenges recur over time, an iterative process of selection can take place, potentially refining the capacity to adapt. To test this idea, we designed an experiment where lineages of bacteria competed to repeatedly achieve, through mutation, phenotypes optimal for growth under two alternating conditions. Lineages that failed to evolve the target phenotype within a set time went extinct and were replaced by successful lineages. This birth-death dynamic created conditions for selection to refine the ability of lineages to evolve between phenotypic states.

RESULTS: During the course of a 3-year selection experiment, involving identification and ordering of more than 500 mutations, a lineage emerged that was capable of rapid mutational transitions between alternate phenotypic states through localized hypermutation. The mutable locus arose through a multistep evolutionary process: Initial mutations targeted a wide range of genes but eventually focused on a single regulator. A series of mutations that alternately activated and inactivated function of the regulatory gene then followed. A subset of these inactivating mutations were compensated for by mutations that increased transcription and, concomitantly, frameshift mutation rate. The overall effect was to promote, through slipped-strand mispairing, the duplication, and then further amplification, of a heptanucleotide sequence. This process led the locus-specific mutation rate to increase ~10,000-fold. In turn, the resulting frameshift mutations enabled reversible phenotypic changes through expansion and contraction of the heptanucleotide sequence, mirroring the contingency loci of pathogenic bacteria. Lineages with the hypermutable locus exhibited enhanced evolvability to altered rates of environmental change and were more likely to acquire additional adaptive mutations, highlighting an unanticipated evolutionary advantage of localized hypermutability.

CONCLUSION: Our study demonstrates how selection can incorporate evolutionary history into the genetic architecture of a single cell, giving rise to a hypermutable locus that appears to anticipate environmental change, thereby accelerating adaptive evolution. This was possible only as an outcome of selection working at two levels. Whereas individual-level selection repeatedly drove cell populations between the same two phenotypic states, the genetic underpinnings of these phenotypes were free to diverge, fueling an exploration of evolutionary potential, the consequences of which only emerged on the timescale of lineages. Ultimately, this exploration generated the variation necessary for construction and cumulative refinement of a lineage-level adaptive trait. More generally, our experiment clarifies the conditions by which evolvability can itself evolve adaptively and highlights the importance of this process for microbial pathogens. ■

The list of author affiliations is available in the full article online.
*Corresponding author. Email: barnett@evolbio.mpg.de (M.B.); rainey@evolbio.mpg.de (P.B.R.)
Cite this article as M. Barnett *et al.*, *Science* **387**, eadr2756 (2025). DOI: 10.1126/science.adr2756

READ THE FULL ARTICLE AT
https://doi.org/10.1126/science.adr2756

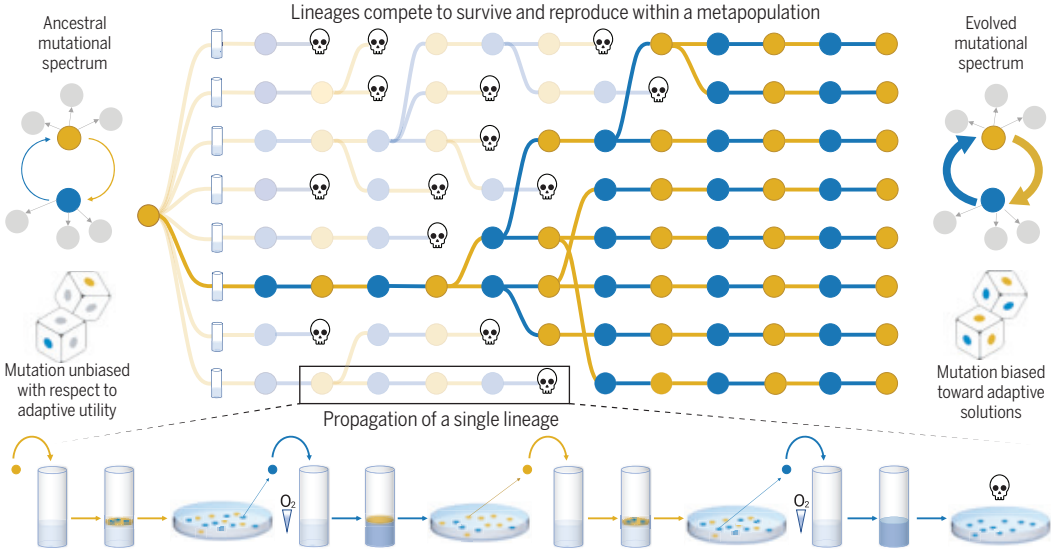

Experimental evolution of evolvability through lineage selection. Mutation and selection are typically viewed as independent processes, but our experiment revealed how they interact, leading mutation to become biased toward adaptive outcomes. Central to this was lineage-level selection: Bacterial lineages (connected nodes) were required to repeatedly evolve between two phenotypic states (indicated by yellow and blue). Mutational transitions were initially unreliable, leading to lineage death (indicated by a skull) and replacement by more successful competitors. Final surviving lineages evolved mutation-prone sequences in a key gene underpinning the phenotypes, enabling rapid transitions between states.

RESEARCH ARTICLE SUMMARY

CRISPR

Antiviral signaling of a type III CRISPR-associated deaminase

Yutao Li†, Zhaoxing Li†, Purui Yan†, Chenyang Hua†, Jianping Kong†, Wanqian Wu, Yurong Cui, Yan Duan, Shunxiang Li, Guanglei Li, Shunli Ji, Yijun Chen, Yucheng Zhao, Peng Yang, Chunyi Hu, Meiling Lu*, Meirong Chen*, Yibei Xiao*

INTRODUCTION: Type III CRISPR-Cas offers immunity against foreign nucleic acids through the production of cyclic oligoadenylate (cOA) molecules that allosterically activate auxiliary effectors, leading to viral clearance or cell dormancy. These effector proteins typically carry a CRISPR-associated Rossmann fold (CARF) sensor domain, which is normally fused to various effector domains. Most CARF effectors characterized to date are nucleases, proteases, or transmembrane proteins. The frequent association of a group of CARF-fused adenosine deaminases with type III CRISPR-Cas raises the question of whether and how CRISPR-Cas and adenosine deaminase are coordinately deployed against infections.

RATIONALE: Recent investigations have demonstrated that enzymatic depletion of the nucleotide pool is a potent antiviral strategy. We therefore hypothesized that the type III CRISPR-Cas–associated adenosine deaminases (CAADs) could be activated by newly synthesized cOAs upon foreign nucleic acid recognition. Therefore, nucleotide depletion might be achieved by adenosine deamination, finally causing host growth arrest to prevent viral spread. To investigate this, we sought to clarify the activity and function of CAAD using biochemical and structural approaches, thereby elucidating the activation mechanism. The experimental outcomes could reveal the function and molecular mechanism of a type III CRISPR-Cas–mediated antiviral strategy through nucleotide depletion.

RESULTS: Using bioinformatics analysis, we identified 121 type III CRISPR-CAAD systems, of which 44 also encode a Nudix hydrolase (NH), which typically cleaves nucleoside diphosphates. Focusing on the type III CRISPR-CAAD-NH system from *Limisphaera ngatamarikiensis*, we biochemically reconstructed the antiviral signaling pathway and found that CAAD could be activated by either cA_4 or cA_6 to specifically convert adenosine triphosphate (ATP) to inosine triphosphate (ITP), and NH subsequently hydrolyzes ITP to inosine monophosphate (IMP). By assessing its immunity against genetic threat in *E. coli*, we confirmed that CAAD activation upon target transcript expression led to ATP depletion and growth arrest of the host cells, which was mitigated by NH. Moreover, using cryo–electron microscopy (cryo-EM), we determined high–resolution structures of CAAD in its apo, cA_4-bound, and cA_6-bound forms. The hexameric CAAD is composed of a trimer of dimers, and each CARF dimer is able to accommodate one cA_4 or cA_6 molecule. Together with biochemical analyses, our studies reveal that the activation of CAAD requires hexamer formation, and the hexameric CAAD is cooperatively activated in a unique neighboring chain–dependent manner. The C-terminal deaminase domain is autoinhibited by the N-terminal flexible CARF domain through destabilization of the deaminase active sites in its apo form. cA_4 or cA_6 binding tightens and rotates the CARF domain, triggering substantial conformational changes of the deaminase domain to reorient the critical catalytic elements for ATP recognition and deamination.

CONCLUSION: Our results elucidate the function and mechanism of an antiviral signaling pathway mediated by type III CRISPR systems. The deamination of ATP to ITP by cOAs activated CAAD, and the hydrolysis of ITP to IMP by NH led to ATP depletion, resulting in the induction of cell growth arrest and the inhibition of viral propagation. Despite the fact that ITP hydrolysis could mitigate the cellular toxicity caused by ITP accumulation and cA_4 could be cleaved by CAAD, the off-switch mechanism enabling the host cells to proliferate after growth arrest remains unclear. Nonetheless, a thorough understanding of CAAD activation may provide insights into the development of controllable base editors and could possibly be repurposed for programmable and dynamic ATP regulation. ■

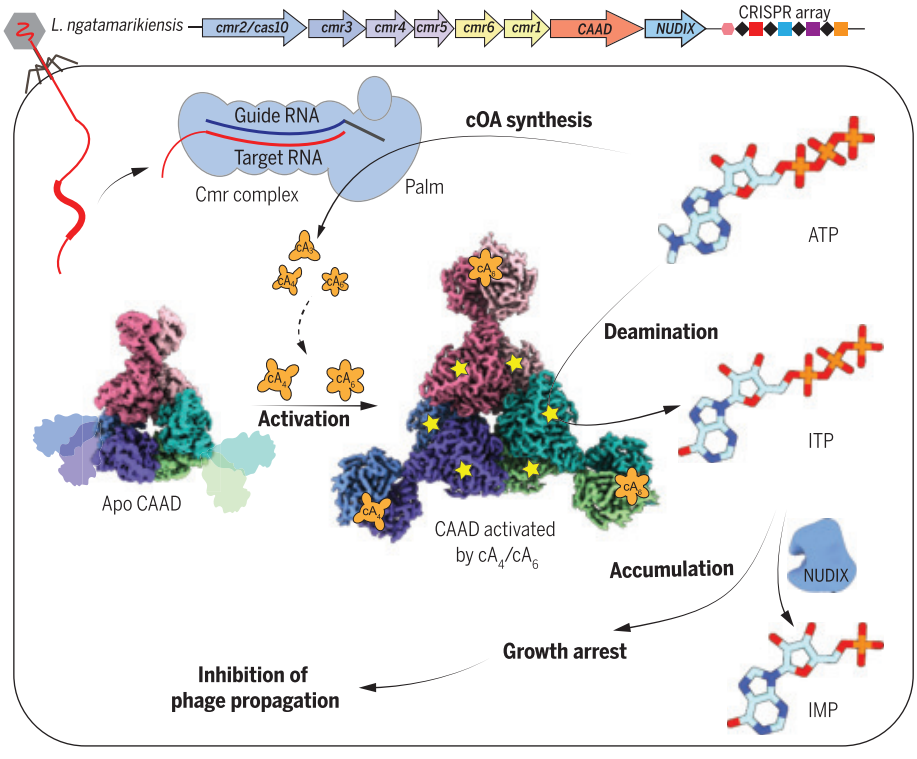

Model of type III CRISPR-CAAD–NH system–mediated antiviral defense. Upon viral infection, cA_4 or cA_6 generated by the activated type III CRISPR-Cas binds to the CARF domain and activates the deaminase activity of CAAD to convert ATP into ITP. ATP depletion and ITP accumulation lead to cell growth arrest and viral propagation inhibition. The coexisting Nudix hydrolase (NUDIX) could hydrolyze ITP into IMP, thereby alleviating growth arrest.

The list of author affiliations is available in the full article online.
*Corresponding author. Email: lumeiling@cpu.edu.cn (M.L.L.); chenmr@cpu.edu.cn (M.R.C.); yibei.xiao@cpu.edu.cn (Y.B.X.)
†These authors contributed equally to this work.
Cite this article as Y. Li *et al.*, *Science* **387**, eadr0393 (2025). DOI: 10.1126/science.adr0393

READ THE FULL ARTICLE AT
https://doi.org/10.1126/science.adr0393

RESEARCH ARTICLE SUMMARY

NEUROSCIENCE

Reviving-like prosocial behavior in response to unconscious or dead conspecifics in rodents

Wenjian Sun†, Guang-Wei Zhang†, Junxiang J. Huang, Can Tao, Michelle B. Seo, Huizhong Whit Tao*, Li I. Zhang*

INTRODUCTION: When humans encounter someone unconscious, they often respond with emergency reactions aimed at reviving that person. However, it remains unclear whether animals naturally exhibit any specific behaviors when faced with an unconscious peer.

RATIONALE: Anecdotal observations of various animal species in the wild have documented behaviors toward peers that have collapsed as a result of sickness, injury, or death. These behaviors include touching, grooming, nudging, and sometimes even more intense physical actions such as striking. Although these actions toward incapacitated conspecifics are reminiscent of human emergency responses involving intense sensory stimulation, it remains difficult to determine the precise nature of these behaviors, how common they are within a species, and the neural mechanisms behind them. In this study, using laboratory mice under controlled conditions, we examined whether animals naturally display any stereotypic behaviors in response to and directed toward their unresponsive social partners, which would allow us to address the above questions.

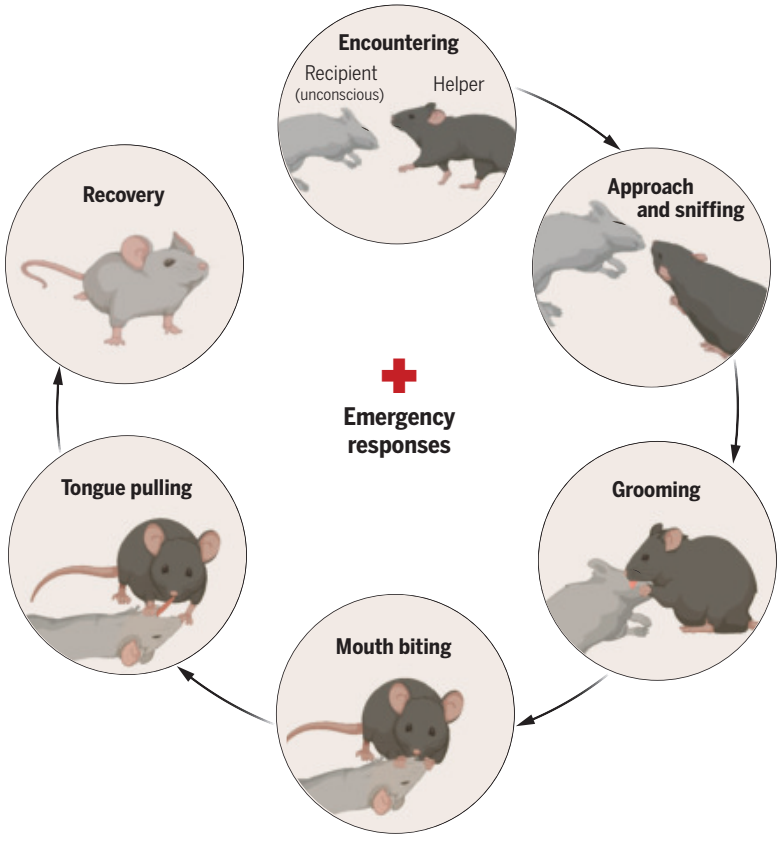

Mouse behaviors toward an unconscious peer. Mice exhibit a stereotypic set of behaviors when encountering an unconscious social partner, reminiscent of human emergency responses. The behavioral reactions escalate from sniffing and grooming to intense stimulatory actions such as mouth biting and tongue pulling during extended periods of unresponsiveness. These reviving-like actions facilitate the recipient's recovery. [Figure created with BioRender.com]

RESULTS: Behavioral monitoring combined with a machine learning–based annotator showed that when mice encountered a familiar social partner in a state of unconsciousness caused by anesthesia, they displayed distinct and consistent behaviors toward the partner, escalating from sniffing and grooming to more forceful actions such as biting the partner's mouth or tongue and pulling its tongue out. The latter intense actions were also observed in mice interacting with a dead familiar partner but were rarely seen when the partner was active or simply sleeping. These behaviors emerged after prolonged immobility and unresponsiveness of the partner and ceased once the partner regained activity, suggesting that they were triggered by observing unresponsive states of others. These behaviors were strongly influenced by familiarity, being more pronounced in familiar pairs, and were unlikely to have been motivated by a desire for reciprocal social interaction or curiosity about something new. The consequences—including clearance of foreign objects from the mouth, improved airway opening, and hastened recovery—suggest reviving-like efforts. Electrophysiological recordings and microendoscopic calcium imaging showed that oxytocin neurons in the hypothalamic paraventricular nucleus as a population exhibited increased activation in the presence of unconscious, compared with active, familiar partners, suggesting that the activity of these neurons can distinguish between the different partner states. Additionally, increased activity was observed in distinct subpopulations of the oxytocin neurons during specific behavioral actions. Furthermore, optogenetic activation of these neurons promoted reviving-like behaviors, whereas inactivation of them or blocking oxytocin signaling through ventricular administration of oxytocin receptor antagonists impaired the behaviors.

CONCLUSION: Our study reveals a stereotypic set of behaviors in mice directed toward unresponsive familiar peers that appear to facilitate the regaining of responsiveness. Similar to other prosocial behaviors, these behaviors rely on the oxytocin system, which is essentially conserved across vertebrate species. Our findings thus suggest that animals exhibit reviving-like emergency responses and that assisting unresponsive group members may be an innate behavior widely present among social animals. Such behavior likely plays a role in enhancing group cohesion and survival. ■

The list of author affiliations is available in the full article online.
*Corresponding author. Email: liizhang@usc.edu (L.I.Z.); htao@usc.edu (H.W.T.)
†These authors contributed equally to this work.
Cite this article as W. Sun *et al.*, *Science* **387**, eadq2677 (2025). DOI: 10.1126/science.adq2677

READ THE FULL ARTICLE AT
https://doi.org/10.1126/science.adq2677

RESEARCH ARTICLE SUMMARY

NEUROSCIENCE

A neural basis for prosocial behavior toward unresponsive individuals

Fangmiao Sun, Ye Emily Wu*, Weizhe Hong*

INTRODUCTION: The partial or complete loss of responsiveness, such as transient unconsciousness, presents a substantial risk to animals, increasing their vulnerability to predators or hazardous environments. The actions of bystanders toward unresponsive individuals can be critical for enhancing survival and well-being. Humans, for instance, can readily recognize and assist unconscious individuals. Similarly, anecdotal reports suggest that some animal species, including nonhuman primates, marine mammals (e.g., whales and dolphins), and elephants, exhibit behavioral reactions to collapsed or unresponsive conspecifics in the wild. However, it is unclear whether such behaviors occur in species beyond those few that have been documented. Additionally, the nature, characteristics, and consequences of these behaviors have not been systematically examined in a controlled experimental setting. Moreover, the neural mechanisms underlying the perception of others' unresponsive states and the ensuing behaviors remain elusive.

RATIONALE: Previous studies have demonstrated that rodents, including mice, can perceive and behaviorally respond to others' negative or needy states. For example, they can display comforting social touch through allogrooming, broadly targeted at various body parts of distressed conspecifics. In addition, they can respond to others' local pain and injury with allolicking behavior focused on the wound site. However, it is unclear how mice react to other animals in an unresponsive state. In this study, we examined the behaviors that mice display toward unresponsive conspecifics, their effects on the recipients, and the neural representation and regulation of these behaviors.

RESULTS: We discovered that mice preferentially approach unresponsive conspecifics over awake ones and engage in distinctive behaviors toward unresponsive conspecifics under deep sedation, characterized by intense contact and grooming directed at the sedated individuals' head region, particularly the facial and mouth areas. These behaviors are observed in both male and female animals and are correlated with the extent of reduction in the responsiveness of the recipients. Physical contact and grooming directed at the head region are more likely to elicit motor responses in the recipients compared with other social behaviors and can expedite the animals' recovery from the unresponsive state.

Moreover, we uncovered an essential role of the medial amygdala (MeA) in regulating this response. MeA neural activity differentiates between awake and sedated conspecifics at both single-cell and population levels, and the neural response to sedated animals does not simply reflect a response to novelty. Optogenetic silencing of MeA γ-aminobutyric acid–producing (GABAergic) neurons suppresses head grooming behavior, whereas their activation promotes this behavior. Although mice respond to sedated, unresponsive conspecifics primarily with head-directed allogrooming and physical contact, their allogrooming response to awake conspecifics experiencing a general state of stress mainly targets other body regions. These two different adverse states and the corresponding behavioral responses (head grooming versus body grooming) are distinguishable by neural activities in the MeA, suggesting that the MeA may be part of the neural circuitry mediating the differentiation between these states.

CONCLUSION: Our findings reveal that mice exhibit rescue-like behaviors toward unresponsive conspecifics, characterized by intense physical contact directed at the recipient's head region. This response accelerates recovery from unresponsiveness, potentially reducing risks to unresponsive individuals and enhancing their survival. We have also uncovered that the MeA encodes the unresponsive state of others and drives head-directed grooming toward them. Notably, the behavioral response toward unresponsive conspecifics differs from that toward awake, stressed individuals, and these responses are differentially represented in the MeA. These findings shed light on the neural mechanisms underlying prosocial responses toward unresponsive individuals, broadening our understanding of animals' ability to detect and behaviorally react to different adverse conditions of others. ■

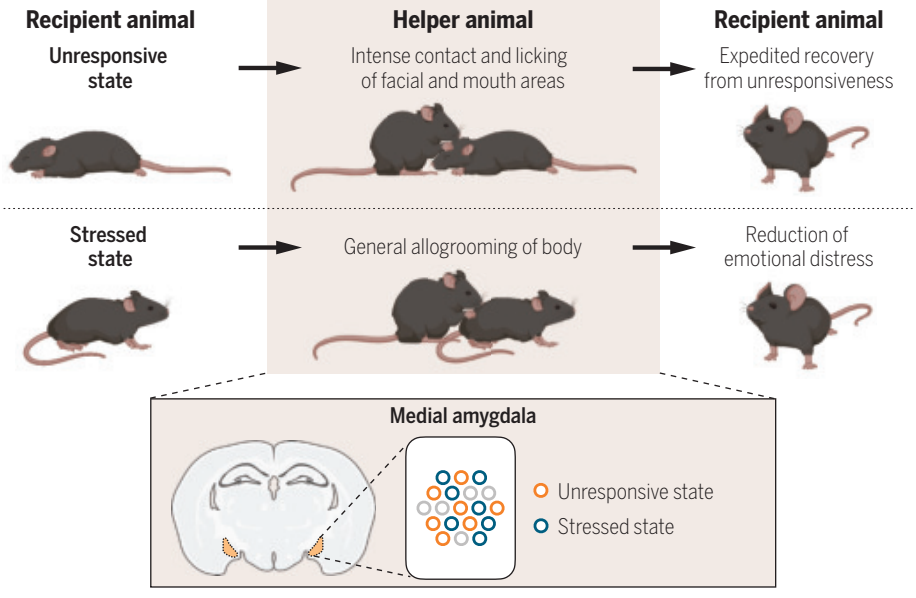

Prosocial behavior toward unresponsive conspecifics. Mice can detect the unresponsive state of other individuals and exhibit rescue-like behavior characterized by intense physical contact directed at the recipient's head region, which facilitates recovery from unresponsiveness. Neural activity in the medial amygdala (MeA) encodes the unresponsive state of others and regulates the ensuing prosocial actions. The behavior exhibited toward unresponsive conspecifics differs from that directed toward stressed individuals, and these interactions are differentially represented in the MeA. [Figure created with BioRender.com]

The list of author affiliations is available in the full article online.
*Corresponding author. Email: whong@ucla.edu (W.H.); ye.wu@ucla.edu (Y.E.W.)
Cite this article as F. Sun. *et al.*, *Science* **387**, eadq2679 (2025). DOI: 10.1126/science.adq2679

READ THE FULL ARTICLE AT
https://doi.org/10.1126/science.adq2679

RESEARCH ARTICLE SUMMARY

IMMUNOLOGY

Disease diagnostics using machine learning of B cell and T cell receptor sequences

Maxim E. Zaslavsky†, Erin Craig†, Jackson K. Michuda, Nidhi Sehgal, Nikhil Ram-Mohan, Ji-Yeun Lee, Khoa D. Nguyen, Ramona A. Hoh, Tho D. Pham, Katharina Röltgen, Brandon Lam, Ella S. Parsons, Susan R. Macwana, Wade DeJager, Elizabeth M. Drapeau, Krishna M. Roskin, Charlotte Cunningham-Rundles, M. Anthony Moody, Barton F. Haynes, Jason D. Goldman, James R. Heath, R. Sharon Chinthrajah, Kari C. Nadeau, Benjamin A. Pinsky, Catherine A. Blish, Scott E. Hensley, Kent Jensen, Everett Meyer, Imelda Balboni, Paul J. Utz, Joan T. Merrill, Joel M. Guthridge, Judith A. James, Samuel Yang, Robert Tibshirani, Anshul Kundaje*‡, Scott D. Boyd*‡

INTRODUCTION: Conventional clinical diagnosis relies on physical examination, patient history, laboratory testing, and imaging, but makes little use of the receptors on B cells and T cells that reflect current and past exposures and responses. Microbial pathogen detection underpins infectious disease diagnosis. Other conditions are more challenging: Autoimmune diseases can require a combination of imaging studies and testing for autoantibodies and other laboratory abnormalities in the blood that may not yield a definitive disease classification. This process can be lengthy and may be complicated by initial misdiagnoses and ambiguous or overlapping symptoms between conditions.

B cell receptors (BCRs) and T cell receptors (TCRs) allow these immune cells to recognize and respond to specific antigens on pathogens and sometimes the body's own tissues. The genes encoding BCRs and TCRs are generated by random recombination of segments in the genome of individual cells during their development, and have potential as a diverse set of sequence biomarkers associated with immune system activity. BCR and TCR populations change after exposure to pathogens, after vaccination, and in response to autoantigens in autoimmune conditions, reflecting clonal expansion and selection of B cells and T cells during immune responses. Sequencing and interpreting BCR and TCR genes could provide a single diagnostic test for simultaneous assessment of many diseases.

RATIONALE: We designed experimental protocols and a data analysis framework for identifying human BCR heavy chain and TCR beta chain features characteristic of infectious and immunological disorders or elicited by therapeutic or prophylactic interventions such as vaccination. Our method, named MAchine Learning for Immunological Diagnosis (Mal-ID), combines traditional immunological analyses, such as shared sequence detection between individuals with the same condition, with more complex features derived from artificial intelligence (AI) models of protein sequences, called protein language models. Although AI systems can be difficult to interpret, we developed ways to understand how the model makes its diagnostic predictions.

RESULTS: We generated large datasets of both BCR heavy chain and TCR beta chain sequences from the same individuals, spanning six disease or immune response states, to train and evaluate the Mal-ID model. Mal-ID accurately identified immune status from blood samples of 542 individuals with COVID-19, HIV, lupus, type 1 diabetes, recent flu vaccination, and healthy controls, achieving a multiclass area under the receiver operating characteristic curve (AUROC) of 0.986 on data not used for training. Combining features from both B cell and T cell receptor data led to the highest classification performance, but even with only BCR sequences, we still achieved high classification performance (0.959 AUROC in an expanded cohort adding 51 individuals for whom only BCR data were available).

Despite the model being trained to classify multiple heterogeneous classes, it can be specialized for detecting a particular condition. When applied to specifically distinguish patients with lupus from other patients and healthy controls, the classifier achieved 93% sensitivity and 90% specificity. This performance relative to current tests indicates the potential for BCR and TCR sequence analysis to detect clinically relevant signals.

We used the model to provide insights into the biologically relevant features that enable accurate disease classification. Examining which sequence categories contributed most to predictions, we confirmed that the patterns discovered from the data matched established immunological knowledge. Additionally, we assessed whether the model identified individual immune receptors known to be associated with disease. The model assigned higher COVID-19 association scores to sequences from an external database of SARS-CoV-2 binding BCRs, compared with sequences from healthy donors. We also verified that batch effects and demographic factors such as age, sex, and ancestry were not responsible for disease classification performance, and the model performed well when tested on external datasets from other laboratories.

CONCLUSION: This pilot study demonstrates that immune receptor sequencing data can distinguish a range of disease states and extract biological insights without prior knowledge of antigen-specific receptor patterns. With further validation and extension, Mal-ID could lead to clinical tools that harness the vast information contained in immune receptor populations for medical diagnosis. ■

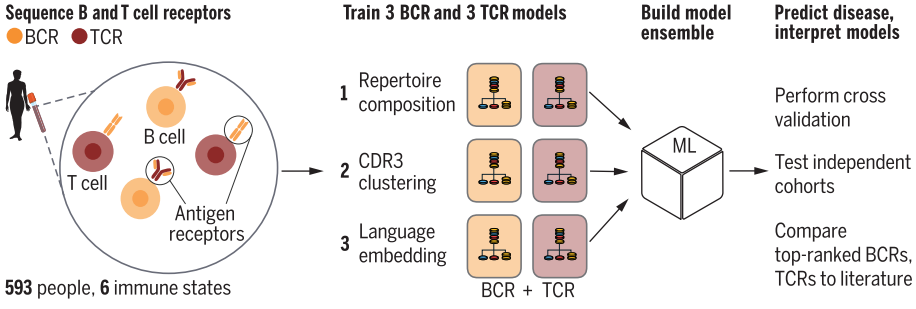

From blood to disease classification with immune receptor sequencing. B and T cell receptors sequenced from 593 individuals were analyzed through receptor population or "repertoire" composition; clustering CDR3 sequence regions, which determine receptor antigen specificity; and protein language modeling. Disease was classified from this BCR and TCR information with a high multiclass AUROC score in cross validation experiments.

The list of author affiliations is available in the full article online.
*Corresponding author. Email: akundaje@stanford.edu (A.K.); sboyd1@stanford.edu (S.D.B.)
†These authors contributed equally to this work.
‡These authors contributed equally to this work.
Cite this article as M. E. Zaslavsky *et al.*, *Science* 387, eadp2407 (2025). DOI: 10.1126/science.adp2407

READ THE FULL ARTICLE AT
https://doi.org/10.1126/science.adp2407

RESEARCH ARTICLES

THERMOELECTRICS

Interfacial bonding enhances thermoelectric cooling in 3D-printed materials

Shengduo Xu*, Sharona Horta, Abayomi Lawal, Krishnendu Maji, Magali Lorion, Maria Ibáñez*

Thermoelectric coolers (TECs) are pivotal in modern heat management but face limitations in efficiency and manufacturing scalability. We address these challenges by using an extrusion-based 3D printing technique to fabricate high-performance thermoelectric materials. Our ink formulations ensure the integrity of the 3D-printed structure and effective particle bonding during sintering, achieving record-high figure of merit (zT) values of 1.42 for p-type bismuth antimony telluride [$(Bi,Sb)_2Te_3$] and 1.3 for n-type silver selenide (Ag_2Se) materials at room temperature. The resulting TEC demonstrates a cooling temperature gradient of 50°C in air. Moreover, this scalable and cost-effective method circumvents energy-intensive and time-consuming steps, such as ingot preparation and subsequently machining processes, offering a transformative solution for thermoelectric device production and heralding a new era of efficient and sustainable thermoelectric technologies.

A thermoelectric cooler (TEC), also known as a Peltier cooler, is a solid-state device that transfers heat from one side to the other when an electrical current passes through it. This cooling method is advantageous because of its precise and localized temperature control capabilities. In addition, TECs are compact, modular, silent, and maintenance-free, eliminating the need for harmful liquids or gases typically used in conventional vapor compression refrigeration systems. Their adaptability to small sizes makes them indispensable for applications in which the target to cool is too small for traditional refrigeration technology (*1*, *2*). As a result, TECs offer a promising approach to thermal management in various applications, such as lab-on-a-chip devices (*3*, *4*), mid-infrared sensors and lasers based on narrow-band semiconductors (*5*), Internet of Things devices (*6*), and personal thermoregulatory clothing (*7*). Despite the benefits and potential applications, implementation of TECs is restricted by low efficiency, limited cooling power, complex and wasteful manufacturing approaches, and the high cost of manufacturing thermoelectric materials (*8*).

The cooling coefficient of performance (COP) and maximum temperature reduction of a TEC are linked to the efficiency of the thermoelectric material, determined by the dimensionless figure of merit, $zT = S^2\sigma T/(\kappa_{ele} + \kappa_{lat})$ (*9*). Here, S represents the thermopower or Seebeck coefficient, σ denotes electrical conductivity, T is the absolute temperature, and κ_{ele} and κ_{lat} are electronic and lattice thermal conductivity, respectively (*10*). Various strategies to optimize simultaneously charge carrier and phonon transport have been explored to achieve materials with high zT (*9*). However, these materials have been manufactured using time-consuming and energy-intense methods that can be challenging to scale up. A clear example is the fabrication of single crystals (*11*), but also the production of dense polycrystalline materials using spark plasma sintering (*12*), bulk machining (*13*), sputtering (*14*), microelectromechanical fabrication (*15*, *16*), and so forth.

Recently, extrusion-based three-dimensional (3D) printing and high-throughput printing systems have emerged as promising alternatives for directly preparing materials with the desired geometry, which makes the device manufacturing process simpler, more efficient, and versatile (*17*–*19*). Rigid thermoelectric materials with different 3D structures have been directly printed and subsequently sintered to remove the carrying liquid medium (*17*, *20*, *21*). However, the corresponding zT values have been substantially lower than those reported from ingots, which can be mainly ascribed to low σ caused by poor connection between the grains. Moreover, the integration of 3D-printed materials into cooling devices has not been reported, most likely owing to the complexity of achieving both high material performance optimization and efficient device engineering to obtain substantial cooling.

We developed ink formulations that ensure structural integrity during 3D printing and promote the formation of interfacially bonded grain networks during the sintering process. Such well-connected structures result in zT values of 1.42 and 1.3 at room temperature for p-type $(Bi,Sb)_2Te_3$ and n-type Ag_2Se (Fig. 1A), respectively, which are among the highest zT values reported for thermoelectric materials near room temperature (*17*, *20*, *22*–*30*). Using the printed p-type and n-type thermoelectric legs, we assembled a TEC that exhibits cooling temperature gradients (ΔT) up to 50°C in air with the hot side fixed at 30°C and an COP of 3.8 with an applied current (I) of 0.15 A at room temperature (Fig. 1, B and C). These performance parameters are comparable to those achieved in state-of-the-art devices (*11*, *12*, *31*, *32*) (Fig. 1D). Our work demonstrates the potential of 3D-printed materials for cost-effective and scalable production of high-performance TECs, avoiding the energy-consuming and inefficient steps—such as high-temperature synthesis, pressure-assisted sintering, and slicing and dicing ingots, commonly used in conventional manufacturing processes (*4*, *5*, *15*, *16*, *33*–*40*)—and minimizing material waste.

Thermoelectric properties of printed materials

In the quest for efficient room-temperature applications, $Bi_{0.5}Sb_{1.5}Te_3$ and Ag_2Se have been identified as leading materials for p-type and n-type thermoelectric performance, respectively (*37*, *38*). To leverage these materials, inks are designed as colloidal suspensions containing the corresponding solid particles within a liquid medium. To ensure the integrity of the 3D-printed structure, ink components and their concentrations are optimized to exhibit loss tangent (tanδ) values below 1 and a high yield stress (τ_y) (fig. S5), achieving solid-like behaviors (*17*, *20*).

We initially printed rectangular-shaped samples of two dimensions, 12 mm by 5 mm by 16 mm and 12 mm by 12 mm by 5 mm (Fig. 1A), to evaluate the material properties in different printing orientations (fig. S6) and determine the optimal ink composition. Subsequently, we printed pillars with an average diameter of 1 mm and a height of 0.8 mm (Fig. 1B) to manufacture the TEC. After printing the desired structure, a sintering step is necessary to remove the liquid medium and bond the particles, forming a continuous material network that allows adequate charge carrier transport. For the rectangular pellets, their surface is polished to ensure proper contact with the probes during transport measurements.

The different crystal structures and bonding nature of $Bi_{0.5}Sb_{1.5}Te_3$ and Ag_2Se require distinct ink formulations to promote the formation of interparticle bonding at relatively low temperatures and without applying pressure. For the n-type material, Ag_2Se particles (~50 to ~300 nm) were mixed with glycerol in a 1:2 mass ratio to form an ink that shows excellent printability without adding any binders. Such adequate viscoelasticity of the Ag_2Se ink originates from the electrostatic interactions between surface-charged Ag_2Se particles (*20*, *37*).

The Ag_2Se bars show a σ of 586 $S{\cdot}cm^{-1}$ (Fig. 2E) and a hall carrier mobility (μ) of 864 $cm^2{\cdot}V^{-1}{\cdot}s^{-1}$ at room temperature (fig. S8). The S is comparable to that of previous works (Fig. 2E) (*37*), owing to the similar carrier concentration (n)

Institute of Science and Technology Austria (ISTA), Am Campus 1, Klosterneuburg, Austria
*Corresponding author. Email: shengduo.xu@ista.ac.at (S.X.); mibanez@ista.ac.at (M.I.)

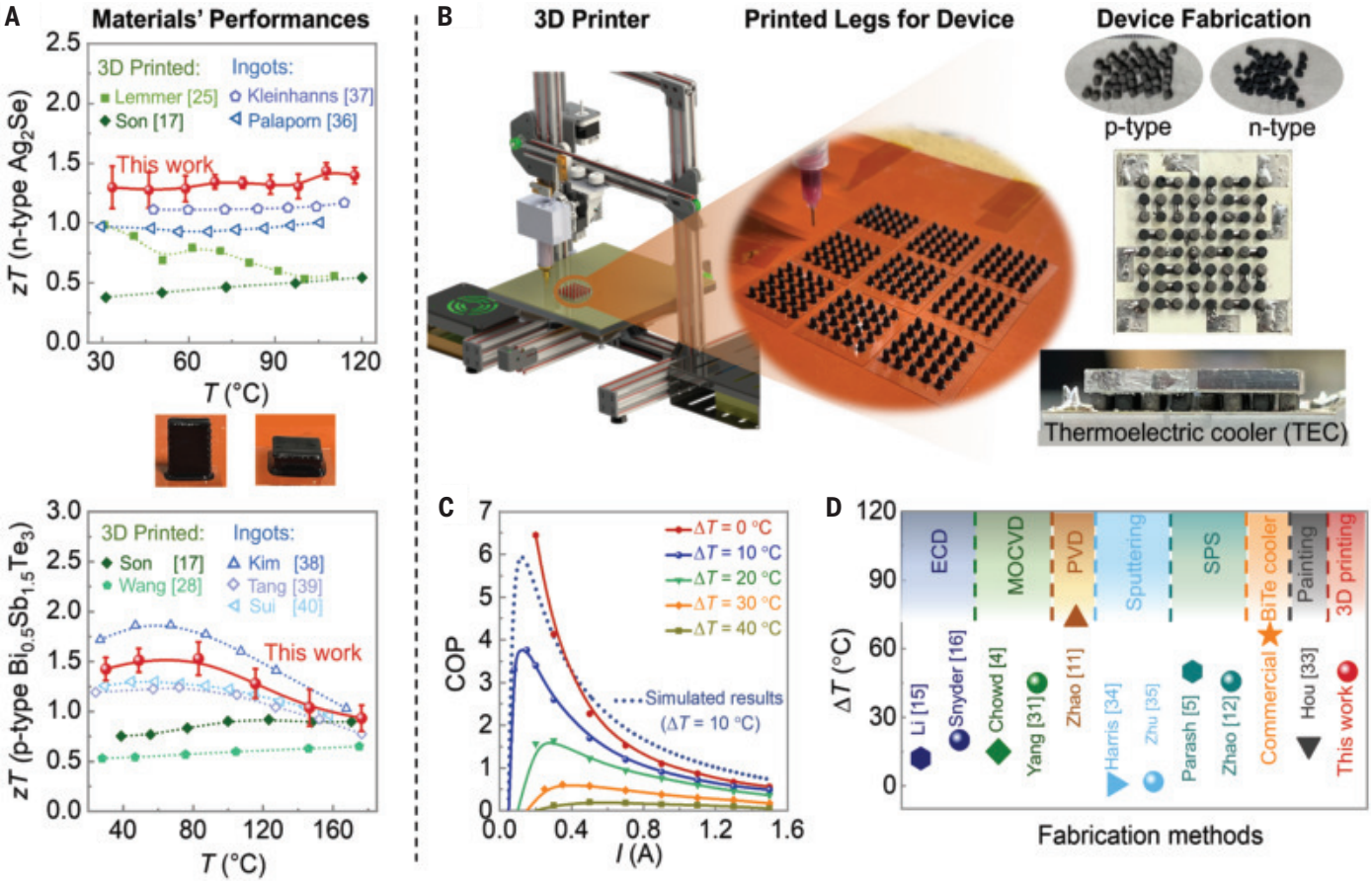

Fig. 1. Synthesis process and performance. (**A**) Comparison of the state-of-the-art *zT* values obtained for n-type (*17*, *25*, *36*, *37*) and p-type (*17*, *28*, *38*–*40*) thermoelectric materials with the ones achieved in this work. The closed symbols represent printed materials, whereas the open symbols denote those obtained from ingots. (**B**) Schematic diagram of the used 3D printer with a picture of the printed thermoelectric legs and their assembly into the device. (**C**) Coefficient of performance (COP) of the fabricated TEC as a function of temperature gradient. (**D**) Comparison of the maximum cooling gradients achieved for TECs fabricated by different methods (*4*, *5*, *11*, *12*, *15*, *16*, *31*, *33*–*35*).

of 3.58×10^{18} cm^{-3} (fig. S8), and the κ_{lat} is substantially lower with a value of 0.12 $W{\cdot}m^{-1}{\cdot}K^{-1}$ (Fig. 2D), leading to a room-temperature *zT* of 1.3 and an average *zT* of 1.32 from 30° to 120°C (Fig. 1A). The resulting materials have a porosity of ~50%; however, the solid matrix has the same features as those reported for highly dense ingots (*37*, *41*): small-angle grain boundaries, dense dislocations arrays, and stacking faults (fig. S9).

We prepared $(Bi,Sb)_2Te_3$-based inks for the p-type material by mixing $Bi_{0.5}Sb_{1.5}Te_3$ powders and two different types of inorganic solid binders, Bi nanoparticles and Sb_2Te_4 chalcogenidometallates (ChaM) (*17*), in ethylene glycol mixed with xanthan gum. We achieved the best-performing inks, named BST-B-ST, using 75% molar content of $Bi_{0.5}Sb_{1.5}Te_3$ (BST), 10% molar content of Bi nanoparticles (B), and 15% molar content of Sb_2Te_4 ChaM (ST) (fig. S12). The BST-B-ST printed pellets display the same commonly observed microstructural features in the solid matrix as those previously reported in dense ingots with similar compositions (fig. S13) (*42*–*45*). These features include micrometer-sized grains with dislocation-rich grain boundaries, nanometer-sized twins, and Sb-rich nanoprecipitates with sizes ranging from 5 to 30 nm (fig. S13E). However, the printed BST-B-ST pellet did not exhibit the characteristic crystallographic texture observed in $(Bi,Sb)_2Te_3$ dense ingots produced by zone melting, hot press, or hot deformation (fig. S15), and the properties measured in different directions demonstrated their isotropic nature (fig. S6).

The BST-B-ST printed pellets show substantially improved thermoelectric properties when compared to those produced with binder-free $Bi_{0.5}Sb_{1.5}Te_3$ inks (BST) or those with only the addition of Sb_2Te_4 ChaM (BST-ST). Notably, we observe an elevated *S* for the BST-B-ST sample compared to the BST-ST and BST samples (Fig. 3F), which can be ascribed to the reduced *n* (fig. S11). Inductively coupled plasma (ICP) results (table S1) show higher Bi content in the BST-B-ST sample, which is responsible for the decrease in *n* because Bi is less likely to create donor-like anti-site defects in the BST system compared to Sb (*46*). Despite the decreased *n*, the σ of the BST-B-ST pellet is also higher than that of the bare BST and BST-ST pellets, owing to the significantly enhanced μ (fig. S11). Overall, the BST-B-ST pellets exhibit a σ of 148 $S{\cdot}cm^{-1}$ (Fig. 3E), *S* of 258 $\mu V{\cdot}K^{-1}$ (Fig. 3F), and κ of 0.21 $W{\cdot}m^{-1}{\cdot}K^{-1}$ (fig. S45A), resulting in a room-temperature *zT* of 1.42 and an average *zT* of 1.3 from 30° to 170°C (Fig. 1A).

We prepared and printed multiple batches of BST-B-ST and Ag_2Se inks under identical conditions to test their reproducibility. We observed consistent *zT* values across all batches, with variations within ± 10% for both p-type and n-type materials (fig. S17 to fig. S20). Moreover, the results were corroborated by measurements conducted in different laboratories and using different systems, confirming the reliability of our findings (figs. S23 and S24).

Creation of interfacially bonded networks

In both cases, Ag_2Se and BST-B-ST pellets show outstanding performance, despite having porosities around 50%. Effective medium theory (EMT) predicts that a decrease in σ offsets the reduction in κ, as both are similarly affected by the presence of an insulating material,

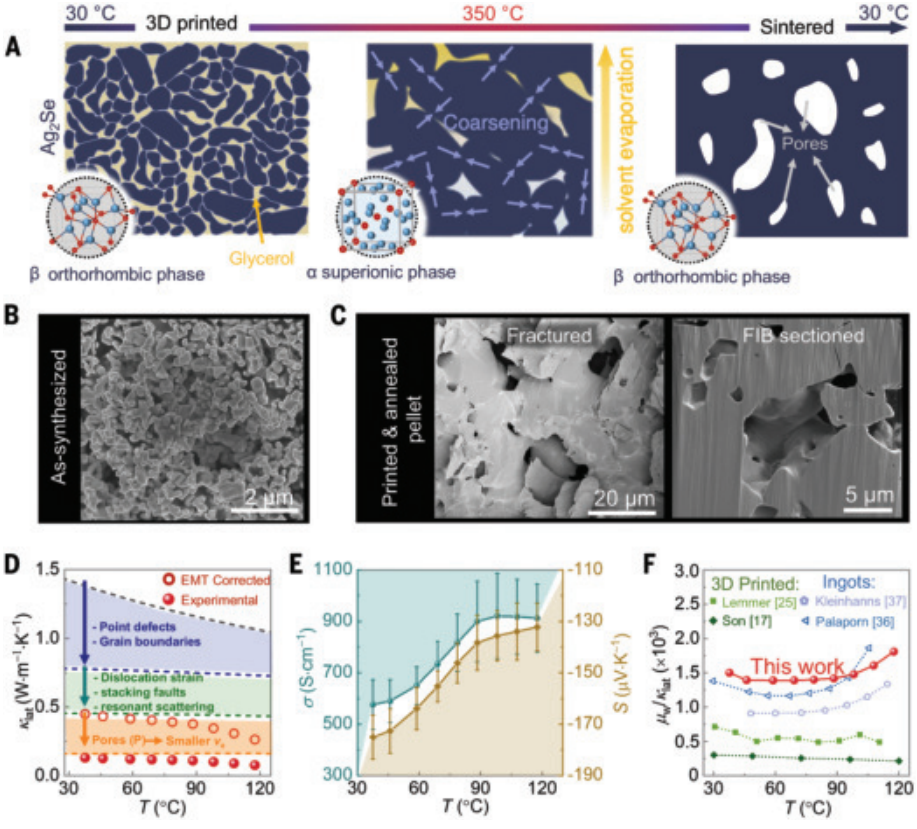

Fig. 2. Porous microstructures and thermoelectric performance of printed Ag_2Se. (**A**) Schematic diagram showing the microstructural evolution in the printed Ag_2Se bars during the sintering process at 350°C for 2 hours. (**B**) Scanning electron microscope (SEM) images of as-synthesized Ag_2Se particles. (**C**) SEM images of fractured and focused ion beam (FIB) cross-sectional areas of the Ag_2Se pellets. (**D**) κ_{lat} of the printed Ag_2Se pellet labeled by the closed red symbols. Open red symbols represent the corrected κ_{lat} using effective medium theory (EMT). (**E**) σ and S of the printed Ag_2Se pellets. (**F**) Comparison of the μ_w/κ_{lat} between state-of-the-art n-type materials and our printed Ag_2Se (*17*, *25*, *36*, *37*). μ_w denotes weighted mobility.

resulting in no difference in zT (*46*). However, porous materials have not been able to match the performance of their state-of-the-art dense counterparts. This is due to the more profound reduction in σ resulting from the disruption of the material's continuity, indicating that the presence of pores yields poor interconnection between grains (*47*).

By examining the balance between charge carrier weighted mobility (μ_w) and κ_{lat}, we can evaluate the trade-off between the benefits of reduced phonon propagation and the disadvantages of hindered charge carrier transport. Both p- and n-type printed pellets in this work display one of the highest μ_w/κ_{lat} values (*48*) reported compared to those of their denser analogs (Figs. 2F and 3G). These results indicate that despite the presence of a large quantity of pores, the sintering process promotes the formation of interfacially bonded grains, which yields sufficiently good charge transport across them (Fig. 2, A and B, for Ag_2Se, and Fig. 3, B to D, for BST-B-ST).

For Ag_2Se, we achived the formation of interfacially bonded grains simply by exploiting the phase transition of the material at around 133°C during sintering (*37*), without any binder. The liquid-like behavior of the high-temperature superionic phase allows Ag ions to become highly mobile (*49*) and promotes mass transfer across different grains (Fig. 2A and fig. S50). Details of this process are provided in the supplementary materials. After the complete transformation back to the low-temperature orthorhombic phase, the rearrangement of Ag and Se atoms produces a microstructure characterized by interconnected grains with small-angle grain boundaries (fig. S9 and Fig. 2C).

BST usually requires pressure-assisted sintering to ensure thermal fusing between the particles (*38*, *39*). For 3D-printed materials, we bypass this step by using binders, Bi nanoparticles, and Sb_2Te_4 ChaM, which transform during the sintering step into a compositionally matching soldering compound and create bonds between the original BST particles. As the temperature increases, Bi nanoparticles start melting (Bi has a melting point of 270°C), promoting atomic diffusions of Sb_2Te_4 ChaM and the surface atoms of ball-milled BST (Fig. 3D and movie S5) (*50*). This diffusion facilitates a chemical reaction between Bi and Sb_2Te_4 to form a new BST phase, which chemically bonds with the original ball-milled BST particles (Fig. 3C and movie S6), facilitating charge transport between grains. The high density of dislocations found at the grain boundaries is indirect proof of this liquid-like sintering phenomenon, as it has been previously reported for the role of liquidized Te during sintering of the BST in pressure-assisted sintering (fig. S13) (*38*, *39*). However, in the 3D-printed material, because no pressure is used during the sintering process, the resulting solid is highly porous.

The reduced κ_{lat} arises from various phonon-scattering mechanisms and the lack of thermal conduction within the pores. On one side, we use EMT theory to subtract the decrease in κ_{lat} attributed to the pores' thermal insulating nature (Fig. 2D for Ag_2Se and fig. S42B for BST-B-ST) and obtain the equivalent if the material were fully dense (κ_{lat}^{EMT}). On the other side, we took into account the different types of defects found by high-resolution transmission electron microscopy (HRTEM), including a Casmir-like phonon interface scattering term to consider the role of the pore interfaces (*46*) and calculate the expected κ_{lat} using the Debye-Callaway model (Fig. 2D for Ag_2Se and fig. S42B for BST-B-ST). The κ_{lat}^{EMT} values are in good agreement with the values predicted in the model for both Ag_2Se (*37*) and $(Bi,Sb)_2Te_3$ (*46*). Such a good fit is an indication of good interfacial bonding across grains.

To gain further insights into the impact of porosity on the κ_{lat}, we calculated the average sound velocity (v_a) based on experimental data. The v_a of the BST-B-ST sample is found to be 1116 m·s^{-1} compared to 2147 m·s^{-1} in $Bi_{0.5}Sb_{1.5}Te_3$ ingots (table S3) (*38*). Similarly, the v_a of our Ag_2Se sample is around 764 m·s^{-1}, much lower than 1472 m·s^{-1} in dense Ag_2Se (*48*). The reduction in the v_a is attributed to the substantial decrease in the elastic modulus, because the pores act as stress concentrators and disrupt the uniform transmission of stress waves, reducing the material's stiffness (*51*). We found a good fit between the Debye Callaway model and the measured κ_{lat}, using the experimentally determined v_a instead of the theoretical one. This alignment validates the use of EMT and the Debye-Callaway model for predicting κ in our porous material, indicating that the reduction in κ_{lat} compared to that in the dense material with similar defects is due to the softening of the material in the presence of pores (*46*).

Applying printed materials for active cooling

Using the optimized BST-B-ST and Ag_2Se inks, we printed both p-type and n-type pillars and

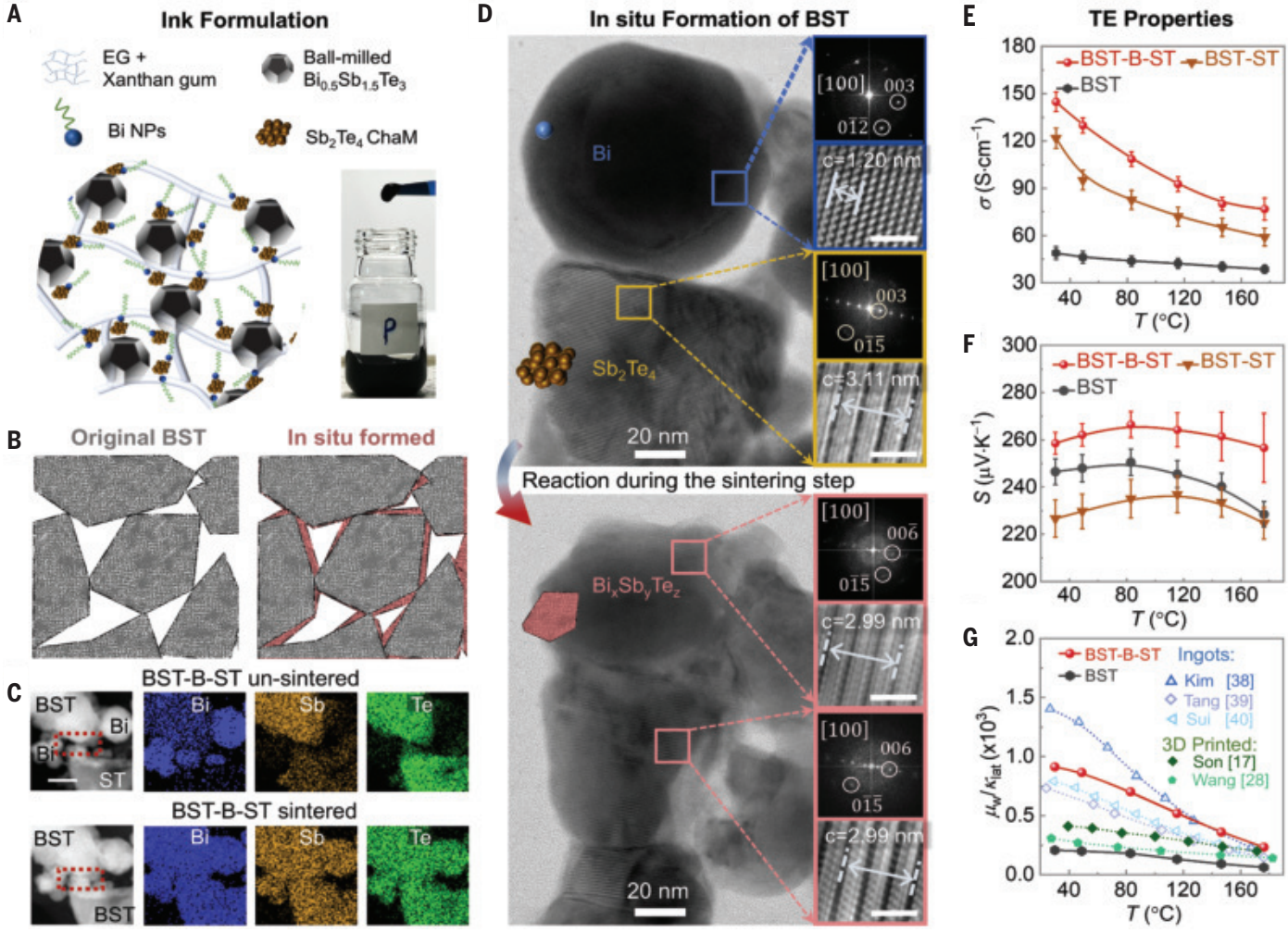

Fig. 3. Improved thermoelectric performance of BST-B-ST by forming interfacial bonding between grains. (**A**) Ink components of the $(Bi,Sb)_2Te_3$-based ink. (**B**) Schematic diagram highlighting the presence of an in situ–formed BST phase connecting the ball-milled BST particles. (**C**) Comparison of the transmission electron microscopy (TEM) images and the corresponding energy dispersive x-ray spectrometry elemental maps of the BST-B-ST ink before (top) and after (bottom) the sintering process performed in situ in the TEM. After heating to 400°C, the original ball-milled BST particles form a continuous phase with the in situ–formed BST phase as indicated by the dotted red box. Scale bar, 100 nm. (**D**) Bright-field TEM images of as-mixed (top) ST and Bi nanoparticles and after being heated to 350°C (bottom) with the corresponding fast Fourier transform and high-resolution TEM images from the boxed areas on the right. (**E**) σ and (**F**) *S* of BST, BST-ST, and BST-B-ST pellets. (**G**) μ_w/κ_{lat} of the BST and BST-B-ST samples and other state-of-the-art p-type thermoelectric materials (*17*, *28*, *38*–*40*).

assembled them in the TEC to build a 32-pair device. We chose the length l and diameter d of both types of legs, 0.8 mm and 1 mm, respectively, to match their resistance. We controlled the pillar size by tuning the printing parameters: nozzle speed, size, and printing pressure (fig. S26). The cone-shaped tips of the printed legs were flattened by a programmed scratching method (movie S3), leaving a smooth top surface to facilitate the soldering process (fig. S39). The electronic contacts with the electrodes were done by evaporating a 0.5-μm-thick layer of platinum onto the top and bottom surfaces of the printed thermoelectric legs (fig. S38), and soldered using Bi-rich soldering paste to minimize the contact resistance.

The fabricated TECs produce a maximum cooling temperature difference (ΔT_{max}) of 50°C between the hot surface and cold surface without a heating load at room temperature (Fig. 4B). Increasing the heating load (Fig. 4B) generated from the heater leads to a gradual increase in the cooling temperature (T_c). The maximum cooling flux density $p_{c,max}$ of 0.87 W·cm^{-2} is achieved with zero ΔT (Fig. 4C, red line). With increasing ΔT, the $p_{c,max}$ decreases, indicating a trade-off effect between the cooling temperature and cooling flux. To ensure the practical application of the as-fabricated TEC, we evaluated the cyclic stability of the fabricated device without a heating load (Fig. 4, D and E). The T_c remains unchanged after a continuous cooling test for 7 days and 200 cooling cycles. These results demonstrate the reliability of the device and the stability of the printed thermoelectric legs upon operation. Notably, the ΔT values reported were measured in air. Under vacuum, the maximum temperature difference exceeded 64°C. Reducing contact resistance could bring the achieved temperature differences closer to the theoretical values predicted by the material's zT (details can be seen in fig. S53).

Conclusions

We demonstrate a reproducible and scalable method for fabricating high-performance TECs using 3D-printed materials. Through extrusion-based 3D printing, thermoelectric materials with high zT values of 1.42 for p-type $(Bi, Sb)_2Te_3$

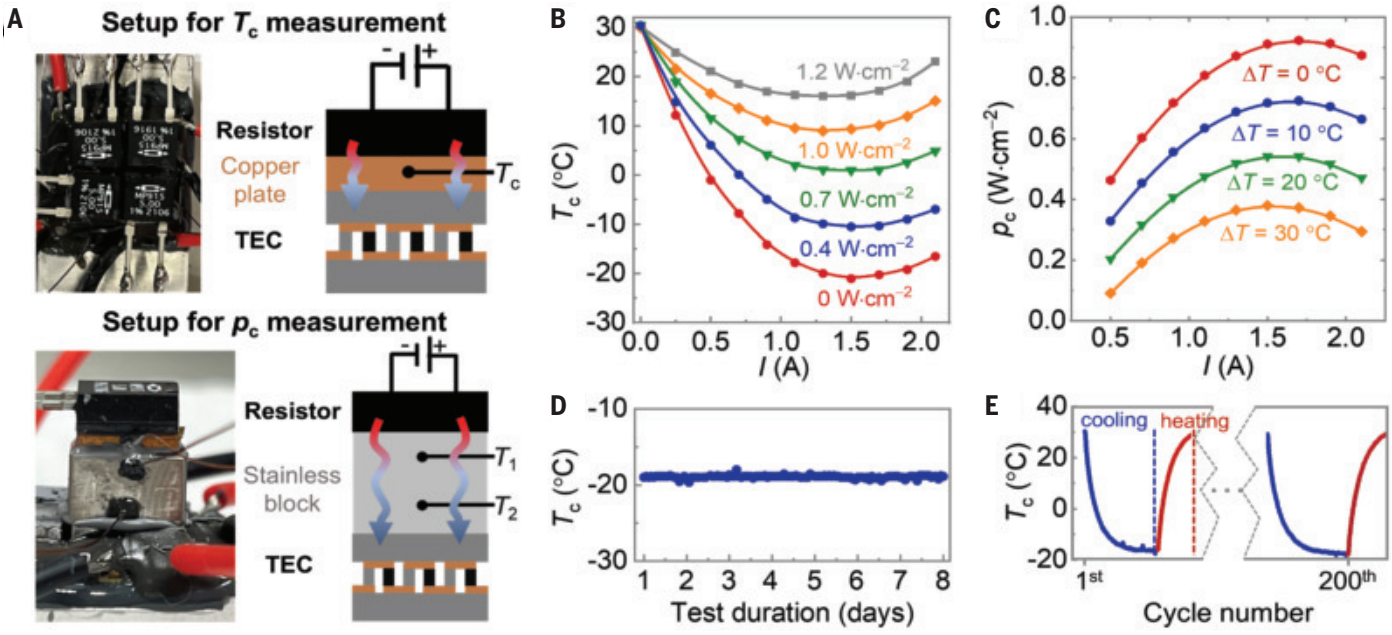

Fig. 4. Cooling performance and stability of the 3D-printed TEC. (**A**) Home-made setups for T_c (top) and p_c (bottom) measurements. For the former, a thermistor was inserted into a copper plate encapsulated by the heater and the TEC to monitor the T_c. For the latter, we use two thermistors to monitor the temperature gradient in a stainless-steel plate and then calculate the heat flow. (**B**) Cooling temperature T_c as a function of heating loads on the cold surface of the TEC. (**C**) Cooling flux density p_c as a function of different temperature gradients ΔT (defined as $T_{hot} - T_{cold}$) across the TEC. (**D**) T_c of the TEC during continuous cooling test for 7 days. (**E**) T_c of the TEC during cyclic cooling tests. For a continuous and prolonged cooling effect, heat dissipation at the hot side is procured using a custom-made water circulator.

and 1.3 for n-type Ag_2Se at room temperature are prepared. The key to achieving high performance lies in tailoring the ink formulation to promote the formation of interfacial bonding between particles during the removal of the liquid media from both materials, allowing our highly porous materials to display excellent thermoelectric properties. Moreover, we integrate the printed materials into a 32-pair device with cooling capability comparable to that of state-of-the-art TECs.

Our approach not only advances thermoelectric technology by achieving high zT values and outstanding cooling performance, but also paves the way for the development of ink formulations in 3D printing of semiconducting particles. By focusing on the material characteristics and identifying binders that enable atomic particle connections without altering the final material composition, we can retain or even improve the functional properties of the target semiconductors. These advances bring us one step closer to the viability of 3D printing as a more sustainable and efficient alternative to traditional manufacturing methods.

REFERENCES AND NOTES

1. G. J. Snyder *et al.*, *Joule* **5**, 748–751 (2021).
2. N. Jakhar, M. Ibáñez, *Science* **383**, 1184 (2024).
3. R. Venkatasubramanian, E. Siivola, T. Colpitts, B. O'Quinn, *Nature* **413**, 597–602 (2001).
4. I. Chowdhury *et al.*, *Nat. Nanotechnol.* **4**, 235–238 (2009).
5. T. Parashchuk *et al.*, *J. Power Sources* **496**, 229821 (2021).
6. J. P. Rojas *et al.*, *ECS J. Solid State Sci. Technol.* **6**, N3036 (2017).
7. S. Hong *et al.*, *Sci. Adv.* **5**, eaaw0536 (2019).
8. Q. Zhang, K. Deng, L. Wilkens, H. Reith, K. Nielsch, *Nat. Electron.* **5**, 333–347 (2022).
9. M. Hong, M. Li, Y. Wang, X. L. Shi, Z. G. Chen, *Adv. Mater.* **35**, e2208272 (2023).
10. Z. H. Zheng *et al.*, *Nat. Sustain.* **6**, 180–191 (2023).
11. Y. Qin *et al.*, *Science* **383**, 1204–1209 (2024).
12. B. Qin *et al.*, *Science* **373**, 556–561 (2021).
13. D. Liu *et al.*, *J. Electron. Mater.* **46**, 2999–3006 (2016).
14. M. Hines, J. Lenhardt, M. Lu, L. Jiang, Z. Xiao, *J. Vac. Sci. Technol. A* **30**, 041509 (2012).
15. G. Li *et al.*, *Nat. Electron.* **1**, 555–561 (2018).
16. G. J. Snyder, J. R. Lim, C. K. Huang, J. P. Fleurial, *Nat. Mater.* **2**, 528–531 (2003).
17. F. Kim *et al.*, *Nat. Energy* **3**, 301–309 (2018).
18. D. Zhang *et al.*, *ACS Energy Lett.* **8**, 332–338 (2022).
19. M. Zeng *et al.*, *Nature* **617**, 292–298 (2023).
20. F. Kim *et al.*, *Nat. Electron.* **4**, 579–587 (2021).
21. D. M. Balazs, M. Ibáñez, *Science* **381**, 1413–1414 (2023).
22. M. R. Burton *et al.*, *Adv. Energy Mater.* **9**, 1900201 (2019).
23. N. Su, P. Zhu, Y. Pan, F. Li, B. Li, *Energy* **195**, 116892 (2020).
24. M. M. Mallick *et al.*, *J. Mater. Chem. A Mater. Energy Sustain.* **8**, 16366–16375 (2020).
25. M. M. Mallick, L. Franke, A. G. Rösch, U. Lemmer, *ACS Energy Lett.* **6**, 85–91 (2020).
26. J. Peng *et al.*, *Nat. Commun.* **10**, 5590 (2019).
27. C. Oztan, S. Ballikaya, U. Ozgun, R. Karkkainen, E. Celik, *Appl. Mater. Today* **15**, 77–82 (2019).
28. Z. Wang *et al.*, *Mater. Today Energy* **31**, 101206 (2023).
29. M. R. Burton *et al.*, *J. Mater. Chem. A Mater. Energy Sustain.* **7**, 25586–25592 (2019).
30. J. Lee *et al.*, *Adv. Energy Mater.* **11**, 2100190 (2021).
31. G. Bulman *et al.*, *Nat. Commun.* **7**, 10302 (2016).
32. Z. Liu *et al.*, *Nat. Commun.* **13**, 1120 (2022).
33. W. Hou *et al.*, *Nano Energy* **50**, 766–776 (2018).
34. Z. Xiao, K. Hedgemen, M. Harris, E. DiMasi, *J. Vac. Sci. Technol. A* **28**, 679–683 (2010).
35. Z. Xiao, X. Zhu, *Sensors* **15**, 17232–17240 (2015).
36. D. Palaporn, S. Pinitsoontorn, K. Kurosaki, G. J. Snyder, *Adv. Mater. Technol.* **9**, 2301242 (2024).
37. T. Kleinhanns *et al.*, *Adv. Energy Mater.* **14**, 2400408 (2024).
38. S. I. Kim *et al.*, *Science* **348**, 109–114 (2015).
39. R. Deng *et al.*, *Sci. Adv.* **4**, eaar5606 (2018).
40. H. Qin *et al.*, *Mater. Today Phys.* **6**, 31–37 (2018).
41. J. Wang *et al.*, *Chem. Mater.* **26**, 5647–5653 (2014).
42. B. Poudel *et al.*, *Science* **320**, 634–638 (2008).
43. Y. Lan *et al.*, *Nano Lett.* **9**, 1419–1422 (2009).
44. Y. Zheng *et al.*, *Adv. Energy Mater.* **5**, 1401391 (2014).
45. D. Wu *et al.*, *J. Am. Chem. Soc.* **136**, 11412–11419 (2014).
46. Y. Pan *et al.*, *Adv. Mater.* **30**, e1802016 (2018).
47. M. He *et al.*, *Small* **11**, 5889–5894 (2015).
48. M. Jin *et al.*, *J. Phys. Chem. Lett.* **12**, 8246–8255 (2021).
49. K. Zhao, P. Qiu, X. Shi, L. Chen, *Adv. Funct. Mater.* **30**, 1903867 (2019).
50. R. M. German, P. Suri, S. J. Park, *J. Mater. Sci.* **44**, 1–39 (2009).
51. Z. Cui, Y. Huang, H. Liu, *J. Mech. Behav. Biomed. Mater.* **71**, 10–22 (2017).

ACKNOWLEDGMENTS

This work was supported by the Scientific Service Units (SSU) of ISTA through resources provided by the Electron Microscopy Facility (EMF), the Lab Support Facility (LSF), the Communication & Events facility, the Miba Machine Shop, and the Nanofabrication Facility (NNF). The Mechanical Response of Materials (MRM) Service Unit of the Technical University of Wien is acknowledged for Mechanical tests. X. L. Yan and S. Bühler-Paschen (Institute of Solid-State Physics, Technical University of Wien) are acknowledged for granting us access to their equipment, which allowed us to perform independent corroborative measurements. M. Qin is acknowledged for help with Au deposition and wire bonding for samples used for PPMS measurements. The lab of B. Hof and Z. Lu is acknowledged for help with rheological properties measurements. The members of the Ibáñez research group, especially N. Jakhar, C. Fiedler, and T. Kleinhanns, are acknowledged for their feedback on the manuscript and fruitful discussions. **Funding:** This work was financially supported by ISTA and the Werner Siemens Foundation.

Author contributions: Conceptualization: S.X., M.I. Methodology: S.X., S.H. Investigation: S.X., A.L., M.L., K.M. Visualization: S.X., M.I., S.H. Funding acquisition: M.I. Project administration: M.I. Supervision: M.I. Writing: S.X., S.H., M.I. **Competing interests:** The authors declare that they have no competing interests. **Data and materials availability:** All data are available in the main text or the supplementary materials. **Data and materials availability:** Copyright © 2025 the authors, some rights reserved; exclusive licensee American Association for the Advancement of Science. No claim to original US government works. https://www.sciencemag.org/about/science-licenses-journal-article-reuse

SUPPLEMENTARY MATERIALS

science.org/doi/10.1126/science.ads0426
Materials and Methods
Supplementary Text
Figs. S1 to S55
Tables S1 to S14
References (*52*–*71*)
Movies S1 to S6

Submitted 10 August 2024; accepted 2 January 2025
10.1126/science.ads0426

PROTEIN DESIGN

Simulating 500 million years of evolution with a language model

Thomas Hayes[1]†, Roshan Rao[1]†, Halil Akin[1]†, Nicholas J. Sofroniew[1]†, Deniz Oktay[1]†, Zeming Lin[1]†, Robert Verkuil[1]†, Vincent Q. Tran[2,3], Jonathan Deaton[1], Marius Wiggert[1], Rohil Badkundri[1], Irhum Shafkat[1], Jun Gong[1], Alexander Derry[1], Raul S. Molina[1], Neil Thomas[1], Yousuf A. Khan[1], Chetan Mishra[1], Carolyn Kim[1], Liam J. Bartie[2], Matthew Nemeth[2], Patrick D. Hsu[2,3], Tom Sercu[1], Salvatore Candido[1], Alexander Rives[1]*

More than 3 billion years of evolution have produced an image of biology encoded into the space of natural proteins. Here, we show that language models trained at scale on evolutionary data can generate functional proteins that are far away from known proteins. We present ESM3, a frontier multimodal generative language model that reasons over the sequence, structure, and function of proteins. ESM3 can follow complex prompts combining its modalities and is highly responsive to alignment to improve its fidelity. We have prompted ESM3 to generate fluorescent proteins. Among the generations that we synthesized, we found a bright fluorescent protein at a far distance (58% sequence identity) from known fluorescent proteins, which we estimate is equivalent to simulating 500 million years of evolution.

The proteins that exist today have developed into their present forms over the course of billions of years of natural evolution, passing through a vast evolutionary sieve. In parallel experiments conducted over geological time, nature creates random mutations and applies selection, filtering proteins by their myriad sequences, structures, and functions.

As a result, the patterns in the proteins that we observe today reflect the action of the deep hidden variables of the biology that have shaped their evolution across time. Gene sequencing surveys of Earth's natural diversity are cataloging the sequences (*1*–*3*) and structures (*4*, *5*) of proteins, containing billions of sequences and hundreds of millions of structures that illuminate patterns of variation across life. A consensus is developing that underlying these sequences is a fundamental language of protein biology that can be understood using language models (*6*–*11*).

A number of language models of protein sequences have now been developed and evaluated (*5*–*10*, *12*–*17*). It has been found that the representations that emerge within language models reflect the biological structure and function of proteins (*6*–*8*, *18*) and are learned without any supervision on those properties (*19*, *20*), improving with scale (*5*, *21*). In the field of artificial intelligence, scaling laws have been found that predict the growth in capabilities with increasing scale, describing a frontier in compute, parameters, and data (*22*–*24*).

Here, we present ESM3, a frontier multimodal generative model that reasons over the sequences, structures, and functions of proteins. ESM3 is trained as a generative masked language model over discrete tokens for each modality. Structural reasoning is achieved by encoding three-dimensional (3D) atomic structure as discrete tokens rather than with the complex architecture and diffusion in 3D space used in recent predictive (*25*) and generative models (*26*–*28*) of proteins. All-to-all modeling of discrete tokens is scalable and allows ESM3 to be prompted with any combination of its modalities, thus enabling the controllable generation of proteins that respect combinations of prompts. We observed that ESM3 is highly responsive to prompts and finds creative solutions to complex combinations of prompts, including solutions for which we can find no matching structure in nature. Models at all scales can be aligned to better follow prompts, and larger models are far more responsive to alignment, showing greater capability to solve the most difficult prompts after alignment. Using ESM3, we report the generation of a variant of green fluorescent protein (GFP) (*29*, *30*) that is diverged from existing proteins to a degree equivalent to simulating >500 million years of evolution.

ESM3

ESM3 achieves a scalable generative model of the three fundamental properties of proteins, sequence, structure, and function, through language modeling. Previous generative modeling efforts for proteins have focused primarily on individual modalities, leveraging complex architectures and training objectives for structures that represent proteins as 3D objects. To date, the only language models that have been scaled are for protein sequences. In ESM3, sequence, structure, and function are represented through alphabets of discrete tokens. The modalities are input and output as separate sequence tracks that are fused into a single latent space within the model. This simplicity enables ESM3 to leverage a scalable transformer architecture to train up to 98 billion parameters and more than one trillion teraflops of compute, demonstrating the emergence of complex reasoning capabilities over sequence, structure, and function.

ESM3 is trained with a generative masked language modeling objective across all its tracks as described by the following equation:

$$\mathcal{L} = -\mathbb{E}_{x,m}\frac{1}{|m|}\sum_{i\in m}\log p(x_i|x_{\setminus m})$$

A random mask m is applied to the tokens x describing the protein, and the model is supervised to predict the identity of the tokens that have been masked. During training, the mask is sampled using a noise schedule that varies the fraction of positions that are masked so that ESM3 sees many different combinations of masked sequence, structure, and function and predicts completions of any combination of the modalities from any other. This differs from classical masked language modeling (*31*) in that the supervision is applied across all possible masking rates rather than to a single fixed masking rate. This supervision factorizes the probability distribution over all possible predictions of the next token given any combination of previous tokens, thus ensuring that tokens can be generated in any order from any starting point (*32*–*34*).

[1]EvolutionaryScale, PBC, New York, NY, USA. [2]Arc Institute, Palo Alto, CA, USA. [3]University of California, Berkeley, Berkeley, CA, USA.
***Corresponding author. Email: arives@evolutionaryscale.ai**
†These authors contributed equally to this work.

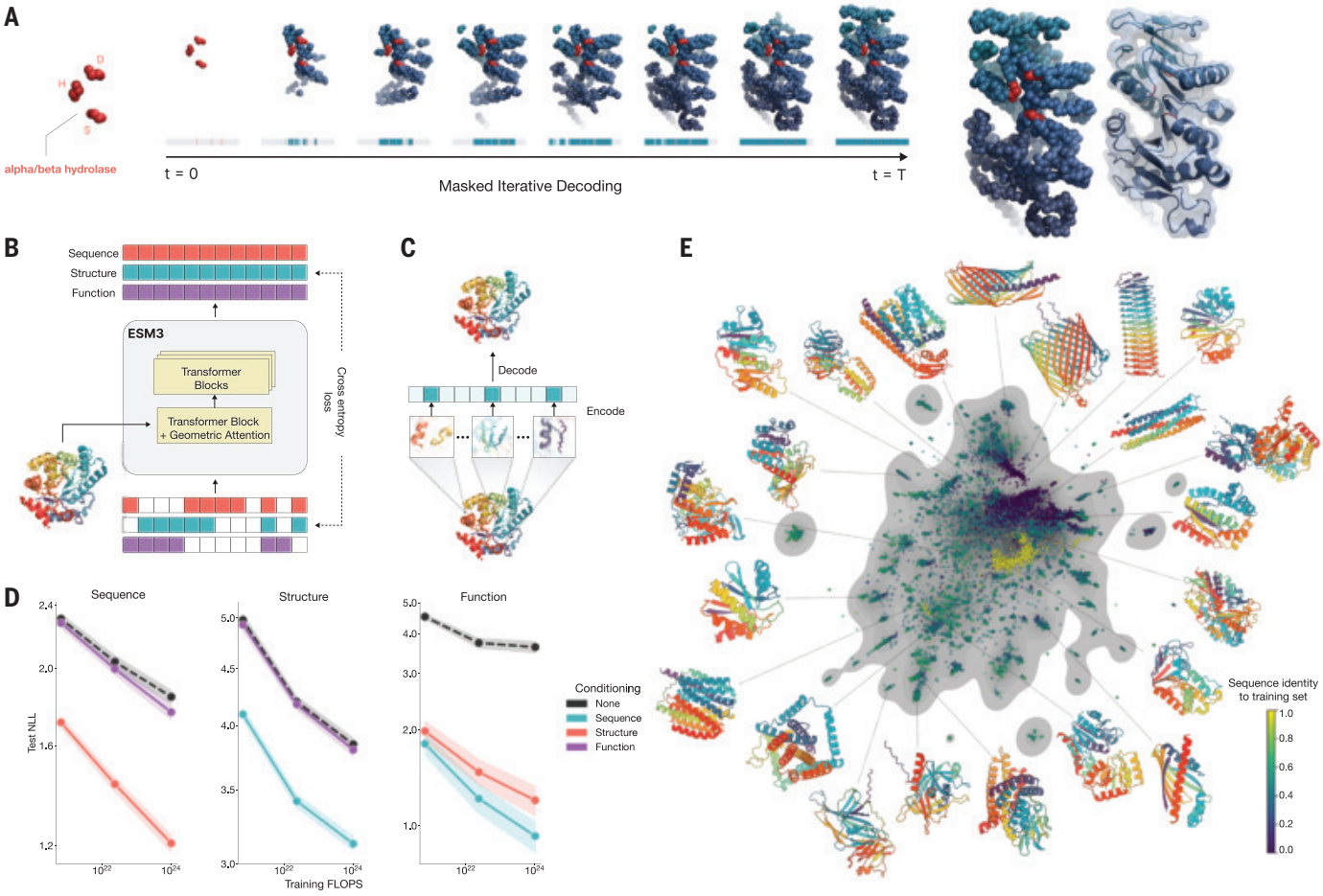

Fig. 1. ESM3 is a generative language model that reasons over the sequence, structure, and function of proteins. (**A**) Iterative sampling with ESM3. Generation of an alpha/beta hydrolase. Sequence, structure, and function can all be used to prompt the model. At each timestep t, a fraction of the masked positions are sampled until all positions are unmasked. (**B**) ESM3 architecture. Sequence, structure, and function are represented as tracks of discrete tokens at the input and output. The model is a series of transformer blocks in which all tracks are fused within a single latent space. Geometric attention in the first block allows conditioning on atomic coordinates. ESM3 is supervised to predict masked tokens. (**C**) Structure tokenization. Local atomic structure around each amino acid is encoded into tokens. (**D**) Models are trained at three scales: 1.4B, 7B, and 98B parameters. Negative log-likelihood (averaged across mask rates) on test set as a function of training FLOPs shows response to conditioning on each of the input tracks, improving with increasing FLOPs (95% confidence interval). (**E**) Unconditional generations from ESM3 98B (colored by sequence identity to the nearest sequence in the training set), embedded by ESM3, and projected by uniform manifold approximation and projection (UMAP) alongside randomly sampled sequences from UniProt (in gray). Generations are diverse, high-quality, and cover the distribution of natural sequences.

To generate from ESM3, tokens are iteratively sampled. Starting from a fully or partially masked context, tokens can be sampled one at a time or in parallel and in any order until all positions are fully unmasked (Fig. 1A). In addition to enabling generation, ESM3's training objective is also effective for representation learning. High masking rates improve the generative capability, whereas lower masking rates improve representation learning. We chose to train ESM3 with a noise schedule that balances generative capabilities with representation learning (supplementary materials, section A.2.2).

ESM3 is a bidirectional transformer. Sequence, structure, and function tokens are embedded and fused at the input and then processed through a stack of transformer blocks (Fig. 1B). At the output of the model, shallow multilayer perceptron heads project the final layer representation into token probabilities for each of the tracks. ESM3 uses tokenization, rather than specialized architectural components, to represent the complexity of proteins in a learned multimodal feature space. This approach enables efficient and highly scalable training.

Protein structures are tokenized by a discrete autoencoder (*35*) that is trained to compress 3D structure into discrete tokens (Fig. 1C). We propose an invariant geometric attention mechanism to efficiently process the 3D structure. The mechanism operates in local reference frames defined by the bond geometry at each amino acid and allows local frames to interact globally through a transformation into the global frame (supplementary materials, section A.1.6). The local structural neighborhoods around each amino acid are encoded into a sequence of discrete tokens, one for each amino acid.

When predicting or generating protein structure, the structure tokens output by ESM3 are passed through the decoder, which reconstructs the full atomic structure. The autoencoder is trained to encode and reconstruct atomic coordinates with a geometric loss that supervises the pairwise distances and relative orientations of bond vectors and normals (supplementary materials, section A.1.7.3.1). This tokenization delivers nearly perfect reconstruction of protein structure [<0.5 Å root mean square difference (RMSD) using CAMEO; fig. S3].

Because the local neighborhoods of each structure token contain information about neighboring parts of the structure, we also provided the model with a mechanism to condition on backbone atomic coordinates directly through geometric attention in the first transformer block. To support higher-level abstractions of structure, we included tracks for secondary structure (SS8) tokens and solvent accessible surface area (SASA) tokens. Key words describing biological activity, such as binding, enzymatic function, and domain or fold classifications allow an even higher-level semantic description of protein architecture and function. Derived from free-text descriptions in InterPro (*36*) and Gene Ontology (GO) terms for each residue, these key words are tokenized (supplementary materials, section A.1.8), embedded, and summed at the network input. Residue-level annotations provide multi-hot labeling of the functions of individual residues, such as catalytic sites and posttranslational modifications (supplementary materials, section A.1.8.3).

The largest ESM3 model is trained on 2.78 billion natural proteins collected from sequence and structure databases (*2*, *36*–*39*). Because a small fraction of structures have been experimentally determined relative to sequences, we leveraged predicted structures (*4*, *5*). Sequences were annotated with function key words using a library of hidden Markov models (*40*). We also generated synthetic sequences with an inverse folding model (supplementary materials, section A.2.1.3) for all structures, including predicted ones. Overall, this increases training data to 3.15 billion protein sequences, 236 million protein structures, and 539 million proteins with function annotations, totaling 771 billion unique tokens. Full details of the training dataset are described in the supplementary materials, section A.2.1.

We trained ESM3 models at three scales: 1.4, 7, and 98 billion parameters (1.4B, 7B, and 98B, respectively). In an initial series of experiments to evaluate representation learning performance in response to architecture hyperparameters, we found a greater response to increasing depth than to width. This behavior informed the choice of relatively deep networks for the final architectures, with the 98B-parameter model incorporating 216 transformer blocks (supplementary materials, section A.1.5).

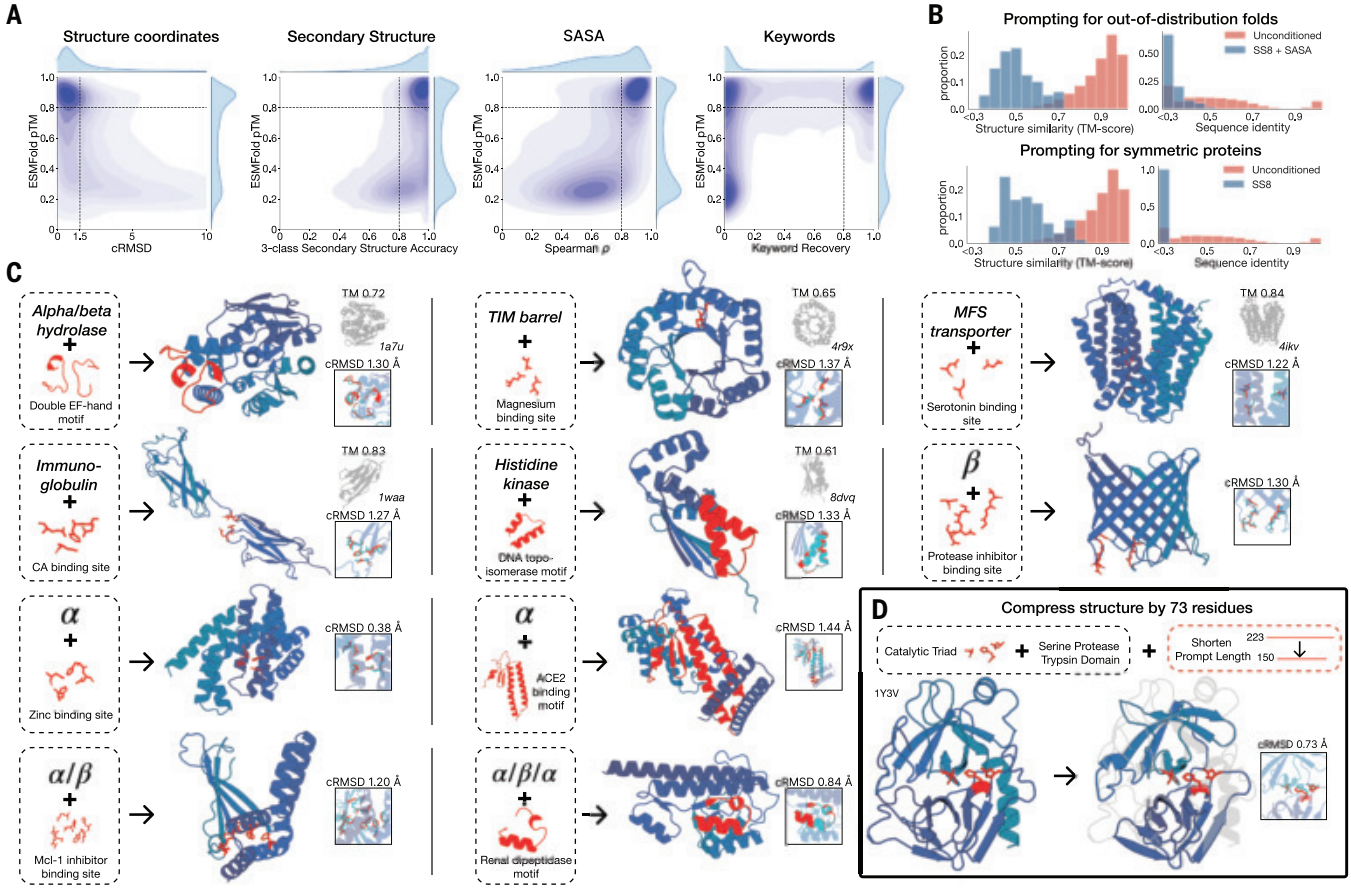

Fig. 2. Generative programming with ESM3. (**A**) ESM3 can follow prompts from each of its input tracks. Density of faithfulness to prompting for each of the tracks is shown. Generations achieve consistency with the prompt (backbone cRMSD, SS3 accuracy, SASA Spearman ρ, and key word recovery) and high structure prediction confidence (pTM). (**B**) ESM3 can be prompted to generate proteins that differ in structure (left) and sequence (right) from the training set and natural proteins. Prompted generations (blue) shift toward a more novel space versus unconditional generations (red) in response to prompts derived from out-of-distribution natural structures (top) and computationally designed symmetric proteins (bottom). (**C**) ESM3 generates creative solutions to a variety of combinations of complex prompts. We show compositions of atomic-level motifs with high-level instructions specified through key words or secondary structure prompts. Fidelity to the prompt is shown through similarity to a reference structure (for key word prompts) and all-atom RMSD (for motif prompts). Solutions differ from the scaffolds where the motif prompt was derived (median TM score 0.36 ± 0.14), and for many motifs (e.g., serotonin, calcium, protease inhibitor, and Mcl-1 inhibitor binding sites), we could find no significant similarity to other proteins that contain the same motif. (**D**) Example of especially creative behavior. ESM3 compresses a serine protease by 33% while maintaining the active site structure.

Scaling ESM3 from 1.4B to 98B parameters results in substantial improvements in the loss for all tracks on the test set, with the greatest improvements observed in sequence loss (Fig. 1D and fig. S11). The gap between unconditional and conditional negative log-likelihoods increases with scale. Conditioning on function keywords primarily constrains sequence at high masking rates, so although responsiveness to key word conditioning is observed at high mask rates, it is less apparent in the averaged negative log-likelihood (fig. S12). These gains in test loss lead to better representation learning (table S8 and fig. S8). In single sequence structure prediction, ESM3 98B surpasses ESMFold [0.880 versus 0.861 mean local distance difference test (LDDT) by the CAMEO test set; table S9). Generating sequences from the model without prompting (unconditional generation) produces high-quality proteins with a mean predicted LDDT (pLDDT) of 0.84 and a predicted template modeling score (pTM) of 0.52, which are diverse in both sequence (mean pairwise sequence identity 0.155) and structure (mean pairwise TM score 0.48), spanning the distribution of known proteins (Fig. 1E and fig. S14).

Our results show that scaling with language modeling, which is enabled by tokenization, efficient architectures, and masked token prediction, yields continued improvements in both representational and generative applications. This approach allows the model to build a shared multimodal representation space that is learned from the data rather than being explicitly hardcoded into its architecture. Given increasing compute and data, the model could learn an increasingly richer and more general feature space. In the following sections, we show that this approach achieves high fidelity for the controllable generation of proteins.

Programmable design with ESM3

We explored the ability of ESM3 to follow complex prompts with different compositions. ESM3 can be prompted with instructions from each of its input tracks: sequence, structure coordinates, SS8, SASA, and function key words. This allows prompts to be specified at multiple levels of abstraction, from atomic-level structure to high-level key words describing the function and fold topology.

We evaluated ESM3's ability to follow prompts in each of the tracks independently (Fig. 2A). A set of prompts are constructed for each of the tracks using a temporally held out test set of natural proteins (supplementary materials, section A.3.8). The resulting generations are evaluated using ESMFold for consistency with the prompt and confidence of structure prediction (pTM). We defined four consistency metrics for each track: (i) constrained site RMSD (cRMSD), the RMSD between the coordinates of the prompt, i.e., the positions of the backbone atoms, and the corresponding coordinates in the generation; (ii) SS3 accuracy, the fraction of residues where three-class secondary structure between the prompt and generations match; (iii) SASA Spearman ρ, the correlation between the SASA prompt and the corresponding region of the generation; and (iv) key word recovery, the fraction of prompt key words recovered by InterProScan (*40*). Across all tracks, the 7B parameter ESM3 finds solutions that follow the prompt and have structures that are confidently predicted by ESMFold (pTM > 0.8). Some mode switching is observed, including under key word prompting, where a fraction of the generations have confidently predicted structures that do not recover the key words.

Unconditional generations reflect the distribution of natural proteins. Because we observed that ESM3 can faithfully follow prompts, we reasoned that prompting could steer the model to generate proteins that differ from the training set and natural proteins. First, we tested the ability of the model to follow out-of-distribution prompts. We constructed a set of prompts combining SS8 and SASA from held-out structures (TM <0.7 to training set). Under these prompts, although the model continues to generate coherent globular structures (mean pTM 0.85 ± 0.03 under ESM3 7B; supplementary materials, section A.3.9), the distribution of similarities to the training set (as measured by TM score and sequence identity) shifts to be more novel (average sequence identity to nearest training set protein <20% and mean TM score 0.48 ± 0.09; Fig. 2B, top). To test the ability to generalize to structures beyond the distribution of natural proteins, we used secondary structure prompts derived from a dataset of artificial symmetric protein designs distinct from the natural proteins found in the training dataset (supplementary materials, section A.3.9). Similarly, ESM3 produces high-confidence generations (pTM > 0.8, pLDDT > 0.8) with low sequence and structure similarity to proteins in the training set (sequence identity <20% and TM score 0.52 ± 0.10; Fig. 2B, bottom), indicating that the model can be used to generate protein sequences and structures highly distinct from those that exist in nature.

ESM3 is able to follow complex prompts and has the ability to compose prompts from different tracks and at different levels of abstraction. To evaluate this ability, we prompted ESM3 with motifs that require solving for spatial coordination of individual atoms, including atoms participating in tertiary contacts between residues far apart in the sequence, such as catalytic centers and ligand-binding

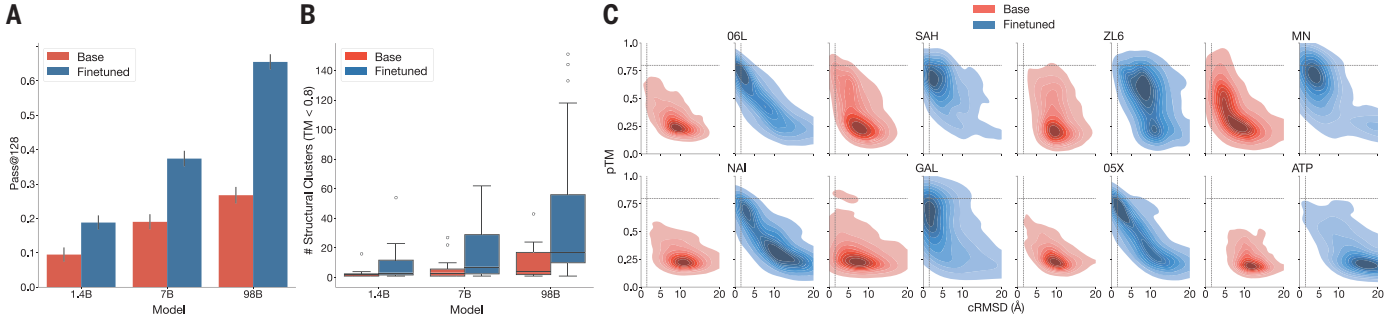

Fig. 3. The ability to solve complex tasks increases with scale through alignment. ESM3 was aligned to follow tertiary coordination prompts with a dataset of preference pairs constructed from prompted generations, where positive samples with good scores for desired properties (high pTM, low cRMSD) are paired with negative samples with worse scores. The preference tuning loss encourages the model to put higher likelihood on the positive samples. After training, models are evaluated by prompting with the backbone atomic coordinates of residues in tertiary contact. (**A**) Effect of fine-tuning on the fraction of tasks solved with 128 generations (Pass@128; error bars indicate 2 SDs). A large gap opens between the models with scale. The response to alignment shows a latent capability to solve complex tasks in the largest model. (**B**) Number of distinct solutions (clustered at TM > 0.8) generated for each tertiary motif. After fine-tuning, there are often many unique solutions for ligands where there are successes. (**C**) Densities of prompted generations are shown for the base model (left) and the aligned model (right) at the 98B scale for a number of randomly selected ligands. After alignment, the fidelity to the prompt (backbone cRMSD) and quality of generations (pTM) tends to improve substantially.

sites. We combined the atomic-level motif prompts with high-level prompts, either secondary structure prompts or key word prompts that specify the fold architecture. For each unique combination of atomic-level motif and high-level prompt, we generated sequences until there was a success (for atomic-level prompts, when all-atom RMSD <1.5 Å; for fold architecture key word prompts, when TM was >0.6 to a representative structure; for secondary structure prompts, when SS3 accuracy was >80%; and for all prompts, when pTM was >0.8 and pLDDT was >0.8 for the entire generated protein).

We found that ESM3 is able to solve a wide variety of such tasks (Fig. 2C). It does so without retrieving the motif's original scaffold (median TM score of 0.40 ± 0.10; supplementary materials, section A.3.10). In some cases, the scaffolds are transferred from existing proteins that have similar motifs (for example, the ESM3-designed alpha-helical scaffold for the zinc-binding motif has high similarity to Ni^{2+}-binding proteins, PDB: 5DQW, 5DQY; Fig. 2C, row 3, column 1). For many motifs (e.g., binding sites for serotonin, calcium, protease inhibitor, and Mcl-1 inhibitor), Foldseek (*41*) finds no other proteins that contain the same motif. In these cases, we observed that sometimes the motif has been grafted into entirely different folds (e.g., a protease inhibitor binding site motif in a beta-barrel that is most similar to a membrane-bound copper transporter, PDB: 7PGE; Fig. 2C, row 3, column 3). At other times, the scaffold has low structural similarity to all known proteins in the PDB, ESMAtlas, and AlphaFold databases (maximum TM score <0.5; Fig. 2C, row 4, column 1), such as for an alpha/beta protein designed to scaffold the Mcl-1 inhibitor binding motif. Overall, the generated solutions have high designability, i.e., confident recovery of the original structure after inverse folding with ESM-IF1 (*42*) and refolding with ESMFold (median pTM 0.80 ± 0.08; scTM 0.96 ± 0.04; supplementary materials, section A.3.10).

Through experiments with prompt engineering, we have observed especially creative responses to prompts. Here, we highlight an example of protein compression (Fig. 2D). Starting from a natural trypsin (PDB 1Y3V), we prompted with the sequence and coordinates of the catalytic triad and functional key words describing trypsin but reduced the overall generation length by a third (from 223 to 150 residues). The ESM3 design maintains the coordination of the active site (all-atom RMSD 0.73 Å) and the overall fold with high designability (pTM 0.84, scTM mean 0.97, SD 0.006) despite the considerable reduction in sequence length and the fold only being specified by the function key word prompt (supplementary materials, section A.3.11).

These examples illustrate ESM3's ability to find creative solutions to prompts specified in any of its input tracks, individually or in combination. This capability enables a rational approach to protein design, providing control at various levels of abstraction, from high-level topology to atomic coordinates, using a generative model to bridge the gap between the prompt and biological complexity.

Biological alignment

Although we have observed meaningful increases in the performance of the base models with scale, larger models could have even greater latent capabilities that we did not observe. The base ESM3 models can be prompted to perform difficult tasks such as tertiary motif scaffolding and composition of prompts despite the fact that the models have not been explicitly optimized for these objectives. Because the properties that we evaluated generative outputs on, such as adherence to the prompt or the confidence of the scaffold, are only seen by the model indirectly during pretraining, aligning the model directly to the generative task with fine-tuning could elicit even greater capability differences with larger models.

We studied how the base models could be aligned (*43*, *44*) to generate proteins that satisfy challenging prompts. For each model, we constructed a dataset of backbone atomic coordinate prompts consisting of contiguous spans of residues and tertiary motifs (which also specify the identities of the contacting amino acids). We generated multiple protein sequences for each prompt and fold each of the sequences using ESM3, scoring for consistency with the prompt (backbone cRMSD) and structure prediction confidence (pTM). High-quality samples were paired with low-quality samples for the same prompt to construct a preference dataset (supplementary materials, section A.4). ESM3 was then fine-tuned with a preference optimization loss (*45*, *46*), which causes the model to put higher likelihood on the high-quality samples relative to the low-quality samples.

After aligning each of the base models, we evaluated their absolute performance and the shift in the distribution of generations. We focused on a series of challenging prompts that require coordination of the backbone atoms of residues in tertiary contact. We used ESMFold to evaluate the ability to generate high-quality scaffolds (pTM >0.8) that follow the prompt with high resolution (backbone cRMSD <1.5Å). We prompted each model with amino acid identities and backbone atomic coordinates from a held-out dataset of 46 ligand-binding motifs (supplementary materials, section A.4.5). For each motif, we created 1024 prompts by permuting the order of the residues, varying their position in the sequence, and varying the length of the sequence. A single protein was generated per prompt. The 1024 generations for each motif were used to construct an unbiased estimator of the fraction of tertiary coordination tasks solved after 128 generations (Pass@128; supplementary materials, section A.4.5).

Aligned models solve double the tertiary coordination tasks compared with base models (Fig. 3A). Although the base models show differences in the percentage of tasks solved (9.5% for 1.4B, 19.0% for 7B, 26.8% for 98B; Fig. 3A), a much larger capability difference was revealed through alignment (increasing from 9.5 to 18.8%, 19.0 to 37.4%, and 26.8 to 65.5% for the 1.4B, 7B, and 98B models, respectively). Preference-tuned models not only solve a greater proportion of tasks, but also find a greater number of solutions per task, as evaluated by the number of distinct structural clusters (TM >0.8) with backbone cRMSD <1.5Å and pTM >0.8 (Fig. 3B). A shift in the distribution of ESMFold pTM and backbone cRMSD for each ligand binding motif was observed (Fig. 3C and fig. S18). At the 98B scale, the fine-tuned model produced more distinct successful clusters than the base model on 37 of the 46 tested ligands, whereas the remaining nine ligands were not solved by either the base or aligned model, indicating that alignment almost universally improves the faithfulness to the prompt and confidence of the structure prediction for the generated proteins. These results represent state-of-the-art motif scaffolding performance (table S16). Compared with a supervised fine-tuning baseline, which only maximizes the likelihood of the positive examples, preference tuning leads to larger improvements at all scales (supplementary materials, section A.4.6).

Our experiments with alignment reveal a considerable difference in capabilities between model scales. The largest aligned model improves substantially relative to the base model before alignment and compared with the smaller models after alignment. Through alignment, the models learn to generalize from a small number of examples; the distribution of generations shifts to improve the quality of scaffolds and consistency with prompts, thus increasing the fraction of tasks solved and the number of distinct solutions.

Alignment requires the models to learn by example. The ability to identify the underlying properties that are illustrated by the fine-tuning examples, and to generalize those demonstrations to new tasks, implies that there is an internal representation of the properties that the fine-tuning accesses. This representation space is learned through the process of pretraining, in which the model is trained on proteins across evolution, suggesting that it reflects and contains the immense variety and complexity of protein biology. Such a representation space is likely to contain features that support the generalization of many biological properties. The greater responsiveness

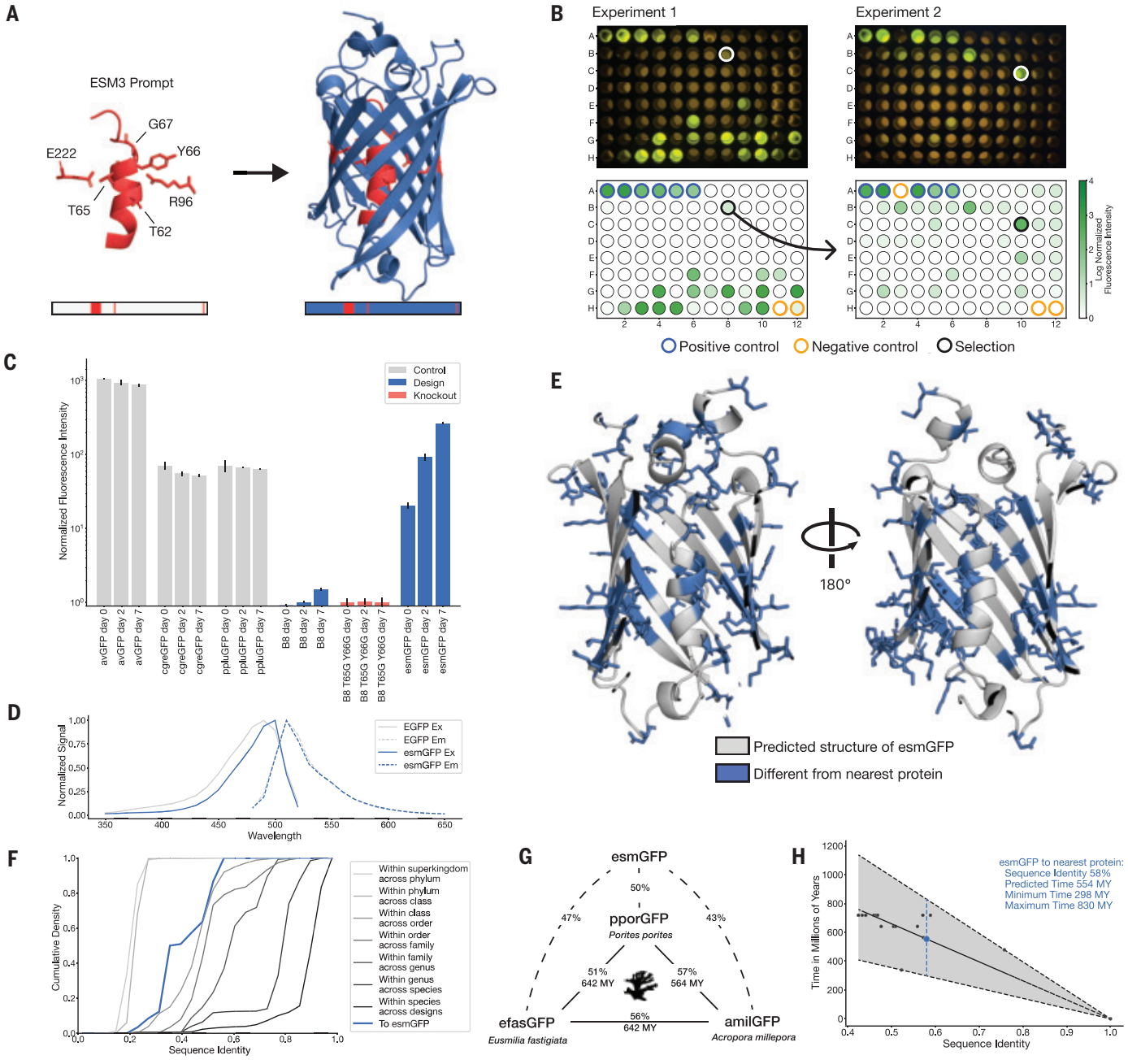

Fig. 4. Generating a distant fluorescent protein with a chain of thought. (**A**) We prompted ESM3 with the sequence and structure of residues required for forming and catalyzing the chromophore reaction, as well as the structure of part of the central alpha helix from a natural GFP (left). Through a chain of thought, ESM3 generates design candidates (right). (**B**) ESM3 found a bright GFP distant from other known GFPs in two experiments. We measured fluorescence in *Escherichia coli* lysate. Top row, photograph of plates. Bottom row, plate reader fluorescence quantification. Positive controls of known GFPs are marked with blue circles, and negative controls with no GFP sequence or no *E. coli* are marked with orange circles. In the first experiment (left), we expressed designs with a range of sequence identities. A notable design with low sequence identity (57%) to known fluorescent proteins appears in the well-labeled B8 (highlighted by a black circle at the bottom and a white circle at the top). We continued the chain of thought from the protein in B8 for the second experiment (right). A bright design appears in the well-labeled C10 (58% sequence identity to known fluorescent proteins; again, highlighted by a black circle at the bottom and a white circle at the top), which we designate esmGFP. (**C**) esmGFP exhibits fluorescence intensity similar to common GFPs. Normalized fluorescence is shown for a subset of proteins in experiment 2. (**D**) Excitation and emission spectra for esmGFP overlaid on the spectra of EGFP. (**E**) Two cutout views of the central alpha helix and the inside of the beta barrel of a predicted structure of esmGFP. The 96 mutations that esmGFP has relative to its nearest neighbor, tagRFP, are shown in blue. (**F**) Cumulative density of sequence identity between fluorescent proteins across taxa. esmGFP has the level of similarity to all other FPs that is typically found when comparing sequences across orders but within the same class. (**G**) Evolutionary distance by time in millions of years (MY) and sequence identities for three example anthozoan GFPs and esmGFP. (**H**) Estimator of evolutionary distance by time (MY) from GFP sequence identity. We estimate that esmGFP is >500 million years of natural evolution removed from the closest known protein.

of larger models to alignment suggests that their internal representation space better approximates those underlying properties, which is evidence of a deep capability for transfer through the features learned in pretraining that improves with scale.

Generating a distant fluorescent protein

We sought to understand whether the base-pretrained ESM3 model has sufficient biological fidelity to generate functional proteins. We set out to create a functional GFP with low sequence similarity to existing ones. We chose the functionality of fluorescence because it is difficult to achieve, easy to measure, and one of the most beautiful mechanisms in nature.

Proteins in the GFP family are responsible for the fluorescence of jellyfish and the vivid colors of coral (*47*), and are unique in their ability to form a fluorescent chromophore without cofactors or substrates (*30*). This property allows the GFP sequence to be inserted into the genomes of other organisms to visibly label molecules, cellular structures, or processes, providing a foundational toolkit that has been broadly applied across the biosciences.

The GFP family has been the subject of decades of protein engineering efforts, but by far most of the known sequence diversity of GFPs has come from prospecting the natural world, because protein engineering efforts have for the most part explored only a few mutations starting from naturally fluorescent sequences. Rational design and mutagenesis have yielded GFP sequences with improved properties, such as higher brightness or stability or differently colored variants, that incorporated small numbers of mutations (typically five to 15 of the total 238 amino acid coding sequence). In a few cases, leveraging high-throughput experimentation and machine learning, scientists have been able to introduce up to 40 to 50 mutations (i.e., 80% sequence identity) while retaining fluorescence (*48*–*50*).

Generating an engineered GFP with considerable sequence distance from natural variants would require materialization of the complex biochemistry and physics that underlie its fluorescence. In all GFPs, an autocatalytic process forms the chromophore from three key amino acids in the core of the protein. The structure of GFP, a kinked central alpha helix surrounded by an 11-stranded beta barrel with inward-facing coordinating residues, enables this reaction (*51*). Once formed, the chromophore must not just absorb light but also emit it to be fluorescent. Light emission is highly sensitive to the local electronic environment of the chromophore. The fitness landscape of GFP reflects the precise configuration of both the active site and the surrounding tertiary interactions required to achieve its function, because a few random mutations are sufficient to reduce fluorescence to zero (*48*, *52*).

In an effort to generate GFP sequences, we directly prompted the base-pretrained 7B parameter ESM3 to generate a 229-residue protein conditioned on the positions Thr^{62}, Thr^{65}, Tyr^{66}, Gly^{67}, Arg^{96}, Glu^{222}, which are critical residues for generating the chromophore (Fig. 4A). We additionally conditioned on the structure of residues 58 through 71 from the experimental structure in 1QY3, which are known to be structurally important for the energetic favorability of chromophore formation (*53*). Specifically, sequence tokens, structure tokens, and atomic coordinates of the backbone are provided at the input, and generation begins from a nearly completely masked array of tokens corresponding to 229 residues, except for the token positions used for conditioning.

We generated designs using a chain-of-thought procedure as follows. The model first generates structure tokens, effectively creating a protein backbone. Backbones that have sufficiently good atomic coordination of the active site but differentiated overall structure from the 1QY3 backbone pass through a filter to the next step of the chain. We added the generated structure to the original prompt to generate a sequence conditioned on the new prompt. We then performed an iterative joint optimization, alternating between optimizing the sequence and the structure. We rejected chains of thought that lose atomic coordination of the active site (supplementary materials, section A.5.1). We drew a computational pool of tens of thousands of candidate GFP designs from the intermediate and final points in the iterative joint optimization stage of the generation protocol. We bucketed the designs by sequence similarity to known fluorescent proteins and filtered and ranked designs using a variety of metrics (supplementary materials, section A.5.1.5).

We performed a first experiment with 88 designs on a 96-well plate, evaluating the top generations in each sequence similarity bucket. Each generated protein was synthesized, expressed in *E. coli*, and measured for fluorescence activity at an excitation wavelength of 485 nm (Fig. 4B, left). We measured brightness similar to positive controls from a number of designs that have higher sequence identity with naturally occurring GFPs. We also identified a design in well B8 (highlighted in a black circle) with only 36% sequence identity to the 1QY3 sequence and 57% sequence identity to the nearest existing fluorescent protein, tagRFP. This design was 50× less bright than natural GFPs, and its chromophore matured over the course of a week, instead of in under a day, but it presents a signal of function in a part of sequence space that to our knowledge has not been found in nature or through protein engineering.

We continued the chain of thought starting from the sequence of the design in well B8 to generate a protein with improved brightness using the same iterative joint optimization and ranking procedure as above. We created a second 96-well plate of designs and, using the same plate reader assay, we found that a few designs in this cohort have a brightness in the range of GFPs found in nature. The best design, located in well C10 of the second plate (Fig. 4B, right), we designated as esmGFP.

We found that esmGFP exhibits brightness in the distribution of natural GFPs. We evaluated the fluorescence intensity at 0, 2, and 7 days of chromophore maturation and plotted these measurements for esmGFP, a replicate of B8, a chromophore knockout of B8, along with three natural GFPs: avGFP, cgreGFP, and ppluGFP (Fig. 4C). esmGFP takes longer to mature than the known GFPs that we measured but achieves a comparable brightness after 2 days. To validate that fluorescence was mediated by the intended Thr^{65} and Tyr^{66}, we showed that B8 and esmGFP variants in which these residues were mutated to glycine lost fluorescence activity (fig. S22).

Analysis of the excitation and emission spectra of esmGFP revealed that its peak excitation occurs at 496 nm, which is shifted 7 nm relative to the 489-nm peak for EGFP, but both proteins emit at a peak of 512 nm (Fig. 4D). The shapes of the spectra indicated a narrower full width at half maximum (FWHM) for the excitation spectrum of esmGFP (39 mm for esmGFP versus 56 nm for EGFP), whereas the FWHMs of their emission spectra were highly comparable (35 and 39 nm, respectively). Overall, esmGFP exhibits spectral properties consistent with known GFPs.

We next sought to understand how esmGFP compares with known proteins. A BLAST (*54*) search against the nonredundant protein sequences database and an MMseqs (*55*) search of ESM3's training set reported the same top hit, tagRFP, which was also the nearest neighbor to B8, with 58% sequence identity representing 96 mutations throughout the sequence. tagRFP is a designed variant, and the closest wild-type sequence to esmGFP from the natural world is eqFP578, a red fluorescent protein that differs from esmGFP by 107 sequence positions (53% identity). Sequence differences between esmGFP and tagRFP occur throughout the structure (Fig. 4E), with 22 mutations occurring in the protein's interior, which is known to be highly sensitive to mutations due to chromophore proximity and a high density of interactions (*56*).

Examination of a sequence alignment of 648 natural and designed GFP-like fluorescent proteins revealed that esmGFP has the level of similarity to all other FPs that is typically found when comparing sequences across taxonomic orders but within the same taxonomic class (Fig. 4F). For example, the difference between esmGFP and other FPs is similar to the

level of difference between FPs belonging to the orders of Scleractinia (stony corals) and Actiniaria (sea anemones), both of which belong to the larger class Anthozoa of marine invertebrates (Fig. 4G). The closest FPs to esmGFP come from the Anthozoa class (corals and anemones; average sequence identity 51.4%), but esmGFP also shares some sequence identity with FPs from the Hydrozoa (jellyfish), in which avGFP was discovered (average sequence identity 33.4%; fig. S23).

We can draw insight from evolutionary biology on the amount of time that it would take for a protein with similar sequence identity to arise through natural evolution. In Fig. 4G, we show esmGFP alongside three anthozoan GFPs. We used a time-calibrated phylogenetic analysis of the anthozoans (*57*) that estimated the millions of years ago (MYA) to last common ancestors to estimate evolutionary time between each pair of these species. Using a larger dataset of six anthozoan GFPs and species for which we have accurate MYA to last common ancestors and GFP sequence identities, we constructed a simple estimator that correlates sequence identity between FPs to MY of evolutionary time between the species (Fig. 4H) to calibrate against natural evolution. On the basis of this analysis, we estimate that esmGFP represents an equivalent of >500 million years of evolution from the closest protein that has been found in nature.

Discussion

We have found that language models can reach a design space of proteins that is distant from the space explored by natural evolution and can generate functional proteins that would take evolution hundreds of millions of years to discover. Protein language models do not explicitly work within the physical constraints of evolution, but instead can implicitly construct a model of the multitude of potential paths that evolution could have followed.

Proteins can be seen as existing within an organized space where each protein is neighbored by every other protein that is one mutational event away (*58*). The structure of evolution appears as a network within this space, connecting all proteins by the paths that evolution can take between them. The paths that evolution can follow are the ones by which each protein transforms into the next without the collective loss of function of the system of which it is a part.

It is in this space that a language model sees proteins. It sees the data of proteins as filling this space, densely in some regions and sparsely in others, revealing the parts that are accessible to evolution. Because the next token is generated by evolution, it follows that to solve the training task of predicting the next token, a language model must predict how evolution can move through the space of possible proteins.

Simulations are computational representations of reality. In that sense, a language model that can predict possible outcomes of evolution can be said to be a simulator of it. ESM3 is an emergent simulator that has learned from solving a token prediction task on data generated by evolution. It has been theorized that neural networks discover the underlying structure of the data that they are trained to predict (*59*, *60*). In this way, solving the token prediction task would require the model to learn the deep structure that determines which steps evolution can take, i.e., the fundamental biology of proteins.

In ESM3's generation of a fluorescent protein, it is the first chain of thought to B8 that is the most intriguing. At 96 mutations to B8's closest neighbor, there are $\binom{229}{96} \times 19^{96}$ possible proteins, of which only a vanishingly small fraction can have function because fluorescence falls off sharply even after just a few random mutations. The existence of C10 and other bright designs in the neighborhood of B8 confirms that in the first chain of thought to B8, ESM3 found a part of the space of proteins that, although unexplored by nature, is dense with fluorescent proteins.

REFERENCES AND NOTES

1. UniProt Consortium, *Nucleic Acids Res.* **43**, D204–D212 (2015).
2. I. V. Grigoriev *et al*., *Nucleic Acids Res.* **40**, D26–D32 (2012).
3. A. L. Mitchell *et al*., *Nucleic Acids Res.* **48**, D570–D578 (2020).
4. M. Varadi *et al*., *Nucleic Acids Res.* **52**, D368–D375 (2024).
5. Z. Lin *et al*., *Science* **379**, 1123–1130 (2023).
6. E. C. Alley, G. Khimulya, S. Biswas, M. AlQuraishi, G. M. Church, *Nat. Methods* **16**, 1315–1322 (2019).
7. M. Heinzinger *et al*., *BMC Bioinformatics* **20**, 723 (2019).
8. A. Rives *et al*., *Proc. Natl. Acad. Sci. U.S.A.* **118**, e2016239118 (2021).
9. A. Madani *et al*., *Nat. Biotechnol.* **41**, 1099–1106 (2023).
10. N. Ferruz, S. Schmidt, B. Höcker, *Nat. Commun.* **13**, 4348 (2022).
11. R. Verkuil *et al*., Language models generalize beyond natural proteins. bioRxiv 521521 [Preprint] (2022); https://doi.org/10.1101/2022.12.21.521521.
12. A. Elnaggar *et al*., *IEEE Trans. Pattern Anal. Mach. Intell.* **14**, 7112–7127 (2022).
13. D. Hesslow, N. Zanichelli, P. Notin, I. Poli, D. Marks, RITA: A study on scaling up generative protein sequence models. arXiv: 2205.05789 [q-bio.QM] (2022).
14. E. Nijkamp, J. A. Ruffolo, E. N. Weinstein, N. Naik, A. Madani, *Cell Syst.* **14**, 968–978.e3 (2023).
15. S. Alamdari *et al*., Protein generation with evolutionary diffusion: sequence is all you need. bioRxiv 556673 [Preprint] (2023); https://doi.org/10.1101/2023.09.11.556673.
16. M. Heinzinger *et al*., Bilingual language model for protein sequence and structure. bioRxiv 550085 [Preprint] (2024); https://doi.org/10.1101/2023.07.23.550085.
17. J. Su *et al*., SaProt: Protein language modeling with structureaware vocabulary. bioRxiv 560349 [Preprint] (2023); https://doi.org/10.1101/2023.10.01.560349.
18. J. Meier *et al*., Language models enable zero-shot prediction of the effects of mutations on protein function. bioRxiv 450648 [Preprint] (2021); https://doi.org/10.1101/2021.07.09.450648.
19. J. Vig *et al*., BERTology meets biology: Interpreting attention in protein language models. arXiv:2006.15222 [cs.CL] (2020).
20. R. Rao, J. Meier, T. Sercu, S. Ovchinnikov, A. Rives, Transformer protein language models are unsupervised structure learners. bioRxiv 422761 [Preprint] (2021); https://doi.org/10.1101/2020.12.15.422761.
21. B. Chen *et al*., xTrimoPGLM: Unified 100B-scale pre-trained transformer for deciphering the language of protein. bioRxiv 547496 [Preprint] (2023); https://doi.org/10.1101/2023.07.05.547496.
22. J. Kaplan *et al*., Scaling laws for neural language models. arXiv:2001.08361 [cs.LG] (2020).
23. T. B. Brown *et al*., Language models are few-shot learners. arXiv:2005.14165 [cs.CL] (2020).
24. J. Hoffmann *et al*., Training compute-optimal large language models. arXiv:2203.15556 [cs.CL] (2022).
25. J. Abramson *et al*., *Nature* **630**, 493–500 (2024).
26. J. L. Watson *et al*., *Nature* **620**, 1089–1100 (2023).
27. J. B. Ingraham *et al*., *Nature* **623**, 1070–1078 (2023).
28. Y. Lin, M. Lee, Z. Zhang, M. AlQuraishi, Out of many, one: Designing and scaffolding proteins at the scale of the structural universe with Genie 2, May 2024. arXiv:2405.15489 [q-bio.BM] (2024).
29. O. Shimomura, F. H. Johnson, Y. Saiga, *J. Cell. Comp. Physiol.* **59**, 223–239 (1962).
30. R. Y. Tsien, *Annu. Rev. Biochem.* **67**, 509–544 (1998).
31. J. Devlin, M.-W. Chang, K. Lee, K. Toutanova, Bert: Pre-training of deep bidirectional transformers for language understanding. arXiv:1810.04805 [cs.CL] (2018).
32. H. Chang, H. Zhang, L. Jiang, C. Liu, W. T. Freeman, Maskgit: Masked generative image transformer. arXiv:2202.04200 [cs.CV] (2022).
33. B. Uria, I. Murray, H. Larochelle, A deep and tractable density estimator. arXiv:1310.1757 [stat.ML] (2014).
34. J. Austin, D. D. Johnson, J. Ho, D. Tarlow, R. van den Berg. Structured denoising diffusion models in discrete state-spaces. arXiv:2107.03006 [cs.LG] (2023).
35. A. van den Oord, O. Vinyals, K. Kavukcuoglu, Neural discrete representation learning. arXiv:1711.00937 [cs.LG] (2017).
36. B. E. Suzek, Y. Wang, H. Huang, P. B. McGarvey, C. H. Wu; UniProt Consortium, *Bioinformatics* **31**, 926–932 (2015).
37. L. Richardson *et al*., *Nucleic Acids Res.* **51**, D753–D759 (2023).
38. T. H. Olsen, F. Boyles, C. M. Deane, *Protein Sci.* **31**, 141–146 (2022).
39. S. K. Burley *et al*., *Nucleic Acids Res.* **47**, D464–D474 (2019).
40. T. Paysan-Lafosse *et al*., *Nucleic Acids Res.* **51**, D418–D427 (2023).
41. M. van Kempen *et al*., Foldseek: fast and accurate protein structure search. bioRxiv 479398 [Preprint] (2022); https://doi.org/10.1101/2022.02.07.479398.
42. C. Hsu *et al*., Learning inverse folding from millions of predicted structures. bioRxiv 487779 [Preprint] (2022); https://doi.org/10.1101/2022.04.10.487779.
43. D. M. Ziegler *et al*., Fine-tuning language models from human preferences. arXiv:1909.08593 [cs.CL] (2019).
44. L. Ouyang *et al*., Training language models to follow instructions with human feedback. arXiv:2203.02155 [cs.CL] (2022).
45. R. Rafailov *et al*., Direct preference optimization: Your language model is secretly a reward model. arXiv:2305.18290 [cs.LG] (2023).
46. R. Y. Pang *et al*., Iterative reasoning preference optimization. arXiv:2404.19733 [cs.CL] (2024).
47. Y. A. Labas *et al*., *Proc. Natl. Acad. Sci. U.S.A.* **99**, 4256–4261 (2002).
48. L. Gonzalez Somermeyer *et al*., *eLife* **11**, e75842 (2022).
49. S. Biswas *et al*., Toward machine-guided design of proteins. bioRxiv 337154 [Preprint] (2018); https://doi.org/10.1101/337154.
50. S. Biswas, G. Khimulya, E. C. Alley, K. M. Esvelt, G. M. Church, *Nat. Methods* **18**, 389–396 (2021).
51. M. Ormö *et al*., *Science* **273**, 1392–1395 (1996).
52. K. S. Sarkisyan *et al*., *Nature* **533**, 397–401 (2016).
53. D. P. Barondeau, C. D. Putnam, C. J. Kassmann, J. A. Tainer, E. D. Getzoff, *Proc. Natl. Acad. Sci. U.S.A.* **100**, 12111–12116 (2003).
54. C. Camacho *et al*., *BMC Bioinformatics* **10**, 421 (2009).
55. M. Steinegger, J. Söding, *Nat. Biotechnol.* **35**, 1026–1028 (2017).
56. J. Y. Weinstein *et al*., *Nat. Commun.* **14**, 2890 (2023).
57. A. M. Quattrini *et al*., *Nat. Ecol. Evol.* **4**, 1531–1538 (2020).
58. J. M. Smith, *Nature* **225**, 563–564 (1970).
59. U. Kamath, J. Liu, J. Whitaker, in *The Philosophy of Artificial Intelligence*, G. E. Hinton, J. L. McClelland, D. E. Rumelhart, Eds. (Springer, 1986); pp. 203–261.
60. N. Tishby, F. C. Pereira, W. Bialek, The information bottleneck method. arXiv:physics/0004057 [physics.data-an] (1999).
61. EvolutionaryScale, "Esm3 source code," Zenodo (2024); https://doi.org/10.5281/zenodo.

ACKNOWLEDGMENTS

We thank E. Schreiter, K. Svoboda, and S. Turaga for feedback on the properties of esmGFP; I. Holmes for feedback on the evolutionary analysis of esmGFP; M. Iskander, V. Kher, and the Andromeda cluster team for support on compute infrastructure; A. Pawluk for assistance with manuscript preparation; the experts who provided feedback on our approach to responsible development; and the experts who participated in the review of the risks and benefits of releasing ESM3-open. Y.A.K. was an intern with EvolutionaryScale during the course of this study. **Funding:** This research was funded by EvolutionaryScale. **Author contributions:** Data: H.A., Z.L., R.R., A.R., T.S., N.T., R.V.; Pretraining: H.A., S.C., J.D., T.H., Z.L., D.O., R.R., A.R., T.S., I.S., R.V., M.W.; Posttraining: H.A., S.C., A.D., J.G., T.H., D.O., R.R., A.R., M.W.; Evaluation and analysis: R.B., J.D., A.D., T.H., Y.A.K., C.K., Z.L., R.S.M., A.R., N.J.S; Open model and responsible development: J.G., I.S., N.J.S., T.S., R.S.M., Z.L., R.R., A.R., N.T.; API and deployment: J.G., C.M., R.S.M., Z.L., T.S.; GFP computation: S.C., T.H., N.J.S., A.R., R.V.; GFP experimental validation: L.J.B., M.N., P.D.H., Y.A.K., N.J.S., N.T., V.Q.T.; Writing: S.C., T.H., R.R., A.R.; N.J.S.; Supplementary materials: H.A., R.B., L.J.B., S.C., J.D., A.D., T.H., C.K., Z.L., R.S.M., D.O., R.R., A.R., N.J.S., T.S., I.S., N.T., V.Q.T., R.V., M.W.; Overall scientific direction: A.R. **Competing interests:** H.A., R.B., S.C., J.D., A.D., J.G., T.H., C.K., Z.L., R.S.M., C.M., D.O., R.R., A.R., N.J.S., T.S., I.S., N.T., R.V., and M.W. are employees of EvolutionaryScale, PBC. S.C., A.R., and T.S. are officers and members of the board of directors of EvolutionaryScale. P.D.H. is a cofounder of Stylus Medicine, Circle Labs, and Spotlight Therapeutics; serves on the board of directors at Stylus Medicine; is a board observer at EvolutionaryScale, Circle Labs, and Spotlight Therapeutics; is a scientific advisory board member at Arbor Biosciences and Veda Bio; and is an advisor to NFDG, Varda Space, and Vial Health. The remaining authors declare no competing interests. Patents have been filed related to aspects of this work. **Data and materials availability:** Weights and code for ESM3-open are provided for academic research use at https://github.com/evolutionaryscale/esm and are permanently archived at Zenodo (*61*). The ESM3-open model was reviewed by a committee of technical experts who found that the benefits of releasing the model greatly outweighed any potential risks. ESM3 models are available through API with a free access tier for academic research. The sequence of esmGFP (along with the other GFPs generated for this work) is committed to the public domain. Plasmids for esmGFP-C10 and esmGFP-B8 have been deposited with Addgene.

SUPPLEMENTARY MATERIALS

science.org/doi/10.1126/science.ads0018
Materials and Methods
Figs. S1 to S24
Tables S1 to S17
References (*62*–*117*)
MDAR Reproducibility Checklist

Submitted 24 July 2024; accepted 7 January 2025
Published online 16 January 2025
10.1126/science.ads0018

ICE SHEETS

Hidden cascades of seismic ice stream deformation

Andreas Fichtner[1]*, Coen Hofstede[2], Brian L. N. Kennett[3], Anders Svensson[4], Julien Westhoff[4], Fabian Walter[5,6], Jean-Paul Ampuero[7], Eliza Cook[4], Dimitri Zigone[8], Daniela Jansen[2], Olaf Eisen[2,8,9]

Ice streams are major regulators of sea level change. However, standard viscous flow simulations of their evolution have limited predictive power owing to incomplete understanding of involved processes. On the Greenland ice sheet, borehole fiber-optic observations revealed a brittle deformation mode that is incompatible with viscous flow, over length scales similar to the resolution of modern ice sheet models: englacial ice quake cascades that are unobservable at the surface. Nucleating near volcanism-related impurities that promote grain boundary cracking, the ice quake cascades appear as a macroscopic form of crystal-scale wild plasticity. A conservative estimate indicates that seismic cascades are likely to produce strain rates that are comparable in amplitude with those measured geodetically, providing a plausible missing link between current ice sheet models and observations.

Ice streams strongly affect the total mass balance of the Antarctic and Greenlandic ice sheets (*1*–*3*). The need to predict their behavior in a changing climate and the concomitant consequences for human society motivates the development of ice sheet simulations (*4*). The predictive power of such simulations—for example, in terms of projected sea level rise or ice sheet retreat rates—is limited by various aspects of existing numerical models, including numerical discretization and rheology as well as material, hydraulic, and stress-strain conditions at the base (*3*, *5*, *6*). To date, however, knowledge of model boundary conditions and rheology is largely limited by the difficulty to perform in situ measurements of glacial properties and processes. We used distributed acoustic sensing (DAS) (*7*, *8*) to detect a mode of ice deformation that cannot be reconciled with the commonly used nonlinear viscous rheology of Glen's flow law (*9*): cascading englacial thrust faulting, observed near the borehole of the East Greenland Ice Core Project (EastGRIP) on the Northeast Greenland Ice Stream (NEGIS) (Fig. 1, A and B). Accounting for ~12% of its total mass discharge (*1*, *10*), NEGIS is the largest ice stream of the Greenland Ice Sheet and a major contributor to current sea level rise (*2*), which underlines the importance of understanding its rheology and deformation mechanisms. In this context, ice core crystallography at EastGRIP has been studied extensively by use of both in situ observations (*11*) and remote geophysical methods (*12*)—for example, to link variations in crystal orientation to large-scale viscous flow patterns (*13*). Optical line scanning has produced images of structures very similar to geological fault-bend folds on thrust ramps, which is a type of thrust structure (Fig. 1C) (*14*) that has not been observed in ice cores before (*15*). Although they evidence that shortening was accommodated by brittle deformation structures in the past, their current activity and contribution to ice deformation remain elusive.

We lowered a loose-tube fiber-optic cable, containing four single-mode fibers, 1500 m into the EastGRIP borehole, which had reached a depth of 2420 m at that time (Fig. 1B). For 14 hours, on 10 August 2022, we measured longitudinal strain rate along the cable using a Silixa iDAS v2 interrogator with 10 m gauge length. Thanks to an average borehole inclination of ~3°, the cable was frictionally coupled to the borehole wall, providing high-quality recordings of seismic body waves that originated from active-shot experiments (*16*). In addition to these, the DAS cable recorded a large variety of natural englacial seismicity, including small individual events as well as event cascades that lasted for several seconds.

Phenomenology

The borehole DAS recordings from 10 August 2022 contain five clear seismic event sequences, possibly representing the dynamic process behind the brittle deformation patterns observed in the EastGRIP ice core. A visual summary of the sequences is shown in Figs. 2 and 3. This is complemented by a more comprehensive data survey in figs. S1 to S4. To tie borehole depth to age, we used the EastGRIP ice chronology of (*17*). Such conversions are indicated in thousand years before 2000 (ka b2k), which uses the year 2000 CE as origin.

The sequences, with one to more than 100 subevents, have several characteristic properties. Most clearly, all subevents have a radiation pattern that is antisymmetric in the vertical direction, regardless of their amplitude and

[1]Department of Earth and Planetary Sciences, ETH Zurich, Zurich, Switzerland. [2]Alfred-Wegener-Institut Helmholtz-Zentrum für Polar- und Meeresforschung, Bremerhaven, Germany. [3]Research School of Earth Sciences, The Australian National University, Acton, Canberra, Australia. [4]Niels Bohr Institute, University of Copenhagen, Copenhagen, Denmark. [5]Swiss Federal Research Institute WSL, Birmensdorf, Switzerland. [6]Laboratory of Hydraulics, Hydrology and Glaciology VAW, ETH Zurich, Zurich, Switzerland. [7]Université Côte d'Azur, IRD, CNRS, Observatoire de la Côte d'Azur, Geoazur Laboratory, Sophia Antipolis, Valbonne, France. [8]Université de Strasbourg/CNRS, Institut Terre et Environnement de Strasbourg, UMR7063, Strasbourg Cedex, France. [9]Fachbereich Geowissenschaften, Universität Bremen, Bremen, Germany.
***Corresponding author. Email: andreas.fichtner@eaps.ethz.ch**

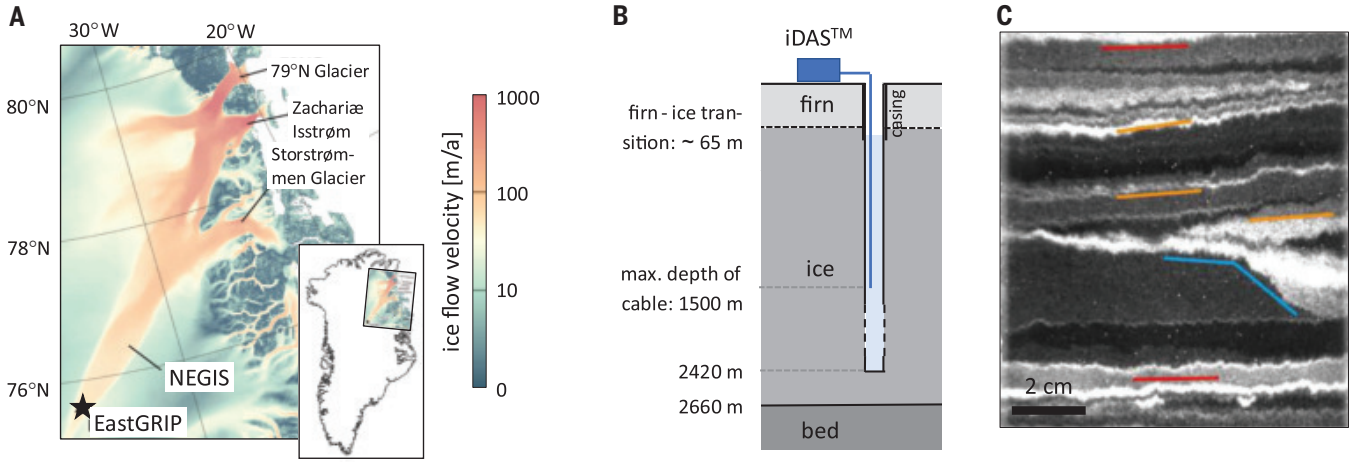

Fig. 1. Experimental setting. (**A**) The Northeast Greenland Ice Stream (NEGIS) and its outlet glaciers shown in the form of surface flow velocities (*41*). (**B**) Schematic, not-to-scale illustration of the experimental setup. The DAS cable (blue line) reached a maximum depth of 1500 m inside the 2420-m-deep borehole within the 2660-m-deep ice (*58*). A Silixa iDAS v2 interrogator was used to perform measurements at a 1 kHz sampling rate and with 1-m channel spacing. (**C**) Optical line scan image of a structure similar to geological thrust faults yet only partly visible because of the narrow diameter of the ice core. The sample is from 1690.65 m depth. Colored lines indicate the ramp (blue), general layering of the section (red), and changed layer tilt inside the structure (orange). [Figure was modified from (*15*).]

location. The subevents generally start with positive strain rates (extension in fiber direction) radiating up and negative strain rates (shortening in fiber direction) radiating down. The character of many of the subevents resembles plane waves, with apparent wave speeds ranging from 2000 to 3000 m/s, which is faster than the *S* wave speed (~1800 m/s) but slower than the *P* wave speed (~3800 m/s) in the ice around EastGRIP (*16*). Thus, they are oblique *S* waves. Within layers of 10 to 20 m thickness, we observed shortening that lasts up to tens of seconds (for example, Fig. 2A, iii) and may be interpreted as creep. These deforming layers seem to temporarily impede the upward propagation of the wave field and in some cases lead to strong downward reflections, with a reflection coefficient of around 0.5 (for example, Fig. 2, A, ii, and B, v).

Despite their complexity, the initial high-amplitude parts of sequences 2 and 5 are notably similar (Fig. 3C). They are composed of an upward-migrating cascade of subevents that originate at identical depths in both sequences. Although each subevent of a cascade radiates a wave field downward, the upward radiation stops after a few tens of meters at a layer where creep occurs for 10 to 50 ms, before the next subevent initiates.

None of the sequences observed in the EastGRIP borehole was detected by the geophone array at the surface, with the closest geophone installed at a distance of 160 m from the borehole (supplementary materials, section S2). This lack of surface observability is consistent with the DAS data, which do not show wave propagation extending beyond the thin creeping layers, and explains the absence of similar observations in the literature. Although weak seismic reflectors have been mapped below EastGRIP (*16*), comparable strong reflections off the creeping layers, such as in subevents 1.ii and 2.v, are not present in active-shot data recorded with DAS in the borehole (supplementary materials, section 3.1) (*16*). This result excludes known changes in fabric orientation (*12*) as the cause for these reflections. The depths of the creeping layers (Fig. 2, asterisk and plus sign) coincide with the depth of two tephra (glass component of volcanic ash) layers that were identified in the EastGRIP ice core: the Mt. Mazama (Crater Lake, USA) tephra dated at 7.6 ka b2k and the Saksunarvatn (Grimsvötn, Iceland) tephra dated at 10.2 ka b2k. (supplementary materials, section S3.2) In a similar context, we observed that many of the subevents in sequences 2 and 5 (Fig. 3C) initiated near depths where sulfate (SO_4) spikes, caused by volcanic eruptions, have been inferred from a projection of GRIP2 SO_4 measurements onto the EastGRIP depth scale (supplementary materials, section S3.3). Numerous subevents—especially in sequences 1, 3, and 4—initiated at 1360 m depth, which is close to the abrupt transition around 14.7 ka b2k from the cold climate of the Oldest Dryas/GS-2 stadial to the milder Bølling-Allerød/GI-1 climatic period. Located at 1375 m depth, this transition is particularly sharp at EastGRIP and manifests itself by increasing ice crystal sizes (*18*) in response to decreasing impurity content (for example, dust particles) by a factor of 10 to 100 (*19*). The end of the Bølling-Allerød/GI-1 at 12.9 ka b2k or 1284 m depth is close to the creeping layer in Fig. 2A, iii, and the occurrence of downward reflections in Fig. 2A, ii. It was preceded by a ~110-year cluster of elevated global volcanic activity that manifested itself in a dense series of SO_4 spikes in Greenland ice cores (*20*, *21*). Abrupt changes in crystallographic fabric orientation are not detectable at any of these depths, neither in ice-core observations nor radar-based inferences (*12*). We therefore excluded changes in fabric as a dominating contributor to the observed nucleation locations.

Source mechanisms and wave field simulations

We can also exclude that the events were cable waves, which are nearly monochromatic oscillations or traveling waves reflecting off the cable end (*22*, *23*), which we did not observe. Furthermore, sequences 2 and 5 seem to have initiated below 1500 m depth, and sequence 1 seems to have propagated beyond 1500 m depth without evidence for upward reflections off the cable end. Correlations of initiation depths with SO_4 content and tephra layers, as well as variable apparent wave speeds, make it even less likely that our observations are cable waves.

Using the approach detailed in the supplementary materials, section S4, we derived general source characteristics of the event sequences that explain key features listed above. The observed antisymmetric radiation pattern in the vertical direction constrains the range of possible fault orientations. In a cylindrical coordinate system—where r denotes distance to borehole axis, z is the depth, and φ is the azimuth—the diagonal moment tensor components M_{rr}, $M_{\varphi\varphi}$, and M_{zz} produce symmetric radiation patterns and therefore can be excluded (supplementary materials, section S4.1). Wave fields excited by moment tensor components $M_{r\varphi}$ and $M_{z\varphi}$ cannot be observed with our experimental geometry. This implies that the sources must have a nonzero M_{rz} component, corresponding to either radially directed slip on a horizontal fault or vertically directed slip

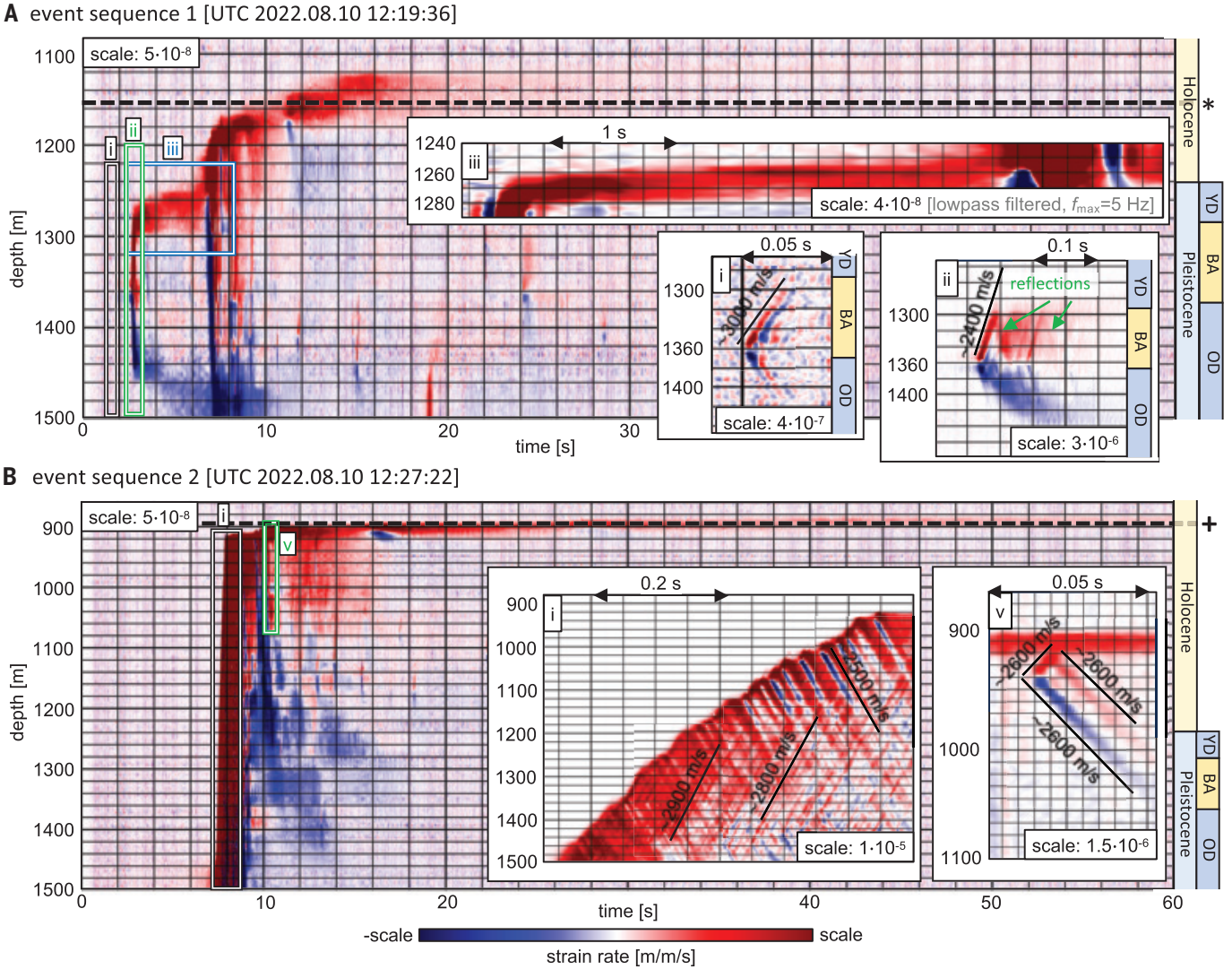

Fig. 2. DAS recordings of seismic events. (**A** and **B**) Sequences (A) 1 and (B) 2 are shown. The asterisk indicates the depth of the Saksunarvatn tephra (Grimsvötn) dated at 10.2 ka b2k, and the plus sign indicates the depth of the Mt. Mazama tephra (Crater Lake) dated at 7.6 ka b2k. (supplementary materials, section S3.1) Here and in Figs. 3 to 5, positive strain rates correspond to extension along the cable, and negative strain rates correspond to shortening. Values for the color scale ranges are provided in the insets. For notational consistency, selected close-ups are labeled in the same way in figs. S1 and S2. (For example, close-ups and subevents ii to iv for sequence 2 that are not shown here are shown in fig. S2.) Abbreviations in the geologic time scales to the right are YD, Younger Dryas/GS-1 stadial; BA, Bølling-Allerød/GI-1 interstadial; and OD, Oldest Dryas/GS-2 stadial (*59*).

on a vertical fault. Furthermore, the source location must be at some distance from the cable because an M_{rz} component source directly at the cable would not be observable. The data require the absence of an isotropic (explosive or implosive) component but are unable to constrain the precise orientation of the slip plane. Because brittle slip is likely to occur along preexisting horizontal layers within the ice sheet, we continued to model the seismic sources as slip on a horizontal plane.

The vertically cascading sequences 2 and 5 hint at a generation mechanism of plane waves with variable apparent wave speeds, as recorded with the DAS system. As explained quantitatively in the supplementary materials, section S4.2.1, and illustrated schematically in Fig. 4A, a linear array of approximately vertically aligned horizontal fault planes that are triggered successively produces plane waves with an apparent wave speed controlled by the triggering speed and the inclination angle. Apparent wave speeds above the *S* wave speed can result from tilting the array toward the DAS cable and/or from *P* wave triggering, which has been previously observed for earthquakes (*24*). Successive excitation of ruptures on horizontal fault planes already allows us to explain less complex parts of the recordings, such as subevent 1.i and sequence 3 (Fig. 4, B and C). In these and all subsequent simulations, sources at distances between 10 and 50 m from the borehole produce synthetic strain rate data that are compatible with the observations.

Large subevents in sequences 1, 2, and 5 caused creep that lasted up to several tens of seconds within thin layers, which produced strong reflections that are not present in the active surface shot data (*16*). The presence of such reflections may be explained by temporary fracturing or unwelding of an internal interface (Fig. 5A). In contrast to welded interfaces (*25*), nonwelded interfaces generate reflections and impede transmission in the absence of a material impedance contrast (*26*, *27*). In the idealized case of a planar interface (supplementary materials, section S4.3), reflection and transmission coefficients can be derived

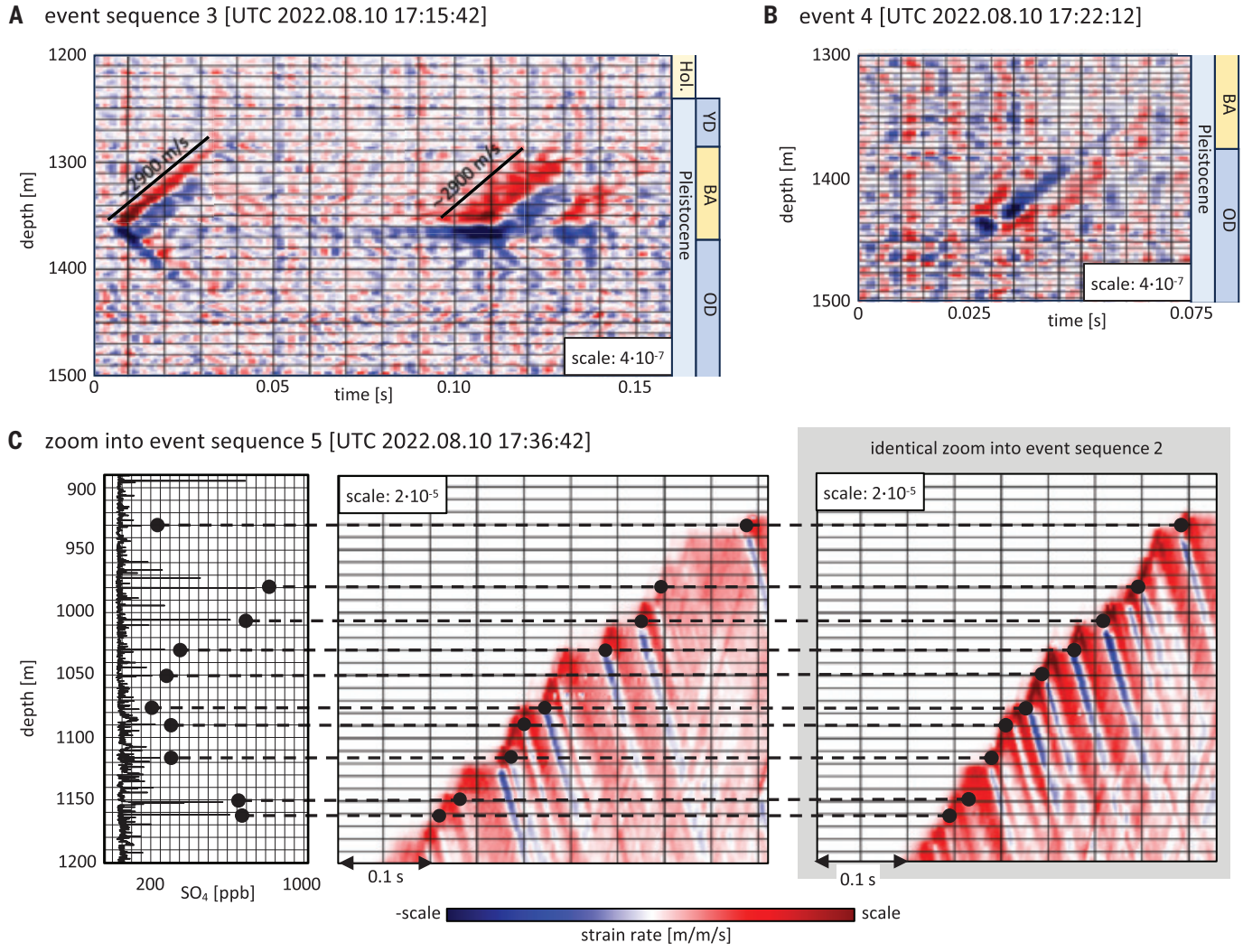

Fig. 3. DAS recordings of seismic events. (**A**) Sequence 3. (**B**) The isolated event 4. (**C**) Part of event sequence 5, which is nearly identical to sequence 2. For comparison of sequences 2 and 5, close-up views of both are shown next to each other. The initiation depths of subevents closely correspond to (left) SO_4 peaks. SO_4 was not measured on the EastGRIP core but was projected onto the EastGRIP depth scale from the GRIP2 dataset (supplementary materials, section S3.2). Abbreviations in the geologic time scales are the same as in Fig. 2.

analytically. The results indicate that a specific compliance of the interfaces on the order of 10^{-9} to 10^{-8} m/Pa can explain observed reflections off the strain accumulation layers and the resulting absence of surface observations of the event sequences. Less idealized distributions of nonwelded interfaces effectively behave as anisotropic layers, with reflection and transmission controlled by geometric properties of the fractures, including their orientation and density (*28*, *29*). A reflector at 1290 m depth allowed us to simulate the more complex event sequence 1.ii, consisting of at least five distinguishable subevents, some of which produce clearly visible reflections (Fig. 5B). Similarly, two subevents from sequence 2.ii are shown in Fig. 5C, simulated with reflectors at 1050 and 1025 m depth. Millimeter- to centimeter-scale fractures in ice have healing times on the order of tens to hundreds of seconds (*30*), which is consistent with our observation that active-shots data obtained several minutes after the natural events do not feature similar strong reflections.

Moment magnitudes (M_w) estimated from DAS recordings of vertical strain ε_{zz} range from $M_w = -2.3$ for the foreshock 1.i to $M_w = -0.24$ for the following main shock sequence 1.ii. They constrain the shear strain ε_{xz} accumulated by a seismic cascade. Only ~10% of actual strain were transferred into the fiber (supplementary materials, section S5), meaning that estimated magnitudes are too low by ~0.67. Magnitude uncertainties are around ±0.5, primarily originating from uncertainties in the distance of the events from the cable and the inability to constrain $M_{r\varphi}$ and $M_{z\varphi}$. The characteristic rupture size L can be deduced from M_w. Assuming that the stress drop $\Delta\sigma$ is 10% of typical ice stream–driving stresses of 100 kPa (*31*), the circular-fault model $L = (7M_0/16\Delta\sigma)^{1/3}$ (*32*) yields rupture sizes on the order of 1 to 10 m for our M_0 estimates between ~3×10^5 and ~2×10^8 Nm. The application of Hooke's law, $\Delta\sigma = \mu D/L$, with shear modulus $\mu \approx 2.8 \times 10^9$ Pa gives rupture displacements D on the order of tens to hundreds of micrometers. Applied to an individual event of sequence 2.i (Fig. 5C), and taking the uncertainty in the moment estimate into account, this analysis yields D between 5×10^{-5} and 2×10^{-4} m per subevent. With $N \approx 50$ subevents spread over a depth range of $Z \approx 600$ m, a cascade such as 2.i accumulates an average shear strain $\varepsilon_{xz} = ND/Z$ on the order of 3×10^{-6} to 2×10^{-5} m/m. A critical component of these estimates is the stress drop, which has a typical uncertainty

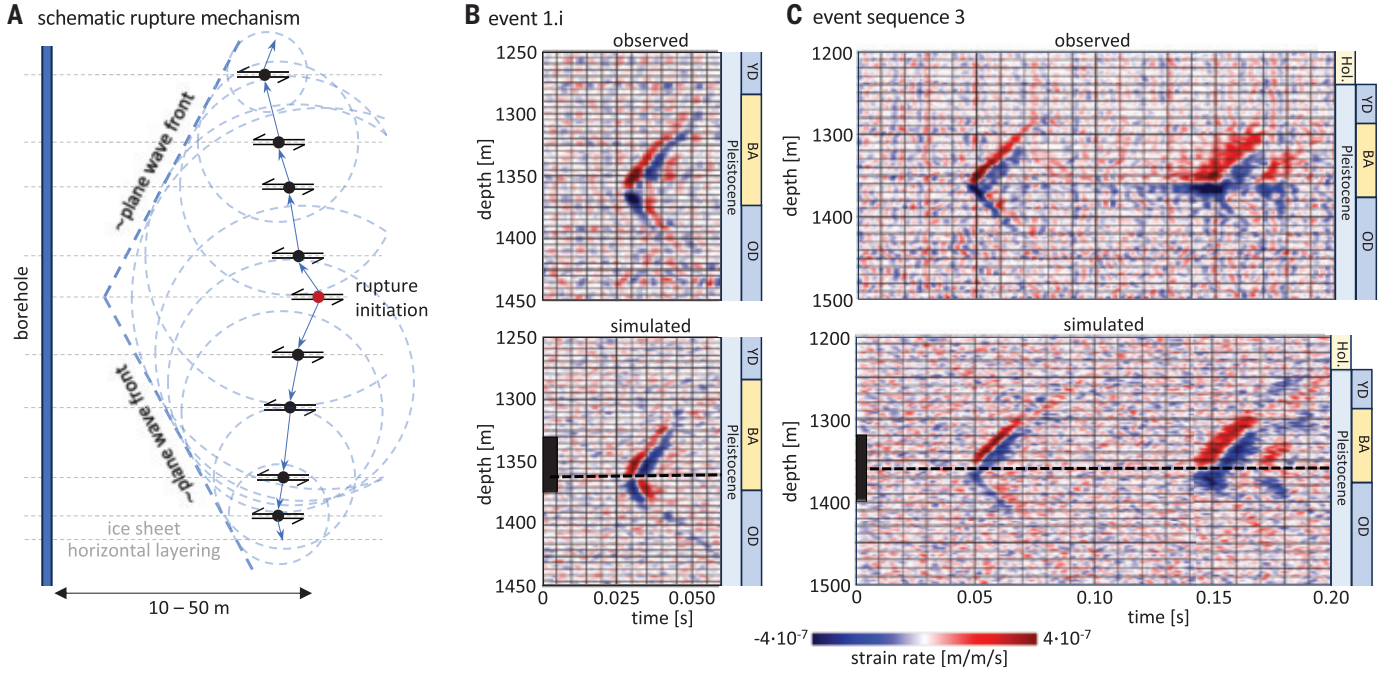

Fig. 4. Comparison of observed and simulated DAS data. (**A**) Cartoon illustration of a vertically oriented array of slip planes. Although their orientation cannot be inferred from the DAS data, they are drawn horizontally for simplicity. The red circle indicates the initiation point, from which subsequent ruptures were triggered in upward and downward directions. The superposition of circular wave fronts from the individual ruptures approximately produces a plane wave. (**B** and **C**) (Top) Observed and (Bottom) simulated DAS recordings of event 1.i and event sequence 3. For a more realistic comparison, we added bandpass-filtered Gaussian noise to the simulations. The black bar in the simulation panels indicates the depth extent of the vertically oriented horizontal slip array, and the black dashed lines indicate the initiation depth. The exact moment density distributions used in the simulations are shown in figs. S14 and S16. For both event 1.i and sequence 3, the source array falls into the Bølling-Allerød/GI-1 depth range, which is characterized by climatically warmer and more viscous ice. Geologic time scale abbreviations are as in Fig. 2.

of a factor of 10 for well-observed earthquakes (*33*). Adopting this uncertainty estimate for our case expands the range of ε_{xz} to 1×10^{-6} to 8×10^{-5} m/m.

Implications for ice stream dynamics

Relevance for ice stream deformation

Cascading englacial ice quakes cannot result from the presence of the borehole (supplementary materials, section S6). However, the characteristics of the events are not typical for glacial microseismicity, which is mostly associated with shear and tensile faulting near the surface and at the bed (*34*). Reported englacial icequakes beneath the surface crevasse zone have tensile source mechanisms (*35*), in contrast to the events observed in this work. Tremor-like shear rupturing was located at the ice bed (*36*). Hence, cascading brittle failure within the ice may be particular to ice streams, where a vertical girdle crystallographic fabric forms to accommodate longitudinal extension (*37*, *38*). The resulting anisotropy causes substantial hardening in the along-flow direction (*13*), which may result in brittle failure when stresses are sufficiently high.

The most conservative estimate of strain induced by the large cascade 2.i, $\varepsilon_{xz} = 10^{-6}$ m/m, implies that around 100 of these event cascades may locally produce deformation that is comparable in amplitude with the 10^{-4} m/m horizontal strain per year inferred from GPS measurements around EastGRIP (*39*). Although the relevance of englacial seismicity for large-scale ice stream deformation depends on its spatiotemporal distribution, our observing two large cascades within only 14 hours suggests that the phenomenon occurs rather frequently.

A similar long-term extrapolation can be made for the creeping deformation within thin layers. The largest-amplitude sequence 1.ii, for example, had average strain rates of ~5×10^{-7} m/m/s that lasted for ~0.1 s. Taking into account that only ~10% of the actual strain was transmitted into the fiber (supplementary materials, section S5), we found that around 100 such events yielded vertical strain rates that are also on the order of 10^{-4} year^{-1}. However, without knowing the exact deformation style, an estimation of the corresponding horizontal strain is not possible.

At this stage, we may only speculate about the spatial distribution of seismic cascades. Radar sounding (*40*) and surface velocity observations (*41*) show that the internal ice structure and kinematics hardly vary over tens of kilometers around EastGRIP. The observed englacial seismicity is therefore unlikely to be a local peculiarity caused by local flow anomalies but instead is likely typical for the regional ice flow pattern. It seems plausible that seismic cascades are a common phenomenon in ice streams, but follow-up investigations are necessary for it to be confidently included in or excluded from ice sheet simulations.

Bridging scales: From laboratory experiments to ice stream dynamics

Englacial seismic cascades near EastGRIP suggest that various properties and phenomena observed in laboratory experiments extrapolate to larger scales. Laboratory tests on mono- and polycrystalline ice show a distinct SO_4-induced reduction in viscosity resulting from increased dislocation density (*42*) and enhanced microcracking along grain boundaries (*43*). Near EastGRIP, these weaknesses promote creep over tens of microseconds, the nucleation of seismic events, and their vertical cascading over more than 600 m. Seismic cascades do not require the presence of pronounced tephra layers, which have not been observed near the large majority of SO_4 peaks. However, when tephra with grain sizes in the tens of micrometers range, compared with the micrometer scale of background dust (*44*), is present it promotes creep over tens of seconds in thin layers and

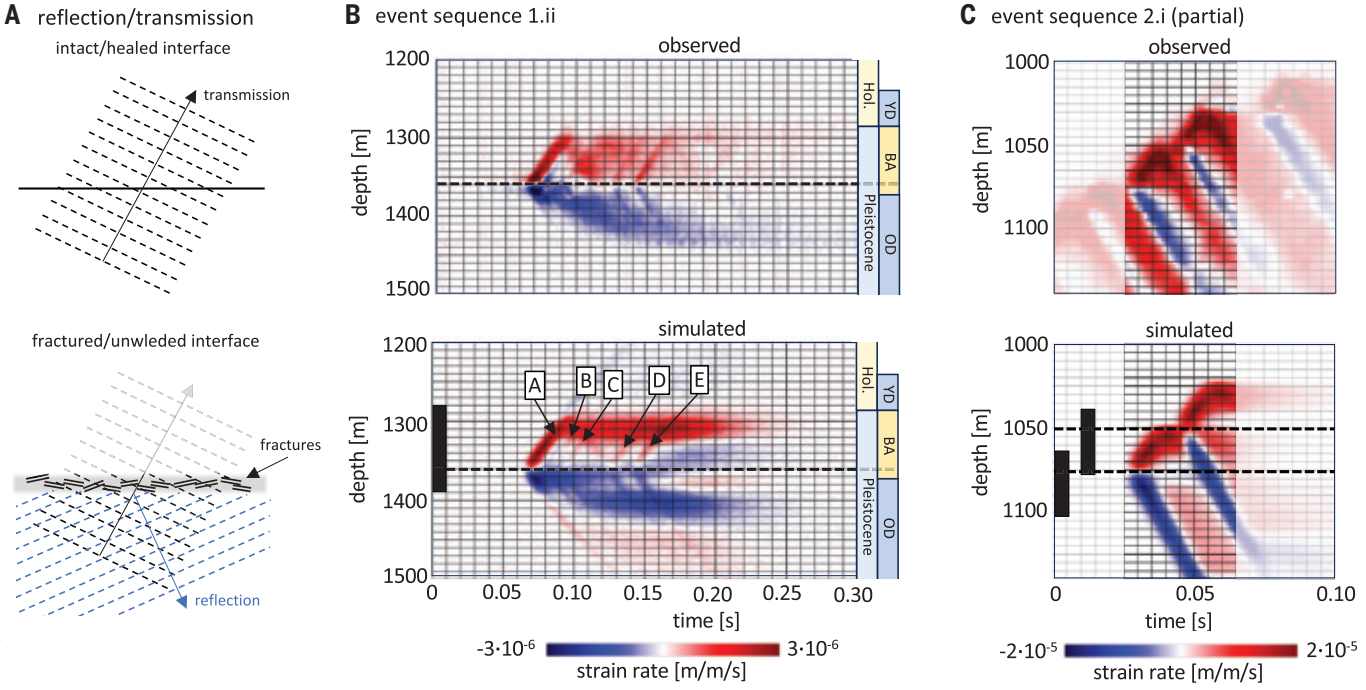

Fig. 5. Comparison of observed and simulated sequences. Shown are sequences 1.ii and 2.i. (**A**) Cartoon illustration of wave transmission and reflection at (top) intact or healed and (bottom) fractured or unwelded interfaces. (**B** and **C**) Similar to Fig. 4, the black bars indicate the depth extent of the vertically oriented horizontal slip array, and the black dashed lines indicate the rupture initiation depths. The exact moment density distributions used in the simulations are shown in figs. S16 and S17. The five subevents used to model sequence 1.ii are labeled "A" to "E." As for events 1.i and 3, the source array of sequence 1.ii falls into the Bølling-Allerød/GI-1 depth range. Geologic time scale abbreviations are as in Fig. 2.

temporary unwelding that impedes the upward propagation of seismic waves. The underlying crystal-scale process may be impurity-induced grain-size reduction that causes the deformation mechanism to switch to grain-boundary sliding, which is known to enhance creep (*45*, *46*). However, direct observations of cracks and deformation-related structures are challenging. Centimeter-scale fractures heal over time scales of minutes (*30*), and ice core samples are too small and too remote from the inferred location of the seismic cascades to provide constraints.

Experiments on single ice crystals have revealed dislocation avalanches that manifest themselves as long-term plasticity (*47*). These avalanches can trigger deformation cascades across grains that are hypothesized to be limited only by the laboratory system size (*48*). Our observations suggest that these microscopic cascades extend to ruptures at the tens of centimeter to meter scale, which then trigger macroscopic seismic cascades across hundreds of meters. When averaged over large enough distances, this deformation style may still produce a smooth stress-strain curve, defining a representative volume element (RVE) for effective viscous deformation. Hence, our observation of seismic cascades propagating over at least 600 m implies that the RVE of ice stream ice is not at the centimeter scale but the kilometer scale.

A plausible missing link: Implications for ice sheet modeling and future research

Our results imply that Glen's flow law for polycrystalline ice (*49*) is not applicable to ice stream modeling at spatial scales close to or smaller than the kilometer-size RVE. This flow law describes secondary creep over time scales longer than the Maxwell time, which itself is orders of magnitude longer than the seismogenic failure of the large-amplitude sequence 1.ii (*34*). Moreover, Glen's flow law is rate strengthening, whereas a rate-weakening rheology is necessary to produce dynamic instability during seismogenic deformation (*50*).

The magnitude of observed englacial seismicity suggests it as a plausible missing link between observed surface velocities in the upstream part of NEGIS and the results of current ice sheet models, which still fail to adequately reproduce the geometry and extent of NEGIS with the commonly used flow-law exponent of $n = 3$ (*51*, *52*).

At scales exceeding the RVE, the observed seismic deformation may be a process that contributes to the macroscopic effect of a larger exponent of around $n = 4$, which was recently proposed for fast-flowing regions of the Greenland and Antarctic ice sheets (*53*–*55*). However, to accurately model narrow ice streams, numerical resolutions as low as a few hundred meters are needed (*56*, *57*), moving the grid spacing below the size of the RVE. Consequently, the impact of cascading seismicity on ice stream deformation should be considered to ensure reliable predictions of ice mass loss and sea level rise. This will require additional and longer borehole DAS experiments to better constrain the spatiotemporal distribution of the phenomenon; investigations on underlying crystal-scale processes; and modeling studies that constrain the interplay between englacial seismicity, rheology, and large-scale flow patterns.

REFERENCES AND NOTES

1. S. A. Khan *et al.*, *Nat. Clim. Chang.* **4**, 292–299 (2014).
2. M. D. King *et al.*, *Commun. Earth Environ.* **1**, 1 (2020).
3. H. Seroussi *et al.*, *Cryosphere* **17**, 5197–5217 (2023).
4. J. A. Church *et al.*, *Climate Change 2013: The Physical Science Basis. Contribution of Working Group I to the Fifth Assessment Report of the Intergovernmental Panel on Climate Change* (Cambridge Univ. Press, 2013).
5. C. Ritz *et al.*, *Nature* **528**, 115–118 (2015).
6. I. Joughin, B. E. Smith, C. G. Schoof, *Geophys. Res. Lett.* **46**, 4764–4771 (2019).
7. A. Hartog, *An Introduction to Distributed Optical Fibre Sensors* (CRC Press, 2017).
8. N. J. Lindsey, E. Martin, *Annu. Rev. Earth Planet. Sci.* **49**, 309–336 (2021).
9. R. Greve, H. Blatter, *Dynamics of Ice Sheets and Glaciers* (Springer, 2009).
10. E. Rignot, J. Mouginot, *Geophys. Res. Lett.* **39**, 2012GL051634 (2012).
11. N. J. Stoll *et al.*, *Cryosphere* **15**, 5717–5737 (2021).
12. O. Zeising *et al.*, *Cryosphere* **17**, 1097–1105 (2023).
13. T. A. Gerber *et al.*, *Nat. Commun.* **14**, 2653 (2023).
14. K. R. McClay, Ed., *Thrust Tectonics* (Chapman & Hall, 1992), pp. 419–433.
15. J. Westhoff, Visual stratigraphy of the EastGRIP ice core. thesis, University of Copenhagen, Niels Bohr Institute (2021).

16. A. Fichtner *et al.*, *Geophys. J. Int.* **235**, 2430–2441 (2023).
17. S. Mojtabavi *et al.*, *Clim. Past* **16**, 2359–2380 (2020).
18. N. J. Stoll *et al.*, *Cryosphere* **17**, 2021–2043 (2023).
19. S. Schüpbach *et al.*, *Nat. Commun.* **9**, 1476 (2018).
20. A. Svensson *et al.*, *Clim. Past* **16**, 1565–1580 (2020).
21. P. M. Abbott *et al.*, *Quat. Sci. Rev.* **274**, 107260 (2021).
22. J. D. Munn, T. I. Coleman, B. L. Parker, M. J. Mondanos, A. Chalari, *J. Appl. Geophys.* **138**, 72–79 (2017).
23. D. Mata Flores, E. D. Mercerat, J. P. Ampuero, D. Rivet, A. Sladen, *Geophys. J. Int.* **234**, 1389–1400 (2023).
24. M. Vallée *et al.*, *Earth Planet. Sci. Lett.* **601**, 117886 (2023).
25. K. Aki, P. Richards, *Quantitative Seismology* (University Science Books, 2002).
26. M. Schoenberg, *J. Acoust. Soc. Am.* **68**, 1516–1521 (1980).
27. E. S. Krebes, *J. Canadian Soc. Expl. Geophys.* **23**, 66 (1987).
28. E. Liu, J. A. Hudson, T. Pointer, *J. Geophys. Res.* **105** (B2), 2981–3000 (2000).
29. S. Jin, A. Stovas, *Geophys. J. Int.* **222**, 260–288 (2020).
30. A. Murdza, E. M. Schulson, C. E. Renshaw, A. Polojärvi, *Geophys. Res. Lett.* **49**, e2022GL099771 (2022).
31. O. V. Sergienko, T. T. Creyts, R. C. A. Hindmarsh, *Geophys. Res. Lett.* **41**, 3925–3932 (2014).
32. H. Kanamoori, D. L. Anderson, *Bull. Seismol. Soc. Am.* **65**, 1073 (1975).
33. R. E. Abercrombie, *Philos. Trans. A Math. Phys. Eng. Sci.* **379**, 20200131 (2021).
34. E. A. Podolskiy, F. Walter, *Rev. Geophys.* **54**, 708–758 (2016).
35. F. Walter *et al.*, *Bull. Seismol. Soc. Am.* **99** (2A), 852–870 (2009).
36. J. Umlauft *et al.*, *Geophys. Res. Lett.* **48**, e2020GL090528 (2021).
37. D. H. Richards, S. S. Pegler, S. Piazolo, N. Stoll, I. Weikusat, *J. Geophys. Res. Solid Earth* **128**, e2023JB027245 (2023).
38. D. A. Lilien, N. M. Rathmann, C. S. Hvidberg, D. Dahl-Jensen, *J. Geophys. Res. Earth Surf.* **126**, e2021JF006306 (2021).
39. C. S. Hvidberg *et al.*, *Cryosphere* **14**, 3487–3502 (2020).
40. S. Franke *et al.*, *Earth Syst. Sci. Data* **14**, 763–779 (2022).
41. I. Joughin, B. E. Smith, I. M. Howat, *J. Glaciol.* **64**, 1–11 (2018).
42. Y. L. Trickett, I. Baker, P. M. S. Pradhan, *J. Glaciol.* **46**, 239–243 (2000).
43. K. Hammonds, I. Baker, *J. Geophys. Res. Earth Surf.* **123**, 535–556 (2018).
44. J. P. Steffensen, *J. Geophys. Res.* **102** (C12), 26755–26763 (1997).
45. D. L. Goldsby, D. L. Kohlstedt, *J. Geophys. Res.* **106** (B6), 11017–11030 (2001).
46. M. D. Behn, D. L. Goldsby, G. Hirth, *Cryosphere* **15**, 4589–4605 (2021).
47. J. Weiss, J. R. Grasso, *J. Phys. Chem. B* **101**, 6113–6117 (1997).
48. J. Weiss, *Philos. Trans. A Math. Phys. Eng. Sci.* **377**, 20180260 (2019).
49. E. M. Schulson, P. Duval, *Creep and Fracture of Ice* (Cambridge Univ. Press, 2009).
50. C. H. Scholz, *Nature* **391**, 37–42 (1998).
51. A. Aschwanden, M. A. Fahnestock, M. Truffer, *Nat. Commun.* **7**, 10524 (2016).
52. M. Rückamp, R. Greve, A. Humbert, *Polar Sci.* **21**, 14–25 (2019).
53. F. Gillet-Chaulet, R. C. A. Hindmarsh, H. F. J. Corr, E. C. King, A. Jenkins, *Geophys. Res. Lett.* **38**, n/a (2011).
54. P. D. Bons *et al.*, *Geophys. Res. Lett.* **45**, 6542–6548 (2018).
55. J. D. Millstein, B. M. Minchew, S. S. Pegler, *Commun. Earth Environ.* **3**, 57 (2022).
56. E. Bueler, *J. Glaciol.* **62**, 230–242 (2016).
57. A. Aschwanden *et al.*, *Sci. Adv.* **5**, eaav9396 (2019).
58. P. Vallelonga *et al.*, *Cryosphere* **8**, 1275–1287 (2014).
59. S. O. Rasmussen *et al.*, *Quat. Sci. Rev.* **106**, 14–28 (2014).
60. A. Fichtner, Hidden cascades of seismic ice stream deformation - raw data. Zenodo (2025); https://doi.org/10.5281/zenodo.14811755.

ACKNOWLEDGMENTS

We gratefully acknowledge the careful and constructive comments of four anonymous reviewers who helped us to sharpen our line of arguments. Our experiment would not have been possible without the immense technical support by S. Børsting, S. Hilmarson, and D. Dahl-Jensen. Invaluable technical support, before and during the experiment, was provided by Silixa (A. Chalari and support team) and Solifos (A. Fasciati). We gratefully acknowledge valuable discussions with R. Alley, D. Dahl-Jensen, T. Dahl-Jensen, S. Fishwick, T. Hudson, B. Lipovsky, R. Pevzner, H. Seroussi, and L. Zoet. O.E. and D.Z. thank M. Bes de Berc for preparing the seismic nodes and managing the associated data. **Funding:** O.E. and D.Z. were supported by the CHIPSM grant of the University of Strasbourg Institute for Advanced Studies and by the French Europe and Foreign Affair ministry and the French Higher Education and Research ministry under the project number 49360YJ–PHC PROCOPE 2023. EastGRIP is directed and organized by the Centre for Ice and Climate at the Niels Bohr Institute, University of Copenhagen. It is supported by funding agencies and institutions in Denmark (A. P. Moller Foundation, University of Copenhagen), the United States (US National Science Foundation, Office of Polar Programs), Germany (Alfred Wegener Institute, Helmholtz Centre for Polar and Marine Research), Japan (National Institute of Polar Research and Arctic Challenge for Sustainability), Norway (University of Bergen and Trond Mohn Foundation), Switzerland (Swiss National Science Foundation), France (French Polar Institute Paul-Emile Victor, Institute for Geosciences and Environmental Research), Canada (University of Manitoba), and China (Chinese Academy of Sciences and Beijing Normal University). **Author contributions:** A.F.: data acquisition, formal data analysis, and interpretation. C.H.: data acquisition and interpretation. B.L.N.K.: formal data analysis. A.S., J.W., J.-P.A., E.C., D.Z., D.J., and O.E.: interpretation of results and linkage to non-seismic data. F.W.: formal data analysis and interpretation. All authors contributed to writing and revision. **Competing interests:** The authors declare no competing interests. **Data and materials availability:** All data presented in this paper, as well as Python code to read and visualize them, is available on Zenodo (*60*).

SUPPLEMENTARY MATERIALS

science.org/doi/10.1126/science.adp8094
Materials and Methods
Supplementary Text
Figs. S1 to S21
References (*61*–*82*)

Submitted 17 April 2024; accepted 21 January 2025
Published online 6 February 2025
10.1126/science.adp8094

METALLURGY

Magnetic modulation of keyhole instability during laser welding and additive manufacturing

Xianqiang Fan[1,2]*, Tristan G. Fleming[3], Samuel J. Clark[4], Kamel Fezzaa[4], Anna C. M. Getley[1,2], Sebastian Marussi[1,2], Hongze Wang[5,6], Chu Lun Alex Leung[1,2]*, Andrew Kao[7]*, Peter D. Lee[1,2]*

Keyhole instability during laser welding and laser powder bed fusion (LPBF) can cause keyhole collapse and pore formation. Using high-speed x-ray imaging, we demonstrate that the flow vortex–induced protrusion on the rear keyhole wall is crucial in initiating keyhole instability. Applying a transverse magnetic field suppresses the keyhole instability by driving a secondary thermoelectric magnetohydrodynamics (TEMHD) flow that alters the net flow vortex. This minimizes protrusions and large-amplitude keyhole oscillations. The suppression effectiveness depends on the laser scanning direction relative to the magnetic field orientation because this controls the Seebeck effect–induced Lorentz force's direction. We show that at LPBF length scales, electromagnetic damping is weak, and for alloys with a large Seebeck coefficient, TEMHD becomes the dominant mechanism controlling flow behind the keyhole.

Additive manufacturing (AM) (*1*–*3*) enables efficient and on-demand production of parts with complex geometries and fine details. Laser powder bed fusion (LPBF) is one of the most popular metal AM techniques, involving repeatedly melting layers of powder into hatched tracks to build complex three-dimensional (3D) objects (*4*). The physics involved in this process is complex, involving melting, vaporization, rapid solidification, multiple reflections of laser rays, fluid flow, and phase transformations (*5*). The intense laser heating of metal causes local surface boiling, which generates a metal vapor jet (*6*, *7*). The recoil pressure pushes the liquid downward to form a vapor depression zone; if the depression zone is narrow and deep, it is referred to as a keyhole. Pore formation resulting from keyhole collapse is strongly correlated with keyhole oscillation—e.g., a periodic keyhole oscillation with a frequency of ~43 kHz often precedes a subsequent chaotic and pore-generating turbulence (*8*). The stochastic formation of large keyhole pores can degrade part qualification and serve as a stress concentrator, potentially acting as fatigue initiation sites during component service.

Optimizing process parameters to minimize keyhole pores can only be achieved by using low-area laser energy densities (*9*), resulting in a narrow and slow–build speed process window. The addition of nanoparticles stabilizes keyholes (*10*), but it adds substantial cost and introduces the risk of altering chemical composition, thereby deviating from the desired material grade. Application of a noncontact external magnetic field mitigates these limitations and promises the potential of modulating

[1]Mechanical Engineering, University College London, London, UK. [2]Research Complex at Harwell, Harwell Campus, Didcot, UK. [3]Department of Physics, Engineering Physics & Astronomy, Queen's University, Kingston, ON, Canada. [4]X-ray Science Division, Argonne National Laboratory, Lemont, IL, USA. [5]State Key Laboratory of Metal Matrix Composites, Shanghai Jiao Tong University, Shanghai, China. [6]School of Materials Science and Engineering, Shanghai Jiao Tong University, Shanghai, China. [7]Computational Science and Engineering Group, Centre for Advanced Simulation and Modelling, University of Greenwich, London, UK.
***Corresponding author. Email: peter.lee@ucl.ac.uk (P.D.L.); xianqiang.fan.19@ucl.ac.uk (X.F.); a.kao@greenwich.ac.uk (A.K.); alex.leung@ucl.ac.uk (C.L.A.L.)**

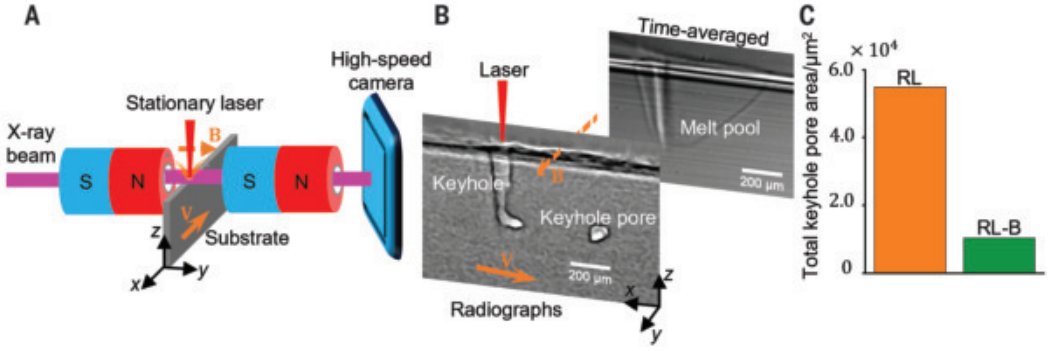

Fig. 1. X-ray imaging system with two ring magnets to provide a static magnetic field at the laser melting site. (**A**) A stationary laser beam is implemented to create a stationary melt pool on the substrate's top surface while it is moving. The x-rays pass through the substrate via the ring magnets and are transformed into visible light using a scintillator, which is then captured by the high-speed camera. (**B**) Captured radiograph and the time-averaged radiograph, which allows us to observe the keyhole and melt pool boundary. (**C**) Comparison of total keyhole pore areas between RL and RL-B scans.

keyhole dynamics through electromagnetic forces (*11*, *12*). Specifically, the Seebeck effect—one of the thermoelectric (TE) effects—has drawn increasing attention across various fields, including lithium transport in nuclear fusion (*13*, *14*), immiscible liquid phase separation (*15*, *16*), and flow disruption during solidification in both conventional casting (*17*, *18*) and directed energy deposition (DED) (*19*). The presence of a high thermal gradient during LPBF is expected to result in substantial thermoelectric currents (TECs) in the melt pool (*20*). An applied external magnetic field can interact with the TECs, inducing a Lorentz force that may enable precision control over keyhole dynamics.

Gaining a better understanding of potential magnetic field control mechanisms related to the Seebeck effect remains challenging. This is primarily because of the lack of direct observation of keyhole dynamics and melt pool flow during laser melting under the influence of a magnetic field. Previous in situ studies (*21*, *22*) have used a laser-based illumination source to light up the keyhole with the imaging speed constrained to a few thousand hertz. In these studies, high-energy lasers were applied to generate a weld pool several hundred times as large as that of a LPBF melt pool.

Magnetic field–enabled mitigation of keyhole porosity

We captured keyhole collapse during laser melting of an AlSi10Mg alloy using high-speed synchrotron x-ray imaging at beamline 32ID of the Advanced Photon Source (APS). The bare substrates (measuring 50 mm by 10 mm by 0.8 to 1.1 mm) used in this work are AlSi10Mg (see materials and methods). Figure 1 shows the x-ray imaging system setup for the magnetic field (Fig. 1A and fig. S1) along with example radiographs acquired (Fig. 1B) with high spatial (2 μm) and temporal (140 kHz) resolutions. When performing zero–magnetic field experiments, the two ring magnets were removed (materials and methods). When the laser scanning direction is from right to left, it is termed as RL and RL-B with a magnetic field applied; for scans from left to right, it is LR and LR-B. The results show a substantial reduction in the total keyhole pore area—by 81%—when a transverse magnetic field of ~0.5 T is applied in the RL-B scan (Fig. 1C and fig. S2).

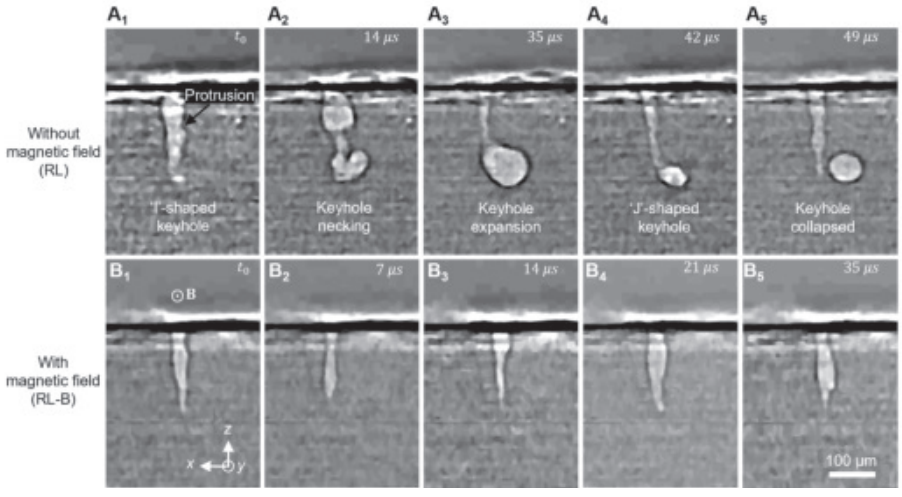

Fig. 2. Comparison of the keyhole morphologies with and without magnetic field. (**A_1** to **A_5**) Keyhole collapse and keyhole pore formation without magnetic field. (**B_1** to **B_5**) Typical keyhole morphological evolution in the presence of a magnetic field (movie S1). Laser power, 225 W; scanning speed, 0.5 m s^{-1}; and laser spot size, 47 μm.

Figure 2 shows a comparison of keyhole dynamics and collapse with and without a magnetic field. During the keyhole collapse process, there are five sequential events and corresponding keyhole morphological changes (Fig. 2, A_1 to A_5). Keyhole porosity is attributed to keyhole collapse caused by keyhole instability (*23*–*25*). Simulations (*26*) have shown that the rear keyhole wall is, on average, lower temperature than the front, hence it has a lower recoil pressure. The weaker recoil pressure makes it more vulnerable to fluctuations and collapse. Therefore, the melt flow behind the rear keyhole wall has a huge impact on keyhole instability (*26*, *27*).

The keyhole collapse process is initiated by the formation of a small protrusion or bulge on the keyhole rear wall (Fig. 2A_1), which reflects the incoming laser beam, heating the keyhole wall unevenly. As a result, the keyhole morphology transforms into an irregular shape (Fig. 2A_2). We hypothesize that the accumulation of recoil pressure in the upper part eventually causes the pressure to breach the narrow section in the middle and extends all the way down to the bottom, triggering a keyhole expansion. This sudden release of recoil pressure in the upper area results in a rapid change in the shape of the upper keyhole section, forming a thin channel, while the keyhole continues to expand in volume at the bottom (Fig. 2A_3). After the keyhole expansion process, a rapid keyhole shrinkage occurs in the bottom section, resulting in the formation of a J-shaped keyhole (Fig. 2A_4) that leads to keyhole collapse (Fig. 2A_5) owing to the combined effect of melt flow toward the rear keyhole wall (*28*) and the Plateau-Rayleigh instability (supplementary text, section 1), which is driven by surface tension (*27*).

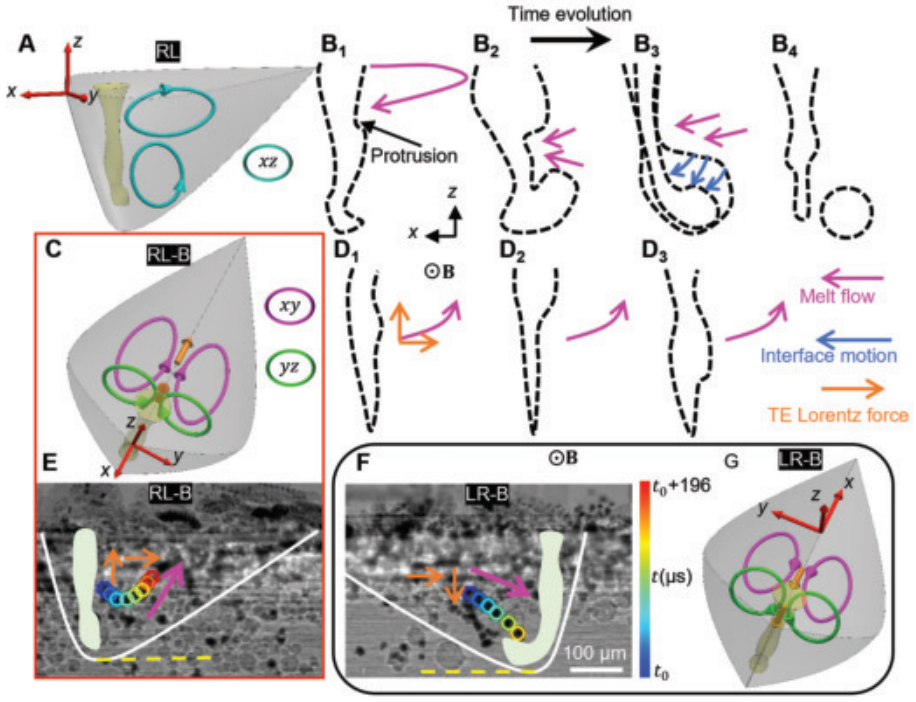

Fig. 3. Melt pool flow with and without magnetic field. (**A**) Schematic of melt pool flow pattern in the absence of a magnetic field (laser beam traversing RL). (**B_1** to **B_4**) The associated keyhole collapse process. (**C**) Melt pool flow in the presence of a magnetic field (RL-B). (**D_1** to **D_3**) Schematic of the backward and upward flows, driven by TE force, that maintain an I-shaped keyhole for (C), the RL-B case. (**E** and **F**) The W particle trajectories in the RL-B and LR-B scans show the flow reversal caused by the TE force reversal when the scan direction is reversed. (**G**) Melt flow pattern when reversing the scanning direction (LR-B case) (movies S2 and S3).

The application of a magnetic field (0.5 ± 0.1 T) perpendicular to the scan direction minimizes keyhole porosity for the RL-B scan, reducing the keyhole pore area by 81%. Throughout the process, the keyhole morphology maintains an I-shaped appearance (Fig. 2, B_1 to B_5, and movie S1), which shows that the magnetic field has made the keyhole more stable. The keyhole behavior and keyhole porosity are independent of the laser scanning direction with zero magnetic field, as shown by the consistent total keyhole pore areas over time. However, this symmetry of the keyhole dynamics with respect to the scanning direction is broken when a magnetic field is applied.

The mechanism of magnetic field–modulated keyhole instability

Figure 3 shows the mechanistic changes to melt flow along with observations that the magnetic field introduces. For the case where a magnetic field is absent, the schematic of the melt pool flow pattern (Fig. 3A) has two flow cells behind the keyhole in the *xz* plane [also reported in (*29*, *30*)] and shows the keyhole collapse process (Fig. 3, B_1 to B_4). The protrusions on the keyhole rear wall, enhanced by the outward Marangoni flow (*27*, *31*, *32*) in the middle of the upper melt pool (Fig. $3B_1$), intensify the keyhole fluctuations by redirecting the laser rays. The region underneath the protrusion receives less energy, whereas an intensified laser heating effect occurs in the upper part (caused by reflected laser light from the bottom). This leads to a local recoil pressure drop in the middle of the keyhole while pressure increases in the upper part. With reduced recoil pressure in the middle section, the surrounding liquid starts filling in the middle part of the keyhole, causing necking (Fig. $3B_2$). Simultaneously, the laser beam undergoes multiple reflections at the bottom of the keyhole, vaporizing the metal. This leads to a rapid expansion of the keyhole root, directed toward the rear of the melt pool, which agrees with previous observations (*24*). Subsequently, the liquid-gas interface of the keyhole contracts at a speed of 5 to 6 m s^{-1} (Fig. $3B_3$), driven by surface tension.

When a magnetic field is applied, the interaction between TECs (fig. S3 and supplementary text, section 2) and the magnetic field gives rise to a TE force, ($\mathbf{J} \times \mathbf{B} = -\mathbf{J}_z\mathbf{B}_y\hat{x} + \mathbf{J}_x\mathbf{B}_y\hat{z}$), where **J** is the thermoelectric current density and **B** is the magnetic field. Scanning in the $-\hat{x}$ direction with a $+\hat{y}$-directed magnetic field (RL-B case) gives rise to a TE force in the $-\hat{x}$ (backward) and $+\hat{z}$ (upward) directions, resulting in a substantial alteration of the flow affecting keyhole dynamics (Fig. 3C). The TE force is directed toward the rear of the melt pool, inducing two new flow cells in the *xy* plane (Fig. 3C, pink circles). As described above, in the zero–magnetic field case, the Marangoni flow destabilizes the keyhole by impinging in the middle to upper region of the keyhole rear (stagnation between the two recirculating flows; Fig. 3A) coupled with the hot fluid reducing surface tension. We hypothesize that for the RL-B case (Fig. 3, C to E), the thermoelectric magnetohydrodynamics (TEMHD) flows created by the TE force counteracts the Marangoni recirculation flow in the bulk, reversing the driving force for protrusion formation and stabilizing the keyhole (Fig. 3C). This is supported by the motion of tracer particles added to the substrate that flow upward and away from the rear of the keyhole (Fig. 3E and movie S2) rather than toward the keyhole (Fig. 3A). TEMHD flows also bring cooler melt from the bottom, which further stabilizes the keyhole through increased surface tension, requiring greater free energy to create the extra surface area in a protrusion. These hypotheses are further supported by the change in the melt pool depth. Convective transport of heat causes the melt pool depth to reduce in the upward-flow RL-B case (Fig. 3E and movie S2), whereas in the LR-B case, the flow is downward, increasing depth (Fig. 3F and movie S3).

Reversing the scanning direction has the same effect as flipping the magnetic field—i.e., the TE force is reversed. Scanning in the LR direction or $-\hat{x}$, the Lorentz force is then aligned with the scanning $-\hat{x}$ (forward) and $+\hat{z}$ (downward) directions. The melt pool dynamics, including melt pool flow and keyhole behavior, show distinct characteristics when operating in the reversed scanning direction (LR-B) (Fig. 3, E and F). The $\hat{x}$ direction Lorentz force is orientated toward the rear keyhole wall, producing two flow cells in the *xy* plane (Fig. 3G, pink circles) with the opposite circulation to the RL-B case (Fig. 3C); these reversed cells assist the formation of protrusions on the keyhole rear wall. Similarly, the vertical cells are reversed (Fig. 3G, green circles). Both these cells bring the hot melt from the top surface down along the keyhole, reducing surface tension and making the keyhole less stable and more prone to form a J shape (Fig. 3F), which is susceptible to collapse and keyhole pore formation. Our observations and theoretical understanding (supplementary text, section 3) are consistent with the results from numerical simulations of AM processes (*33*–*36*) and welding (*37*) that consider the TEMHD.

We tracked 10 tracer particles along the scanning direction (fig. S5) to confirm the melt flow direction. Although the flow is 3D, the TE force is introduced in the *xz* plane; therefore, the flow information obtained from the *xz* projection (i.e., radiographs) represents the component of the flow driven by the TE force. Keyhole wall perturbations could potentially be

caused by Kelvin-Helmholtz instability owing to the presence of a fluid velocity gradient across the keyhole wall. However, on the basis of our observations, we believe that protrusion plays a more important role than the Kelvin-Helmholtz instability in keyhole instability (supplementary text, section 4).

Quantification of keyhole oscillation

The frequency of keyhole fluctuations was analyzed by creating a transient cross section (tCS) image of the radiographs (see fig. S6 for methodology)—i.e., cross sections were taken at three positions along the keyhole depth and are presented as waterfall plots with time (x axis), distance (y axis), and intensity (z axis). From the tCSs, keyhole fluctuation frequency and amplitude information could be obtained (Fig. 4; full-length reconstructed images are in fig. S7).

Cross sections at three heights—⅓, ½, and ⅔ of the average keyhole depth—are given in Fig. 4A. Figure 4B is the reconstructed tCS (detailed in the data analysis section in the supplementary materials), where the bright vertical zone represents the keyhole width. The upper edge of this bright zone corresponds to the rear keyhole wall, whereas the lower edge represents the front keyhole wall. Therefore, each bright peak in Fig. 4B indicates a keyhole oscillation event at its maximum amplitude—i.e., the largest distance between the front and back walls. Using a similar method to Huang *et al.* (*24*), we calculated the average peak-to-peak frequency. Two prominent trends emerge from our analysis of keyhole oscillation. First, near the keyhole aperture (at the ⅓ position), the keyhole has an oscillation frequency of 0.7 kHz and lower amplitudes compared with the region closer to the keyhole bottom (at the ⅔ position), where both the frequency (2.3 kHz) and amplitude are notably higher (Fig. 4, C to E). Our observations suggest that the oscillation near the keyhole bottom contributes most to overall keyhole instability and hence porosity. Second, it was observed that the rear wall of the keyhole experiences more pronounced oscillation than the front wall (as indicated by a greater number of peaks in the reconstructed image on the rear wall side; Fig. 4B). This highlights that the keyhole rear wall plays a large role in determining the overall keyhole instability. This observation contrasts with previous studies (*9*, *38*), which stressed the role of protrusions on the keyhole front wall in leading to keyhole collapse for Ti6Al4V. Because of the substantial difference in material properties, such as thermal conductivity (90 to 160 W m^{-1} K^{-1} for AlSi10Mg versus 16 to 32 W m^{-1} K^{-1} for Ti6Al4V) and viscosity (0.001 Pa s for AlSi10Mg versus 0.005 Pa s for Ti6Al4V) (*34*, *39*), the Al alloy might have a different keyhole collapse mechanism. Therefore, we focused our analysis on how rear wall oscillation near the bottom (at the ⅔ position) affects keyhole pore formation.

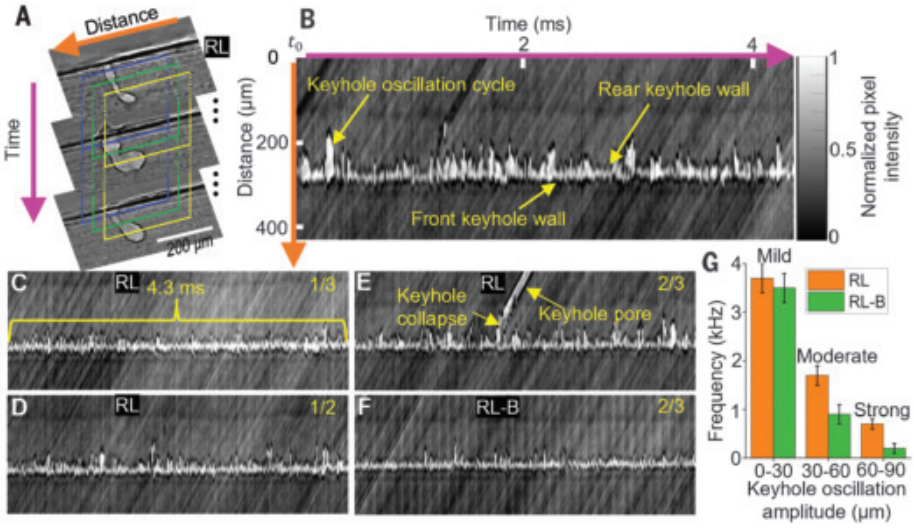

Fig. 4. Quantification of keyhole oscillation. (**A**) An image stack capturing keyhole dynamics; blue, green, and yellow cross sections are located at the height of ⅓, ½, and ⅔ of average keyhole depth, respectively. (**B**) The tCS created by time-slicing the image stack (A); each peak represents a cyclic keyhole oscillation event. (**C** to **E**) The tCS at locations of ⅓, ½, and ⅔ of the average keyhole depth, as depicted in (A). (**F**) The magnetic counterpart of (E) shows a reconstructed image of the RL-B case. (**G**) Comparison of keyhole oscillation frequency versus keyhole oscillation amplitude with and without magnetic field. The slanting lines in the reconstructed images represent features from the moving substrate—e.g., once the keyhole pore is trapped in the solid, it becomes static to the substrate and manifests as a bright slanting strip (moving in both time and along the cross section) in (E).

Under the condition of zero magnetic field at ⅔ depth, the keyhole oscillation exhibits amplitudes ranging from 0 to 90 μm (0 amplitude is defined as the average keyhole width at that position). We classified the oscillation into three intervals to categorize the extent of the amplitude: mild (0 to 30 μm), moderate (30 to 60 μm), and strong (60 to 90 μm). The overall keyhole oscillation frequency is 6.1 kHz, which is in agreement with measurements of ~2.5 to ~10 kHz from prior studies (*24*, *40*, *41*). The oscillation frequency is much lower than that in the Ti alloy of 16 kHz, which could be attributed to the difference in material properties between Al and Ti alloys (supplementary text, section 5). It decreases with increasing amplitude; specifically, the mild oscillations occur at a rate of 3.7 kHz, the moderate oscillations at 1.7 kHz, and the strong oscillations at 0.7 kHz. A stable keyhole tends to oscillate at a mild level.

The introduction of a magnetic field leads to a substantial reduction in the overall keyhole oscillation frequency (4.6 kHz compared with 6.1 kHz). At the moderate oscillation level, the frequency reduces by almost 47% to 0.9 kHz, and at the strong oscillation level, it drops by 71% to 0.2 kHz (Fig. 4G). However, the impact of the magnetic field on the frequency of mild oscillation is minimal (<6%). We also observed a similar frequency reduction for a laser power of 200 W and scan speed of 0.5 m s^{-1} (fig. S8), where the keyhole collapse rarely occurs. These findings suggest that with the application of a magnetic field, large oscillations are effectively stabilized, whereas in the absence of the magnetic field, protrusions at the rear wall cause frequent large amplitude (strong and moderate) oscillations.

Melt pool dynamics with opposing scanning directions

To better understand the dependence of keyhole dynamics on the laser scanning direction when a magnetic field is applied, we carried out laser melting experiments on a high-silicon Al alloy, AlSi7Mg. We conducted our paired experiments on the same substrate to ensure identical experimental conditions, with the sole variation being the scanning direction.

We found a large contrast in the keyhole behavior and keyhole porosity formed between the RL-B and LR-B scans (Fig. 5 and movie S4). The RL-B scan produced a relatively stable I-shaped keyhole with minimal changes in shape over time (Fig. 5, A_1 to A_4), and only small keyhole pores were produced (Fig. 5C). By contrast, the LR-B scan exhibited a cyclic I-J keyhole transformation accompanied by large-amplitude keyhole oscillations (Fig. 5, B_1 to B_4), which resulted in the formation of large pores (Fig. 5D). The RL-B scan had 83% less porosity compared with the LR-B scan (Fig. 5E), demonstrating the importance of the Seebeck effect for high–silicon content aluminum alloys. The average equivalent pore

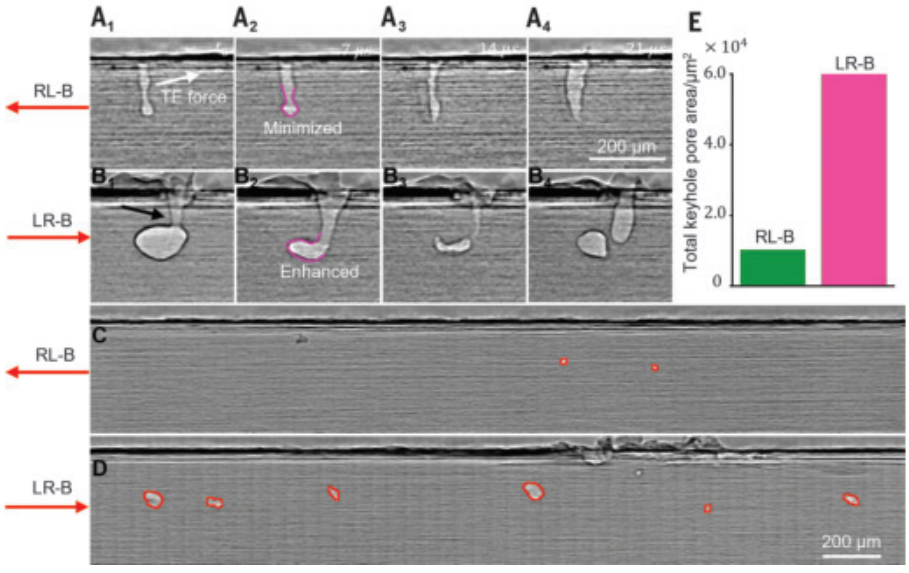

Fig. 5. Keyhole dynamics and pore formation of AlSi7Mg with a reversed laser scanning direction in the presence of a magnetic field. (**A_1** to **A_4**) Typical keyhole morphology evolution with scanning direction from right to left (RL-B). (**B_1** to **B_4**) The scanning direction is left to right (LR-B). (**C** and **D**) Pore distribution along the tracks for the RL-B and LR-B cases, respectively. (**E**) Comparison of total keyhole pore areas for the two opposite scanning directions with a magnetic field applied (movie S4).

diameter increased by 144% going from the RL-B to LR-B scan (9 μm to 22 μm). Likewise, the average keyhole width increased by 31% from 32 μm in the RL-B scan to 42 μm in the LR-B scan owing to the enhanced keyhole oscillation in the LR-B scan. It was observed that under LR-B scan conditions, the application of a magnetic field has the effect of stretching the keyhole—i.e., the keyhole depth increases and strongly fluctuates. A deeper keyhole increases the chance of the keyhole tip contacting the melt pool bottom and being trapped by the advancing solidification front (fig. S9). Additionally, we found that inclination of the front keyhole wall does not seem to change under the conditions of RL-B and LR-B scans. The observed phenomena, such as changes in keyhole width and depth, can be attributed to changes in flow.

Reversing the scanning direction also has an impact on the melt pool depth. In the absence of a magnetic field, we found that the melt pool depth is consistent and independent of the scanning direction (fig. S10). However, when a magnetic field is applied, the melt pool depth becomes contingent on the scanning direction, resulting in a noticeably deeper melt pool during the LR-B scan (fig. S4). This observation agrees with high-fidelity computational findings (*35*), where melt pool depth was predicted to strongly depend on the orientation of the magnetic field relative to scan direction. That is, bidirectional scanning in the presence of a magnetic field led to the formation of an alternating thin and thick layered structure.

The changes in keyhole and melt pool behavior observed with opposite scanning directions can be explained by variations in melt pool flow driven by the TE forces because the TE force is the only force whose direction depends on the scanning direction. In the RL-B scan, the TE force is directed upward and toward the back of the pool (Fig. 5A_1, black arrow), generating flow vortices as depicted in Fig. 3C. Conversely, in the LR-B scan, the TE force is directed downward and toward the front of the pool (Fig. 5B_1, black arrow), reversing the flow vortices (Fig. 3G). This reversal helps propel the hot melt flow downward, deepening the melt pool. Reversing the scan direction (LR-B scan), the TE force–induced flow is directed toward the front of the pool, enhancing protrusion formation and resulting in a more fluctuating, deeper, and wider keyhole, on average.

Discussion

We estimate that the TE and Marangoni forces are around 7 to 18% of surface tension and recoil pressure (supplementary text, section 6). These values are reasonable because if the TE or Marangoni forces were on the scale of surface tension or recoil pressure, then the keyhole would be massively deformed rather than just perturbed. Surface tension also acts against recoil pressure, and so the difference between them determines the perturbation. Marangoni forces assist surface tension, whereas the TE force will either assist recoil pressure or surface tension depending on the sign of the magnetic field. Simply put, for stability the TEMHD should act against Marangoni forces to mitigate the perturbing force.

In this work, the TE force dominates over the traditional electromagnetic damping (EMD) force that acts as a breaking force on fluid motion. This is observed in the breaking of symmetry between scan directions in melt pool and keyhole dynamics. EMD has been attributed to stabilizing keyholes in prior studies under welding conditions (*11*, *12*); however, the contrasting behavior seen in our study using LPBF conditions is due to two key differences: Seebeck coefficient, S (up to two orders of magnitude larger in our work), and length scale, L (one order of magnitude smaller in our work), which also affect the thermal gradient, $|\nabla T| \approx \Delta T/L$. We determine the dominant mechanism by taking relative forces and using dimensionless analysis. That is, the scaling behavior can be approximated by taking ratios of the EMD force to Marangoni force $\left(\frac{|F_{EMD}|}{|F_{Ma}|} = \frac{\sigma|u|\mathbf{B}|^2L^2}{\gamma|\nabla T|}\right)$ and the TE force to Marangoni force $\left(\frac{|F_{TE}|}{|F_{Ma}|} = \frac{\sigma S|\mathbf{B}|L}{\gamma}\right)$. In table S3, we list the material properties, the scale of the melt pool, and the calculated dimensionless numbers for our study and prior welding studies (*11*, *37*, *42*, *43*). Assuming that all other properties are the same [e.g., our work and (*11*)], $\frac{|F_{TE}|}{|F_{Ma}|}$ scales as L^2, and so in our work, EMD will be two orders of magnitude smaller than that in Liu *et al.* (*11*), whereas $\frac{|F_{TE}|}{|F_{Ma}|}$ scales as the product SL, and so the TE force will be one order of magnitude larger. At the length scales of LPBF, this dimensionless analysis shows that changing alloy composition to increase S (e.g., by adding silicon to aluminum alloys) is a viable mechanism without substantially increasing the magnetic field ($|\mathbf{B}| \gg 1$ T into the range of super conducting magnets). A detailed analysis is provided in supplementary text 7.

Existing literature that explores the Seebeck effect (*34*, *36*, *44*, *45*) typically performs experiments or modeling using high-silicon Al alloys. As evidenced in directional solidification (*18*), a higher silicon concentration in aluminum alloys demonstrates a strong Seebeck effect, and hence they hypothesize that Si increases the Seebeck coefficient of the alloy. To test the influence of silicon content on the Seebeck effect, experiments were conducted with an Al6061 alloy, which has a negligible silicon content. The melt pool depth remained unchanged when reversing the scanning direction (195 μm; fig. S11, A and B) when the magnetic field is present. This observation is in direct contrast to the AlSi7Mg alloy, where we observed 230-μm melt pool depth for the left-to-right (LR-B) scan and 210-μm depth for the reversed (RL-B) scan (fig. S11, C and D). This indicates that the Seebeck effect in Al6061 alloy is substantially reduced compared with AlSi7Mg.

Conclusions

By performing high-speed synchrotron x-ray imaging in the frame of reference of the laser beam, we demonstrated that the protrusion formation on the keyhole rear wall, driven by melt flow, initiates instability, which leads

to keyhole collapse. Through the application of a 0.5 ± 0.1–T magnetic field during the laser melting of high-silicon aluminum alloys (e.g., AlSi10Mg), with a right-to-left scan (RL-B), we achieved an 81% reduction in keyhole porosity. This reduction stemmed from the magnetic field altering melt flow owing to the Seebeck effect, thereby suppressing the formation of protrusions on the keyhole rear wall, which predominantly causes the large-amplitude keyhole oscillation. We revealed that the direction of the Seebeck effect–induced Lorentz force is dependent on the laser scanning direction relative to the magnetic field orientation; hence, the protrusion suppression is only effective in the RL-B scan conditions—the keyhole foot is minimized in the RL-B scan but enhanced in the LR-B scan. Our dimensionless analysis shows that stabilizing keyhole oscillations with EMD is not feasible in LPBF under low–magnetic field conditions (<1 T), but increasing Seebeck power (e.g., by increasing silicon content) activates TE forces, creating a viable stabilization mechanism. This work resolves long-standing conflicting theories on the effect of static magnetic fields on weld pool dynamics, showing that in LPBF, with scales much smaller than those in welding, TE forces primarily govern melt pool flow, stabilizing the keyhole and preventing porosity. We encapsulate our observations using dimensionless ratios of forces to guide the application of magnetic control over a range of AM and welding processes, including variations of processing parameters and materials where the Seebeck effect is expected to be large, such as functionally graded materials, bimetallic materials, composites, dual-phase materials, and other materials.

REFERENCES AND NOTES

1. D. Gu *et al*., *Science* **372**, eabg1487 (2021).
2. C. Panwisawas, Y. T. Tang, R. C. Reed, *Nat. Commun.* **11**, 2327 (2020).
3. J. Zhang *et al*., *Science* **383**, 639–645 (2024).
4. T. DebRoy *et al*., *Prog. Mater. Sci.* **92**, 112–224 (2018).
5. C. Zhao *et al*., *Rev. Mod. Phys.* **94**, 045002 (2022).
6. I. Bitharas *et al*., *Nat. Commun.* **13**, 2959 (2022).
7. J. Liu, P. Wen, *Mater. Des.* **215**, 110505 (2022).
8. S. A. Khairallah, T. Sun, B. J. Simonds, *Addit. Manuf. Lett.* **1**, 100002 (2021).
9. C. Zhao *et al*., *Science* **370**, 1080–1086 (2020).
10. M. Qu *et al*., *Nat. Commun.* **13**, 1079 (2022).
11. F. Liu *et al*., *J. Mater. Process. Technol.* **304**, 117569 (2022).
12. X. Meng, M. Bachmann, A. Artinov, M. Rethmeier, *J. Mater. Process. Technol.* **307**, 117636 (2022).
13. G. G. van Eden, V. Kvon, M. C. M. van de Sanden, T. W. Morgan, *Nat. Commun.* **8**, 192 (2017).
14. M. A. Jaworski *et al*., *Phys. Rev. Lett.* **104**, 094503 (2010).
15. Y. Zhong *et al*., *Mater. Des.* **100**, 168–174 (2016).
16. M. Li, T. Tamura, *Philos. Mag.* **99**, 2221–2235 (2019).
17. X. Fan *et al*., *Acta Mater.* **256**, 119107 (2023).
18. B. Cai *et al*., *Acta Mater.* **196**, 200–209 (2020).
19. X. Fan *et al*., *Addit. Manuf.* **71**, 103587 (2023).
20. S. M. H. Hojjatzadeh *et al*., *Nat. Commun.* **10**, 3088 (2019).
21. M. Li, J. Xu, Y. Huang, Y. Rong, *J. Miner. Met. Mater. Soc.* **70**, 1261–1266 (2018).
22. Ö. Üstündağ, N. Bakir, A. Gumenyuk, M. Rethmeier, *Opt. Laser Technol.* **135**, 106715 (2021).
23. Z. Gan *et al*., *Nat. Commun.* **12**, 2379 (2021).
24. Y. Huang *et al*., *Nat. Commun.* **13**, 1170 (2022).
25. Z. Ren *et al*., *Science* **379**, 89–94 (2023).
26. L. Wang, Y. Zhang, H. Y. Chia, W. Yan, *NPJ Comput. Mater.* **8**, 22 (2022).
27. R. Lin, H. Wang, F. Lu, J. Solomon, B. E. Carlson, *Int. J. Heat Mass Transf.* **108**, 244–256 (2017).
28. T. Yu, J. Zhao, *Addit. Manuf.* **72**, 103642 (2023).
29. N. Kouraytem *et al*., *Phys. Rev. Appl.* **11**, 064054 (2019).
30. Q. Guo *et al*., *Int. J. Mach. Tools Manuf.* **175**, 103861 (2022).
31. Q. Guo *et al*., *Addit. Manuf.* **31**, 100939 (2020).
32. L. Aucott *et al*., *Nat. Commun.* **9**, 5414 (2018).
33. A. Kao, T. Gan, C. Tonry, I. Krastins, K. Pericleous, *IOP Conf. Ser. Mater. Sci. Eng.* **861**, 012009 (2020).
34. A. Kao, T. Gan, C. Tonry, I. Krastins, K. Pericleous, *Phil. Trans. R. Soc. A* **378**, 20190249 (2020).
35. A. Kao *et al*., *IOP Conf. Ser. Mater. Sci. Eng.* **1281**, 012022 (2023).
36. L. Wang, W. Yan, *Phys. Rev. Appl.* **15**, 064051 (2021).
37. M. Kern, P. Berger, H. Hügel, *Weld. J.* **79**, 72–78 (2000).
38. C. Zhao *et al*., *Phys. Rev. X* **9**, 021052 (2019).
39. L. Wang, Y. Zhang, W. Yan, *Phys. Rev. Appl.* **14**, 064039 (2020).
40. D. Farson, K. Hillsley, J. Sames, R. Young, *J. Laser Appl.* **8**, 33–42 (1996).
41. S. Ao, Z. Luo, M. Feng, F. Yan, *Int. J. Adv. Manuf. Technol.* **81**, 277–287 (2015).
42. G. Ambrosy, P. Berger, H. Huegel, D. Lindenau, *First International Symposium on High-Power Laser Macroprocessing*, I. Miyamoto, K. F. Kobayashi, K. Sugioka, R. Poprawe, H. Helvajian, Eds (International Society for Optics and Photonics, 2003), pp. 175–179.
43. L. Cao, Q. Zhou, H. Liu, J. Li, S. Wang, *Int. J. Heat Mass Transf.* **162**, 120390 (2020).
44. D. Du *et al*., *Mater. Des.* **181**, 107923 (2019).
45. D. Du *et al*., *Int. J. Mach. Tools Manuf.* **183**, 103965 (2022).

ACKNOWLEDGMENTS

All authors are grateful for the use of the facilities provided at APS and thank APS for providing the beamtime (GUP-73825) and the staff in beamline ID32 for their technical assistance. This research used resources of the APS, a US Department of Energy (DOE) Office of Science user facility operated for the DOE Office of Science by Argonne National Laboratory under contract no. DE-AC02-06CH11357. **Funding:** This study was supported by UK-EPSRC grants (EP/W031167/1, EP/W032147/1, EP/W006774/1, EP/P006566/1, EP/W003333/1, EP/N509577/1, and EP/V061798/1); MAPP: EPSRC Future Manufacturing Hub in Manufacture using Advanced Powder Processes (EP/P006566/1); the Royal Academy of Engineering Chair in Emerging Technologies (CiET1819/10); IPG Photonics/Royal Academy of Engineering Senior Research Fellowship in SEARCH (ref. RCSRF2324-18-71); the National Key Research and Development Program of China (no. 2024YFE0105700); and the National Natural Science Foundation of China (52075327). **Author contributions:** Conceptualization: P.D.L., X.F., A.K.; Funding acquisition: P.D.L., C.L.A.L., A.K.; Investigation: T.G.F., S.J.C., K.F., A.C.M.G., X.F.; Methodology: S.J.C., K.F., T.G.F., X.F., S.M., H.W.; Project administration: P.D.L., A.K.; Supervision: P.D.L., A.K.; Visualization: T.G.F., S.J.C., K.F., A.C.M.G., X.F.; Writing – original draft: X.F.; Writing – review & editing: X.F., T.G.F., S.J.C., K.F., A.C.M.G., S.M., H.W., C.L.A.L., A.K., P.D.L. **Competing interests:** The authors declare that they have no competing interests. **Data and materials availability:** All data are available in the main text or the supplementary materials.

SUPPLEMENTARY MATERIALS

science.org/doi/10.1126/science.ado8554
Materials and Methods
Supplementary Text
Figs. S1 to S11
Tables S1 to S3
References (*46*–*58*)
Movies S1 to S4

Submitted 1 March 2024; accepted 22 January 2025
10.1126/science.ado8554

CATALYSIS

Nickel promotes selective ethylene epoxidation on silver

Anika Jalil[1]†, Elizabeth E. Happel[2]†, Laura Cramer[2]†, Adrian Hunt[3], Adam S. Hoffman[4,5], Iradwikanari Waluyo[3], Matthew M. Montemore[6]*, Phillip Christopher[1]*, E. Charles H. Sykes[2,7]*

Over the last 80 years, chlorine (Cl) has been the primary promoter of the ethylene epoxidation reaction valued at ~40 billion USD per year, providing a ~25% selectivity increase over unpromoted silver (Ag) (~55%). Promoters such as cesium, rhenium, and molybdenum each add a few percent of selectivity enhancements to achieve 90% overall, but their codependence on Cl makes optimizing and understanding their function complex. We took a theory-guided, single-atom alloy approach to identify nickel (Ni) as a dopant in Ag that can facilitate selective oxidation by activating molecular oxygen (O_2) without binding oxygen (O) too strongly. Surface science experiments confirmed the facile adsorption/desorption of O_2 on NiAg, as well as demonstrating that Ni serves to stabilize unselective nucleophilic oxygen. Supported Ag catalyst studies revealed that the addition of Ni in a 1:200 Ni to Ag atomic ratio provides a ~25% selectivity increase without the need for Cl co-flow and acts cooperatively with Cl, resulting in a further 10% initial increase in selectivity.

Ethylene oxide [(EO) C_2H_4O] is a platform chemical in the production of many consumer goods including plastics and antifreeze, with a growing global market currently valued at ~40 billion USD per year (*1*). It is produced from ethylene (C_2H_4) and molecular oxygen (O_2) using Ag/α-alumina (α-Al_2O_3) heterogeneous catalysts. Because of the instability of EO, industrial reactors are operated at only ~10 to 15% per-pass ethylene conversion to minimize combustion of EO into CO_2 and H_2O (*2*).

The low per-pass conversion, low reactant partial pressures (>50% of the feed is inert to

mitigate thermal runaway), and high production volumes all necessitate large-volume recycle streams. These energy-intensive separation processes add to the 10% CO_2 emitted as a by-product of the 90% selective EO production process, so EO has the highest CO_2 emission among high-value chemicals on a per volume basis (*3*). Thus, even small improvements in EO selectivity could lead to large decreases in associated CO_2 emissions and energy costs, making the design of selective EO production catalysts a subject of continued interest (*4*, *5*).

Achieving high EO selectivity requires minimizing both the direct combustion of ethylene and the secondary combustion of EO to CO_2. The relatively high fraction of EO produced over silver (Ag) catalysts has been widely attributed to its oxygen adsorption properties (*6*–*8*). Ag/α-Al_2O_3 catalysts exhibit ~50 to 60% EO selectivity at <10% ethylene conversion, although selectivity decreases with increasing ethylene conversion through EO combustion.

Despite safety issues and environmental impacts in addition to its corrosive nature, chlorine (Cl) is used ubiquitously to promote the selectivity of industrial EO catalysts which consist of large (50 nm to 1 μm diameter) Ag particles supported on low surface area (<1 m^2/g) α-Al_2O_3. Chlorine is co-fed as an alkyl chloride and increases EO selectivity by ~25% at low ethylene conversion compared with pure Ag/α-Al_2O_3, and enables EO selectivity to be retained at higher conversion (*9*), which suggests that Cl promotes EO formation by depressing the rates of both the primary and secondary combustion reactions (*9*–*11*).

Other promoters of industrial EO catalysts include alkali metals such as cesium (Cs) and lithium (Li), and oxyanions of transition metals such as molybdenum (Mo) and rhenium (Re), which each offer modest ~1 to 5% increases in EO selectivity but require the presence of Cl to be effective. Furthermore, promoters can be codependent on one another. For example, Re only increases selectivity in the presence of Cs, which itself requires Cl. These requirements make the system complex, as the addition of parts per million (ppm) levels of alkyl chloride and other promoters (promoter: Ag molar ratios of 10^{-4}-10^{-2}) required for ~90% EO selectivity at 10 to 15% ethylene conversion results in crowded, multicomponent catalytic surfaces (*12*–*16*).

Promoters are thought to influence the amount, accessibility, and reactivity of oxygen species (*9*, *14*, *17*–*22*). The ubiquity of Cl as a promoter in most catalyst formulations has limited research on identification of new promoters that act independently of Cl. A few reports exist of modest (5 to 10%) selectivity increases by using unconventional (not currently used in industrial formulations) promoters, but high EO selectivity at reasonable ethylene conversion remains a challenge without Cl (*23*–*25*).

We report that the addition of parts per million amounts of Ni to supported Ag catalysts substantially enhanced EO selectivity by ~25%, rivaled only by the ubiquitously used Cl promoter. Our theoretical and experimental surface science studies demonstrate that dispersed Ni in Ag(111) simultaneously influenced the quantity and reactivity of adsorbed oxygen species. Catalytic studies revealed that dilute Ni promoters (at 200:1 Ag:Ni ratio) on supported Ag/α-Al_2O_3 catalysts function synergistically with Cl feeds to enable 90% EO selectivity at 2 to 2.5% ethylene conversion, indicating that Ni offers a new avenue for catalyst and process optimization in EO production.

Theory-guided catalyst discovery

We initially searched for promoters for Ag-based EO-producing catalysts using our single-atom alloy (SAA) approach that has identified new selective (de)hydrogenation catalysts, including rhodium (Rh), platinum (Pt), and palladium (Pd) doped copper (Cu) SAAs (*26*–*29*). These catalysts derive their function from the facile dissociation of strong bonds and weak binding of intermediates enabled by the SAA geometry that can decouple transition and final state energies. We applied this concept to selective oxidations using density functional theory (DFT) calculations to identify single-atom dopants in Ag surfaces with a low dissociative oxygen chemisorption activation barrier ($E_{a,diss}$) and weak atomic oxygen binding energy when bound in hollow sites on each side of the dopant site ($E_{ads,2O}$; fig. S2) as shown in Fig. 1A (*6*). Among the screened dopants, Ni stood out as breaking the scaling relationship (fig. S1) between $E_{a,diss}$ and $E_{ads,2O}$, with DFT predicting near-barrierless dissociation of O_2 (<0.05 eV) while maintaining moderate atomic oxygen atom binding (−2.2 eV) (*30*).

Surface adsorption experiments

To test this prediction, we conducted surface-science studies of O_2 activation on 1% Ni-doped Ag(111) single-crystal surfaces. In these experiments, 1% monolayer (ML) of Ni was alloyed into the Ag(111) surface to obtain dispersed Ni in the surface and subsurface (Fig. 1C and S5). The dissociative sticking probability of O_2 on Ag(111) is ~10^{-6} which requires high O_2 pressures

[1]Department of Chemical Engineering, University of California, Santa Barbara, CA, USA. [2]Department of Chemistry, Tufts University, Medford, MA, USA. [3]National Synchrotron Light Source II, Brookhaven National Laboratory, Upton, NY, USA. [4]Stanford Synchrotron Radiation Light Source, SLAC National Accelerator Laboratory, Menlo Park, CA, USA. [5]SUNCAT Center for Interfacial Science and Catalysis, SLAC National Accelerator Laboratory, Menlo Park, CA, USA. [6]Department of Chemical and Biomolecular Engineering, Tulane University, New Orleans, LA, USA. [7]Department of Chemical and Biological Engineering, Tufts University, Medford, MA, USA.
***Corresponding author. Email: mmontemore@tulane.edu (M.M.M.); pchristopher@ucsb.edu (P.C.); charles.sykes@tufts.edu (E.C.H.S.)**
†These authors contributed equally to this work.

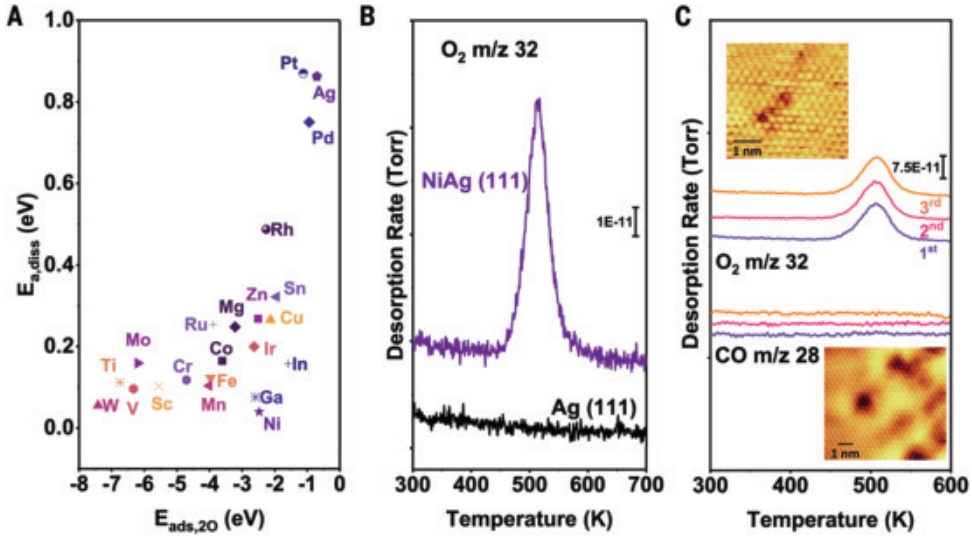

Fig. 1. Theory-guided identification of Ni dopant that enables facile O_2 dissociation and spillover of oxygen to Ag. (**A**) DFT calculations of the O_2 dissociation barrier $E_{a,diss}$ as a function of the adsorption energy of the resulting dissociated O atoms ($E_{ads,2O}$) for various single-atom dopants in Ag(111). (**B**) O_2 TPD traces for Ag(111) and ~1% NiAg(111) after 500 Langmuirs (L) of O_2 dosed at 350 K, cooling to room temperature, and recording the TPD with a 1 K/s heating rate. (**C**) Sequential TPD traces involving a 500 L exposure to O_2 at 350 K and TPD, followed by 0.5 L CO exposure at 90 K and TPD. Insets show 13 K STM images of subsurface Ni in Ag(111) immediately after Ni deposition (lower image, image conditions 0.2 nA, 100 mV) and Ni at the surface of Ag(111) after cooling from 473 K in O_2 (upper image, 0.3 nA, 50 mV).

in the Torr range, or a more reactive oxidant such as NO_2, to saturate the surface with atomic oxygen (*31*, *32*). However, Fig. 1B shows that the addition of 1% monolayer (ML) Ni to Ag(111) enabled uptake of oxygen on Ag at 10^{-6} Torr pressure of O_2.

Specifically, the NiAg(111) sample was exposed to 500 L (1 L = 1×10^{-6} Torr/sec) of O_2 at 350 K. Temperature-programmed desorption (TPD) of adsorbed oxygen demonstrates facile uptake and spillover of the dissociated oxygen atoms to sites on Ag(111). Calibration of the trace in Fig. 1B indicated that 1% ML Ni enabled the uptake of ~4% ML O. Furthermore, O_2 desorbed from NiAg at 520 K. This temperature is ~70 K lower than typically observed from pure Ag (Fig. 1B) and consistent with our DFT prediction (Fig. 1A and table S1) of promoted O_2 uptake and release by Ni dopants (*31*, *33*).

Consecutive CO and O_2 adsorption TPDs demonstrated that the Ni atoms were mobile within the Ag sample. The Ni atoms were in the Ag(111) surface under oxidizing conditions but moved to the subsurface under vacuum conditions (Fig. 1C). Specifically, we used CO as a probe molecule to measure the surface concentration of Ni. Although CO does not bind to Ag(111) above ~50 K, the introduction of Ni to Ag(111) led to observation of a CO desorption peak at ~350 K (fig. S6) (*34*). This CO desorption temperature is ~80 K lower than that observed for Ni(111) and is further evidence of the high dispersion of Ni in Ag(111) (*35*).

After O_2 exposure and subsequent TPD, we exposed the NiAg surface to 0.5 L of CO, but no CO desorption was observed in TPD. This result indicated that Ni moved to the subsurface by the end of the O_2 desorption TPD ramp to 700 K. Subsequent exposure to O_2 brought Ni back to the surface. This preference is expected based on the more oxophilic nature of Ni, and the reversibility of Ni surface segregation over three full cycles is shown in Fig. 1C.

Nanoparticle catalysts for epoxidation

To determine if the surface-science and theoretical studies could be translated to supported catalysts, we synthesized highly dilute NiAg nanoparticle alloys and compared their performance in ethylene epoxidation with pure Ag/α-Al_2O_3 catalysts (Fig. 2). Ag nanoparticles ~70 nm in diameter were synthesized (figs. S4, S7, and S8) with varying Ni content through a colloidal approach. This particle size was chosen because smaller (5 to 50 nm) and larger (>250 nm) diameter Ag particles exhibit lower reaction rates, and smaller Ag particles are prone to rapid sintering (*11*, *36*–*38*). The Ag nanoparticles were post synthetically doped with Ni to ensure a constant Ag particle size distribution (*39*, *40*).

Our TPD results showing Ni mobility and segregation to the surface after O_2 exposure emphasized that under ethylene epoxidation

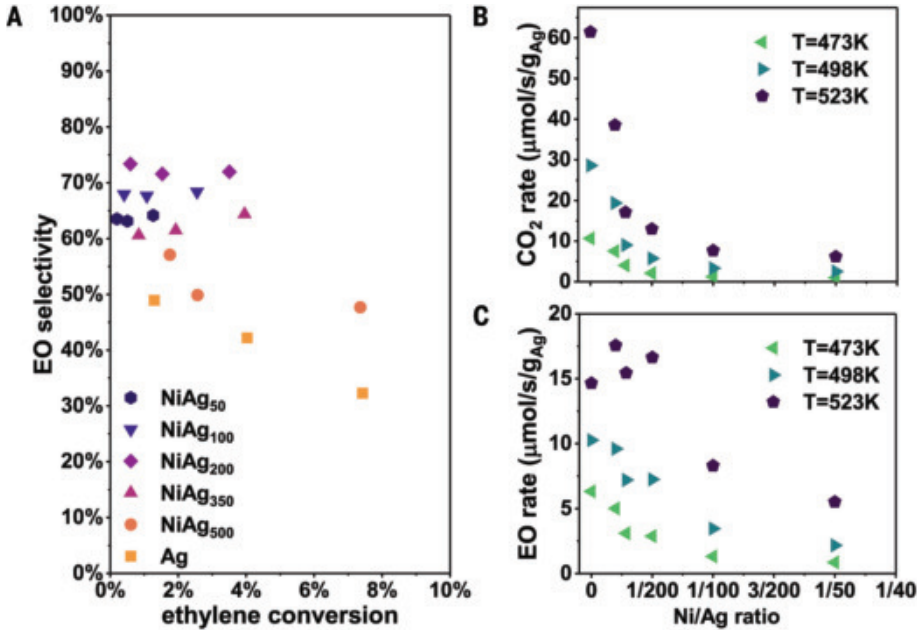

Fig. 2. Ni doping of Ag nanoparticles at a molar ratio of 1:200 Ni:Ag increases EO selectivity by ~25% compared with pure Ag. Influence of Ni loading on 5 wt% Ag/α-Al_2O_3 catalyst reactivity in 10% C_2H_4, 10% O_2, balance He inlet with 100 to 150 mg catalyst. The Ni:Ag molar ratio was varied from 0:100 (pure Ag) to 1:50 (2% Ni). (**A**) EO selectivity as a function of steady-state ethylene conversion. The ethylene conversion was varied by changing the temperature between 473, 498, and 523 K, and holding for 2 hours to allow the system to reach a new steady state. (**B**) CO_2 and (**C**) EO formation rates at different temperatures as a function of Ni:Ag molar ratio.

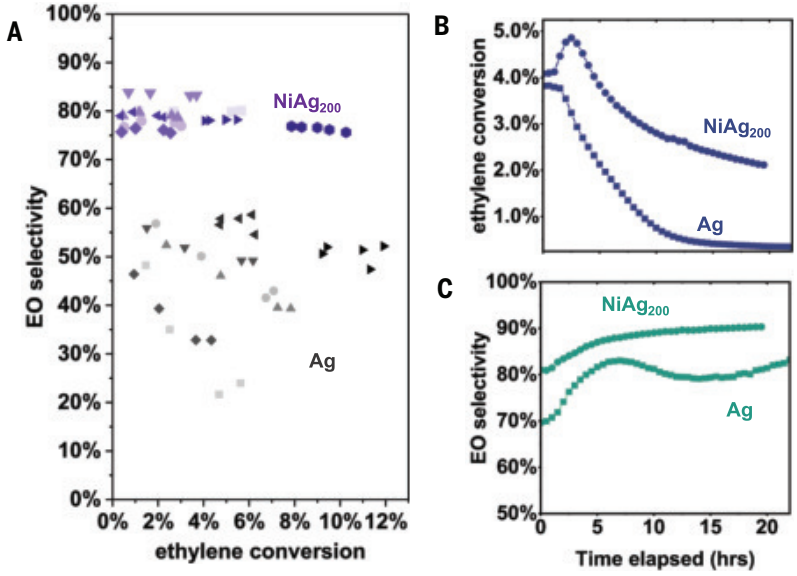

Fig. 3. $NiAg_{200}$ catalysts show a consistent ~25% selectivity enhancement over Ag and additive influence of Cl co-promoter. (**A**) EO selectivity as a function of ethylene conversion for seven batches of ~8 wt% Ag and $NiAg_{200}$ on α-Al_2O_3 at 10% C_2H_4, 10% O_2, balance He. The reactivity of separate batches is shown by using various shades of purple ($NiAg_{200}$) and gray (Ag). See table S5 for details on all samples. (**B** and **C**) Effect of Cl co-flow at 25% C_2H_4, 10% O_2, 0.5% CO_2, and 0.5 ppm EtCl, balance He (total flow rate 40 standard cubic centimeters per minute) at 523 K: (B) $NiAg_{200}$ and Ag ethylene conversion (see fig. S21 for product formation rates over time) and corresponding (C) $NiAg_{200}$ and Ag selectivity.

reaction conditions, the oxophilicity of Ni should provide a thermodynamic driving force for Ni to move to the Ag nanoparticle surface. Further, the reaction temperature (473 to 523 K) is high enough to kinetically enable Ni to segregate to the surface as observed in TPD when Ni diffusion to the surface occurred at 350 K. Therefore, to calculate nominal Ni

surface coverage, we made the simplifying assumption that all the Ni in a nanoparticle resided at the Ag surface when O_2 is present. This allowed us to calculate a range of target Ni:Ag ratios for the synthesis, assuming spherical nanoparticles (fig. S7). We then synthesized catalysts with Ni loadings ranging from 1:500 (0.2 mol%) to 1:50 (2 mol%) which corresponded to 10 and 80% estimated Ni surface coverage, respectively. It should be noted that this is an upper limit as the thermodynamics of Ni partitioning between the bulk and surface is dependent on particle size and environmental conditions.

Catalysts were characterized with a variety of techniques (figs. S8 to S11, S14 to S17, and tables S2 to S4). Inductively coupled plasma (ICP) measurements showed that the desired Ni loadings were achieved (table S4). Ni K-edge high-energy resolution fluorescence detection–X-ray absorption near-edge structure (HERFD-XANES) spectroscopy measurements were collected for an as-prepared 9 weight percent (wt%) $NiAg_{200}/\alpha\text{-}Al_2O_3$ catalyst and for ~5 nm NiO particles on $\alpha\text{-}Al_2O_3$ (figs. S14 to S16) during a temperature programmed reduction (TPR). Linear-combination fitting of the NiO TPR produced negligible residuals, demonstrating that the spectra were fit well using NiO and reduced Ni nanoparticle basis sets (figs. S15 and S16A). The spectrum of the as-prepared $NiAg_{200}$ samples was poorly fit by the same basis set. The different electronic structure and local coordination environment of Ni in $NiAg_{200}$ compared with pure Ni on $\alpha\text{-}Al_2O_3$, evidenced by HERFD-XANES, indicated that the synthetic procedure effectively incorporated Ni in Ag and is different from pure dispersed Ni on $\alpha\text{-}Al_2O_3$.

Steady-state reactivity experiments were performed with a feed of 10% ethylene and 10% molecular oxygen (at 1 bar in 80% inert) at 473, 498, and 523 K. Ni-doped 5 wt% $Ag/\alpha\text{-}Al_2O_3$ ($NiAg_x/\alpha\text{-}Al_2O_3$) catalysts with stoichiometries ranging from $NiAg_{500}$ to $NiAg_{50}$ were all prepared from the same parent batch of Ag colloids (see figs. S18 and S20 and table S5 for details on the reactivity protocols). Steady-state ethylene conversion for $Ag/\alpha\text{-}Al_2O_3$ was varied from 2 to 8% with 100 to 150 mg of catalyst in the reactor by varying the reaction temperature (Fig. 2A).

The EO selectivity for $Ag/\alpha\text{-}Al_2O_3$, calculated as $\frac{N_{EO}}{N_{EO}+0.5N_{CO_2}}$, where N_i is the molar flow rate of each species, decreased from 50 to 30% as conversion increased, consistent with previous reports (table S6) (*36*, *41*–*43*). The addition of just 1:350 Ni:Ag (0.3 atom percent of Ni) to Ag resulted in an increase in EO selectivity by 5 to 10% at all conversions. Increasing the Ni loading further increased EO selectivity and decreased ethylene conversion. $NiAg_{200}$ appeared to be the optimum Ni content for this batch of Ag particles, which exhibited a 25 to 30% increase in selectivity over Ag, comparable to the known behavior of Cl promoters. Figure S12 shows the effect of increasing Ni loading on selectivity at 2% ethylene conversion revealing a maximum selectivity at a 1:200 Ni:Ag molar ratio which improves EO selectivity by ~25% over pure Ag. The selectivity at low conversion (< 2%) can be considered the primary selectivity (at the limit of low EO combustion rate), and at higher ethylene conversions, the rate of secondary EO combustion is relevant. Thus, the results in Fig. 2A demonstrate that 1:200 Ni:Ag (0.5% Ni) mitigated both primary ethylene and secondary EO combustion. At Ni loadings higher than $NiAg_{200}$, both selectivity and conversion decreased, suggesting that extended NiO_x domains may block reactive sites on Ag and further facilitate EO combustion (see fig. S19).

Increasing the Ni loading led to a decrease in CO_2 production rate whereas the EO production rate decreased to a lesser degree, resulting in overall increased EO selectivity (Fig. 2, B and C). The ethylene conversion at 473 K was <2% and thus the CO_2 and EO production (as shown in Fig. 2, B and C) demonstrates the influence of Ni on the primary reaction pathways (conversion of ethylene to CO_2 or EO). At 523 K, where ethylene conversion was higher and the secondary reaction of EO combustion was likely more prevalent, the depression in CO_2 production rates with Ni addition was clearly observed with no change (or even a small increase) in EO production rates. The larger influence of Ni incorporation on selectivity at higher temperatures supported the conclusion that Ni suppressed secondary EO combustion while also promoting primary selectivity. Notably, the trends in selectivity and rates of product formation as a function of Ni concentration were similar to how Cl performs as a promoter (fig. S13).

The $NiAg_{200}$ formulation offered consistent performance improvement over Ag catalyst samples across multiple catalyst syntheses. The magnitude and statistical significance of the optimal Ni loading was quantified by comparing the reactivity of seven independently prepared batches of $Ag/\alpha\text{-}Al_2O_3$ and $NiAg_{200}/\alpha\text{-}Al_2O_3$ at an ~8 wt% Ag loading. The temperature, catalyst loading, and total flow rate were varied to compare EO selectivity at a broad range of ethylene conversions. Figure 3A shows that even with batch-to-batch performance variation, $NiAg_{200}$ repeatedly improved EO selectivity by at least 20% over a broad range of ethylene conversions up to 10%.

To explore the promoting influence of Ni at more industrially relevant reaction conditions, a feed composition containing 25% C_2H_4, 10% O_2, 0.5% CO_2, and 0.5 ppm ethyl chloride (EtCl) was used (*44*). Although the conversion of $Ag/\alpha\text{-}Al_2O_3$ declined substantially with time upon Cl introduction, decreasing from 3.8 to 0.3% in 18 hours (Fig. 3B and fig. S21A), the selectivity increased from 68% to 82% (Fig. 3C). $NiAg_{200}$ had a comparatively lower decrease in rates (~2× as compared to >10× for Ag) after an

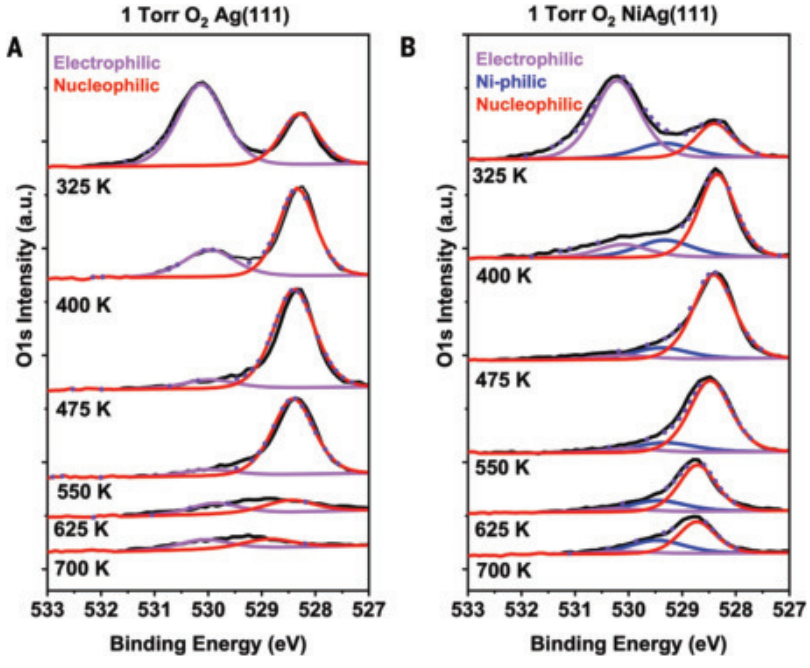

Fig. 4. Electronic structure of oxygen on Ag(111) and NiAg(111) as a function of temperature in 1 Torr O_2. AP-XP spectra showing a change in oxygen species from primarily electrophilic oxygen (purple, ~530.2 eV) to more nucleophilic oxygen (red, ~528.5 eV) as the temperature was increased on (**A**) Ag(111) and (**B**) ~5% NiAg(111). The Ni-philic O species (529.3 eV) is shown in blue and was only observed for the NiAg sample. O 1s spectra were taken at 760 eV from 325 to 700 K in 1 Torr O_2. The dotted traces represent the combined fits of the oxygen species overlaid with the solid black raw spectra.

initial increase in reactivity, with selectivity increasing to just >90%. The initial increase in EO formation rate for $NiAg_{200}$ and lower decrease in rate due to Cl introduction (fig. S21B) suggested that Ni and Cl were interacting on the Ag surface to modify the epoxidation pathways, which further supports the hypothesis that Ni is incorporated directly into the Ag nanoparticles rather than being located on the support. We note that optimized performance of Cl with other promoters is known to require co-optimization as a function of reaction conditions, suggesting that further improvements in performance are possible.

Ambient-pressure surface spectroscopy

Ambient-pressure x-ray photoelectron spectroscopy (AP-XPS) experiments demonstrated that the addition of Ni stabilized nucleophilic oxygen, which is generally believed to be responsible for non-selective primary and secondary combustion reactions on the Ag surface (*45*). Specifically, exposure of both Ag(111) and NiAg(111) surfaces to 1 Torr O_2 at 325 K led primarily to the formation of electrophilic (~530.2 eV) and nucleophilic (~528.5 eV) oxygen species (Fig. 4). The NiAg sample exhibited an additional O 1s peak at 529.3 eV (blue trace, Fig. 4B), consistent with a Ni-O species (labeled as "Ni-philic"; table S7) (*46*). Apart from the presence of the Ni-philic oxygen species on the NiAg(111) sample, both the Ag(111) and NiAg(111) surfaces behave similarly from 325 to 550 K: as the surface temperature is raised, the electrophilic oxygen is seen converting to nucleophilic oxygen on both surfaces. However, it is clear from Fig. 4B that on the NiAg surface nucleophilic oxygen persists up to 700 K versus 550 K on Ag(111). We hypothesize that this increased thermal stability of the nucleophilic oxygen induced by Ni incorporation should decrease its reactivity, lowering the non-selective primary and secondary combustion rates thereby enhancing EO selectivity compared with the Ni-free system, as seen in the catalytic measurements. Our DFT calculations show that Ni stabilizes nucleophilic O on Ag (fig. S3), rendering the nucleophilic oxygen which typically drives combustion more "spectator-like," and less reactive to ethylene combustion (*47*).

Our reactivity data in Fig. 3 also support this hypothesis in that the addition of Ni to Ag decreased the combustion rate more than the EO formation rate, providing a coherent picture of the proposed mechanism whereby Ni decreases unselective reactions of ethylene and EO with nucleophilic oxygen by stabilizing the O atoms in the structure. Further studies are aimed at developing scalable synthetic protocols on low surface area supports that further increase EO selectivity by minimizing secondary combustion sites for operation at higher reactor pressures.

Discussion

Guided by theory and experimental surface science results, we synthesized and tested dilute Ni-doped Ag nanoparticles and found an EO selectivity increase of ~25% compared with pure Ag, a promotion magnitude previously only achievable with a co-flow of Cl. Our study identified dilute (~1:200) Ni:Ag alloys as an optimal concentration for promoting selective EO formation on ~75 nm Ag nanoparticles, and the addition of Cl was found to further promote the selectivity of NiAg to ~90% without the need for promoters like Cs and Re that are normally required to reach this selectivity. Our AP-XPS results suggest that the ~25% selectivity enhancement results from Ni-induced stabilization of nucleophilic oxygen on the Ag surface, thereby decreasing the rates of ethylene and EO combustion. Overall, this study highlights the potential of theory-led exploration in dilute alloy materials space and the utility of our single-atom alloy approach for the design of selective oxidation catalysts.

REFERENCES AND NOTES

1. Ethylene Oxide and Ethylene Glycol Market by Product and Geography - Forecast and Analysis 2021-2025. (Technavio, 2021); https://www.technavio.com/report/ethylene-oxide-and-ethylene-glycol-market-industry-analysis.
2. J. H. Miller, A. Joshi, X. Li, A. Bhan, *J. Catal.* **389**, 714–720 (2020).
3. IEA, Technology Roadmap - Energy and GHG Reductions in the Chemical Industry via Catalytic Processes. (IEA Report, 2013); https://www.iea.org/reports/technology-roadmap-energy-and-ghg-reductions-in-the-chemical-industry-via-catalytic-processes.
4. Shell Global, Ethylene Oxide Catalysts. (Shell, 2025); https://www.shell.com/business-customers/catalysts-technologies/catalysts/petrochemical-catalysts/ethylene-oxide-catalysts.html.
5. C. Stegelmann, N. C. Schiødt, C. T. Campbell, P. Stoltze, *J. Catal.* **221**, 630–649 (2004).
6. H. Li, A. Cao, J. K. Nørskov, *ACS Catal.* **11**, 12052–12057 (2021).
7. M. O. Ozbek, I. Onal, R. A. Van Santen, *J. Catal.* **284**, 230–235 (2011).
8. A. Kokalj, P. Gava, S. de Gironcoli, S. Baroni, *J. Catal.* **254**, 304–309 (2008).
9. C. T. Campbell, *J. Catal.* **99**, 28–38 (1986).
10. C. J. Chen, J. W. Harris, A. Bhan, *Chemistry* **24**, 12405–12415 (2018).
11. A. J. F. Van Hoof, E. A. R. Hermans, A. P. Van Bavel, H. Friedrich, E. J. M. Hensen, *ACS Catal.* **9**, 9829–9839 (2019).
12. J. T. Jankowiak, M. A. Barteau, *J. Catal.* **236**, 379–386 (2005).
13. M. Huš, A. Hellman, *J. Catal.* **363**, 18–25 (2018).
14. A. Hwang, J. Klaucke, C. Lizandara-Pueyo, A. Karpov, E. Iglesia, *ChemCatChem* **16**, 1–24 (2023).
15. W. Diao, C. D. Digiulio, M. T. Schaal, S. Ma, J. R. Monnier, *J. Catal.* **322**, 14–23 (2015).
16. T. Pu, H. Tian, M. E. Ford, S. Rangarajan, I. E. Wachs, *ACS Catal.* **9**, 10727–10750 (2019).
17. S. Linic, M. A. Barteau, *J. Am. Chem. Soc.* **124**, 310–317 (2002).
18. S. Wu, B. J. Tatarchuk, A. J. Adamczyk, *Surf. Sci.* **708**, 121834 (2021).
19. S. V. Dhalewadikar, E. N. Martinez, A. Varma, *Chem. Eng. Sci.* **41**, 1743–1746 (1986).
20. E. A. Carbonio *et al.*, *Chem. Sci.* **9**, 990–998 (2017).
21. S. Linic, M. A. Barteau, *J. Catal.* **214**, 200–212 (2003).
22. D. Jingfa, Y. Jun, Z. Shi, Y. Xiaohong, *J. Catal.* **138**, 395–399 (1992).
23. J. C. Dellamorte, J. Lauterbach, M. A. Barteau, *Appl. Catal. A Gen.* **391**, 281–288 (2011).
24. S. Linic, J. Jankowiak, M. A. Barteau, *J. Catal.* **224**, 489–493 (2004).
25. M. Huš *et al.*, *Angew. Chem. Int. Ed.* **62**, e202305804 (2023).
26. M. D. Marcinkowski *et al.*, *ACS Catal.* **7**, 413–420 (2017).
27. G. Giannakakis *et al.*, *J. Am. Chem. Soc.* **143**, 21567–21579 (2021).
28. G. Kyriakou *et al.*, *Science* **335**, 1209–1212 (2012).
29. R. T. Hannagan *et al.*, *Science* **372**, 1444–1447 (2021).
30. M. M. Montemore, M. A. van Spronsen, R. J. Madix, C. M. Friend, *Chem. Rev.* **118**, 2816–2862 (2018).
31. S. R. Bare, K. Griffiths, W. N. Lennard, H. T. Tang, *Surf. Sci.* **342**, 185–198 (1995).
32. C. T. Campbell, *J. Catal.* **94**, 436–444 (1985).
33. A. Klust, R. J. Madix, *Surf. Sci.* **600**, 5025–5040 (2006).
34. W. Hansen, M. Bertolo, K. Jacobi, *Surf. Sci.* **253**, 1–12 (1991).
35. F. P. Netzer, T. E. Madey, *J. Chem. Phys.* **76**, 710–715 (1982).
36. J. E. van den Reijen *et al.*, *J. Catal.* **356**, 65–74 (2017).
37. K. R. Iyer, A. Bhan, *J. Catal.* **420**, 99–109 (2023).
38. B. T. Egelske, W. Xiong, H. Zhou, J. R. Monnier, *J. Catal.* **410**, 221–235 (2022).
39. J. Liu *et al.*, *Catal. Sci. Technol.* **7**, 4276–4284 (2017).
40. X. Gao *et al.*, *Sci. Rep.* **10**, 1365 (2020).
41. P. Christopher, S. Linic, *ChemCatChem* **2**, 78–83 (2010).
42. P. H. Keijzer, J. E. van den Reijen, C. J. Keijzer, K. P. de Jong, P. E. de Jongh, *J. Catal.* **405**, 534–544 (2022).
43. C. J. Keijzer, L. C. J. Smulders, D. Wezendonk, J. W. de Rijk, P. E. de Jongh, *Catal. Today* **428**, 114447 (2024).
44. J. R. Lockemeyer, T. L. Lohr, *ChemCatChem* **15**, e202201511 (2023).
45. V. I. Bukhtiyarov, I. P. Prosvirin, R. I. Kvon, *Surf. Sci.* **320**, L47–L50 (1994).
46. M. A. Peck, M. A. Langell, *Chem. Mater.* **24**, 4483–4490 (2012).
47. K.-H. Dostert, C. P. O'Brien, F. Ivars-Barceló, S. Schauermann, H. J. Freund, *J. Am. Chem. Soc.* **137**, 13496–13502 (2015).

ACKNOWLEDGMENTS

E.E.H. thanks P. Kress, C. Easton, and A. Daniels for their assistance during AP-XPS experiments at BNL. A.J. thanks J. Perez-Aguilar, J. Hong, S. R. Bare, and D. Sokaras for their assistance during XAS experiments at SSRL. **Funding:** A.J. and P.C. acknowledge primary financial support from the US Department of Energy, BES, Catalysis Science program under contract DE-SC0021124. E.E.H., L.C., and E.C.H.S. acknowledge primary financial support from the US Department of Energy, BES, CPIMS program under contract DE-SC0004738. M.M.M. acknowledges support from Tulane University and the National Science Foundation through grant CHE-2154952. A.S.H., part of Co-ACCESS and part of the SUNCAT Center for Interface Science and Catalysis, is supported by the U.S. Department of Energy, Office of Basic Energy Sciences, Chemical Sciences, Geosciences and Biosciences Division. The use of the Stanford Synchrotron Radiation Lightsource, SLAC National Accelerator Laboratory, is supported by the U.S. Department of Energy, Office of Science, Office of Basic Energy Sciences under contract DE-AC02-76SF00515. Use of the ICP and microscopy equipment in the UCSB MRL Shared Experimental Facilities is acknowledged, which are supported by the MRSEC Program of the National Science Foundation under award DMR 1720256. This research used resources of the 23-ID-2 (IOS) beamline of the National Synchrotron Light Source II, a U.S. Department of Energy (DOE) Office of Science User Facility operated for the DOE Office of Science by Brookhaven National Laboratory under Contract No. DE-SC0012704. High performance computing resources and services were provided by Technology Services at Tulane University, New Orleans, LA, USA. **Competing interests:** UCSB submitted a US provisional patent (63/392,370, filed on 26 July 2022) and a PCT International patent (PCT/US23/68581, filed on 16 June 2023) entitled "Highly selective catalyst composition for the oxidation of alkenes to Epoxides" on which A.J., P.C., M.M.M., L.C., and E.C.H.S. are listed as inventors. All other authors declare no other competing interests. Author contributions: Conceptualization: M.M.M., E.C.H.S., P.C., and A.J. Investigation: A.J., E.E.H., L.C., A.H., A.S.H., I.W., and M.M.M. Funding acquisition: M.M.M., E.C.H.S., P.C., and I.W. Supervision: M.M.M., E.C.H.S., P.C., and I.W. Writing, review, and editing: A.J., E.C.H.S., P.C., M.M.M., I.W., E.E.H., L.C., A.H., and A.S.H. **Data and materials availability:** All data is available in the main text or the supplementary materials. **License information:** Copyright © 2025 the authors, some rights reserved; exclusive licensee American Association for the Advancement of Science. No claim to original US government works. https://www.science.org/about/science-licenses-journal-article-reuse

SUPPLEMENTARY MATERIAL

science.org/doi/10.1126/science.adt1213
Materials and Methods
Supplemental Text
Figs. S1 to S21
Tables S1 to S7
References (*48*–*87*)

Submitted 14 September 2024; accepted 8 January 2025
10.1126/science.adt1213

POLYMER CHEMISTRY

Visible light–triggered depolymerization of commercial polymethacrylates

Hyun Suk Wang[1], Mikhail Agrachev[2], Hongsik Kim[3], Nghia P. Truong[1], Tae-Lim Choi[3], Gunnar Jeschke[2], Athina Anastasaki[1]*

The reversion of vinyl polymers with carbon-carbon backbones to their monomers represents an ideal path to alleviate the growing plastic waste stream. However, depolymerizing such stable materials remains a challenge, with state-of-the-art methods relying on "designer" polymers that are neither commercially produced nor suitable for real-world applications. In this work, we report a main chain–initiated, visible light–triggered depolymerization directly applicable to commercial polymers containing undisclosed impurities (e.g., comonomers, additives, or dyes). By in situ generation of chlorine radicals directly from the solvent, near-quantitative (>98%) depolymerization of polymethacrylates could be achieved regardless of their synthetic route (e.g., radical or ionic polymerization), end group, and molecular weight (up to 1.6 million daltons). The possibility to perform multigram-scale depolymerizations and confer temporal control renders this methodology a versatile and general route to recycling.

Although indispensable in our daily lives, plastics have led to serious environmental concerns ranging from landfill accumulation to microplastic contamination. Addressing these challenges necessitates a transition to a circular economy through recycling. Unfortunately, the predominant method, thermomechanical recycling, results in downcycling into lower-grade products through reduction of molecular weight (*1*, *2*). To circumvent product deterioration, alternatives such as "(photochemical) upcycling" (*3*–*10*) and chemical recycling to monomer (*1*, *11*, *12*) have been explored. Chemical recycling is a highly appealing option, as it not only establishes the smallest closed-loop cycle but also circumvents product deterioration (i.e., downcycling) through the synthesis of virgin-grade materials, with the option of even upgrading their properties (*1*, *13*). Vinyl polymers possess all-carbon backbones that render them chemically stable (e.g., from hydrolysis) but challenging to deconstruct owing to the absence of any heteroatom-associated weak links. The most conventional approach to break these bonds is pyrolysis, an industrially important reaction, but the extreme temperatures required (>400°C) lead to energy waste and undesirable byproducts. For example, pyrolysis of poly(methyl methacrylate) (PMMA) leads to formation of 2,3-butanedione, a compound that imparts a pungent odor to the recycled PMMA (*14*).

To alleviate these hurdles, polymers with preinstalled labile groups have recently been explored, the vast majority of which are synthesized by reversible deactivation radical polymerization (RDRP), also known as controlled radical polymerization (*15*–*20*). RDRP enables the production of well-defined polymers and precise control over their macromolecular characteristics, including architecture, sequence, dispersity, molecular weight, and end-group fidelity. Labile chain ends, usually halogens or thiocarbonylthio compounds, not only allow for the controlled synthesis of block copolymers but also facilitate depolymerization at lower temperatures than conventional pyrolysis (120° to 170°C) (*21*–*36*). The feasibility of depolymerizing RDRP polymers was first documented independently by the groups of Raus and Gramlich, who showed that low temperatures and high initial monomer concentrations are prerequisites for the successful polymerization of bulky monomers through atom transfer radical polymerization (ATRP) or reversible addition–fragmentation chain-transfer (RAFT) polymerization (*34*, *37*). Ouchi and co-workers then realized that the nonbulky PMMA could be partially depolymerized back to monomer, although low monomer recovery (i.e., up to 24%) was recorded and side reactions dominated the unzipping pathway (*35*). These seminal papers changed the perspective of the field, highlighted the possibility to trigger low-temperature depolymerizations, and initiated a number of exciting research directions. Matyjaszewski and co-workers demonstrated in a series of reports the full potential of halogen chain ends by using Cu or Fe halide salt catalysts to cleave the terminal C–Cl bond and achieve >80% depolymerization in solution and bulk (*23*–*25*). Sumerlin and co-workers used thiocarbonylthio esters to trigger depolymerization through photolytic cleavage of the terminal thiocarbonylthio C–S bond either in solution or a completely solvent-free process (*31*, *32*). More recently, the same group demonstrated depolymerization of PMMA triggered by thermolytically labile *N*-hydroxyphthalimide ester comonomers (*38*, *39*), whereas Diao and co-workers leveraged a comonomer-induced weak link in the backbone (*40*). Our group has also reported up to 92% depolymerization for various polymethacrylates using thiocarbonylthio– and halogen-terminated chain ends (*26*–*30*).

Despite these remarkable advances, these methods are restricted to "designer polymers" containing preinstalled weak links that render these materials thermally unstable. In fact, depolymerization of these materials relies precisely on their instability. Such polymers pose serious limitations for real-world applications and are not commercially produced. Thus, ATRP- or RAFT-based depolymerization strategies cannot

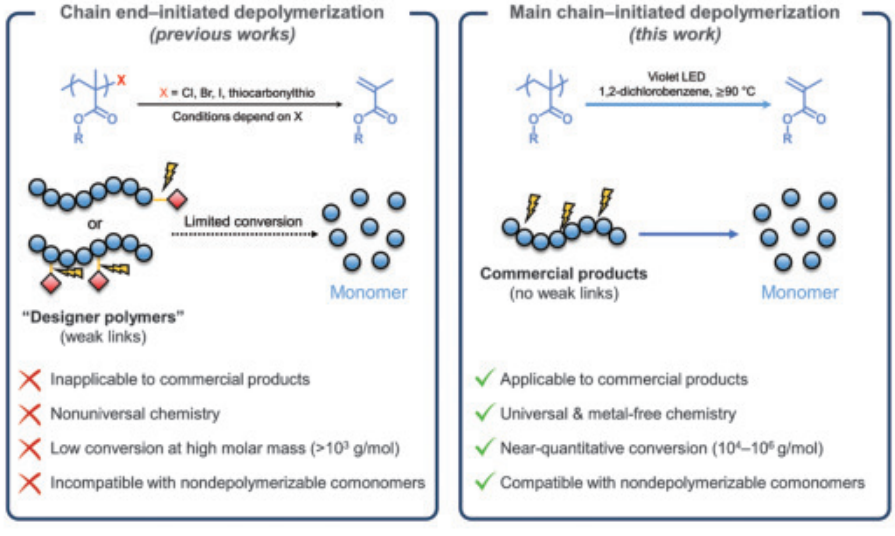

Fig. 1. Depolymerization approaches for PMMA. (Left) Chain end–initiated depolymerization through a labile chain end. (Right) Main chain–initiated depolymerization without the need for any labile group.

[1]Laboratory of Polymeric Materials, Department of Materials, ETH Zurich, Vladimir-Prelog-Weg 5, Zurich, Switzerland. [2]Institute for Molecular Physical Science, Department of Chemistry and Applied Biosciences, ETH Zurich, Vladimir-Prelog-Weg 2, Zurich, Switzerland. [3]Laboratory of Polymer Chemistry, Department of Materials, ETH Zurich, Vladimir-Prelog-Weg 5, Zurich, Switzerland.
*Corresponding author. Email: athina.anastasaki@mat.ethz.ch

address the annual inflow of 3.9 million metric tons of PMMA or existing waste (~90% unrecycled) (*41*, *42*). Notably, most end group–triggered depolymerizations are inherently limited to lower-molecular weight polymers and are severely affected by the presence of additional components (e.g., comonomers can prematurely quench depolymerization).

In this work, we report a one-step, near-quantitative, and visible light–triggered depolymerization of commercial PMMA that diverges from conventional methods through a main chain initiation pathway without reliance on any preinstalled weak bonds (Fig. 1). Notably, near-quantitative depolymerization can be achieved at high molecular weights (up to 10^6 g/mol) in the presence of nondepolymerizable comonomers and even after the polymer has been subjected to prolonged (solvo)thermal exposure. Our method is directly applicable to commercial products, such as Plexiglas, at a multigram scale (>10 g) without prior removal of the undisclosed additives contained within.

End group–independent depolymerization

A main chain–initiated depolymerization of vinyl polymers was serendipitously discovered while investigating the photothermal depolymerization of a high-molecular weight, dithiobenzoate-terminated PMMA (PMMA-DTB; number average molecular weight M_n = 212,500 g/mol, dispersity $Đ$ = 1.09) synthesized

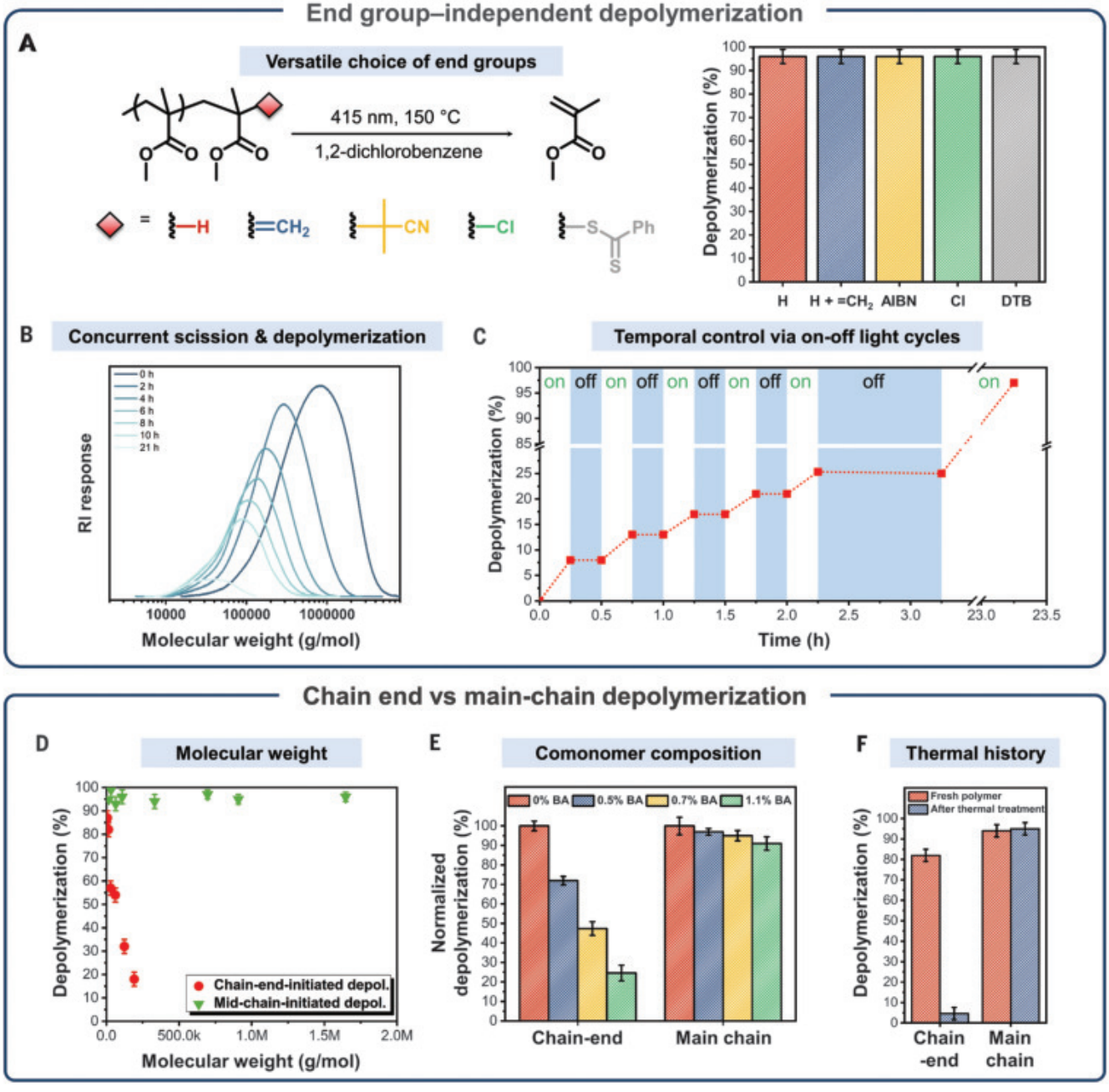

Fig. 2. Visible light–triggered depolymerization of PMMA through main chain initiation. (**A**) Depolymerization of PMMA with various end groups. AIBN, azobisisobutyronitrile. (**B**) SEC traces during depolymerization of PMMA synthesized by free radical polymerization. (**C**) Temporal control of depolymerization with on-off light cycles. Effect of (**D**) molecular weight, (**E**) BA content, and (**F**) thermal history on the final conversion for chain end– and main chain–initiated depolymerization. PMMA-DTB was used for chain end–initiated depolymerization. Error bars represent the standard deviation of >3 experiments.

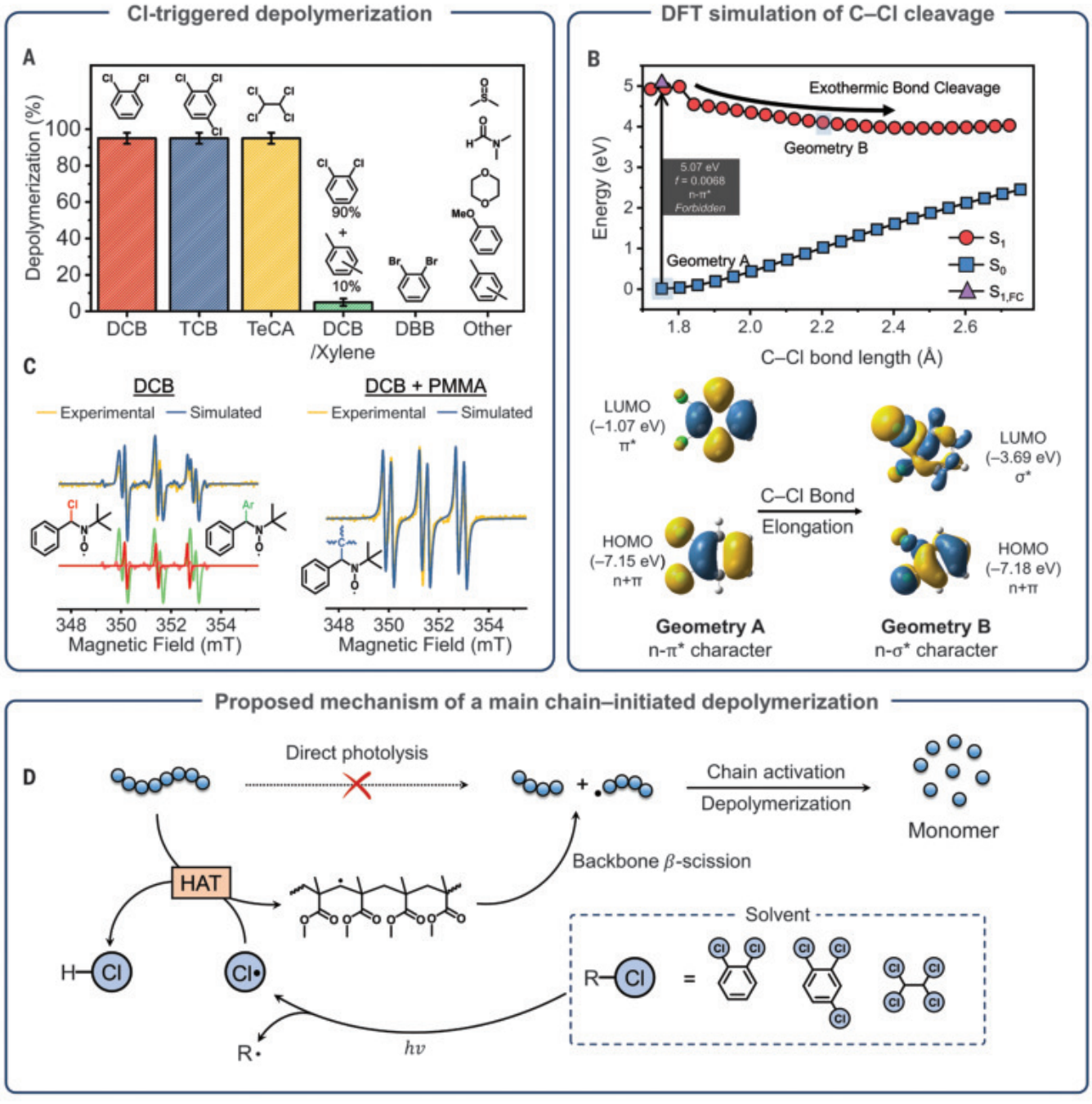

Fig. 3. Probing the mechanism of the main chain–initiated depolymerization. (**A**) Depolymerization conversions in different solvents under 415-nm irradiation. (**B**) DFT-calculated potential pathway for the photodissociation of DCB. *f*, oscillator strength; LUMO, lowest unoccupied molecular orbital; HOMO, highest occupied molecular orbital. (**C**) EPR spectra and simulations of irradiated DCB (left) and PMMA solution in DCB (right) in the presence of N-*tert*-butyl-α-phenylnitrone spin trap. (**D**) Proposed scheme of the HAT-induced depolymerization. Error bars represent the standard deviation of >3 experiments.

by RAFT polymerization (figs. S1 to S4). Depolymerization of PMMA-DTB in dioxane at 150°C and under ultraviolet (UV) irradiation led to no appreciable depolymerization after 6 hours (only ~10% conversion; fig. S3, A to D), in line with previous literature (*31*, *43*). Instead, when the reaction was repeated in 1,2-dichlorobenzene (DCB) under otherwise identical conditions, unusually high monomer recovery was observed (74%) within the same time frame (fig. S3F and table S1). Size exclusion chromatography (SEC) analysis of aliquots taken during the reaction in DCB showed an even greater decrease in molecular weight (90% reduction), indicating an unusual main chain scission depolymerization. Intrigued by these results, we screened various reaction conditions to further improve the conversion and discovered that near-quantitative depolymerization (>95%) of PMMA-DTB could be achieved at 150°C even under visible light (violet light–emitting diode, wavelength λ = 415 nm) irradiation (table S2).

We hypothesized that comparable depolymerization conversions could be reached regardless of the chain-end structure if indeed depolymerization proceeded through main chain

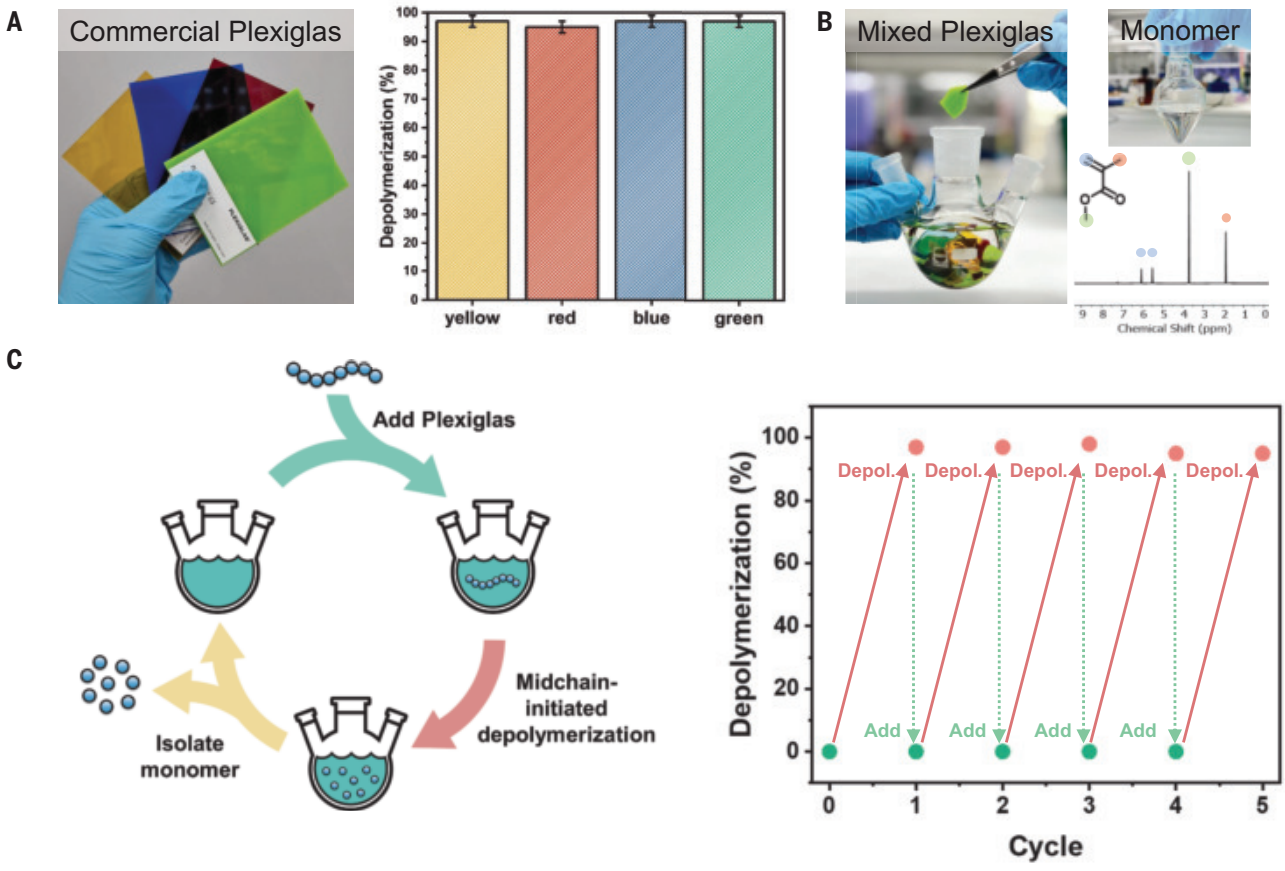

Fig. 4. Depolymerization of commercial Plexiglas. (**A**) Final depolymerization conversions of Plexiglas of varying color, (**B**) large-scale 2-M depolymerization of mixed Plexiglas, and (**C**) multicycle use of solvent for blue Plexiglas depolymerization. Error bars represent the standard deviation of >3 experiments. ppm, parts per million.

initiation. To this end, a series of polymers with various end groups were investigated. Different end groups were introduced by synthesizing PMMA through anionic polymerization (C–H end group), conventional free radical polymerization (mixture of C–H and C=C end groups), and ATRP (C–Cl end group) (table S3). In addition, PMMA terminated by a 2-cyano-2-propyl group (C–C end group) was synthesized by removing the end group of PMMA-DTB with excess radical initiator (azobisisobutyronitrile) (fig. S5). In accordance with our hypothesis, all samples underwent >95% depolymerization under 415-nm irradiation, further evidencing the end group–independent nature of this reaction (Fig. 2A). Even anionically synthesized PMMA underwent an efficient depolymerization (99%) despite it being the least reactive form of PMMA, reported to be thermally stable up to ~350°C (*30*). Under our conditions, depolymerization seemed to be occurring at significantly lower temperatures and in the absence of preinstalled weak bonds, opening up the possibility to potentially depolymerize commercial PMMA products.

To further investigate this unorthodox depolymerization pathway, PMMA synthesized by free radical polymerization (M_n = 331,600 g/mol, $Đ$ = 1.90) was selected as the model system. Detailed kinetic analysis showed a gradual reduction in molecular weight, further supporting a main chain–initiated pathway (Fig. 2B). Notably, high conversions could be achieved at temperatures as low as 90°C (fig. S6), albeit at reduced rates. Next, we tested the light-dependent nature of this reaction, as an ideal depolymerization should only proceed on demand. Multiple on-off cycles were performed in 1,2-dichlorobenzene to assess any unwanted thermal depolymerization. In four on-off cycles (15 min on, 15 min off), depolymerization only commenced during the "on" periods, proving that light is an essential trigger of the reaction (Fig. 2C). Even after an additional 1-hour-long "off" period, the final conversion was unaffected (>97%), highlighting the robust nature of the methodology. These results starkly contrast with previous (photo)thermal depolymerization of Cl-terminated polymethacrylates in which a sharp decline in the end-group fidelity (and thereby the extent of depolymerization) was observed after prolonged exposure to heat and/or light (*26*, *44*).

Chain end– versus main chain–initiated depolymerization

To contextualize our findings within the current landscape of depolymerization approaches and assess industrial feasibility, we compared our methodology with the labile chain end–initiated approach (*28*). PMMA-DTB was used as a benchmark, as it is arguably the most depolymerizable version of PMMA, capable of undergoing ~90% depolymerization, albeit at low molecular weights (~6000 g/mol) (*28*). We first examined the effect of molecular weight on the final depolymerization conversion for PMMA-DTB through a previously established chain end–initiated depolymerization protocol in 1,4-dioxane. A major decline in the final conversion from 87 to 9% was observed as the molecular weight increased from 6200 g/mol to 175,300 g/mol, in line with previous reports on the inverse relationship between molecular weight and conversion (Fig. 2D and table S4) (*31*, *43*). By contrast, our main chain–initiated depolymerization showed consistent conversions of 90 to 98% across a broad range of molecular weights up to 1,642,200 g/mol (Fig. 2D, fig. S7, and tables S5 and S6). This stark

improvement can be attributed to multiple initiation points within a single chain until full depolymerization is attained. This attribute is particularly appealing, as industrially produced PMMA typically exhibits molecular weights in the range of 10^4 to 10^6 g/mol.

Next, we were interested in probing the effect of the butyl acrylate (BA) comonomers within the chain, as commercially produced PMMA typically contains a small fraction (~1%) of acrylate comonomers to prevent depolymerization during thermal processing. As such, statistical P(MMA-*co*-BA)-DTB copolymers (BA = 0 to 1.1 mol %) were first synthesized by RAFT polymerization (table S7). The copolymers were then subjected to conventional thermal chain end–initiated depolymerization, and the final conversions were normalized to that of the homopolymer. Notably, the presence of BA had a remarkably negative impact on the final conversion: A relative conversion of 25% was observed when 1.1 mol % BA was present (Fig. 2E and fig. S8). Such high sensitivity to acrylate content is reasonable when considering that a polymethacrylate chain can only depropagate until reaching a single acrylate unit, after which termination will be favored, thereby kinetically trapping the remainder of the PMMA chain from further depolymerization (fig. S9). Instead, these molecular roadblocks can be bypassed by initiating depolymerization at multiple points within the chain. Indeed, when the same P(MMA-*co*-BA)-DTB samples underwent our main chain–initiated depolymerization, a remarkable relative conversion of 90% was reached even for the highest BA content (1.1 mol %), once more highlighting the importance of a multipoint initiation approach for materials that closely mimic commercial plastics (Fig. 2E).

Lastly, we examined the role of a polymer's thermal history on its susceptibility to depolymerization, as commercial products are typically thermally processed (e.g., at 190 to 220°C) and exposed to heat in their lifetime. When PMMA-DTB was heated for 30 min at 190°C under N_2 prior to chain end–initiated depolymerization, a conversion of only 5% was reached (compared to 82% for nonpreheated pristine samples) owing to end-group degradation, as confirmed by the loss of the UV response in SEC (Fig. 2F and fig. S10). This highlights another limitation of RDRP-synthesized polymers, as their susceptibility to depolymerization depends on the preservation of the weakest bond in the chain. This observation was also confirmed by the Matyjaszewski group's report of limited depolymerization of preheated ATRP-synthesized polymers (*44*). By contrast, when a main chain–initiated approach was used, no detectable change in the final conversion (95%) was observed for PMMA after the same thermal pretreatment (Fig. 2F), thereby demonstrating high tolerance to the thermal history of waste plastics, which removes a major limitation of approaches that rely on labile bonds.

Proposed mechanism of a main chain–initiated depolymerization

A series of experiments were conducted to gain a clearer picture of the mechanism. The first step was to identify the species responsible for initiating the depolymerization. Our earlier experiments showed that main chain scission can only occur in DCB; in dioxane, negligible, if any, shift in the molecular weight was observed throughout the reaction (fig S3, D and F). In addition, when the DCB experiment was conducted in the dark, no scission took place (fig S3E). Various other chlorinated and nonchlorinated solvents were also used under 415-nm irradiation, and whereas xylene, dimethylsulfoxide, dimethylformamide, and anisole solutions showed no appreciable scission under light irradiation, 1,2,4-trichlorobenzene solutions exhibited scission and depolymerization in a similar fashion to DCB, further suggesting that a chlorinated solvent is indeed necessary for main chain scission to occur (Fig. 3A and figs. S11 and S12). From these results, we suspected photodissociation of C–Cl bonds, leading to the formation of a reactive Cl radical and, presumably, an aryl radical. Density functional theory (DFT) simulations confirmed that homolytic cleavage of the C–Cl bond is energetically favorable in the first excited state (Fig. 3B). This is attributed to the elongation of the C–Cl bond in its excited state, which increases the electron density in the $\sigma^*_{C\text{–}Cl}$ orbital, thereby breaking the bond (fig. S13 and tables S8 and S9). However, a question remained regarding the absorption of visible light by DCB, as the UV–visible light spectrum of DCB in acetonitrile showed no detectable absorption above 290 nm (fig. S14). However, when neat DCB was analyzed with air as the background, a small yet distinct absorption band spanning from UV to violet (λ = 300 to 390 nm) was observed, with a molar absorptivity at peak wavelength of $\varepsilon = 4.5 \times 10^{-3}$ L mol^{-1} cm^{-1}. This absorption feature remained evident even after various purification methods (figs. S15 and S16 and table S10), strongly indicating that the observed absorption is intrinsic to the DCB molecule and not an artifact. Time-dependent DFT identified this absorption as the S_0 to S_1 transition involving a forbidden electronic transition from the nonbonding orbital of Cl to the benzene π^* orbital, which explains the observed extremely low molar absorptivity. Thermal contributions to C–Cl cleavage seemed minor, as PMMA could undergo scission even when irradiated at room temperature in DCB (fig. S17). It is also worth mentioning that excitation at wavelengths above the absorbance wavelength has been comprehensively reported by Barner-Kowollik and co-workers (*45*, *46*), further supporting the plausibility of photodissociation under our reaction conditions.

Photodissociation of DCB was supported by electron paramagnetic resonance (EPR) using N-*tert*-butyl-α-phenylnitrone as a spin trap to detect unstable radicals (*47*). The spectrum of irradiated pure DCB consisted of three components (Fig. 3C) that exhibit hyperfine couplings with ^{1}H, ^{14}N, and ^{35,37}Cl nuclei. From spectral simulations, these components were identified as aryl (green: ^{14}N = 1.43 G, ^{1}H = 0.20 G) and, most likely, Cl (red: ^{14}N = 1.21 G, ^{1}H was unresolved, ^{35}Cl = 0.58 G, ^{37}Cl = 0.50 G; salmon: ^{14}N = 1.26 G, ^{1}H and ^{35,37}Cl couplings were unresolved) radical adducts (see supplementary materials for further discussion). In the presence of PMMA, the spectrum can be well simulated with a single component, with parameters consistent with an alkyl radical (^{14}N = 1.46 G, ^{1}H = 0.32 G) and particularly close to those of secondary radicals, which can be attributed to PMMA fragments. Signals resembling aryl radicals were also observed with a 2,4,6-tri-*tert*-butylnitrosobenzene spin trap (fig. S18). Detection of chlorinated biphenyl species after irradiation of DCB further evidenced the formation of aryl radicals through homolytic C–Cl scission (fig. S19). Notably, these chlorinated biphenyls are only present in trace concentrations and can still function as active reagents that can initiate further depolymerization until complete dechlorination. With this evidence, we propose that the Cl radical generates a C-centered PMMA backbone radical through hydrogen atom transfer (HAT) of a backbone methyl or methylene unit (*48*), followed by β scission of the backbone and depolymerization under thermodynamically favorable conditions (Fig. 3D and figs. S20 to S23). A HAT pathway through a Cl radical was further supported by the detection of HCl during irradiation (fig. S24). Moreover, a HAT pathway proceeding from the backbone was supported by small-molecule chlorination experiments (figs. S25 to S38), retarded depolymerization kinetics for backbone-deuterated PMMA (kinetic isotope effect $k_H/k_D \approx 5$; fig. S39), high depolymerization conversions of polymethacrylates possessing various side chains (fig. S40 and table S11), and the depolymerization of poly(α-methylstyrene) (fig. S41). Notably, the depolymerization of poly(α-methylstyrene) confirms that decarboxylation is not a prerequisite in the depropagation of PMMA and that depropagation likely proceeds through the alkene-terminated fragment. To confirm that the Cl radical, rather than the aryl species, is indeed responsible for the scission, a nonaromatic chlorine solvent (1,1,2,2-tetrachloroethane) was used and also resulted in main chain scission and comparable conversions to that in DCB (Fig. 3B, fig. S42, and table S12). This finding further suggested that the main reactive species is indeed the chlorine radical. Notably, the Br equivalent of DCB

(i.e., 1,2-dibromobenzene) did not lead to either scission or depolymerization (Fig. 3B and fig. S11), presumably because of the lower reactivity of Br radicals toward aliphatic 1° and 2°C (sp^3)–H (bond-dissociation energy of HBr BDE_{HBr} = 87 kcal/mol versus BDE_{HCl} = 103 kcal/mol). When a DCB/xylene mixture (90/10 vol/vol) was used, much lower conversions (<10%) were reached in the same timeframe. Considering that the weak C–H bond of the xylene methyl and the stable benzylic radical formed after HAT, we postulated that the Cl radical preferentially reacts with xylene rather than the polymer, therefore suppressing both scission and the subsequent depolymerization. Naturally, these results exclude direct photolysis of the backbone, in line with the lack of scission in nonchlorinated solvents (fig. S11). Further evidence of the proposed Cl-induced HAT was seen when lower wavelengths (365 and 395 nm) resulted in faster scission and depolymerization kinetics (fig. S43 to S45). Despite the rate differences, similarly high final depolymerization conversions were reached in all cases (i.e., 95%). Instead, no scission was observed at higher wavelengths (i.e., 460 nm), likely owing to insignificant photoexcitation.

Depolymerization of Plexiglas

In the previous sections, we demonstrated the depolymerization of various PMMA samples resembling industrially produced PMMA (i.e., with various end groups and different comonomer concentrations). However, we were also interested in exploring the applicability of our developed methodology directly to commercial products. Commercial PMMA, often known by the tradename Plexiglas, typically contains a variety of undisclosed comonomers and additives, such as radical inhibitors, plasticizers, and dyes, which may interfere with the reaction. To investigate this, we purchased a series of different commercial Plexiglas materials with varying color (yellow, blue, red, and green), and transparency (4 to 64% transmission) (Fig. 4A, fig. S46, and table S13). All four samples were subjected to our depolymerization conditions without any prior purification. Notably, all four samples underwent near-quantitative depolymerization (94 to 98%) (Fig. 4A), highlighting the robust nature of this approach to additives and the immediate applicability of this strategy to commercial products. Furthermore, multigram-scale (16 g) reactions of a mixture of these samples could be conducted at a concentration (2 M) above the solubility limit of the solvent (1,2,4-trichlorobenzene, at 170°C to reduce viscosity and improve yield), and high-purity monomer (99%) could be simply distilled from the solution owing to the large difference in the boiling points (100° versus 213°C) (Fig. 4B, fig. S47, and table S14). It is worth noting that, at 2 M, a final depolymerization conversion of 51% (41% yield) was attained as the system reached a thermodynamic equilibrium (equilibrium monomer concentration $[M]_{eq} \approx 1.3$ M at 170°C). Upon distillation of the regenerated MMA, depolymerization could be further driven to similar final conversions (fig S48). Subsequently, we tested the possibility of reusing the solvent for multiple reactions by conducting a series of depolymerization-monomer evaporation cycles in the same solvent. Even after five cycles, near-quantitative (<95%) depolymerization could be reached with only a minor decrease in rate, suggesting a minor impact of impurity accumulation and showing promise in both process simplification and the economics of this methodology (Fig. 4C). For further scale-up and a higher number of cycles, solvent management will be important to reduce chlorocarbon waste generated from this process (e.g., minimizing solvent deterioration by removing unknown plastic additives prior to depolymerization). Lastly, we tested our methodology in a mixed-waste stream containing either polyethylene terephthalate (PET), low-density polyethylene (LDPE), polypropylene (PP), polyurethane (PU), or polyvinyl chloride (PVC). Overall, our depolymerization methodology proved highly compatible with PET, LDPE, PP, and PU (>90%), whereas moderate conversions (69 to 85%) were observed in the presence of PVC (table S15).

Conclusions and outlook

We have developed a one-step, main chain–initiated depolymerization methodology that operates at temperatures far lower than that of traditional pyrolysis without relying on "designer polymers." The method is therefore directly applicable to commercial polymers while yielding near-quantitative monomer recovery. Furthermore, versatility was demonstrated by depolymerizing PMMAs with high molecular weights (e.g., $M_n = 10^6$ g/mol) and those containing acrylate comonomers. Lastly, as the method does not rely on labile end groups, no special care to preserve end group fidelity is needed (e.g., preventing exposure to heat and light).

REFERENCES AND NOTES

1. G. W. Coates, Y. D. Getzler, *Nat. Rev. Mater.* **5**, 501–516 (2020).
2. Z. O. G. Schyns, M. P. Shaver, *Macromol. Rapid Commun.* **42**, e2000415 (2021).
3. S. Oh, E. E. Stache, *J. Am. Chem. Soc.* **144**, 5745–5749 (2022).
4. C. Jehanno *et al*., *Nature* **603**, 803–814 (2022).
5. O. G. Mountanea, E. Skolia, C. G. Kokotos, *Green Chem.* **26**, 8528–8549 (2024).
6. S. Zhang, M. Li, Z. Zuo, Z. Niu, *Green Chem.* **25**, 6949–6970 (2023).
7. F. Eisenreich, *Angew. Chem. Int. Ed.* **62**, e202301303 (2023).
8. R. Cao, D. Xiao, M. Wang, Y. Gao, D. Ma, *Appl. Catal. B* **341**, 123357 (2024).
9. H. Cui, X. Chen, F. Lan, B. An, X. Zhang, *Trends Chem.* **6**, 392–405 (2024).
10. E. Skolia, O. G. Mountanea, C. G. Kokotos, *Trends Chem.* **5**, 116–120 (2023).
11. B. A. Abel, R. L. Snyder, G. W. Coates, *Science* **373**, 783–789 (2021).
12. T. M. McGuire, A. Buchard, C. Williams, *J. Am. Chem. Soc.* **145**, 19840–19848 (2023).
13. C. Shi *et al*., *Chem* **7**, 2896–2912 (2021).
14. C. B. Godiya *et al*., *J. Environ. Manage.* **231**, 1012–1020 (2019).
15. G. Moad, in *Macromolecular Engineering*, N. Hadjichristidis, Y. Gnanou, K. Matyjaszewski, M. Muthukumar, Eds. (Wiley-VCH, ed. 2, 2022), pp. 1–61.
16. P. Krys, K. Matyjaszewski, *Eur. Polym. J.* **89**, 482–523 (2017).
17. K. Parkatzidis, H. S. Wang, N. P. Truong, A. Anastasaki, *Chem* **6**, 1575–1588 (2020).
18. D. T. Gentekos, R. J. Sifri, B. P. Fors, *Nat. Rev. Mater.* **4**, 761–774 (2019).
19. C. Boyer *et al*., *Chem. Rev.* **109**, 5402–5436 (2009).
20. C. Barner-Kowollik, *Handbook of RAFT polymerization* (Wiley, 2008).
21. M. R. Martinez, K. Matyjaszewski, *CCS Chem.* **4**, 1–36 (2022).
22. M. R. Martinez, F. De Luca Bossa, M. Olszewski, K. Matyjaszewski, *Macromolecules* **55**, 78–87 (2021).
23. M. R. Martinez, S. Dadashi-Silab, F. Lorandi, Y. Zhao, K. Matyjaszewski, *Macromolecules* **54**, 5526–5538 (2021).
24. M. R. Martinez, D. Schild, F. De Luca Bossa, K. Matyjaszewski, *Macromolecules* **55**, 10590–10599 (2022).
25. F. De Luca Bossa, G. Yilmaz, K. Matyjaszewski, *ACS Macro Lett.* **12**, 1173–1178 (2023).
26. K. Parkatzidis, N. P. Truong, K. Matyjaszewski, A. Anastasaki, *J. Am. Chem. Soc.* **145**, 21146–21151 (2023).
27. H. S. Wang, K. Parkatzidis, T. Junkers, N. P. Truong, A. Anastasaki, *Chem* **10**, 388–401 (2023).
28. H. S. Wang, N. P. Truong, Z. Pei, M. L. Coote, A. Anastasaki, *J. Am. Chem. Soc.* **144**, 4678–4684 (2022).
29. V. Bellotti, H. S. Wang, N. P. Truong, R. Simonutti, A. Anastasaki, *Angew. Chem. Int. Ed.* **62**, e202313232 (2023).
30. R. Whitfield, G. R. Jones, N. P. Truong, L. E. Manring, A. Anastasaki, *Angew. Chem. Int. Ed.* **62**, e202309116 (2023).
31. J. B. Young *et al*., *Chem* **9**, 2669–2682 (2023).
32. J. B. Young, J. I. Bowman, C. B. Eades, A. J. Wong, B. S. Sumerlin, *ACS Macro Lett.* **11**, 1390–1395 (2022).
33. S. Huang, X. Su, Y. Wu, X.-G. Xiong, Y. Liu, *Chem. Sci.* **13**, 11352–11359 (2022).
34. M. J. Flanders, W. M. Gramlich, *Polym. Chem.* **9**, 2328–2335 (2018).
35. Y. Sano, T. Konishi, M. Sawamoto, M. Ouchi, *Eur. Polym. J.* **120**, 109181 (2019).
36. G. R. Jones *et al*., *J. Am. Chem. Soc.* **145**, 9898–9915 (2023).
37. V. Raus, E. Čadová, L. Starovoytova, M. Janata, *Macromolecules* **47**, 7311–7320 (2014).
38. R. W. Hughes *et al*., *J. Am. Chem. Soc.* **146**, 6217–6224 (2024).
39. J. B. Young *et al*., *Angew. Chem. Int. Ed.* **63**, e202408592 (2024).
40. M. T. Chin *et al*., *J. Am. Chem. Soc.* **146**, 5786–5792 (2024).
41. J. De Tommaso, J.-L. Dubois, *Polymers* **13**, 2724 (2021).
42. M. Sponchioni, S. Altinok, *Advances in Chemical Engineering*, **vol. 60**, D. Moscatelli, M. Pelucchi, Eds. (Academic Press, 2022), pp. 269–287.
43. H. S. Wang, N. P. Truong, G. R. Jones, A. Anastasaki, *ACS Macro Lett.* **11**, 1212–1216 (2022).
44. M. R. Martinez, F. De Luca Bossa, M. Olszewski, K. Matyjaszewski, *Macromolecules* **55**, 78–87 (2021).
45. S. L. Walden, J. A. Carroll, A.-N. Unterreiner, C. Barner-Kowollik, *Adv. Sci. (Weinh.)* **11**, e2306014 (2024).
46. D. E. Fast *et al*., *Macromolecules* **50**, 1815–1823 (2017).
47. G. R. Buettner, *Free Radic. Biol. Med.* **3**, 259–303 (1987).
48. P. Ulanski, E. Bothe, K. Hildenbrand, C. von Sonntag, *Chemistry* **6**, 3922–3934 (2000).

ACKNOWLEDGMENTS

Funding: A.A. gratefully acknowledges ETH Zurich for financial support. N.P.T. acknowledges the award of a DECRA Fellowship from the ARC (DE180100076). H.S.W. acknowledges the award of the Swiss Government Excellence Scholarship (ESKAS; no. 2020.0324). This project received funding from the European Research Council (ERC) under the European Union's Horizon 2020 Research and Innovation Programme (DEPO; grant agreement no.

949219). G.J. acknowledges funding from NCCR Catalysis, a National Centre of Competence in Research funded by the Swiss National Science Foundation. We thank T. Nauser and M.-N. Antonopoulou for fruitful discussions. **Author contributions:** H.S.W. and A.A. conceived the initial idea and managed the overall project. H.S.W. designed and performed the experiments with input from M.A. (EPR experiments) and H.K. (DFT simulations). H.S.W. and A.A. cowrote the manuscript with input from M.A., N.P.T., H.K., T.-L.C., and G.J. **Competing interests:** H.S.W. (ETH Zurich) and A.A. (ETH Zurich) have filed a patent related to the depolymerization methodology (EUROP/259). Other authors declare that they have no competing interests. **Data and materials availability:** All data are available in the main text or the supplementary materials.

SUPPLEMENTARY MATERIALS
science.org/doi/10.1126/science.adr1637
Materials and Methods
Figs. S1 to S48
Tables S1 to S15
Reference (*49*)

Submitted 18 June 2024; accepted 13 January 2025
10.1126/science.adr1637

ROBOTICS

Material-like robotic collectives with spatiotemporal control of strength and shape

Matthew R. Devlin[1], Sangwoo Kim[1,2], Otger Campàs[1,3,4,5]*, Elliot W. Hawkes[1]*

The vision of robotic materials—cohesive collectives of robotic units that can arrange into virtually any form with any physical properties—has long intrigued both science and fiction. Yet, this vision requires a fundamental physical challenge to be overcome: The collective must be strong, to support loads, yet flow, to take new forms. We achieve this in a material-like robotic collective by modulating the interunit tangential forces to control topological rearrangements of units within a tightly packed structure. This allows local control of rigidity transitions between solid and fluid-like states in the collective and enables spatiotemporal control of shape and strength. We demonstrate structure-forming and healing and show the collective supporting 700 newtons (500 times the weight of a robot) before "melting" under its own weight.

The concepts of robotic materials (*1*), "programmable matter" (*2*), "claytronics" (*3*), and robotic systems inspired by the multicellular organization of living organisms (*4*, *5*) all share a similar vision: a cohesive collective of robotic units that work together to form a material-like assembly with adaptability and functionality (*6*, *7*). Making this vision a reality would change static objects—with properties set at the time of design—into dynamic matter that could reconfigure into myriad forms with diverse physical properties. However, this requires overcoming a fundamental physical challenge: to be strong and stiff like a solid yet locally flow like a fluid when a new form is needed. Industrial processes, such as molding and forging, achieve this by applying external heat and force to inert materials. Robotic materials would instead be internally powered and actively controlled to switch from rigid to flowing states anywhere in the material, akin to living systems.

Current self-reconfigurable modular robots and robotic collectives have demonstrated a variety of complex behaviors. Specifically, some show intricate shape changes but are not cohesive and do not support loads (*8*, *9*). Others show emergent locomotion behaviors but do not directly control reconfiguration (*10*, *11*). Yet others can support or even push loads but cannot reconfigure (*12*–*15*), reconfigure only after breaking cohesion (*16*–*18*), only rearrange units at the perimeter of the collective (*3*, *19*–*23*), or rearrange by means of movements of single expanding units (*24*, *25*). Additional behaviors have been explored through simulations but have not been implemented in a robotic system (*5*, *26*–*28*). Achieving a strong, material-like collective that can support loads but also selectively flow anywhere in its interior to reshape at will remains a challenge.

In contrast to inert materials and current robotic systems, living embryonic tissues internally control their mechanics in space and time through tightly coordinated rearrangements of thousands of cells (*29*, *30*), enabling them to achieve exceptional behaviors (*30*–*33*), including self-shaping, self-healing, and regeneration. To self-shape and fine-tune their strength, embryonic tissues use two mechanisms, namely convergent extension (*34*–*36*) and tissue fluidization (*30*, *37*). Convergent extension is an evolutionarily conserved mechanism that drives tissue elongation by polarizing cell-cell contact tensions in a specific spatial direction, thereby forcing oriented cell rearrangements (T1 transitions) that progressively cause the thinning of the tissue in one direction and its elongation in a perpendicular one (Fig. 1A). Tissue fluidization enables solid-like tissues to switch to fluid-like states (*38*) and even control these material states in space and time (*30*, *37*, *38*) (Fig. 1B), through spatiotemporally controlled cellular rearrangements (T1 transitions). These two mechanisms allow developing embryos to maintain shape and mechanical strength to sustain loads like a solid, while being able to remodel like a fluid during morphogenesis or healing.

Inspired by these cellular processes, we have engineered robotic collectives to actively control local unit rearrangements (T1 transitions) throughout the collective, enabling adjustable spatiotemporal changes in the solid and fluid states of the robotic collective. The collective is strong and stiff yet rapidly switches states anywhere in the system, flowing to form alternate shapes or to modulate strength.

From embryo to robot

Cells in embryonic tissues control several processes to coordinate their behaviors across the tissue. We focus on three of these processes. First, cells apply active forces on one another with defined magnitude and fluctuating characteristics, enabling relative movements within the bulk of the collective. Second, biochemical signaling allows cells to coordinate these behaviors in space and time. Some signals polarize cells along specific spatial directions, helping them orient their active forces across the collective, thereby connecting local cell behaviors to large-scale shape transformations. Third, cells adhere to each other, offering cohesion and strength to the collective.

To recapitulate these behaviors in a robotic system, we built into each robotic unit the processes that control cell-cell interactions (*30*, *39*): fluctuating interunit tangential force, polarity, and adhesion (Fig. 1C). First, and most importantly for enabling rearrangements throughout the collective, we incorporated eight motorized gears, each with only a fraction of its teeth exposed, around the perimeter of the robotic unit (Fig. 1C, fig. S1, and methods). The relative movement of the exposed teeth in contacting robotic units creates forces tangential to the unit's surface, similar to the tension at cellular junctions. Both the magnitude and fluctuating characteristics of the interunit forces can be independently tuned. These interunit tangential forces can drive topological rearrangements between neighboring units, even in tightly packed collectives, because the pattern of tangent forces creates synergistic resultant forces on neighboring units (fig. S1). This is in contrast to previous robotic collectives, which

[1]Department of Mechanical Engineering, University of California, Santa Barbara, Santa Barbara, CA, USA. [2]Institute of Mechanical Engineering, École Polytechnique Fédérale de Lausanne, Lausanne, Switzerland. [3]Cluster of Excellence Physics of Life, TU Dresden, Dresden, Germany. [4]Max Planck Institute of Molecular Cell Biology and Genetics, Dresden, Germany. [5]Center for Systems Biology Dresden, Dresden, Germany.
***Corresponding author. Email: ewhawkes@ucsb.edu (E.W.H.); otger.campas@tu-dresden.de (O.C.)**

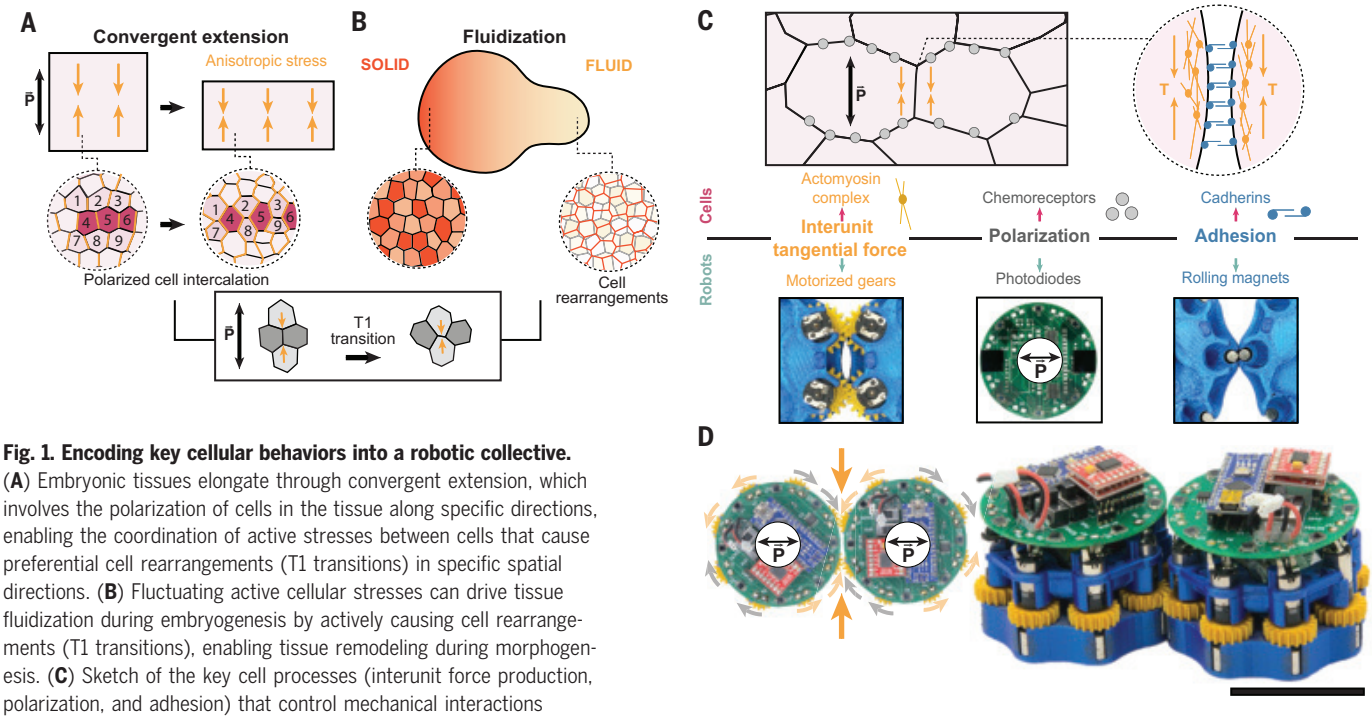

Fig. 1. Encoding key cellular behaviors into a robotic collective. (**A**) Embryonic tissues elongate through convergent extension, which involves the polarization of cells in the tissue along specific directions, enabling the coordination of active stresses between cells that cause preferential cell rearrangements (T1 transitions) in specific spatial directions. (**B**) Fluctuating active cellular stresses can drive tissue fluidization during embryogenesis by actively causing cell rearrangements (T1 transitions), enabling tissue remodeling during morphogenesis. (**C**) Sketch of the key cell processes (interunit force production, polarization, and adhesion) that control mechanical interactions between cells in embryonic tissues. Each of these cell processes are encoded into the robotic units: For interunit force production, the actomyosin complex is mapped to motorized gears; for polarization, chemoreceptors are mapped to photodiodes with polarizing filters; and for adhesion, cadherins are mapped to rolling magnets. The robotic units use a polarity direction convention that is orthogonal to that of biology. (**D**) Photographs of two robotic units, top view (left) and isometric view (right). Rotation directions of motorized gears are shown, along with net force applied to neighboring units. Scale bar: 5 cm.

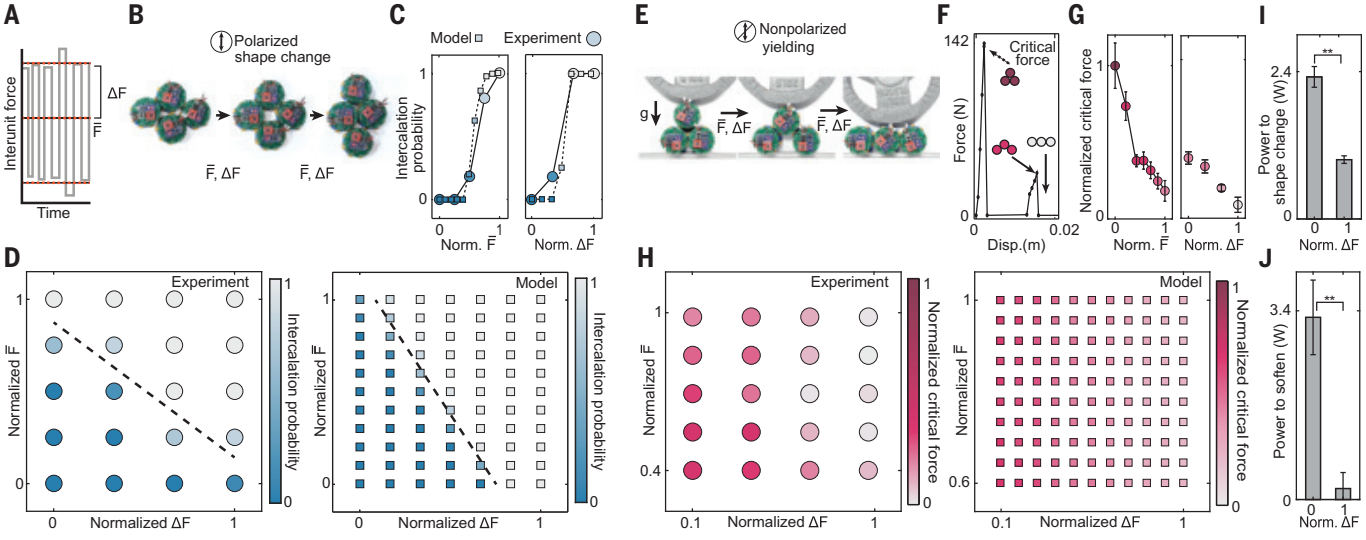

Fig. 2. Rearrangements enable shape and strength change in fundamental "building blocks" of robotic collectives. (**A**) Interunit tangential force profile has two key parameters: average ($\bar{F}$) and fluctuation amplitude (ΔF). (**B**) T1 transition of a polarized 4-block. (**C**) T1 transition probability in a 4-block as a function of, at left, the interunit force $\bar{F}$ (for a low fluctuation amplitude ΔF) and, at right, the force fluctuation amplitude ΔF (for a low interunit force $\bar{F}$). $\bar{F}$ and ΔF normalized to full range throughout. (**D**) Experimentally measured (left) and computed (right) T1 transition probability for varying $\bar{F}$ and ΔF. Each point: $N = 10$ trials. (**E**) Nonpolarized 3-block yielding under an externally applied load as fluctuating interunit force decreases yield strength. (**F**) Yielding in a 3-block with no interunit forces requires an external load of 142 N. (**G**) Critical force, normalized to maximum value, as a function of increasing interunit forces (left) and fluctuation amplitude (right). (**H**) Critical force as a function of both interunit force $\bar{F}$ and fluctuation amplitude ΔF from experiments (left) and simulations (right). $N = 10$ trials. (**I**) Power required to drive a T1 transition is significantly lower with high fluctuations ($N = 10$ trials, $^{**}P < 0.01$). (**J**) Power required to drive unit rearrangements under an applied external load is significantly lower with high fluctuations ($N = 5$ trials, $^{**}P < 0.01$). Error bars (G, I, J) represent one standard error.

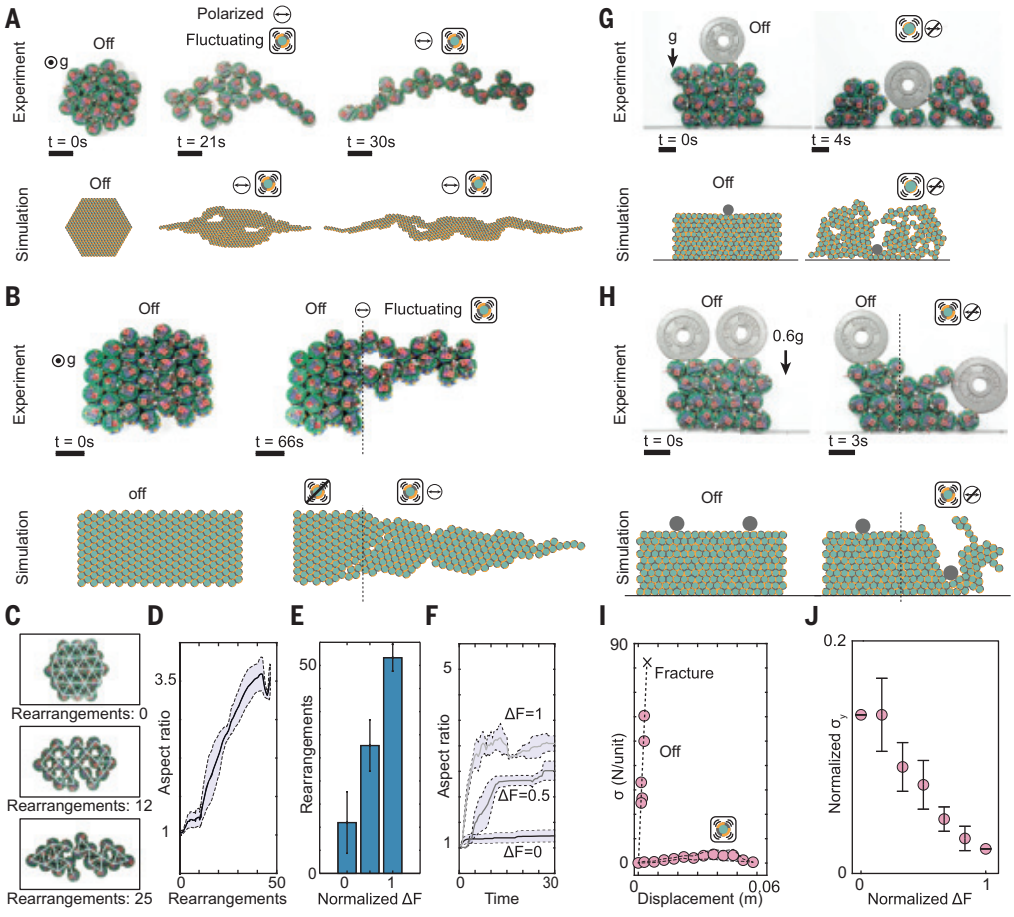

Fig. 3. From fundamental building blocks to robotic collectives: Scaling shape and strength control to many-unit collectives. (**A**) Robotic and simulated collectives elongating in polarization direction. Rounded-square icon indicates fluctuations ON. Robotic: 19 units, $\bar{F} = 0.86$, $\Delta F = 1$. Simulated: 217 units, $\bar{F} = 1$, $\Delta F = 1$. All $\bar{F}$ and ΔF normalized to full range throughout figure. (**B**) Elongation only occurs where fluctuating forces are ON. Experiments: (Left) $\bar{F} = 0$, $\Delta F = 0$; (Right) $\bar{F} = 0.57$, $\Delta F = 0.5$. Simulations: (Left) $\bar{F} = 1$, $\Delta F = 0$; (Right) $\bar{F} = 1$, $\Delta F = 1$. (**C**) Network graph of contacts between units. (**D**) Aspect ratio depends directly on unit rearrangements. $N = 3$ trials. (**E**) Number of rearrangements increases with fluctuation amplitude. $N = 3$ trials. (**F**) Aspect ratio changes more rapidly with increasing fluctuation amplitude. $N = 3$ trials. (**G**) The introduction of force fluctuations (right) decreases the yield strength, and the load deforms the collective. Experiments: (Left) $\bar{F} = 0$, $\Delta F = 0$; (Right) $\bar{F} = 1$, $\Delta F = 1$. Simulations: (Left) $\bar{F} = 0$, $\Delta F = 0$; (Right) $\bar{F} = 1$, $\Delta F = 1$. (**H**) Force fluctuations in one region decrease yield strength only there. Experiments: (Left) $\bar{F} = 0$, $\Delta F = 0$; (Right) $\bar{F} = 1$, $\Delta F = 1$. Simulations: (Left) $\bar{F} = 0$, $\Delta F = 0$; (Right) $\bar{F} = 1$, $\Delta F = 1$. (**I**) Stress-strain relation for a 20-unit robotic collective. With fluctuations OFF, strength (90 N per unit) and stiffness (20,190 N per unit per m) are high. When ON, strength drops to 6 N per unit, and yield occurs. $N = 3$ trials. (**J**) Yield stress decreases with increasing fluctuation amplitude. $N = 3$ trials. Scale bars: 10 cm. Shading [(D) and (F)] and error bars [(E) and (J)] represent one standard error.

generally either push off of the ground surface [e.g., (*8*)] or create rolling motions of units around others [e.g., (*23*)], limiting rearrangements to the perimeter of tightly packed robotic collectives. Second, we mimicked cell polarization in response to global biochemical cues by incorporating photoreceptors on each robotic unit that detect global polarized light (Fig. 1C, fig. S2, and methods). This allowed each robotic unit to change its polarity in real time according to a global light-based signal. Third, we implemented cell-cell adhesion by incorporating magnets into small chambers around the perimeter of the robotic unit to achieve unit-unit "adhesion" in our system (Fig. 1C, fig. S3, and methods). Magnets are diametrically magnetized and can roll within their chamber for orientation-independent adhesion, similar to some previous collective robots (*11*, *16*). Beyond these physical robots (Fig. 1D, fig. S4, and table S1), to enable a systematic study of the emergent behaviors of the robotic collective, we developed a mathematical model of the system wherein each unit experiences tangential stresses at the surface and distance-based adhesion forces and can align to a global polarity (fig. S5, movie S1, and methods).

Controlling shape and strength in minimal robotic building blocks

To achieve control of shape and material strength throughout a tissue, cells in embryonic tissues actively control their rearrangements. In such events, a group of adjacent cells change their contact topology (often a T1 transition; Fig. 1), driving both a local shape change and the relaxation of mechanical stresses in the system, or yielding.

We actively controlled T1 transitions of robotic units by varying the average interunit tangential force $\bar{F}$ and amplitude of force fluctuations ΔF in both experiment and simulation (Fig. 2A, figs. S5 to S7, and movie S2). We first focused on a polarized four-unit building block, abbreviated "4-block," which can undergo active T1 transitions along the direction of polarization, mimicking polarized cell intercalation in embryonic tissues (Fig. 2B). We found that intercalation only occurs after the average interunit force $\bar{F}$ exceeds a threshold (for a given amplitude of force fluctuations ΔF), and similarly, intercalation only occurs after the amplitude of force fluctuations ΔF exceeds a threshold (for a given average interunit force $\bar{F}$) (Fig. 2C). Further, as we varied both the average interunit force $\bar{F}$ and the amplitude of force fluctuations ΔF together, we found that the average interunit force $\bar{F}$ required for intercalation decreased with the amplitude of force fluctuations ΔF (Fig. 2D). These results show that both the magnitude of interunit forces and the characteristics of their fluctuations play a role in the control of unit rearrangements, with fluctuations facilitating local restructuring in the robotic collective.

Beyond local shape changes, T1 transitions are known to control stress relaxation, yielding, and fluidization in granular materials such as foams and emulsions (*40*, *41*) as well as in living tissues (*42*). To understand the control of yielding in minimal robotic collectives, we applied external loads on a minimal three-unit building block (or "3-block") with random polarization (Fig. 2E). In the absence of interunit

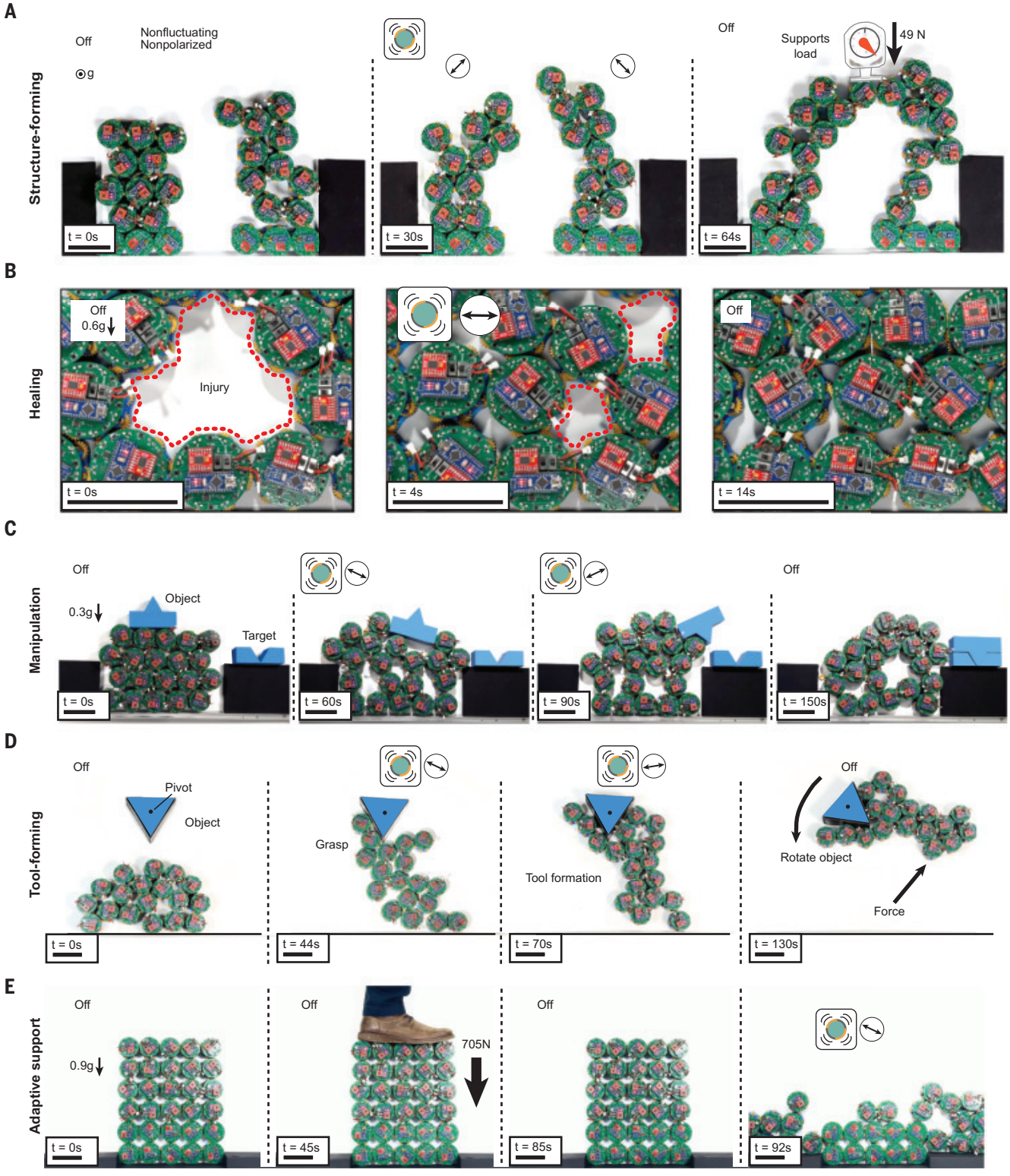

Fig. 4. Demonstrations of "robotic material" behaviors. (**A**) Structure-forming: A collective can fluidize, reshape itself into an arch, then resolidify to support a load with the newly formed structure. (**B**) Healing: When a region of the collective is removed, it can undergo a rigidity transition, locally fluidizing the collective, which flows to fill in the void. (**C**) Manipulation: Controlled localized flow within the collective can move objects. Here, the collective applies forces to an object to direct it toward a target. (**D**) Tool-forming: A collective can fluidize, flow around an object, then rigidify and act as a "wrench" to rotate the object. (**E**) Adaptive support: A collective can remain strong enough to support a person (>700 N) and then fluidize to flow under the collective's own weight. Scale bars: 10 cm.

force or fluctuations, we found that 3-blocks are able to resist applied forces up to a threshold value of 142 N, at which point the robotic units in the 3-block rearrange (Fig. 2F). Upon activation of interunit forces or force fluctuations, the maximal resistive force (critical force) of the 3-block decreases (Fig. 2G). A low average interunit force together with low force fluctuations results in a high critical force, whereas a high interunit force coupled with high force fluctuations creates a low critical force (Fig. 2H). These results show that both the average interunit forces and the magnitude of fluctuations affect the yield strength of robotic building blocks, as observed in inert granular materials and living embryonic tissues.

In both of these building-block systems, we found that introducing force fluctuations lowers the mean power required for unit rearrangements during both shape change (Fig. 2I) and yield strength change (Fig. 2J). This is so because noise in interunit forces helps overcome the energy barriers for rearrangements, reducing the required mean interunit force and, consequently, the mean power. These results indicate that in power-limited robotic collectives that are unable to produce enough mean power to drive unit rearrangements, fluctuations facilitate rearrangements, enabling reconfigurations in the system that would be otherwise impossible.

Building up the collective

In robotic collectives (~20 units in hardware, ~400 in simulation), we explored how controlled unit rearrangements enable local fluidization, which in turn allows modulation of shape and strength. Both our experiments and simulations showed that when the robotic collective is polarized, aligning interunit forces across robotic units, the robotic collective elongates unidirectionally along the specified axis (Fig. 3A), as occurs during convergent extension in living tissues (*35*). If the polarization direction is changed during elongation, we observed that the robotic collective dynamically readjusts and elongates along the new specified direction (fig. S8 and movie S5). Moreover, by spatially controlling the interunit forces, it is possible to drive elongation in the target section of the collective while keeping the rest of the collective immobile (Fig. 3B). We found that the elongation of the robotic collective was driven by polarized rearrangements caused by polarized interunit forces (Fig. 3, C and D), as occurs for convergent extension in living tissues (*35*). Further, we observed that the number and rate of unit rearrangements depend strongly on the amplitude of force fluctuations (Fig. 3E) and facilitate elongation of the robotic collective (Fig. 3F), all behaviors that mirror tissue fluidization by active cell rearrangements induced through fluctuating forces (*42*). These results show that the robotic collective can globally change its shape (elongation) by actively controlling the rate and direction of local rearrangements between neighboring units.

To understand the ability of the robotic collective to actively control its strength and yielding, we studied its response to externally applied loads. Whereas in the absence of internal active forces, the robotic collective behaves as a solid and can sustain substantial loads, activating fluctuating interunit forces changes the material characteristics of the collective, fluidizing it and allowing an external load to deform it (Fig. 3G). By restricting the fluctuating forces to specific regions of the robotic collective, it is possible to fluidize only these regions, providing spatial control over its material state (Fig. 3H). Quantification of the stress-strain relation for the robotic collective showed that it switched from a brittle, elastic solid material in the absence of force fluctuations to a yield stress material when force fluctuations are activated (Fig. 3I). To reveal the effect of force fluctuations on the yield stress, we held the interunit force constant and measured the yield stress of the robotic collective for increasing force fluctuation amplitudes. We found that the yield stress decreases with increasing force fluctuations and that it can be controlled across nearly an order of magnitude (Fig. 3J), enabling substantial changes in strength. These behaviors are reminiscent of jamming and glass (rigidity) transitions in particulate systems (*40*, *43*). Our results show that it is possible to control changes in the material state of the robotic collective (by means of rigidity transition or fluidization), as well as its strength, in space and time.

Functional behaviors of robotic materials

We next demonstrated proof-of-concept "robotic material" behaviors, including structure forming, healing, manipulation, tool forming, and structure melting. We first formed a structure by controlling force fluctuations and polarization of the units in space and time, enabling local softening and shaping into pillars that merged to form an arch (Fig. 4A). Switching off force fluctuations rigidified the arch, allowing it to sustain substantial loads. Beyond the formation of structures, the ability to locally drive fluidization of the robotic collective facilitated the closure of defects in a structure, akin to healing wounds in living tissues (Fig. 4B). More complex spatiotemporal tuning of shape and strength of the collective enabled manipulation of objects, for instance, by applying force to the object that moves it to a target location (Fig. 4C). It was also possible to reshape the robotic collective into "tools," allowing it to perform tasks. For instance, by flowing the robotic collective around objects and rigidifying it afterward, we created a custom "wrench," with which an object could be rotated (Fig. 4D). Finally, we created adaptive supporting structures. The collective was able to support a human (~700 N), which is >500 times the weight of a single robotic unit (1.3 N), and then flow under its own weight (Fig. 4E). These examples show that robotic collectives can be turned into programmable materials with the ability to change their shape and strength in space and time, enabling them to perform specific functions (Fig. 4, figs. S9 and S10, and movies S4 and S6).

Conclusions

In this study, we built robotic collectives that encode key cellular processes into individual robotic units, enabling units to rearrange deep inside an otherwise jammed system. This allowed us to make substantial changes to the shape and strength of the system: Starting from a stiff, jammed collective, we controlled the fluidization of certain regions and then transitioned it all back to rigid. This overcomes the inability to reconfigure robotic collectives in the bulk and opens the possibility of robotic materials with dynamic shape and strength. Although currently limited to 20 robotic units at a relatively large scale, our simulations indicate that these properties are scalable to systems with large numbers of miniaturized units. Beyond robotics, these collectives will enable the study of phase transitions in active matter and the properties of active mechanics in particulate systems and will potentially help define hypotheses for biological research. Indeed, our results showing that fluctuations reduce the power required for changes in strength and shape raise the possibility that biological tissues introduce active tension fluctuations for similar energetic constraints. Finally, the combination of these robotic collectives with state-of-the-art control methods to modulate the interunit interactions could lead to exciting emergent capabilities in robotic materials.

REFERENCES AND NOTES

1. M. A. McEvoy, N. Correll, *Science* **347**, 1261689 (2015).
2. T. Toffoli, N. Margolus, *Physica D* **47**, 263–272 (1991).
3. S. C. Goldstein, J. D. Campbell, T. C. Mowry, *Computer* **38**, 99–101 (2005).
4. T. Fukuda, T. Ueyama, Y. Kawauchi, F. Arai, *Comput. Electr. Eng.* **18**, 11–39 (1992).
5. M. Jelasity *et al*., *IEEE Intell. Syst.* **21**, 50–58 (2006).
6. M. Yim *et al*., *IEEE Robot. Autom. Mag.* **14**, 43–52 (2007).
7. D. Mackenzie, *Science* **301**, 754–756 (2003).
8. M. Rubenstein, A. Cornejo, R. Nagpal, *Science* **345**, 795–799 (2014).
9. I. Slavkov *et al*., *Sci. Robot.* **3**, eaau9178 (2018).
10. W. Savoie *et al*., *Sci. Robot.* **4**, eaax4316 (2019).
11. S. Li *et al*., *Nature* **567**, 361–365 (2019).
12. M. Le Goc *et al*., in *Proceedings of the 29th Annual Symposium on User Interface Software and Technology (UIST) '16*, pp. 97–109.
13. J. Werfel, K. Petersen, R. Nagpal, *Science* **343**, 754–758 (2014).
14. J. Lipton, L. Chin, J. Miske, D. Rus, in *2019 IEEE/RSJ International Conference on Intelligent Robots and Systems (IROS)*, pp. 7460–7466.
15. M. A. Karimi, V. Alizadehyazdi, B.-P. Busque, H. M. Jaeger, M. Spenko, in *2020 3rd IEEE International Conference on Soft Robotics (RoboSoft)*, pp. 291–296.
16. S. Li *et al*., *Sci. Adv.* **7**, eabe8494 (2021).

17. J. Paulos *et al*., *IEEE Trans. Autom. Sci. Eng.* **12**, 958–968 (2015).
18. J. Wang *et al*., *Nat. Commun.* **15**, 8853 (2024).
19. J. W. Romanishin, K. Gilpin, D. Rus, in *2013 IEEE/RSJ International Conference on Intelligent Robots and Systems*, pp. 4288–4295.
20. G. Liang, H. Luo, M. Li, H. Qian, T. L. Lam, in *2020 IEEE/RSJ International Conference on Intelligent Robots and Systems (IROS)*, pp. 6506–6513.
21. P. Swissler, M. Rubenstein, in *2020 IEEE/RSJ International Conference on Intelligent Robots and Systems (IROS)*, pp. 3340–3347.
22. C. Liu, Q. Lin, H. Kim, M. Yim, *Auton. Robots* **47**, 211–228 (2023).
23. B. Saintyves, M. Spenko, H. M. Jaeger, *Sci. Robot.* **9**, eadh4130 (2024).
24. D. Rus, M. Vona, *Auton. Robots* **10**, 107–124 (2001).
25. A. Vergara, Y. S. Lau, R.-F. Mendoza-Garcia, J. C. Zagal, *PLOS ONE* **12**, e0169179 (2017).
26. W. Savoie, H. Tuazon, I. Tiwari, M. S. Bhamla, D. I. Goldman, *Soft Matter* **19**, 1952–1965 (2023).
27. J. Campbell, P. Pillai, *Int. J. Robot. Res.* **27**, 299–314 (2008).
28. H. Bojinov, A. Casal, T. Hogg, in *Proceedings 2000 ICRA. Millennium Conference. IEEE International Conference on Robotics and Automation. Symposia Proceedings (Cat. No.00CH37065)*, vol. 2, pp. 1734–1741.
29. T. Lecuit, L. Le Goff, *Nature* **450**, 189–192 (2007).
30. O. Campàs, I. Noordstra, A. S. Yap, *Nat. Rev. Mol. Cell Biol.* **25**, 252–269 (2024).
31. C.-P. Heisenberg, Y. Bellaïche, *Cell* **153**, 948–962 (2013).
32. C. Collinet, T. Lecuit, *Nat. Rev. Mol. Cell Biol.* **22**, 245–265 (2021).
33. D. Gilmour, M. Rembold, M. Leptin, *Nature* **541**, 311–320 (2017).
34. M. Tada, C.-P. Heisenberg, *Development* **139**, 3897–3904 (2012).
35. T. Lecuit, P.-F. Lenne, *Nat. Rev. Mol. Cell Biol.* **8**, 633–644 (2007).
36. J. B. Wallingford, S. E. Fraser, R. M. Harland, *Dev. Cell* **2**, 695–706 (2002).
37. P.-F. Lenne, V. Trivedi, *Nat. Commun.* **13**, 664 (2022).
38. A. Mongera *et al*., *Nature* **561**, 401–405 (2018).
39. T. Lecuit, P.-F. Lenne, E. Munro, *Annu. Rev. Cell Dev. Biol.* **27**, 157–184 (2011).
40. D. Bonn, M. M. Denn, L. Berthier, T. Divoux, S. Manneville, *Rev. Mod. Phys.* **89**, 035005 (2017).
41. S. Cohen-Addad, R. Höhler, O. Pitois, *Annu. Rev. Fluid Mech.* **45**, 241–267 (2013).
42. S. Kim, M. Pochitaloff, G. A. Stooke-Vaughan, O. Campàs, *Nat. Phys.* **17**, 859–866 (2021).
43. P. J. Lu, D. A. Weitz, *Annu. Rev. Condens. Matter Phys.* **4**, 217–233 (2013).
44. M. R. Devlin, S. Kim, O. Campàs, E. W. Hawkes, Material-like robotic collectives with spatiotemporal control of strength and shape [Dataset], version v1.0, Zenodo (2024); https://doi.org/10.5281/zenodo.14536490.

ACKNOWLEDGMENTS

We thank S. Man and K. Morozov for assistance in the development of the robots, and D. Goldman for discussions. **Funding:** NSF grant 1925373 (E.W.H., M.R.D.); Deutsche Forschungsgemeinschaft (DFG, German Research Foundation) under Germany's Excellence Strategy–EXC 2068–390729961 (O.C., S.K.); Cluster of Excellence Physics of Life of TU Dresden. **Author contributions:** Conceptualization: M.R.D., O.C., E.W.H. Investigation: M.R.D., S.K. Methodology: M.R.D., S.K., O.C., E.W.H. Software: S.K., M.R.D. Supervision: O.C., E.W.H. Visualization: M.R.D., S.K. Writing– original draft: M.R.D., O.C., E.W.H. Writing – review & editing: M.R.D., S.K., O.C., E.W.H. **Competing interests:** The authors declare that they have no competing interests. **Data and materials availability:** The custom-made robotics, data processing, and code used in this article are publicly available in Zenodo (*44*).

SUPPLEMENTARY MATERIALS

science.org/doi/10.1126/science.ads7942
Materials and Methods
Supplementary Text
Figs. S1 to S10
Tables S1 and S2
Reference (*45*)
Movies S1 to S6

Submitted 28 August 2024; accepted 13 January 2025
10.1126/science.ads7942

ORGANIC CHEMISTRY

Spiro-C(sp^3)-atom transfer: Creating rigid three-dimensional structures with Ph_2SCN_2

Qiu Sun[1], Jan-Niklas Belting[1], Julian Hauda[1], David Tymann[1], Patrick W. Antoni[1], Richard Goddard[2], Max M. Hansmann[1]*

The introduction of a single C-atom into organic substrates typically results in the formation of flat molecules containing unsaturated C(sp)-centers. Adding a single C(sp^3)-atom surrounded by four σ-C–C bonds, which opens up the three-dimensional space, is an unresolved problem in synthetic chemistry. We report the synthesis and application of the diazosulfur ylide $Ph_2S{=}C{=}N_2$ reagent that combines the reactivity of both sulfur ylides and diazo compounds to create carbon spiro-centers in a general fashion by the sequential or single-step installation of a C(sp^3)-atom. New C–C and C–X (where X is O or N) bonds can be created around the C(sp^3)-atom, which can ultimately be extended to four C–C σ-bonds in one step without resorting to transition metal catalysis. Ph_2SCN_2 can also be used to access highly strained frameworks containing (oxa) spiro[2.2]pentanes as well as tricyclic spiro-compounds.

The formation of three-dimensional (3D) structures is of fundamental importance in organic chemistry and fragment-based drug discovery (*1*, *2*). In particular, the quest to create 3D scaffolds such as cubanes (*3*), propellanes (*4*, *5*), bicyclobutanes (*6*), or spiro[2.2]pentanes (*7*–*9*) has pushed the development of synthetic methods and triggered strong interest to deviate from the widely explored 2D landscape. Carbon insertion in the context of skeletal editing (*10*) in general relates to methods that introduce "C–R" fragments into C(sp^2)–C(sp^2) bonds, which typically generates flat, aromatic (hetero)cycles (*11*–*15*). Pure C-atom transfer reactions, in which a single atom is transferred, include textbook reactions such as the Seyferth-Gilbert homologation (**I**) (*16*), the Corey-Fuchs reaction (**IV**) (*17*) (Fig. 1A), or the Doering-LaFlamme allene synthesis (*18*). Recently, we were able to expand the repertoire for C-atom transfer by introducing Ph_3PCN_2 (**III**) (where Ph is phenyl) (*19*). However, all of the previously described methods proceed via an unsaturated carbene or vinylidene intermediate (**VI**), which results in sp-hybridized C-atoms. Hence, three-dimensionality is not generated by these types of C(sp)-atom transfer reactions. By contrast, C-atom transfer reactions that accomplish the transfer of a C(sp^3)-atom have rarely been documented and represent a challenging endeavor (Fig. 1B) (*20*, *21*). Carbon arc discharge methods (*22*–*24*), C-atom precursors such as carbon suboxide or diazotetrazole (*25*), or chromium carbido complexes (*26*) were reported to react unselectively and resulted in only very low yields of C-atom transfer products (*20*, *21*). In 2010, Kato, Baceiredo, and co-workers reported the synthesis of the bis(ylide) **VIII**, which exhibited promising activity (*27*); however, no further studies regarding applications have been carried out. A different approach was described by Tobisu and co-workers in 2023, who succeeded in using *N*-heterocyclic carbenes (**X**) as a C(sp^3)-atom transfer reagent (*28*, *29*). By forming one new C–C bond, acrylamides (**IX**) could be cyclized to γ-lactams (**XI**). Nevertheless, a generalizable strategy for precise and high-yielding installation of C(sp^3)-atoms to efficiently form four new C–C single bonds remains a major challenge for synthetic chemistry.

Both the Seyferth-Gilbert reagent **I** and bis(ylide) **VIII** can be regarded as C-atom transfer reagents of the general structure X=C=Y, which we aimed to modify in such a way that carbene or vinylidene intermediates during the C-atom transfer process are avoided. Both sulfur ylides (*30*, *31*) and diazo compounds (*32*, *33*) are known to exhibit carbene-free cyclopropanation reactivity (Fig. 1C). Combining both functionalities in one molecule should give access to an ideal reagent for the creation of spiro-C-centers, particularly for the direct formation of spiro[2.2]pentanes in which four new C–C bonds are created. In this work, we describe the synthesis and isolation of the crystalline diazosulfur ylide $Ph_2S{=}C{=}N_2$ (**3**) and its successful application as a single-step C(sp^3)-atom transfer reagent for the construction of sp^3-rich, 3D, and rigid spirocyclic scaffolds from readily available 2D feedstock molecules.

Preparation, structure, and computational investigation of diazosulfur ylide 3

Recently, we described the reaction of hexaphenylcarbodiphosphorane ($Ph_3P{=}C{=}PPh_3$) with nitrous oxide (N_2O) to generate $Ph_3P{=}C{=}N_2$ along with triphenylphosphine oxide ($Ph_3P{=}O$) via a Ph_3P/N_2 exchange (*19*). Considering the formal exchange of phosphorus and sulfur ylides ($R_3P{=}[C]$ versus $R_2S{=}[C]$), we aimed to use N_2O to access the desired diazosulfur ylide

[1]Fakultät für Chemie und Chemische Biologie, Technische Universität Dortmund, Otto-Hahn-Str. 6, Dortmund, Germany. [2]Max-Planck-Institut für Kohlenforschung, Kaiser-Wilhelm-Platz 1, Mülheim an der Ruhr, Germany.
***Corresponding author. Email: max.hansmann@tu-dortmund.de**

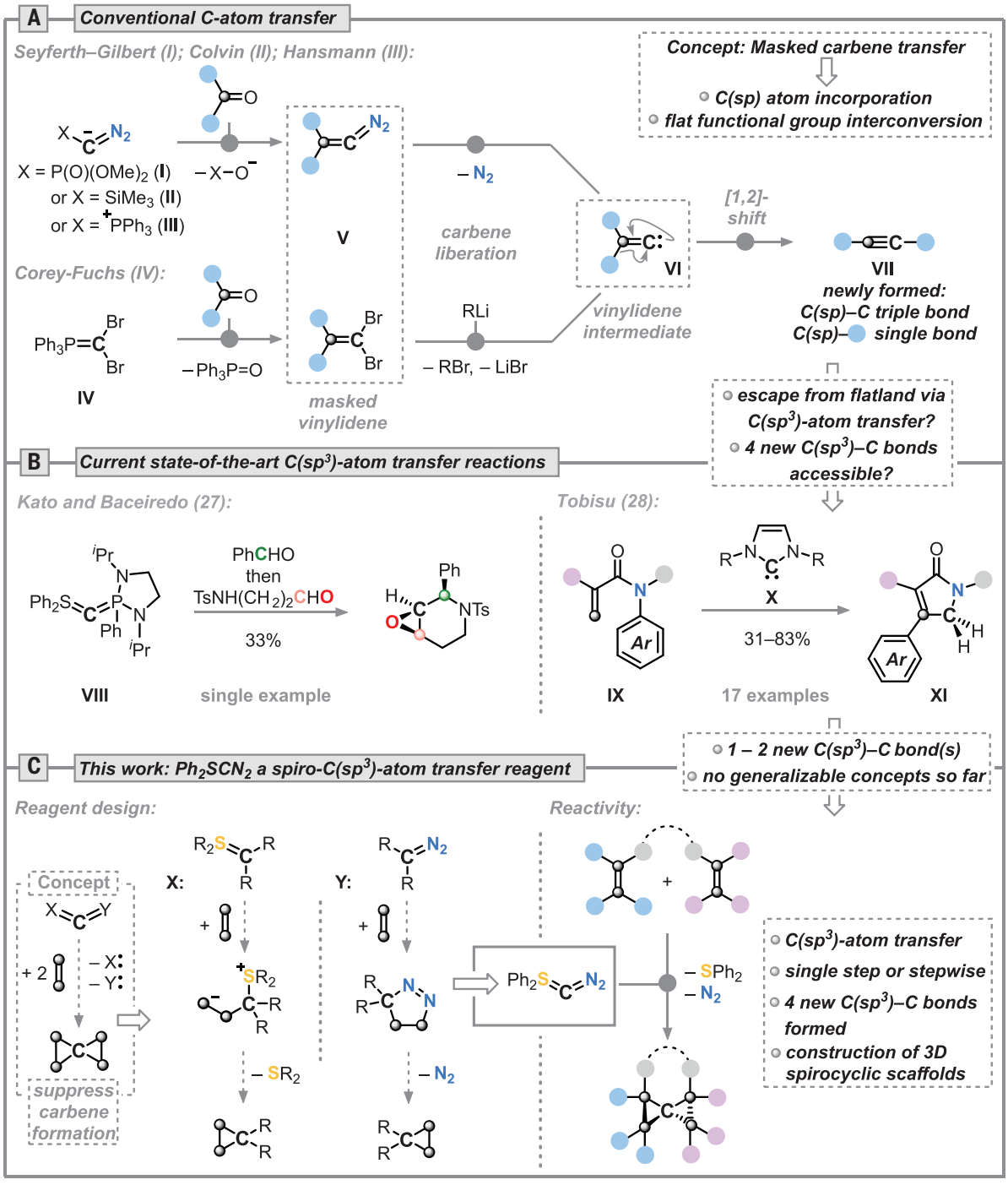

Fig. 1. Progress toward a general C(sp^3)-atom transfer reagent. (**A**) Alkyne syntheses via one-carbon homologation. (**B**) Limited literature precedents for C(sp^3)-atom transfer reagents (*20*, *21*). (**C**) Diazosulfur ylide Ph_2SCN_2 as a C(sp^3)-atom transfer reagent for the single-step construction of 3D scaffolds. Ar, aryl; Me, methyl; Ph, phenyl; ^{i}Pr, *iso*-propyl; Ts, tosyl.

$Ph_2S{=}C{=}N_2$ (**3**); hence, $Ph_2S{=}C{=}PPh_3$ (**2a**) was considered to be a suitable precursor. Inspired by the work of Kato and Baceiredo (*27*), we deprotonated the phosphonium salt **1a** [see supplementary materials (SM) for experimental details] with potassium bis(trimethylsilyl) amide (KHMDS) to obtain the new mixed P/S-ylide **2a** (57%). Subsequent reaction of **2a** with N_2O (–78°C to room temperature) showed full conversion after 1 hour. Additionally, ^{31}P nuclear magnetic resonance (NMR) indicated the formation of $Ph_3P{=}O$ (**4a**) (fig. S32), whereas in situ infrared spectroscopy showed a characteristic diazo N=N stretching band at 1960 cm^{-1} (fig. S33) (*34*). Note that the concomitant formation of diphenyl sulfoxide ($Ph_2S{=}O$) was not observed. Isolation and separation of the desired diazosulfur ylide **3** from $Ph_3P{=}O$ proved challenging but was solved by switching to Kato-Baceiredo ylide **2b**, in which the phosphine oxide **4b** could be simply separated

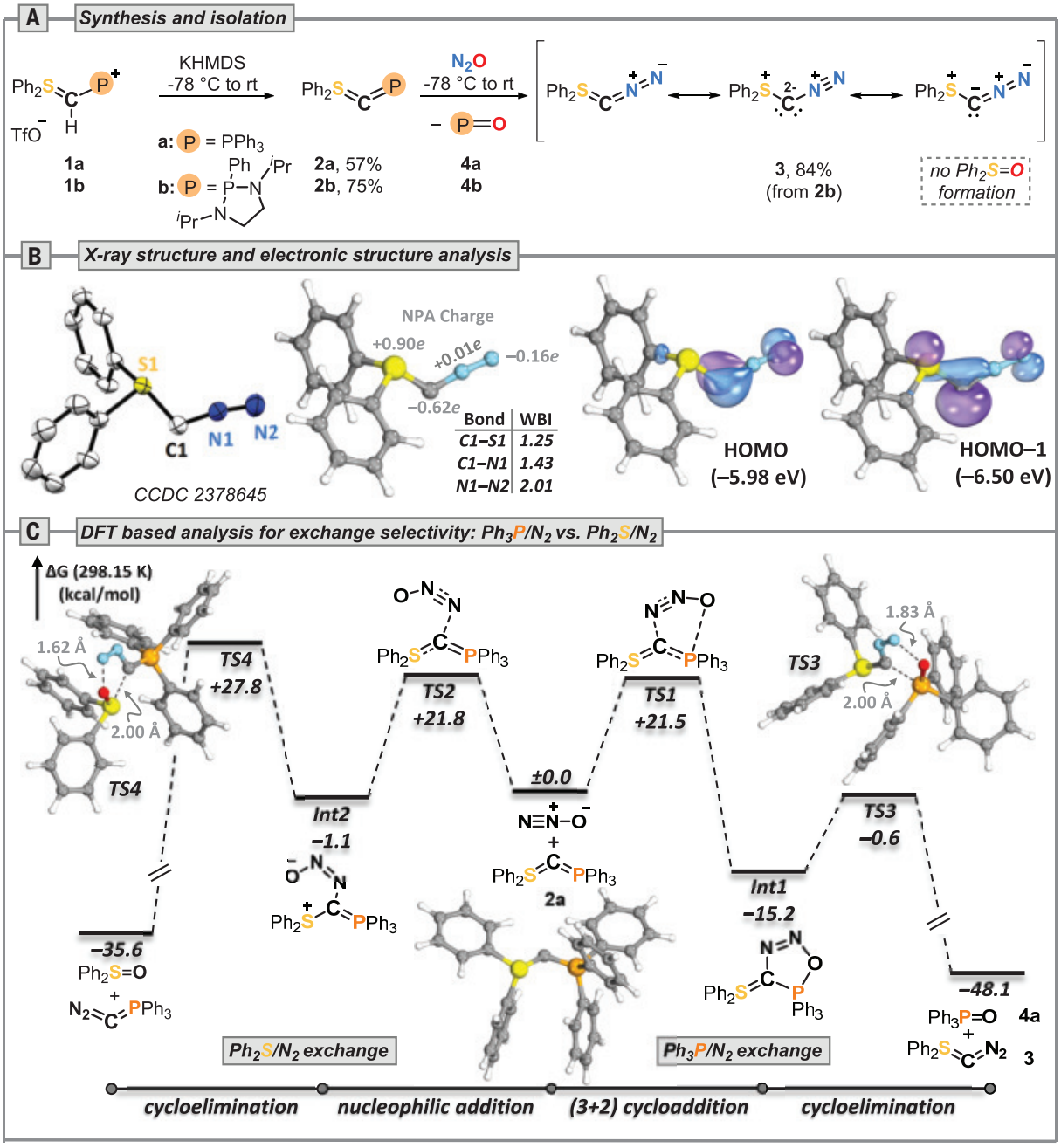

Fig. 2. Preparation, structure, and computational investigation of diazosulfur ylide 3. (**A**) PR_3/N_2 exchange to access diazosulfur ylide **3**. Conditions are as follows: N_2O (1.0 bar), −78°C to room temperature (rt), and 1 hour in THF. (**B**) X-ray solid-state structure and frontier molecular orbitals (isovalue = 0.6), charges, and WBIs. (**C**) Energy profile at the PBE0-D3(BJ)/def2-TZVP/SMD(THF) level of theory. ^{t}Bu, *tert*-butyl; Et, ethyl; NPA, natural population analysis; OTf, triflate.

by washing. This procedure resulted in the isolation of the target **3** as a crystalline, light yellow solid with a yield of 84%.

The structure of **3** from x-ray diffraction analysis (Fig. 2B) shows a S1–C1 bond length [1.727(2) Å] that is longer than that of its precursor (**2b**) [1.684(3) Å] but still in the range of the S=C bond lengths of sulfur ylides (fig. S288). The C1–N1 bond [1.286(3) Å] is longer and the N1–N2 bond [1.151(3) Å] is shorter than those in Ph_3PCN_2 [1.268(5) and 1.169(5) Å, respectively] (*19*) which hints at the increased lability toward dinitrogen release. The angle at the central carbon S1–C1–N1 [112.6(2)°] is slightly increased compared with that of its precursor (**2b**) [109.8(2)°]; however, it is more acute compared with that of Ph_3PCN_2 [121.6(3)°], as well as that of all diazoalkene structures deposited in the Cambridge Crystallographic Database (CCD) [118.5(2)° to 125.9(3)°] (*35*). The ^{13}C NMR shift of the central carbon resonance appears at 21.3 parts per million (THF-d_8, where THF is tetrahydrofuran), which was confirmed by ^{13}C-labeling experiments ($Ph_2S^{13}CN_2$; fig. S36) and gauge-invariant atomic orbital calculations (fig. S312).

Natural population analysis indicated that the central C-atom of **3** bears a partial negative charge (−0.62 *e*), whereas the sulfur atom possesses an almost entirely positive charge (+0.90 *e*). The internal N-atom is neutral (+0.01 *e*), and the terminal N-atom has a slightly negative charge (−0.16 *e*). Wiberg bond indices (WBIs) indicate a pronounced C–S single bond character (WBI = 1.25) and a N–N double bond (WBI = 2.01), whereas the C–N

bond lies in between a single and a double bond (WBI = 1.43). These values are positioned in the range of those of other unsaturated S-ylides [WBI(S–C) in **2b** = 1.21 (*27*); WBI(S–C) in $Ph_2S{=}C{=}SPh_2$ = 1.22 (*36*)] and unsaturated diazo compounds (*37*). Molecular orbital analysis and natural bond orbital analysis (fig. S313 and S314) indicated that the central C atom bears two orthogonal lone pairs. The highest occupied molecular orbital–1 (HOMO-1) possesses σ-symmetry, whereas the HOMO has π-symmetry (Fig. 2B). In addition to the heterocumulene representation, the resonance structures [$R_2S^+–C^{2-}–N^+{\equiv}N$] and [$R_2S^+–C^-{=}N^+{=}N^-$] (see Fig. 2A) are required to adequately describe the binding situation in ***3***. Hence, ***3*** can also be attributed to a divalent carbon(0) substance class (*38*). Differential scanning calorimetry and thermal gravimetric analysis experiments of ***3*** show a sharp exergonic decomposition at 80°C [enthalpy change (ΔH) ~ 1100 J g^{-1}; figs. S27 to S29], highlighting the lower stability of S- versus P-ylides. Compound ***3*** decomposes slowly over hours in solution at room temperature to diphenyl sulfide and a solid precipitate that we assume to be mainly carbon. Nevertheless, ***3*** can be easily generated cleanly and stored for more than 6 months as a solid at −40°C under inert conditions.

To get an understanding of the exclusive Ph_3P/N_2 over Ph_2S/N_2 exchange selectivity, we performed density functional theory calculations (Fig. 2C). High HOMO-1 and HOMO energy levels (fig. S313) make **2a** a pronounced carbon nucleophile, triggering a nucleophilic attack on the terminal N-atom of N_2O (*39*). Two competing transition states, **TS1** [free Gibbs energy change ($\Delta G^{\ddagger}$) = 21.5 kcal mol^{-1}] and **TS2** ($\Delta G^{\ddagger}$ = 21.8 kcal mol^{-1}), can be accessed, which finally leads to Ph_3P/N_2 or Ph_2S/N_2 exchange. Whereas **TS1** leads irreversibly to the P–O adduct **Int1** via a highly asynchronous concerted (3+2) cycloaddition, **TS2** leads to the almost energy-neutral formation of the zwitterion **Int2**. Furthermore, a low rotation barrier along the newly formed C–N bond enables a rapid interconversion of **Int2** to **Int1** (fig. S315). Whereas both cycloelimination processes possess a high thermodynamic driving force [free Gibbs energy change of Ph_3P and N_2 exchange ($\Delta G_{P\rightarrow N2}$) = −48.1 kcal mol^{-1}; free Gibbs energy change of Ph_2S and N_2 exchange ($\Delta G_{S\rightarrow N2}$) = −35.6 kcal mol^{-1}], the barrier for the elimination of the sulfoxide is markedly higher (**TS4**: $\Delta G^{\ddagger}$ = +27.8 kcal mol^{-1} versus **TS3**: $\Delta G^{\ddagger}$ = −0.6 kcal mol^{-1}), which is most likely due to the intrinsic property of sulfur to avoid the tetravalent species (sulfuranes; for a more in-depth analysis, see SM) (*40*).

Reactivity studies: (3+2) Cycloaddition and consecutive C(sp^3)-atom transfer

Reactivity studies of ***3*** toward consecutive C(sp^3)-atom transfer were subsequently carried out

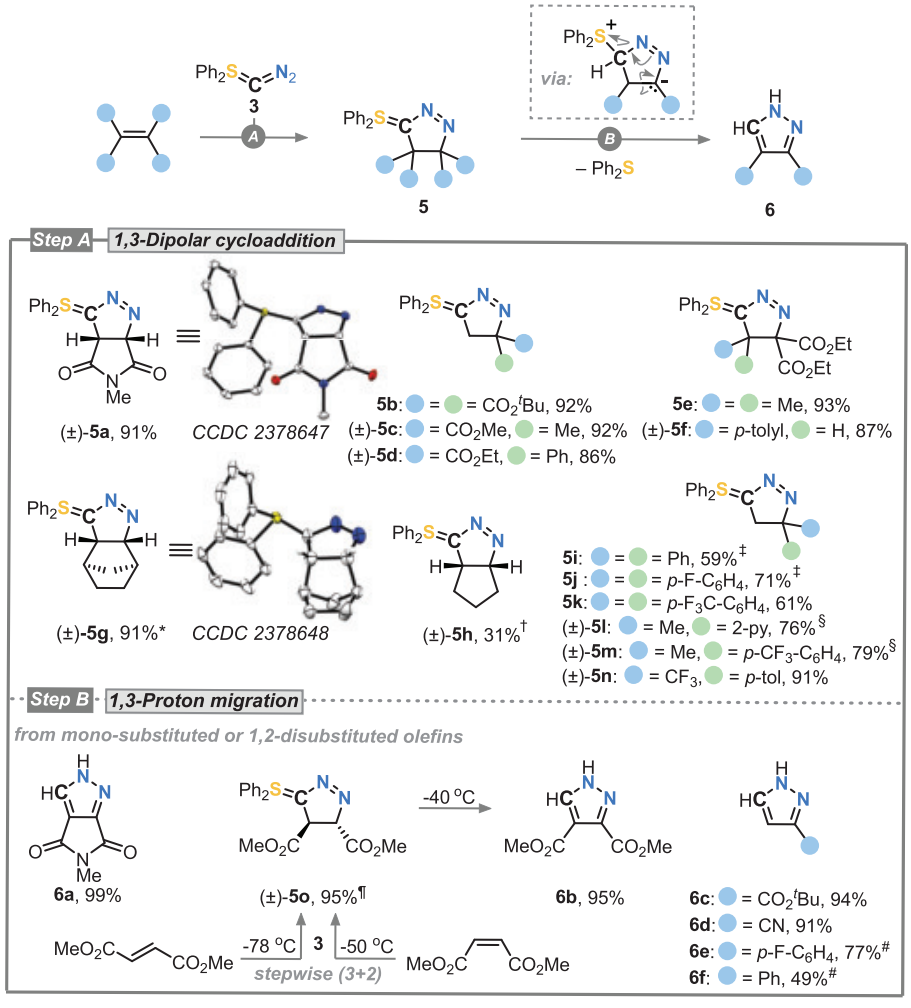

Fig. 3. (3+2) Cycloaddition to sulfur ylides 5 (step A) and pyrazoles 6 (step B). Step A: The reaction with olefins (1 equiv.) was conducted in THF at room temperature for 15 min. *5.0 equiv. of norbornene for 12 hours; †20.0 equiv. of cyclopentene for 96 hours; ‡48-hour reaction time; §24-hour reaction time. Step B: The reaction with monosubstituted or 1,2-disubstituted olefins were conducted in THF at room temperature for 1 hour. ¶NMR yield; #12-hour reaction time.

(Fig. 3). Upon treatment of ***3*** with π-acceptor–substituted olefins, complete consumption of the starting materials was observed in a few minutes at room temperature (step A in Fig. 3). For instance, in the case of *N*-methyl maleimide, the desired pyrazoline sulfur ylide **5a** can be isolated after 15 min with an excellent yield (91%). 1,1-Disubstituted olefins with two or one ester groups (**5b** to **5d**), and tri- and tetrasubstituted olefins all yielded the desired cycloadducts (**5e** and **5f**) cleanly. Olefinic reactants that are not π-acceptor–substituted were also reactive. Norbornene led to **5g** isolated as a single exo diastereomer (91%) and even cyclopentene afforded very slowly (4 days) the desired cycloadduct **5h** (31%), whereas cyclohexene and 1-octene were unreactive. The reactivity of angle-tensioned double bonds follows the same trend as that observed for the kinetics of the reaction of azides with dipolarophiles (*41*). Nonactivated styrene derivatives required longer reaction times (48 hours for **5i** and **5j**, 15 min for **5k**) but afforded the desired cycloadducts (**5i** to **5k**) in moderate to good yields (59 to 71%). Heteroaromatic olefins such as a 2-pyridine–derived olefin and alkyl or aryl olefins as well as fluorinated (CF_3) olefins afforded the (3+2) cycloaddition products **5l** to **5n**, respectively. If longer reaction times were chosen for the reaction of ***3*** with monosubstituted olefins or 1,2-disubstituted olefins, instead of the expected cycloaddition products **5**, the functionalized pyrazoles **6a** to **6f** could also be obtained in high yields (49 to 99%) (*42*). In this case, the fast (3+2) cycloaddition is followed by a slower 1,3-proton shift and Ph_2S elimination, which leads to the aromatic pyrazoles (step B in Fig. 3). Products **5g** and **5h** do not aromatize to the pyrazoles, most likely because of the lack of C–H acidity. Low-temperature NMR studies with dimethyl fumarate and dimethyl malonate confirmed a stepwise (3+2) cycloaddition

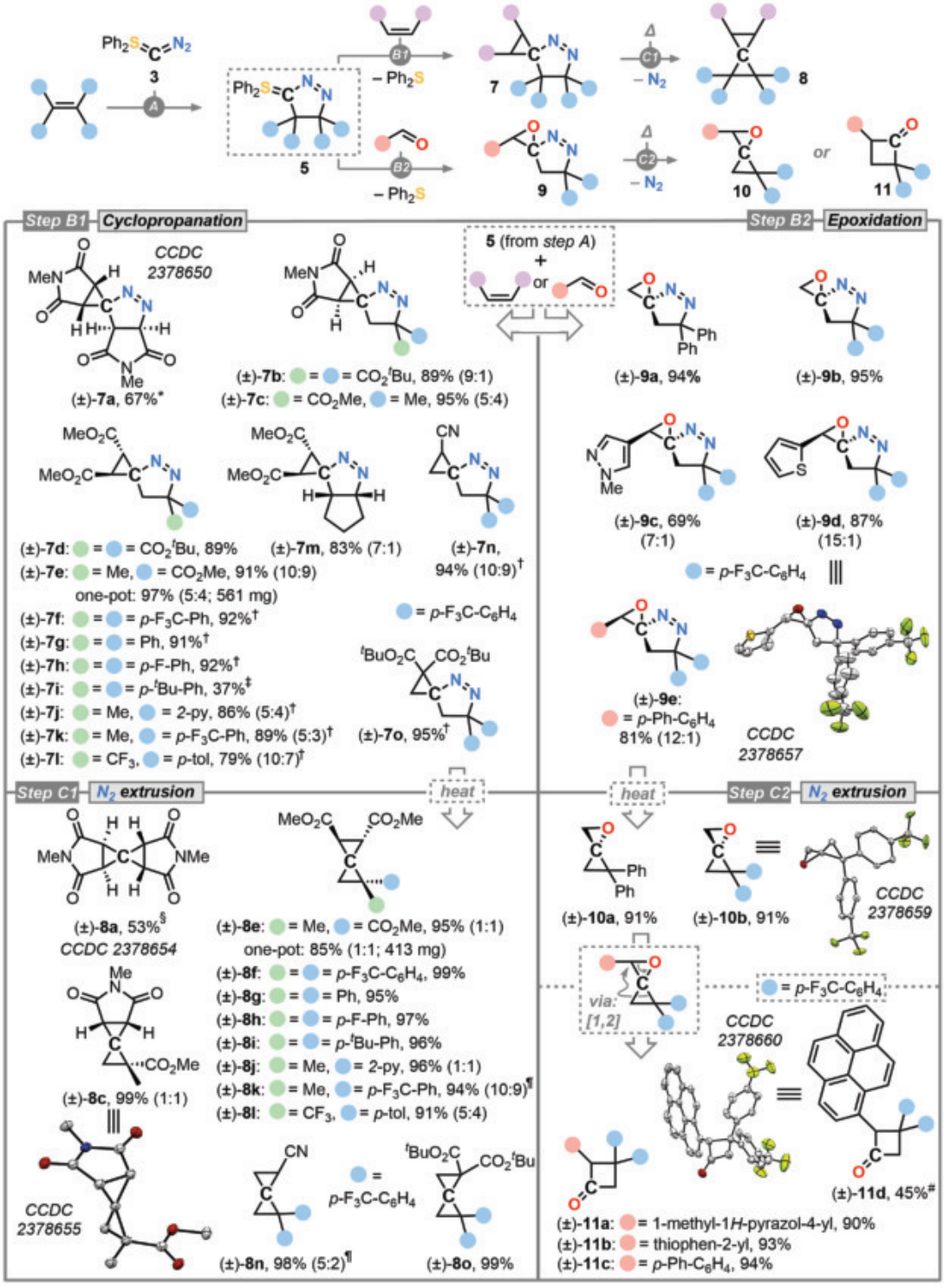

Fig. 4. Stepwise C(sp^3)-atom transfer to access spiro[2.2]pentanes (steps B1 and C1) and oxaspiro[2.2] pentanes (steps B2 and C2). Step B1: The one-pot reaction with olefins in two steps was conducted in THF at 50°C for 2 hours. *Conducted starting at −40°C and then warmed up to room temperature with 3.0 equiv. of *N*-methyl maleimide; †Conducted with isolated S-ylides; ‡One-pot reaction in which the first step took 96 hours. Step C1: N_2 extrusion reaction at 130°C in deuterated bromobenzene (C_6D_5Br) for 3 hours. §At 165°C for 48 hours; ¶At 150°C for 5 hours. Step B2: The reactions of pyrazoline **5** with aldehydes were conducted in THF. Step C2: N_2 extrusion at 80°C in C_6D_6. #Conducted in one step from **5k** and pyrene-1-carbaldehyde.

mechanism in which both afforded the same trans-stereochemical outcome (**5o**) (figs. S76 and S77).

Next, we investigated whether the remaining S-ylide moiety of the pyrazolines **5** shows the desired cyclopropanation reactivity (step B1 in Fig. 4). The maleimide-based sulfur ylide **5a** was treated with one equivalent (equiv.) of *N*-methyl maleimide to afford cyclopropane **7a** in good yield (67%), which could also be obtained directly from **3** with 3.0 equiv. of *N*-methyl maleimide in a one-pot process with the same yield (67%). This result showcases a C(sp^3)-atom transfer, forming three new C–C bonds in a single step. The use of the sulfur ylides **5b** and **5c** together with *N*-methyl maleimide led to the corresponding cyclopropanes **7b** and **7c** in excellent yields. The reaction of the S-ylides **5** with fumaric and maleic acid esters afforded the spiro compound **7d** with the same relative configuration in agreement with a stepwise Corey-Chaykovsky–type mechanism (*43*). Diester S-ylide **5b**, ester/alkyl S-ylide **5c**, diaryl S-ylides **5i** to **5k**, heteroaromatic/alkyl S-ylide **5l** and

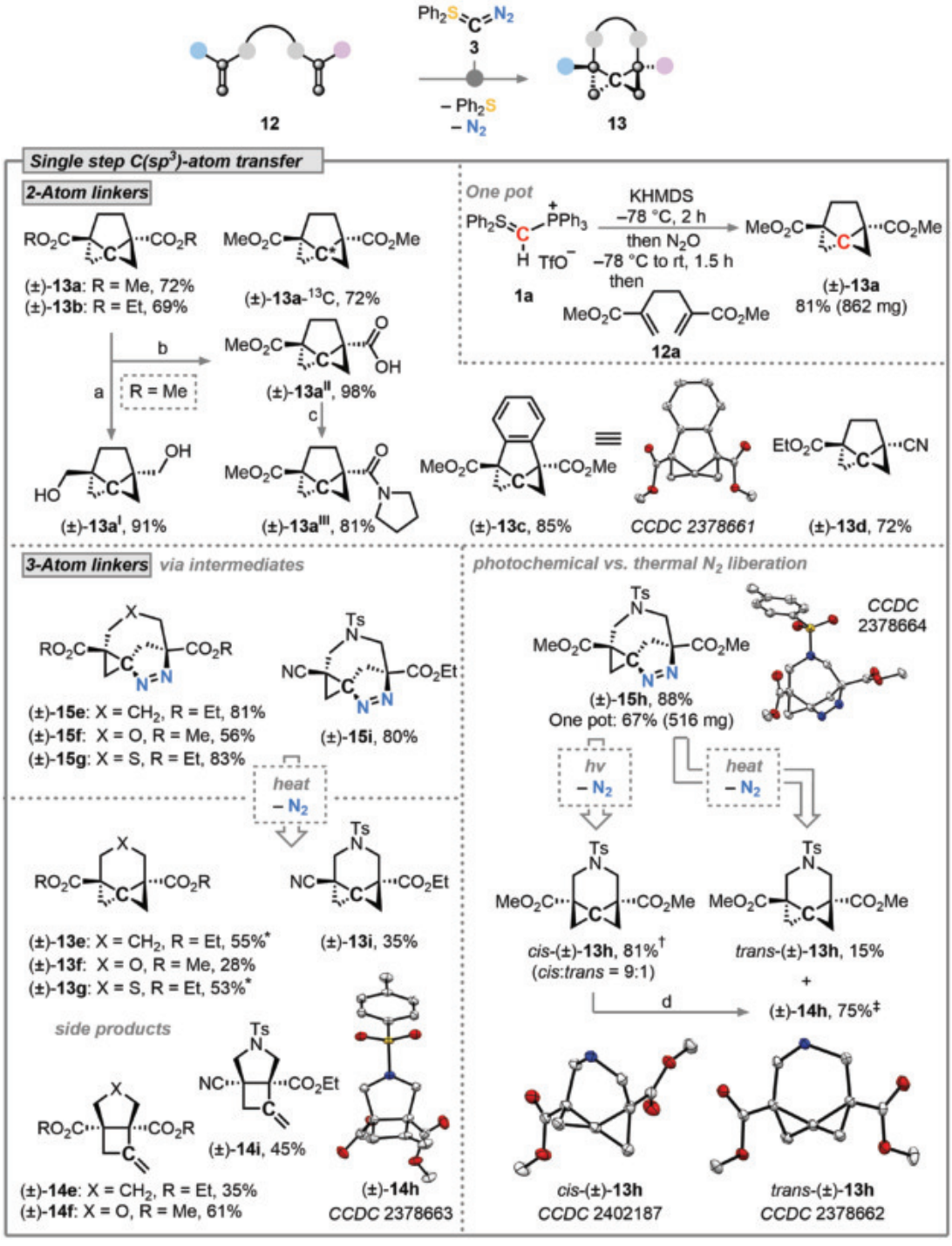

Fig. 5. Single step spiro-C(sp^3)-atom transfer to afford bridged spiropentanes. The reactions were performed in THF. The two-atom linker reactions (**13a** to **13d**) were conducted at room temperature. The three-atom linker reactions were conducted starting at –78°C, with the temperature gradually increased to 70°C. The generation of tricycles **15** was conducted at –78°C and warmed up to room temperature. *Conducted at –78°C and heated to 120°C; †The irradiation reaction was conducted with 370 nm light at room temperature for 12 hours; ‡70°C for the thermolysis reaction of *cis*-**13h**. In the x-ray structures of cis- and trans-**13h**, the *N*-tosyl group was omitted for clarity. a: $LiAlH_4$ (2.0 equiv.) in THF, 0°C, 40 min; b: NaOH (1.05 equiv.), THF-methanol (THF-MeOH) (40:1), room temperature, 17 hours; c: pyrrolidine (1.4 equiv.), 1-ethyl-3-(3-dimethylaminopropyl)carbodiimide (EDC) (1.6 equiv.), 4-dimethylaminopyridine (DMAP) (0.2 equiv.), CH_2Cl_2, room temperature, 16 hours; d: slow reaction at room temperature or quantitative upon heating (see SM).

fluorinated S-ylides **5m** and **5n** could all be trapped with dimethyl fumarate to afford the cyclopropanation products **7e** to **7l**. Only S-ylides substituted in the α-position (**5e** and **5f**) were unreactive; however, the α-substituted cyclopentane–containing S-ylide **5h** also gave the desired product **7m**. The trapping was not limited to maleimide and dimethyl fumarate but could also be applied to other electron-deficient olefins, including acrylonitrile or 1,1-diester olefins to give **7n** and **7o** in high yields (94 to 95%).

The next step was to complete the consecutive C(sp^3)-atom transfer (step C1 in Fig. 4). Spirocyclopropane-containing 1-pyrazolines are known substrates for ring-contraction processes, which can be used to synthesize spiro[2.2]pentanes through liberation of N_2 (*44*, *45*). This strategy was exemplified for all 15 1-pyrazolines **7a** to **7o**, which were typically heated to 130°C. Regardless of the substitution pattern (except **7b** and **7d** featuring 1,1-diester moieties and **7m** containing the cyclopentane fragment), N_2 was released smoothly, and highly substituted spiro[2.2]pentanes **8a**, **8c**, and **8e** to **8o** were obtained in typical excellent yields.

As a proof of concept, a one-pot sequence was developed for the intermolecular C-atom transfer starting from the bench-stable S/P salt **1a** with in situ–generated ***3***. Without isolation of either **2a** or ***3***, sequential addition of two different olefins afforded the cyclopropanation product **7e** in 97% yield (561 mg). N_2-liberation under heating gives the C-atom

transfer product **8e** in 85% yield (413 mg) (see SM for details).

S-ylides are also established in the synthesis of epoxides (*30*, *31*). Aiming to broaden the applicability of reagent ***3***, we targeted the synthesis of spirocyclic epoxides. As a proof of concept, sulfur ylides **5i** and **5k** reacted with formaldehyde or (hetero)aromatic aldehydes to give the spiro-heterocycles **9a** to **9e** in good to excellent yields (69 to 95%; step B2 in Fig. 4). In the case of the unsubstituted epoxides **9a** and **9b**, the desired thermally induced release of N_2 proved to be unproblematic [80°C for 24 hours in deuterated benzene (C_6D_6)] to afford the oxaspiro[2.2]pentanes **10a** and **10b** in high yields (91%; step C2 in Fig. 4). Aromatic epoxides **9c** to **9e** gave the substituted cyclobutanones **11a** to **11c** in excellent yields (90 to 94%), which could also be accessed in one step without isolation of the spiro-cycle (45% for **11d**). In the latter case, the generation of the desired spirocyclic epoxide is most likely followed by a Meinwald-type rearrangement, whereby the higher-substituted carbon atom migrates (*46*, *47*). The three-step sequence we have presented demonstrates the capacity of ***3*** to incorporate two flat olefins or olefin/aldehyde moieties into a 3D (oxa)spiro[2.2]pentane scaffold via C(sp^3)-atom transfer in excellent overall yields.

Reactivity studies: Single-step spiro-C(sp^3)-atom transfer

Encouraged by the reaction sequence leading to (oxa)spiro[2.2]pentanes, we aimed for a single-step spiro-C(sp^3)-atom transfer and selected acceptor-substituted 1,5-hexadienes **12a** to **12d** as starting materials in which cycloaddition and cyclopropanation can occur in the same molecule. Intriguingly, after only 30 min at room temperature, the reaction of ***3*** with dimethyl or diethyl 2,5-dimethylenehexanedioate afforded in one step the complex tricyclic spiropentanes **13a** and **13b** (69 to 72%) in which N_2 loss occurred (Fig. 5). The underlying highly strained (strain energy around 80 kcal mol^{-1}) (*48*, *49*) tricyclic scaffold (tricyclo[4.1.0.$0^{1,3}$]heptane) was first reported by Skattebøl in 1966 (*50*). However, synthetic access proved to be problematic and low yielding, and for functionalized representatives, synthetic approaches are completely lacking. As a proof of concept, the reaction could also be performed with ^{13}C-labeled ***3***-^{13}C, cleanly resulting in **13a**-^{13}C in which a single ^{13}C-atom is directly incorporated. Such labeling could be interesting for future advanced labeling strategies (^{11}C or ^{14}C). Also, a one-pot strategy was developed for the intramolecular C(sp^3)-atom transfer with in situ–generated compound ***3*** (Fig. 5, top right). Without isolation of any air-sensitive intermediate, the one-pot transformation afforded tricycle **13a** in 81% yield (862 mg; see SM for details). Additionally postfunctionalization of the tricyclo[4.1.0.$0^{1,3}$]heptane building block was demonstrated by reduction to give the diol **13a^{I}** (91%), which proved to be robust toward degradation at 80°C over several hours (fig. S283). Selective monosaponification afforded the stable ester/acid building block **13a^{II}** (98%), which could be coupled to give the amide **13a^{III}** (81%), paving the way toward embedding the 3D structures into pharmaceutically relevant drug targets.

The *ortho*-phenyl–bridged diene gave the tetracyclic system (**13c**) with a yield of 85%. This is notable considering the complexity of the underlying mechanism, the number of elementary steps involved in this one-pot transformation, and the markedly high strain of the system. The newly introduced spiro-C-atom contains four new C–C bonds and is highly distorted into a seesaw-disphenoidal geometry, in which the annulated C–C bond [1.412(2) Å] is elongated to decrease the strain (*51*). Because of the high strain, **13c** undergoes slow decomposition in solution (fig. S225) (*51*), whereas all the other saturated tricycles are stable at room temperature. The C_2 symmetric tricycle class features two ester moieties which, based on x-ray analysis, are oriented para in 3D space, but with a sideways-shifted offset (fig. S311). The C-atom transfer is also applicable to an unsymmetrical two-atom-linker starting material, which affords the ester/nitrile functionalized tricyclo[4.1.0.$0^{1,3}$]heptane **13d**.

Ring-size variation and heteroatom incorporation were then investigated. Switching to a longer three-atom tether (CH_2, O, and S moieties) enables isolation of the heterosubstituted tricyclo[5.1.0.$0^{1,3}$]octanes **15e** to **15g** in high yields in which three new stereocenters are introduced. Presumably owing to the decreased ring strain of the tricyclic intermediate, no spontaneous dinitrogen liberation occurred. A nonsymmetrical diene afforded the tricycle **15i**, in which the (3+2) cycloaddition occurred on the ester substituted olefin while the cyclopropanation occurred on the nitrile substituted olefin.

Using a 1,6-heptadiene that also contains heteroatoms (O, S) in the linker chain gave, upon heating, the desired bridged spirotricycles **13e** to **13g** in moderate (**13e**, 55%; **13f**, 28%; and **13g**, 53%) yield, without the isolation of the intermediate **15** being required. Besides the desired products (**13e** to **13g**), azabicyclo[3.2.0]heptanes **14e** and **14f** were formed as by-products. Thermal isomerization of spiro[2.2]pentanes to methylenecyclobutanes is well known but usually requires harsh reaction conditions, for example, 355°C for 27 hours (*52*), and does not proceed with isolated **13e** to **13g** under the reaction conditions. A *N*-tosyl (*N*-Ts) bridge led to tricycle **15h**, which could be scaled up in a one-pot sequence (67%, 516 mg), analogous to the conditions for **13a**. Heating at 70°C afforded the expected tricycle **13h** in low yield (15%), whereas the main product is the bicycle **14h**. However, irradiation of **15h** with a light-emitting diode (LED) (370 nm) led in 81% yield to the unknown *cis*-tricyclo[5.1.0.$0^{1,3}$]octane **13h** (cis:trans = 9:1). Addition of a triplet photosensitizer such as benzophenone (*53*) led to a decrease in the cis:trans selectivity (3:1; fig. S261). The *cis*-tricyclo[5.1.0.$0^{1,3}$]octane core was calculated to have a high strain energy (97 versus 66 kcal mol^{-1} for trans) (*54*), which shows the largest structural deformation (twisting) of any reported spiro-cyclopentane based on a CCD search (see fig. S310). At room temperature, the cis compound slowly rearranged to the olefin **14h**. We assume that the thermal N_2 liberation generates both cis and trans tricycles, whereas under these conditions, the cis product rearranges to **14** (for a mechanistic proposal, see fig. S273).

These fascinating, rigid 3D scaffolds have so far received no attention in drug design as bioisosteres (*55*). Considering the ease of accessing the functionalized tricyclo[4.1.0.$0^{1,3}$]heptane and cis- or trans-heteroatom–substituted tricyclo[5.1.0.$0^{1,3}$]octane cores, we are convinced that besides applications of these scaffolds, other distinct chiral 3D building blocks could easily be assembled using the new C(sp^3)-atom transfer reagent.

Conclusions

We have demonstrated that diazosulfur ylide $Ph_2S{=}C{=}N_2$ (***3***) is a broadly applicable C(sp^3)-atom transfer reagent for the stepwise or single-step construction of up to four new C–C bonds around a highly strained spiro-C-atom. (Oxa)spiropentanes can be rapidly generated and even embedded into rigid tricyclic scaffolds. We are convinced that these findings will stimulate the exploration of additional C(sp^3)-atom transfer reactions, enable access to advanced 3D scaffolds, and extend C-atom transfer into other fields such as main-group and transition-metal chemistry.

REFERENCES AND NOTES

1. F. Lovering, J. Bikker, C. Humblet, *J. Med. Chem.* **52**, 6752–6756 (2009).
2. H. F. Klein, D. J. Hamilton, I. J. P. de Esch, M. Wijtmans, P. O'Brien, *Drug Discov. Today* **27**, 2484–2496 (2022).
3. M. P. Wiesenfeldt *et al.*, *Nature* **618**, 513–518 (2023).
4. R. Gianatassio *et al.*, *Science* **351**, 241–246 (2016).
5. X. Zhang *et al.*, *Nature* **580**, 220–226 (2020).
6. C. B. Kelly, J. A. Milligan, L. J. Tilley, T. M. Sodano, *Chem. Sci.* **13**, 11721–11737 (2022).
7. K. Hiesinger, D. Dar'in, E. Proschak, M. Krasavin, *J. Med. Chem.* **64**, 150–183 (2021).
8. A. de Meijere, S. I. Kozhushkov, *Chem. Rev.* **100**, 93–142 (2000).
9. Y. Cohen, D. Toledano, I. Marek, *J. Am. Chem. Soc.* **144**, 16732–16736 (2022).
10. J. Jurczyk *et al.*, *Nat. Synth.* **1**, 352–364 (2022).
11. W. J. Teo, J. Esteve Guasch, L. Jiang, B. Li, M. G. Suero, *J. Am. Chem. Soc.* **146**, 21837–21846 (2024).
12. Z. Wang, A. G. Herraiz, A. M. Del Hoyo, M. G. Suero, *Nature* **554**, 86–91 (2018).
13. B. D. Dherange, P. Q. Kelly, J. P. Liles, M. S. Sigman, M. D. Levin, *J. Am. Chem. Soc.* **143**, 11337–11344 (2021).
14. F.-P. Wu *et al.*, *Nat. Catal.* **7**, 242–251 (2024).

15. S. Timmann, T.-H. Wu, C. Golz, M. Alcarazo, *Chem. Sci.* **15**, 5938–5943 (2024).
16. J. C. Gilbert, V. Weerasooriya, *J. Org. Chem.* **44**, 4997–4998 (1979).
17. E. J. Corey, P. L. Fuchs, *Tetrahedron Lett.* **13**, 3769–3772 (1972).
18. W. von E. Doering, P. M. LaFlamme, *Tetrahedron* **2**, 75–79 (1958).
19. T. Koike, J.-K. Yu, M. M. Hansmann, *Science* **385**, 305–311 (2024).
20. For a recent overview of carbon atom transfer, see (*21*).
21. H. Fujimoto, M. Tobisu, *ChemistryEurope* **2**, e202400005 (2024).
22. P. S. Skell, J. J. Havel, M. J. McGlinchey, *Acc. Chem. Res.* **6**, 97–105 (1973).
23. P. S. Skell, R. R. Engel, *J. Am. Chem. Soc.* **87**, 1135 (1965).
24. P. S. Skell, R. R. Engel, *J. Am. Chem. Soc.* **88**, 3749–3758 (1966).
25. P. B. Shevlin, *J. Am. Chem. Soc.* **94**, 1379–1380 (1972).
26. T. Kurogi, K. Irifune, K. Takai, *Chem. Sci.* **12**, 14281–14287 (2021).
27. N. Dellus *et al.*, *Angew. Chem. Int. Ed.* **49**, 6798–6801 (2010).
28. M. Kamitani *et al.*, *Science* **379**, 484–488 (2023).
29. H. Fujimoto, B. Nakayasu, M. Tobisu, *J. Am. Chem. Soc.* **145**, 19518–19522 (2023).
30. A. W. Johnson, R. B. LaCount, *J. Am. Chem. Soc.* **83**, 417–423 (1961).
31. E. J. Corey, M. Chaykovsky, *J. Am. Chem. Soc.* **87**, 1353–1364 (1965).
32. P. S. Engel, *Chem. Rev.* **80**, 99–150 (1980).
33. T. V. Van Auken, K. L. Rinehart, *J. Am. Chem. Soc.* **84**, 3736–3743 (1962).
34. M. Regitz, G. Maas, *Diazo Compounds: Properties and Synthesis* (Academic Press, 1986).
35. M. M. Hansmann, *Angew. Chem. Int. Ed.* **62**, e202304574 (2023).
36. T. Morosaki *et al.*, *Chemistry* **23**, 8694–8702 (2017).
37. P. W. Antoni, C. Golz, J. J. Holstein, D. A. Pantazis, M. M. Hansmann, *Nat. Chem.* **13**, 587–593 (2021).
38. R. Tonner, F. Öxler, B. Neumüller, W. Petz, G. Frenking, *Angew. Chem. Int. Ed.* **45**, 8038–8042 (2006).
39. A. Genoux, K. Severin, *Chem. Sci.* **15**, 13605–13617 (2024).
40. F. Volatron, O. Eisenstein, *J. Am. Chem. Soc.* **109**, 1–14 (1987).
41. R. Huisgen, G. Szeimies, L. Möbius, *Chem. Ber.* **100**, 2494–2507 (1967).
42. S. P. Chandrasekharan, A. Dhami, S. Kumar, K. Mohanan, *Org. Biomol. Chem.* **20**, 8787–8817 (2022).
43. Y. Xiang, X. Fan, P.-J. Cai, Z.-X. Yu, *Eur. J. Org. Chem.* **2019**, 582–590 (2019).
44. Y. V. Tomilov, I. V. Kostyuchenko, E. V. Shulishov, O. M. Nefedov, *Russ. Chem. Bull.* **46**, 511–518 (1997).
45. I. V. Kostyuchenko, E. V. Shulishov, R. R. Rafikov, Y. V. Tomilov, *Russ. Chem. Bull.* **57**, 1712–1717 (2008).
46. B. M. Trost, M. J. Bogdanowicz, *J. Am. Chem. Soc.* **95**, 5321–5334 (1973).
47. D. Frank, S. I. Kozhushkov, T. Labahn, A. de Meijere, *Tetrahedron* **58**, 7001–7007 (2002).
48. K. B. Wiberg, *J. Org. Chem.* **50**, 5285–5291 (1985).
49. R. Boese, D. Bläser, K. Gomann, U. H. Brinker, *J. Am. Chem. Soc.* **111**, 1501–1503 (1989).
50. L. Skattebøl, *J. Org. Chem.* **31**, 2789–2794 (1966).
51. U. H. Brinker, J. Streu, *Angew. Chem. Int. Ed.* **19**, 631–632 (1980).
52. M. C. Flowers, H. M. Frey, *J. Chem. Soc.* 1689–1694 (1962).
53. T. Karatsu *et al.*, *J. Org. Chem.* **60**, 8270–8277 (1995).
54. T. Miebach, U. H. Brinker, *J. Org. Chem.* **58**, 6524–6525 (1993).
55. J. Tsien, C. Hu, R. R. Merchant, T. Qin, *Nat. Rev. Chem.* **8**, 605–627 (2024).

ACKNOWLEDGMENTS

We thank S. Henke for access to the thermal gravimetric analysis and differential scanning calorimetry instruments; J. Holstein for assistance with x-ray diffraction; W. Hiller for assistance with ^{15}N NMR experiments; P. Saedi and Y. Lyu for synthetic help; and the faculty of chemistry and chemical biology for support. **Funding:** We thank the Deutsche Forschungsgemeinschaft (NMR: DFG project 452669591; Computational resources: 271512359) under Germany's Excellence Strategy—EXC2033—project number 390677874-RESOLV. This work was funded by the European Commission [ERC-StG "CC-CHARGED" (101077332)]. **Author contributions:** Q.S. devised and synthesized the Ph_2SCN_2 reagent, Q.S., J.-N.B., J.H., P.W.A., and D.T. performed the synthetic experiments; P.W.A. and R.G. performed the x-ray analysis; and D.T. performed the computational studies. Q.S., D.T., and M.M.H. discussed and wrote the manuscript. M.M.H. managed the project. **Competing interests:** A German patent application with the inventors Q.S. and M.M.H. (Technische Universität Dortmund) is pending. All other authors declare no competing interests. **Data and materials availability:** The details of the experimental methods, NMR spectra, x-ray analysis, infrared spectra, and computational studies are available in the supplementary materials. Crystallographic data for the structures reported in this article have been deposited at the Cambridge Crystallographic Data Centre under deposition numbers CCDC 2378645/2378646 (**3**), 2378647 (**5a**), 2378648 (**5g**), 2378649 (**6a**), 2378650 (**7a**), 2378651 (**7b-A**), 2378652 (**7c-A**), 2378653 (**7d**), 2378654 (**8a**), 2378655 (**8c-A**), 2378656 (**8f**), 2378657 (**9d**), 2378658 (**9e**), 2378659 (**10b**), 2378660 (**11d**), 2378661 (**13c**), 2378662 (*trans*-**13h**), 2402187 (*cis*-**13h**), 2378663 (**14h**), and 2378664 (**15h**). These data are provided free of charge via www.ccdc.cam.ac.uk/data_request/cif. All other data supporting the findings of this project are available within the article or the supplementary materials. Correspondence and requests for materials should be addressed to the corresponding author. This research was funded in whole or in part by the European Research Council (ERC StG grant 101077332), a cOAlition S organization. The author will make the Author Accepted Manuscript (AAM) version available under a CC BY public copyright license.

SUPPLEMENTARY MATERIALS

science.org/doi/10.1126/science.ads5974
Materials and Methods
Figs. S1 to S334
References (*56*–*82*)

Submitted 20 August 2024; accepted 14 January 2025
10.1126/science.ads5974

NEUROSCIENCE

Neuronal FAM171A2 mediates α-synuclein fibril uptake and drives Parkinson's disease

Kai-Min Wu[1], Qian-Hui Xu[2,3], Yi-Qi Liu[1], Yi-Wei Feng[1], Si-Da Han[1], Ya-Ru Zhang[1], Shi-Dong Chen[1], Yu Guo[1], Bang-Sheng Wu[1], Ling-Zhi Ma[4], Yi Zhang[1], Yi-Lin Chen[1], Liu Yang[1], Zhao-Fei Yang[5], Yu-Jie Xiao[6], Ting-Ting Wang[7], Jue Zhao[1], Shu-Fen Chen[1], Mei Cui[1], Bo-Xun Lu[8], Wei-Dong Le[5,9], You-Sheng Shu[6], Keqiang Ye[10,11], Jia-Yi Li[12,13], Wen-Sheng Li[14], Jian Wang[1], Cong Liu[2,15,16]*, Peng Yuan[1,17]*, Jin-Tai Yu[1]*

Neuronal accumulation and spread of pathological α-synuclein (α-syn) fibrils are key events in Parkinson's disease (PD) pathophysiology. However, the neuronal mechanisms underlying the uptake of α-syn fibrils remain unclear. In this work, we identified *FAM171A2* as a PD risk gene that affects α-syn aggregation. Overexpressing FAM171A2 promotes α-syn fibril endocytosis and exacerbates the spread and neurotoxicity of α-syn pathology. Neuronal-specific knockdown of FAM171A2 expression shows protective effects. Mechanistically, the FAM171A2 extracellular domain 1 interacts with the α-syn C terminus through electrostatic forces, with >1000 times more selective for fibrils. Furthermore, we identified bemcentinib as an effective blocker of FAM171A2–α-syn fibril interaction with an in vitro binding assay, in cellular models, and in mice. Our findings identified FAM171A2 as a potential receptor for the neuronal uptake of α-syn fibrils and, thus, as a therapeutic target against PD.

Parkinson's disease (PD) is a neurodegenerative disorder affecting motor and cognitive functions (*1*–*3*). Aggregations of pathological α-synuclein (α-syn) in various brain regions mediate the progression of the disease (*4*, *5*). Aggregated α-syn proteins form fibrils that act in a prion-like manner, spreading α-syn pathology in various regions of the brain (*6*, *7*). However, the molecular mechanism underlying the interneuronal transmission remains unknown.

Previous studies indicated that the pathological α-syn is internalized by endocytosis (*8*, *9*) with different receptors (*10*–*12*); however, the

[1]Department of Neurology and National Center for Neurological Diseases, Huashan Hospital, State Key Laboratory of Medical Neurobiology and Ministry of Education Frontiers Center for Brain Science, Shanghai Medical College, Fudan University, Shanghai, China. [2]Interdisciplinary Research Center on Biology and Chemistry, Shanghai Institute of Organic Chemistry, Chinese Academy of Sciences, Shanghai, China. [3]University of Chinese Academy of Sciences, Beijing, China. [4]Department of Neurology, Qingdao Municipal Hospital, Qingdao University, Qingdao, China. [5]Liaoning Provincial Key Laboratory for Research on the Pathogenic Mechanisms of Neurological Diseases, The First Affiliated Hospital of Dalian Medical University, Dalian, China. [6]Department of Neurology, Huashan Hospital, State Key Laboratory of Medical Neurobiology, Institute for Translational Brain Research, MOE Frontiers Center for Brain Science, Fudan University, Shanghai, China. [7]Department of Pharmacy, Huashan Hospital, Fudan University, Shanghai, China. [8]Neurology Department at Huashan Hospital, State Key Laboratory of Medical Neurobiology and MOE Frontiers Center for Brain Science, Institutes of Brain Science, School of Life Sciences, Fudan University, Shanghai, China. [9]Institute of Neurology, Sichuan Provincial People's Hospital, Medical School of University of Electronic Science and Technology of China, Chengdu, China. [10]Department of Pathology and Laboratory Medicine, Emory University School of Medicine, Atlanta, GA, USA. [11]Faculty of Life and Health Sciences, Shenzhen Institute of Advanced Technology, Chinese Academy of Sciences, Shenzhen, Guangdong, China. [12]Neural Plasticity and Repair Unit, Department of Experimental Medical Science, Wallenberg Neuroscience Center, Lund University, Lund, Sweden. [13]Institute of Health Sciences, China Medical University, Liaoning, Shenyang, China. [14]Department of Anatomy, Histology and Embryology, School of Basic Medical Sciences, State Key Laboratory of Medical Neurobiology, MOE Frontiers Center for Brain Science, Institutes of Brain Science, Fudan University, Shanghai, China. [15]State Key Laboratory of Small Molecule Modulation of Biological Processes, Shanghai Institute of Organic Chemistry, University of Chinese Academy of Sciences, Shanghai, China. [16]Shanghai Academy of Natural Sciences (SANS), Fudan University, Shanghai, China. [17]Department of Rehabilitation Medicine, Huashan Hospital, State Key Laboratory of Medical Neurobiology, Institute for Translational Brain Research, MOE Frontiers Center for Brain Science, MOE Innovative Center for New Drug Development of Immune Inflammatory Diseases, Fudan University, Shanghai, China.
***Corresponding author. Email: liulab@sioc.ac.cn (C.L.); pyuan@fudan.edu.cn (P.Y.); jintai_yu@fudan.edu.cn (J.-T.Y.)**

A

FAM171A2 meta-analysis (12 overlapping SNPs)

UKB	+	Chang 2017, Stage1	+	Finngen
11,324 PD+proxy cases 188,484 controls		20,184 PD cases 397,324 controls		4,681 PD cases 407,500 controls

Marker Name	Pos	Effect Allele	Reference Allele	Freq	Meta-P	PD risk odds Ratio
rs850738	42434630	G	A	0.427	1.95×10^{-9}	1.05
rs708383	42437754	A	G	0.392	4.97×10^{-9}	1.05
rs708384	42437682	A	C	0.392	5.38×10^{-9}	1.05
rs71371993	42437000	A	G	0.099	4.74×10^{-6}	1.10
rs35941271	42436220	A	G	0.116	5.93×10^{-5}	1.08

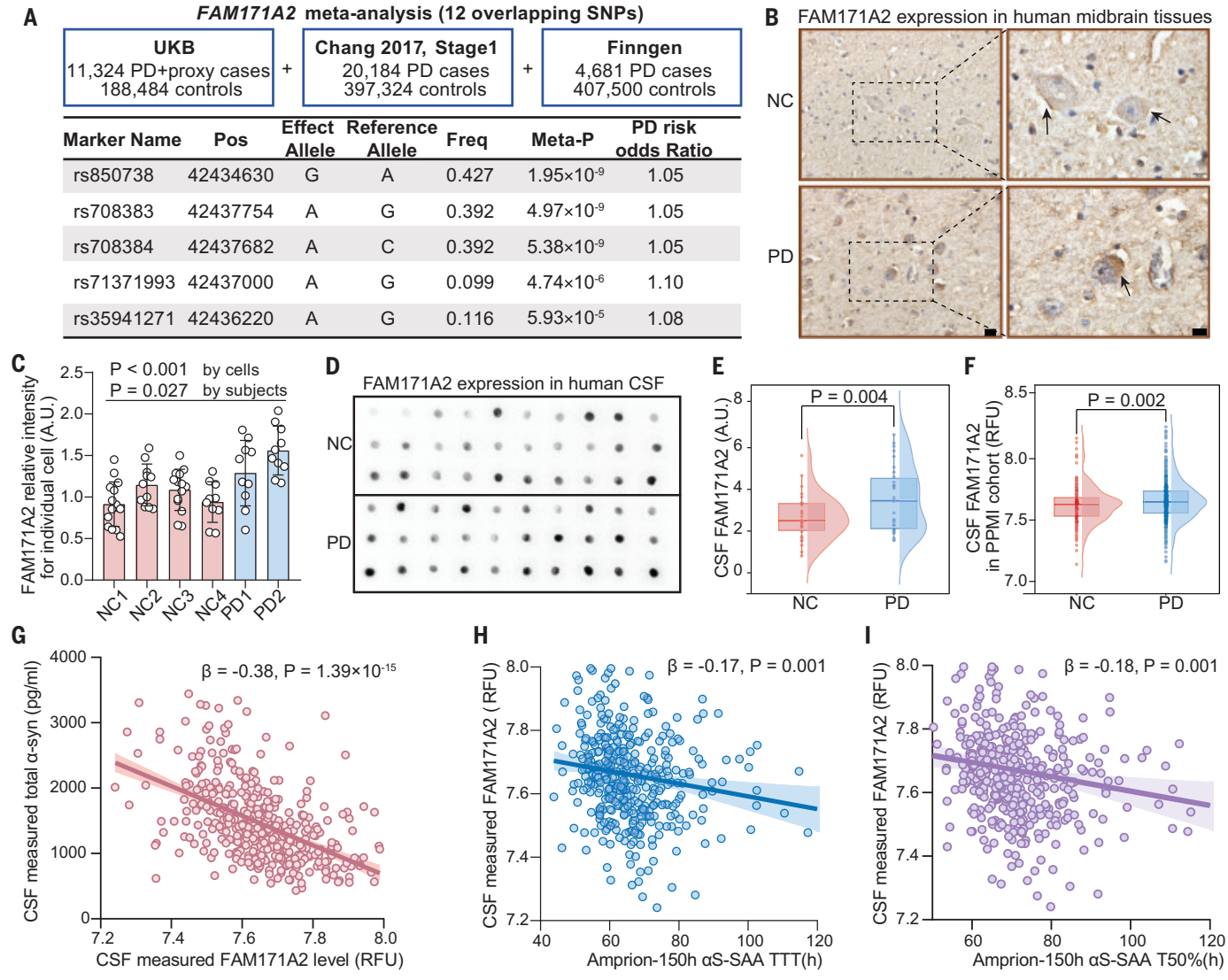

Fig. 1. Elevated FAM171A2 expression correlates with α-syn pathology in patients with PD. (**A**) Associations between *FAM171A2* variants and PD risk. Chang 2017 refers to reference (*34*). (**B**) Immunohistochemical images of FAM171A2 protein expression in human midbrain tissues. The insets show examples of higher magnification in the dashed rectangles. Arrows indicate heightened staining of FAM171A2. Scale bar, 20 μm. NC, normal control. (**C**) Quantification of FAM171A2 expression in (B) by average optical density measurement (N = 10 to 15 cells). Data are expressed as means ± SEM and were tested with one-way analysis of variance (ANOVA) by cells and unpaired t test by subjects. A.U., arbitrary units. (**D**) Representative dot blot image of FAM171A2 expression in CSF samples from sporadic PD patients (N = 30) and age- and sex-matched neurological NCs (N = 30). (**E**) Densitometric analysis of FAM171A2 amounts in PD patients and NCs. Boxplots depict the median and 25th and 75th quartiles, whereas whiskers represent the full range. Statistical significance was determined with an unpaired t test. (**F**) CSF FAM171A2 amounts in PD patients and NCs from PPMI cohort. Boxplots depict the median and 25th and 75th quartiles, and whiskers represent the full range. Statistical significance was determined by using regression models adjusted for sex and age. RFU, relative fluorescence units. (**G** to **I**) Scatterplots showing the correlation between FAM171A2 and total α-syn amounts in CSF (G), the time to threshold (TTT) of α-syn SAA (αS-SAA) (H), and the time to 50% max fluorescence (T50%) of α-syn SAA (I) in patients with PD. Measurements in (G) to (I) were adjusted for age, sex, and progranulin expression. Linear trend lines are shown, and the 95% confidence intervals are indicated by shading. Coefficients of determination (R^2) are 0.29 (G), 0.07 (H), and 0.06 (I). Estimate regression coefficients (β) and P values are shown. UKB, UK Biobank; Meta-P, P value for meta-analysis; SNPs, single-nucleotide polymorphisms; Pos, the chromosomal position in base pairs according to the human genome build hg19; Freq, frequency; NC, neurological normal control; PPMI, Parkinson's Progression Markers Initiative cohort; h, hours.

specific receptors on neurons remain to be fully identified. We previously reported that the single-nucleotide polymorphism rs708384 of *FAM171A2* is associated with an increased risk for PD (*13*). The amount of FAM171A2 in the cerebrospinal fluid (CSF) is increased in individuals with PD and correlates with indications of high α-syn aggregations in the brain (Fig. 1). In this study, we hypothesized that FAM171A2 may be involved in the interneuronal spread of α-syn pathology. We systematically tested this hypothesis by using a mouse model of α-syn pathology propagation. We established a causal relationship between FAM171A2 expression and neuronal uptake of α-syn fibrils as well as its downstream neurotoxicity. Combining biochemical and structural approaches, we identified the biophysical basis underlying the FAM171A2–α-syn interaction. We further found that a small molecule, bemcentinib, blocked this interaction in cultured cells and in vivo. Taken together, our data revealed that FAM171A2 is a specific mediator for α-syn fibril internalization and that antagonizing this interaction may

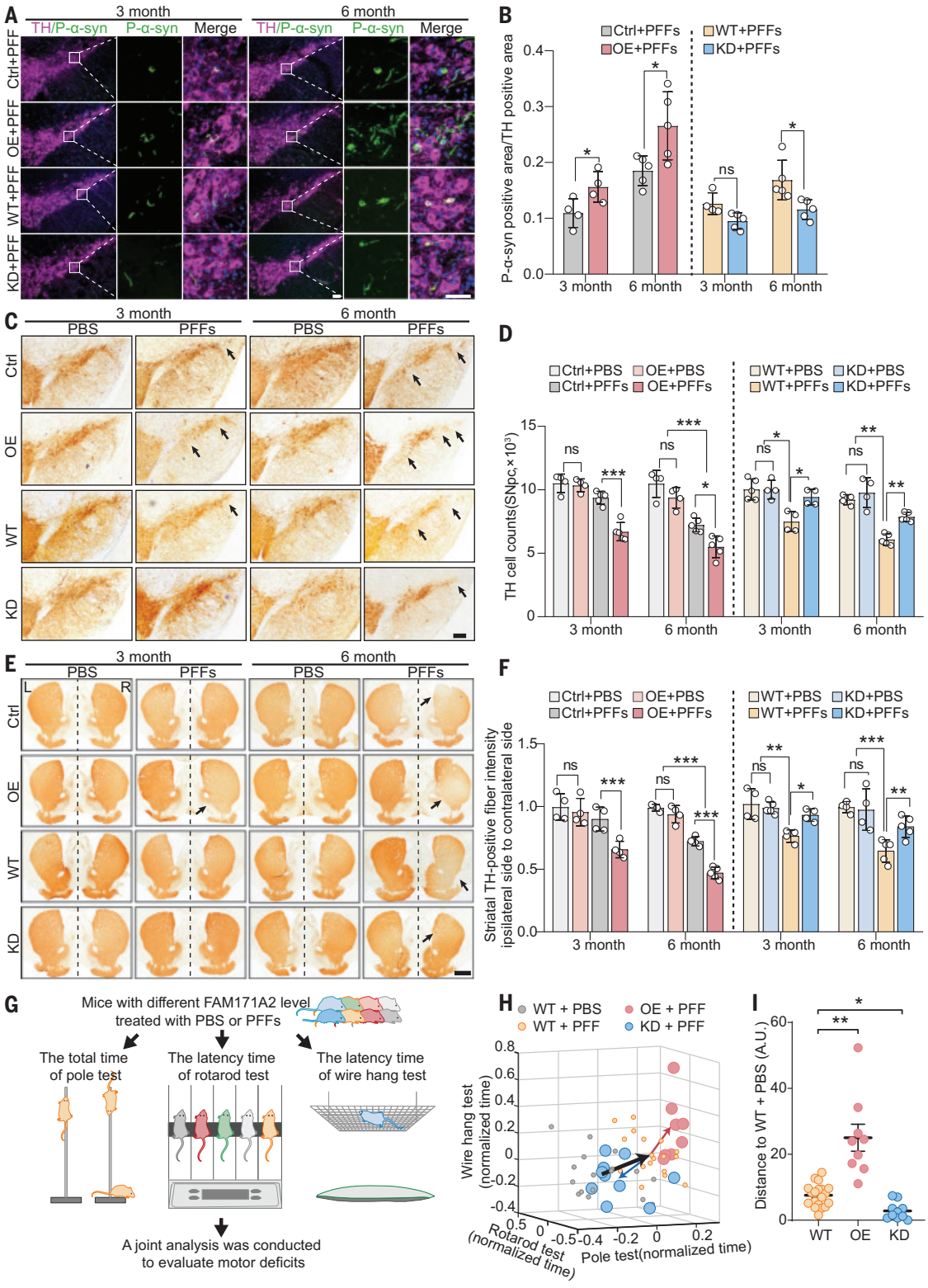

Fig. 2. FAM171A2 controls PFFs inoculation-induced α-syn pathology and neurotoxicity. (**A**) Representative images of double immunostaining for p-α-syn (green) and TH (magenta) in the SN of different groups 3 or 6 months after α-syn PFF treatment. Staining with 4′,6-diamidino-2-phenylindole (DAPI) is shown in blue. Scale bar, 100 μm. Insets show examples of higher magnification; scale bar, 50 μm. (**B**) Quantification of the ratio of p-α-syn–positive area to the TH-positive area in the SN on the PFF injection side (N = 4 to 5 mice per group, 6 brain sections per mouse). (**C**) Representative images of TH immunohistochemistry in SN sections from different groups 3 or 6 months after PBS or α-syn PFF treatment. Arrows indicate lesions. Scale bar, 200 μm. (**D**) Stereological counting of TH-positive neurons in the right SN of mice from the indicated experimental group (N = 4 to 5 mice per group, 7 to 9 brain sections per mouse). (**E**) Representative images of TH immunohistochemistry in striatum sections 3 or 6 months after PBS or α-syn PFF treatment. Arrows indicate lesions. Scale bar, 500 μm. (**F**) Quantification of TH fiber density in striatum determined by average optical density measurement (N = 4 to 5 mice per group). (**G**) Schematic of the motor function tests in different groups treated with PBS or α-syn PFFs at 6 months after treatments. (**H**) Three-dimensional (3D) scatterplot of the mice motor performance. The black arrow connects the centroid of the PBS-treated wild-type group to α-syn PFF-treated wild-type group. The red arrow indicates the distance between α-syn PFF-treated wild-type to the FAM171A2-overexpressing group. The blue arrow identifies the distance between α-syn PFF-treated wild-type to FAM171A2-knockdown groups. (**I**) Quantification of the Mahalanobis population vector distances toward the PBS-treated wild-type group 6 months after treatment in the 3D scatter plot shown in (H). In all panels, data are presented as mean ± SEM. For (I), one-way ANOVA with a Tukey's post-test was used. For panels B, D, and F, two-way ANOVA with a Tukey's post hoc test was used. ns, not significant; *P < 0.05; **P < 0.01; ***P < 0.001. Ctrl, control; OE, overexpression; WT, wild type; KD, knockdown; SNpc, substantia nigra pars compacta; L, left; R, right.

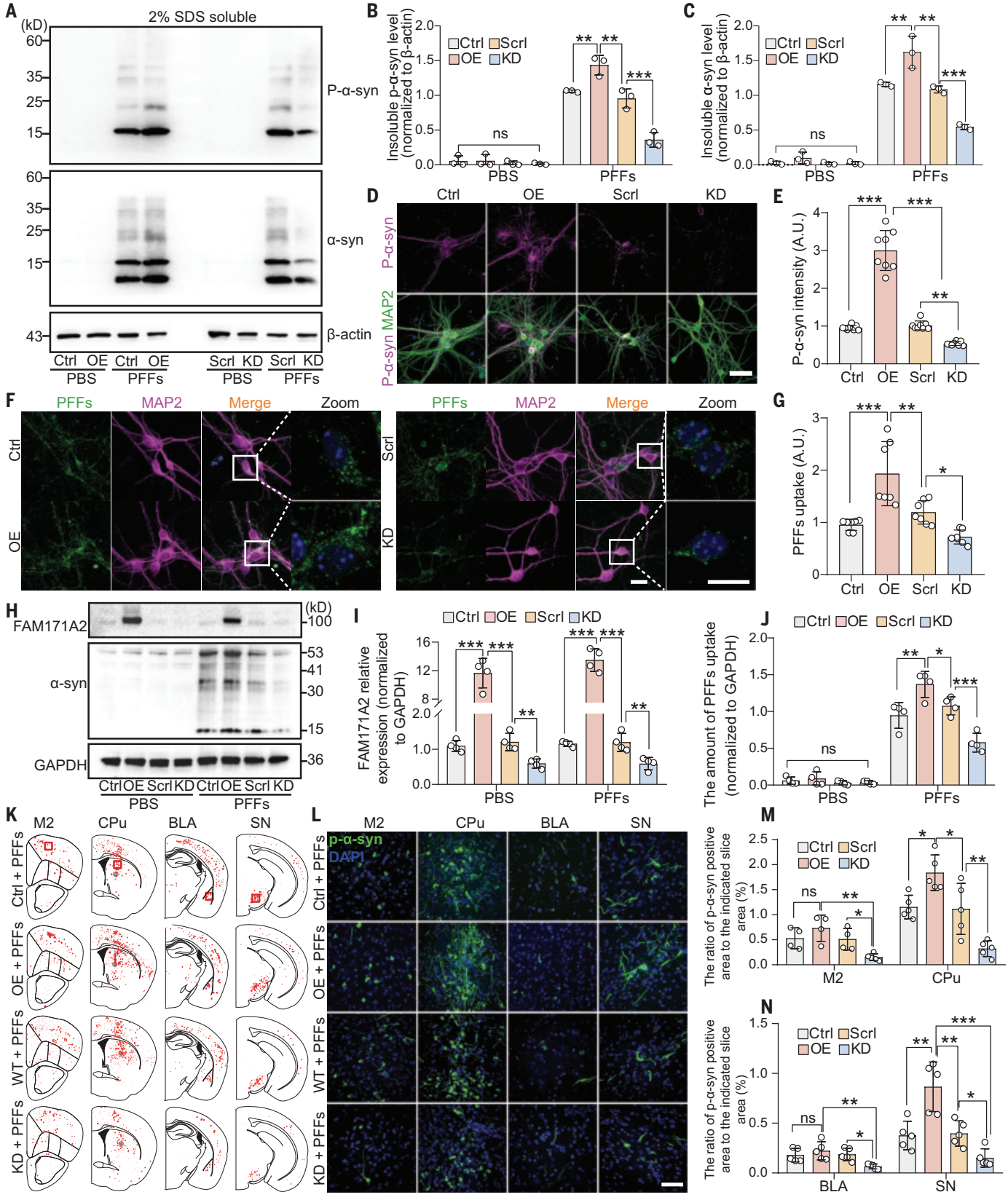

Fig. 3. FAM171A2 mediates α-syn endocytosis and regulates α-syn pathology spread. (**A**) Representative immunoblots of insoluble α-syn, p-α-syn, and β-actin in primary cortical neurons after PBS or α-syn PFF treatment in indicated groups. (**B** and **C**) Quantification of insoluble p-α-syn (B) and α-syn (C) amounts in (A). *N* = 3 independent experiments. (**D**) Representative p-α-syn (magenta) immunofluorescence images in primary cortical neurons with different FAM171A2 amounts after treatment with α-syn PFFs for 14 days. MAP2, green; DAPI, blue. *N* = 8 independent experiments. Scale bar, 20 μm. (**E**) Quantification of p-α-syn

immunofluorescence. (**F**) Representative images of α-syn PFF uptake in indicated groups 3 hours after incubation with α-syn PFFs-488; *N* = 7 independent experiments. The insets show examples of higher magnification; scale bars, 20 μm. (**G**) Quantification of the amount of internalized α-syn PFFs in (F). (**H**) Western blots showing the expression of FAM171A2 and the amount of α-syn PFF uptake in different groups of primary cortical neurons 3 hours after incubation with either α-syn PFFs or PBS. Glyceraldehyde-3-phosphate dehydrogenase (GAPDH) is blotted as loading controls. (**I** and **J**) Quantification of the expression of FAM171A2 (I) and the amount of α-syn PFF uptake (J) in (H). *N* = 4 independent experiments. (**K**) Representative distribution of p-α-syn pathology (red dots) on several coronal sections in different groups 6 months after α-syn PFF treatment. Gray circles denote injected sites. (**L**) Representative images of p-α-syn pathology on M2, CPu, BLA, and SN regions in the red boxes in (K). Scale bar, 20 μm. (**M** and **N**) Quantification of the percentage of the p-α-syn occupied area to the total area of the corresponding slice on the PFFs injection side. *N* = 4 to 5 mice per group. For (B), (C), (I), and (J), a two-way ANOVA with a Tukey's post hoc test was performed. For (E), (G), (M), and (N), a one-way ANOVA with a Tukey's post hoc test was performed. In all panels, data are expressed as mean ± SEM. ns, not significant; **P* < 0.05; ***P* < 0.01; ****P* < 0.001. Ctrl, control; OE, FAM171A2 overexpression; Scrl, scramble control; KD, FAM171A2 knockdown; WT, wild type.

represent a therapeutic target against α-syn propagation in PD.

Increased FAM171A2 expression correlates with α-syn pathology in samples from individuals with PD

We previously reported that *FAM171A2* rs708384 is associated with the risk of PD (*13*). To further characterize the associations between all common variants of *FAM171A2* and PD risk, we performed a large meta–genome-wide association study (GWAS) in PD using data from more than 1 million total participants. Our analyses revealed significant associations between PD risk and five variants of *FAM171A2*: rs850738 [odds ratio (OR) = 1.05, $P = 1.95 \times 10^{-9}$], rs708383 (OR = 1.05, $P = 4.97 \times 10^{-9}$), rs708384 (OR = 1.05, $P = 5.38 \times 10^{-9}$), rs71371993 (OR = 1.10, $P = 4.74 \times 10^{-6}$), and rs35941271 (OR = 1.08, $P = 5.93 \times 10^{-5}$) (Fig. 1A and table S1). We then performed immunohistochemical staining of FAM171A2 in postmortem human brain tissues and found neuronal staining in the midbrain taken from four healthy brains (controls) and two brains from patients with PD, with particularly high signal observed on the plasma membrane (Fig. 1B). We observed elevated FAM171A2 expression in patients with PD compared with controls (Fig. 1C). Transcriptional analysis further showed that FAM171A2 is expressed in the dopaminergic neurons of the substantia nigra (SN) as well as in other cell types across different regions (fig. S1).

We then collected CSF samples from 30 patients with PD and 30 age- and sex-matched controls and evaluated their FAM171A2 expression by immunoreactivity-based dot blot (Fig. 1D and table S2). We found that patients with PD had elevated amount of FAM171A2 in CSF compared with controls (Fig. 1E), which was validated by analyzing data from a larger cohort of 517 PD cases and 169 controls, obtained from the Parkinson's Progression Markers Initiative (PPMI) cohort (Fig. 1F and table S3). We next examined the correlation between FAM171A2 and α-syn in the CSF of individuals with PD. Consistent with previous reports (*14*), we observed reduced total α-syn expression in individuals with PD in both cohorts (fig. S2, A to D), suggesting increased accumulation of α-syn aggregates in the brain. We also found a significant negative correlation between FAM171A2 and CSF α-syn expression among individuals with PD in the PPMI cohort (β = −0.38, $P = 1.39 \times 10^{-15}$; Fig. 1G). These results suggested a correlation between elevated FAM171A2 and α-syn aggregation in the brain. Furthermore, the PPMI cohort measured pathological α-syn seed using a fluorescence-based amplification assay (SAA) and showed that higher FAM171A2 expression correlated with shorter times to reach threshold for detection (β = −0.17, *P* = 0.001; Fig. 1H) or 50% of the maximum fluorescence (β = −0.18, *P* = 0.001; Fig. 1I) in patients with PD, indicating an association of higher FAM171A2 expression with increased amounts of pathological α-syn seeds. We controlled for the potential confounding effect of progranulin (*13*). The progranulin expression in CSF showed no reduction in individuals with PD compared with controls (fig. S2, E to H). Thus, elevation of FAM171A2 is associated with α-syn aggregation in the brain, potentially contributing to PD pathogenesis.

FAM171A2 controls preformed-fibril inoculation–induced α-syn pathology and neurotoxicity

To test the causal effect of FAM171A2 on α-syn pathology, we used a mouse model with intrastriatal inoculation of recombinant α-syn preformed fibrils (α-syn PFFs). Inoculation of α-syn PFFs leads to a time-dependent accumulation of misfolded α-syn pathology in the interconnected brain regions (*4*, *15*, *16*). This approach allowed us to dissect the specific process of pathogenic α-syn propagation. We visualized the fibrils formed from α-syn monomers with transmitted electron microscopy (fig. S3A) and confirmed the multimeric forms by SDS–polyacrylamide gel electrophoresis analysis (fig. S3B). In addition, these α-syn PFFs were fully capable of inducing the formation of phospho-Ser^{129} α-syn (p-α-syn)–positive inclusions (fig. S3C), a feature indicative of pathological misfolding of α-syn (*17*, *18*). To manipulate FAM171A2, we developed FAM171A2 overexpression and knockdown mouse models. Injection of adeno-associated viruses (AAVs) into the right SN increased the expression of FAM171A2 protein (fig. S4, A to F). In addition, we utilized the CRISPR-Cas9 genome editing system to delete the exons 4 to 7 in *FAM171A2* gene. Because of the lethality of homozygous FAM171A2 knockouts, heterozygous mice (*FAM171A2*$^{+/-}$) were used for this study; these animals showed no evident morphological or behavioral abnormalities (fig. S4, E to N).

Injection of α-syn PFFs (2 μg/μl) into the right dorsal striatum resulted in uptake of PFFs through axonal terminals (fig. S5), leading to accumulation of α-syn PFFs in the ipsilateral SN. Three or 6 months after inoculation, we found that FAM171A2 overexpression led to an increased p-α-syn pathology in SN compared with control mice, whereas FAM171A2 knockdown reduced the accumulation of p-α-syn pathology compared with controls (Fig. 2, A and B). Previous work showed that p-α-syn pathology produces toxicity to tyrosine hydroxylase (TH)–positive dopaminergic neurons, leading to motor dysfunction in PD (*19*, *20*). Having found that FAM171A2 controlled the accumulation of p-α-syn pathology in SN, we next examined the impact of FAM171A2 amounts on α-syn PFF–induced neurotoxicity. Consistent with the effect on α-syn pathology, FAM171A2 overexpression led to a more pronounced loss of TH-positive neurons and fiber degeneration, whereas FAM171A2 knockdown was neuroprotective (Fig. 2, C to F). Furthermore, pole test, rotarod test, and wire hang test revealed that FAM171A2 overexpression worsened α-syn PFF–induced behavior deficits, whereas FAM171A2 knockdown showed performance similar to that measured in wild-type mice (Fig. 2, G to I, and fig. S6). To directly test the necessity of FAM171A2 of neuronal origin for α-syn PFF–induced pathology, we developed a mouse model with neuronal-specific knockout of FAM171A2 (Nes-Cre^{+}:*FAM171A2*$^{flox/flox}$; fig. S4, E and F). Following a 3-month incubation period with α-syn PFFs, the neuron-specific knockout of FAM171A2 reproduced all the protective phenotypes observed in the whole-body knockdown mice (fig. S7). Taken together, our findings indicate that neuronal FAM171A2 bidirectionally modulates the accumulation of α-syn pathology and affects PFFs neurotoxicity.

FAM171A2 mediates the endocytosis of α-syn fibrils

We next used an in vitro cellular model to study the mechanism underlying FAM171A2's regulation on α-syn pathology. Primary cortical neurons were transfected with AAV to either overexpress or knockdown FAM171A2 (fig. S8). Following a

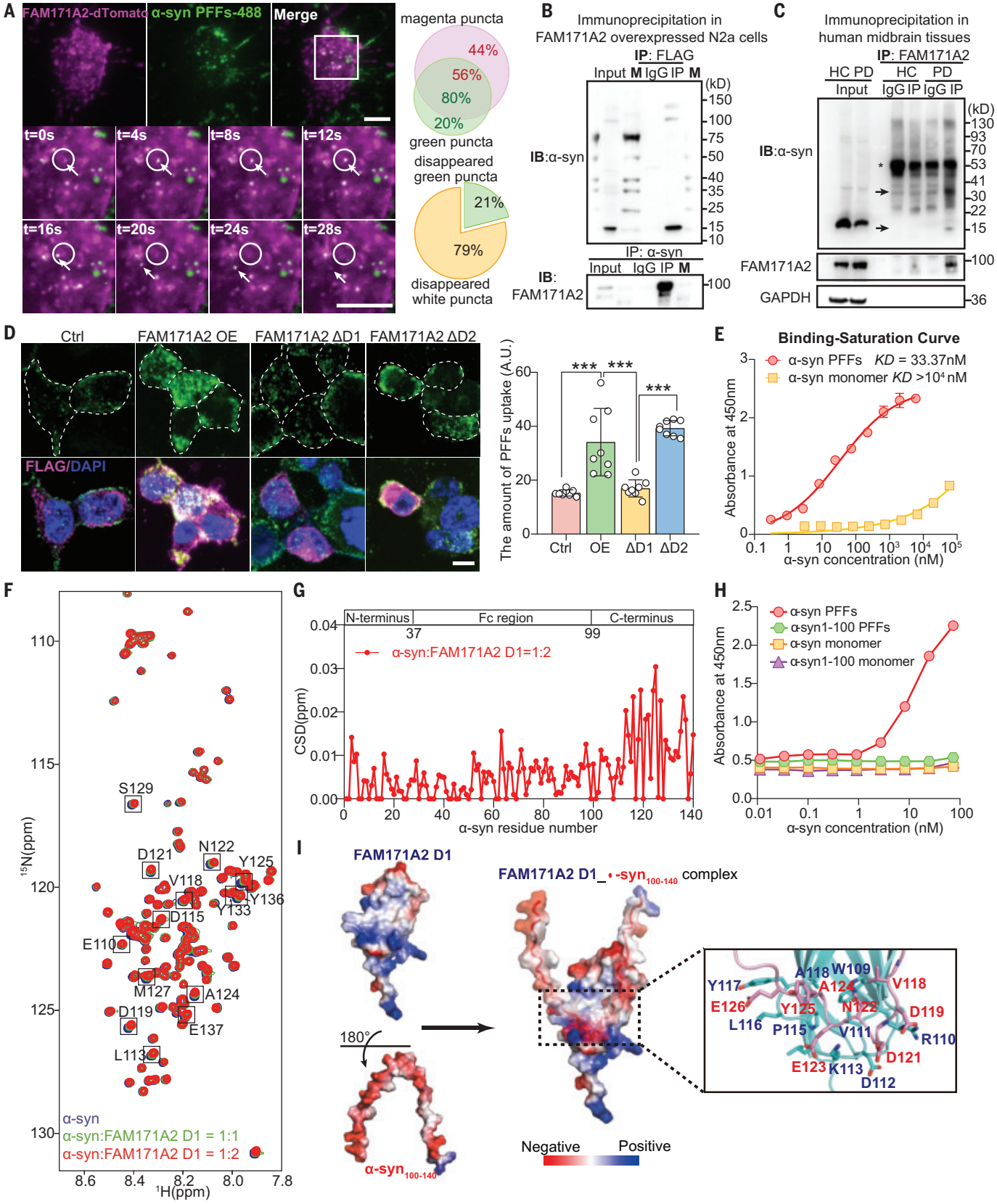

Fig. 4. FAM171A2 directly interacts with α-syn fibrils. (**A**) Representative TIRF images showing colocalization of α-syn PFFs (green) with FAM171A2 (magenta) in N2a cells transfected with FAM171A2-dTomato. Insets show examples of higher magnification of FAM171A2 and α-syn PFFs-488 (indicated by white arrows) at different times. The white circle is in a fixed position. Scale bars, 5 μm. The upper right panel shows the Venn diagram for FAM171A2 puncta and α-syn PFFs-488 puncta in all imaged cells. The lower right panel presents the proportion of single labeled puncta in disappeared α-syn PFFs. (**B**) Coimmunoprecipitation blots testing the interaction between α-syn PFFs and FAM171A2 in N2a cells

overexpressing FAM171A2-FLAG. (**C**) Coimmunoprecipitation testing the interaction between α-syn and FAM171A2 from the postmortem midbrain tissues of controls and individuals with PD. The asterisk represents a nonspecific band; arrows indicate possible α-syn bands. *N* = 2 controls and 2 patients with PD. (**D**) Representative images showing the amount of α-syn PFFs binding to HEK293 cells transfected with full-length or truncated FAM171A2-FLAG. Scale bar, 10 μm. The right panel shows quantification of PFFs fluorescence as mean ± SEM. *N* = 8 independent experiments. A one-way ANOVA followed by Tukey's post hoc test for multiple comparisons was performed. (**E**) The binding curves for α-syn PFFs or monomers to FAM171A2 domain 1 protein fitted to logistic functions. *N* = 3 independent experiments. (**F**) Overlay of the 2D ^{1}H-^{15}N HSQC spectra of ^{15}N-labeled α-syn alone (blue) and in the presence of FAM171A2 domain 1 protein at molar ratios of 1:1 (green) or 1:2 (red). Black boxes show residues in α-syn with significant CSDs. (**G**) CSDs of α-syn in the presence of FAM171A2 domain 1 protein at the molar ratio of 1:2. Fc, crystallizable fragment. (**H**) Binding affinity of FAM171A2 domain 1 protein with different α-syn forms tested by ELISA assay. *N* = 3 independent experiments. (**I**) Predicted electrostatic surface model of the α-syn$_{100–140}$ residues in complex with FAM171A2 domain 1. The model confidence is 0.38. M, marker; IP, immunoprecipitation; IB, immunoblotting; FAM171A2 ΔD1, FAM171A2 domain 1 deletion; FAM171A2 ΔD2, FAM171A2 domain 2 deletion. Single-letter abbreviations for the amino acid residues referenced throughout the figures are as follows: S, Ser; N, Asn; D, Asp; V, Val; Y, Tyr; G, Gly; E, Glu; M, Met; A, Ala; L, Leu; W, Trp; R, Arg; K, Lys; P, Pro.

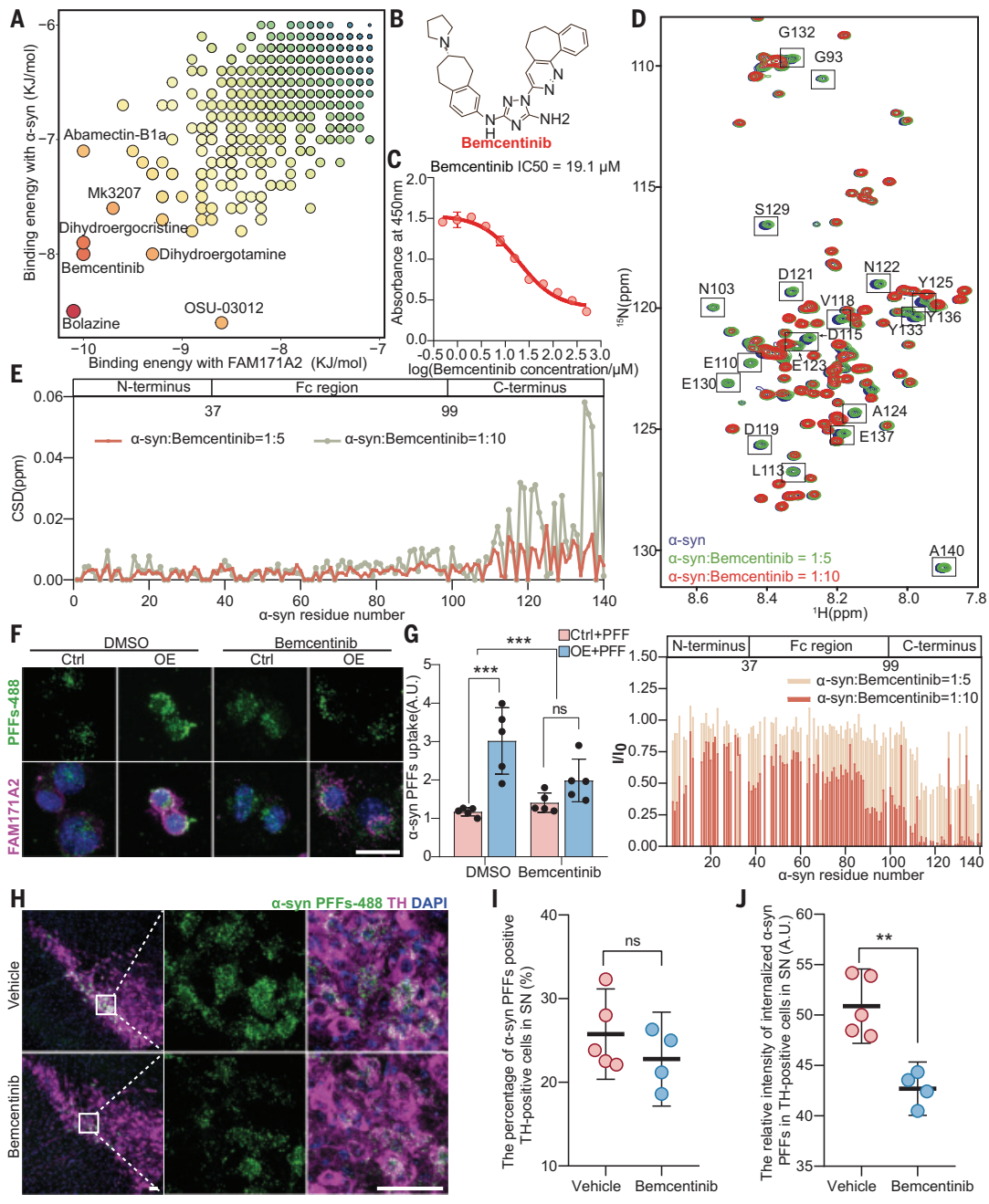

Fig. 5. Blocking the interaction between FAM171A2 and α-syn fibrils by bemcentinib prevents α-syn fibril uptake. (**A**) Binding energies of compounds to FAM171A2 and α-syn binding sites predicted by MTiOpenScreen. (**B**) The chemical structure of bemcentinib. (**C**) The inhibition activity curve for bemcentinib to block the binding of FAM171A2 domain 1 protein and α-syn PFFs. *N* = 3 independent experiments. (**D**) Overlay of the 2D ^{1}H-^{15}N HSQC spectra of 20-μM ^{15}N-labeled α-syn alone (blue) and in the presence of bemcentinib protein at molar ratios of 1:5 (green) or 1:10 (red). Black boxes around individual amino acids show the residues of α-syn with significant CSDs. The lower panel shows the residue-specific intensity ratio (I/I_0) of α-syn titrated by bemcentinib at different ratios. (**E**) CSDs of α-syn in the presence of bemcentinib at a molar ratio of 1:5 or 1:10. The domain organization of α-syn is shown on top. (**F**) Representative immunofluorescence images showing the uptake of α-syn PFFs in FAM171A2-overexpressed or control N2a cells. Scale bar, 20 μm. (**G**) Quantified data of the amount of α-syn PFF uptake in (F). Data are expressed as means ± SEM; *N* = 5 independent experiments, compared by two-way ANOVA with a Tukey's post hoc test for multiple comparisons. (**H**) Representative images showing the uptake of α-syn PFFs-488 by TH-positive neurons in SN after receiving a 7-day treatment with vehicle or bemcentinib. The insets show examples at higher magnification. Scale bars = 50 μm. (**I**) Quantification of the percentage of α-syn PFFs-488–positive, TH-positive neurons in the SN in indicated experiment groups. Data are expressed as means ± SEM; *N* = 4 to 5 mice per group, compared by unpaired *t* test. (**J**) Quantification of the relative mean intensity of α-syn PFFs-488 in the SN in indicated experiment groups. Data are expressed as means ± SEM; *N* = 4 to 5 mice per group, compared by unpaired *t* test. ns, not significant; $^{**}P < 0.01$; $^{***}P < 0.001$. ppm, parts per million.

14-day incubation with 2 μg/ml of α-syn PFFs, we assessed the pathological α-syn contents in the neurons. Consistent with the in vivo findings, increase in insoluble p-α-syn and total insoluble α-syn amounts were detected in neurons overexpressing FAM171A2, whereas FAM171A2 knockdown resulted in a marked reduction of p-α-syn and α-syn (Fig. 3, A to E). We observed similar effects when incubation of α-syn PFFs preceded FAM171A2 manipulation (fig. S9). The ratio of insoluble p-α-syn to total insoluble α-syn was not affected by FAM171A2 manipulation (fig. S10A), indicating no effect of FAM171A2 on the phosphorylation propensity of α-syn. Moreover, neurons treated with phosphate-buffered saline (PBS) instead of α-syn PFFs showed similar endogenous soluble α-syn expression with or without FAM171A2 manipulations (fig. S10, B to E), suggesting that FAM171A2 did not influence the equilibrium between endogenous α-syn production and degradation. Given these results, we hypothesized that FAM171A2 might regulate the internalization of extracellular α-syn fibrils.

To test our hypothesis, we used a short incubation assay of fluorescently labeled α-syn PFFs (Alexa-Flour 488) in primary neurons under different conditions (FAM171A2 overexpression or knockdown). FAM171A2 overexpression enhanced the uptake of α-syn PFFs compared with wild-type neurons as determined by immunofluorescence and western blot. By contrast, FAM171A2 knockdown led to a substantial reduction in the uptake compared with control neurons (fig. 3, F to J). Internalized α-syn PFFs and FAM171A2 colocalized with transferrin, an indicator substrate for clathrin-mediated endocytosis (CME), and with cholera toxin B, a marker for caveolae-mediated endocytosis (CvME) (fig. S11), consistent with prior reports suggesting that α-syn PFFs are internalized through endocytosis (*8*, *21*, *22*). To directly test the necessity of endocytic pathways, we used dynasore, an inhibitor targeting CME, and MβCD, an inhibitor of CvME. We observed that the heightened α-syn PFF endocytosis caused by FAM171A2 overexpression was effectively abolished by both these inhibitors, indicating that these two pathways are necessary for FAM171A2-mediated internalization of α-syn PFFs (fig. S12). Thus, these results suggest that FAM171A2 might regulate the endocytosis of α-syn PFFs.

To test whether FAM171A2 may affect the spread of α-syn pathology between neurons, we performed in vivo studies measuring the brain distribution of p-α-syn pathology 6 months after α-syn PFF inoculation in mice with either overexpression or knockdown of FAM171A2. We examined key brain regions known to be implicated in this model, including the SN, secondary motor cortex (M2), basolateral amygdala (BLA), and striatum region (CPu). FAM171A2 overexpression led to an increase in p-α-syn pathology in SN and CPu compared with that in wild-type animals (Fig. 3, K to N). In addition, whole-body as well as neuronal FAM171A2 knockdown reduced the spread of p-α-syn pathology across all four brain regions (Fig. 3, K to N, and fig. S13). Together, these data indicate that neuronal FAM171A2 controls the endocytosis of α-syn fibrils and also regulates the spread of α-syn pathology in the brain.

FAM171A2 directly binds α-syn fibrils

To visualize the FAM171A2-mediated endocytosis of α-syn PFFs, we used total internal reflection microscopy (TIRF) (movie S1). In N2a cells expressing dTomato-tagged FAM171A2, we observed that most α-syn PFFs (we used α-syn PFFs-488; see materials and methods) colocalized with FAM171A2-positive puncta (Fig. 4A). Furthermore, we investigated the disappearance of α-syn PFF puncta from the plasma membrane, indicative of their internalization into cells. Our findings revealed that 79% of α-syn PFF disappearance events happened in puncta with FAM171A2-positive labeling (Fig. 4A, fig. S14, and movie S2), suggesting that FAM171A2-mediated endocytosis is among the main routes of α-syn PFF internalization. Immunoprecipitation experiments in N2a cells showed that molecular interaction exists between FAM171A2 and α-syn PFFs (Fig. 4B). Similar immunoprecipitation experiments in freshly frozen postmortem human midbrain tissues showed binding between FAM171A2 and α-syn in samples from individuals with PD but not in brains from healthy controls (Fig. 4C). These findings support the interaction between FAM171A2 and pathological α-syn in both preclinical models and in clinical samples.

To locate the binding site of α-syn on FAM171A2, we measured the binding of α–syn PFFs to the cell surface in human embryonic kidney (HEK) 293 cells overexpressing full-length or domain-truncated FAM171A2 (domain 1, amino acids 30 to 125, and domain 2, amino acids 126 to 315). We found that FAM171A2 domain 1 is necessary for the uptake of α-syn PFFs (Fig. 4D). We then purified the FAM171A2 domain 1 and established an enzyme-linked immunosorbent assay (ELISA). Domain 1 of FAM171A2 binds to α-syn PFFs with high affinity [estimated equilibrium dissociation constant (K_D) around 33 nM], which was about three orders of magnitude stronger than that measured from monomeric α-syn (Fig. 4E). On the other hand, tau and amyloid β (Aβ) monomers or fibrils showed lower or no affinity to FAM171A2 domain 1 (fig. S15). Incubating FAM171A2-overexpressing N2a cells with purified FAM171A2 domain 1 proteins blocked the internalization of α-syn PFFs (fig. S16), further verifying the binding between FAM171A2 domain 1 and α-syn PFFs. We further dissected the molecular interactions between FAM171A2 domain 1 and α-syn using nuclear magnetic resonance (NMR) spectroscopy. By labeling the nitrogen atoms in α-syn with ^{15}N, we were able to map individual amino acid residues with the ^{1}H-^{15}N heteronuclear single-quantum coherence (HSQC) spectrum (*23*). When we titrated the solution with purified FAM171A2 domain 1, we observed chemical shift deviations (CSDs) in C-terminal residues of α-syn (Fig. 4, F and G, and fig. S17), suggesting a potential binding site. Consistently, deleting the C-terminal region of α-syn (amino acids 101 to 140) completely abolished the binding to FAM171A2 domain-1 (Fig. 4H).

We then used AlphaFold-Multimer to predict the structure of the FAM171A2–α-syn complex. The resulting structure revealed that the negatively charged α-syn C terminus (Val^{118}, Asp^{119}, Asp^{121}, Asn^{122}, Glu^{123}, Ala^{124}, Tyr^{125}, Glu^{126}) aligned with the positively charged surface of FAM171A2 domain-1 (Trp^{109}, Arg^{110}, Val^{111}, Asp^{112}, Lys^{113}, Pro^{115}, Leu^{116}, Tyr^{117}, Ala^{118}) (Fig. 4I). The predicted interacting residues on α-syn were closely aligned with those that showed chemical shift deviations in our NMR titration experiments, indicating a faithful representation of the binding interface. Binding of FAM171A2 to the α-syn C terminus could potentially explain the selective affinity of FAM171A2 toward α-syn fibrils, as our previous study found that the α-syn C-terminal region was partially shielded in monomers (*24*) but fully exposed and densely packed in fibrils (*25*). Altogether, our data demonstrated specific binding between FAM171A2 and α-syn PFFs, providing the structural basis for FAM171A2-mediated α-syn uptake.

Bemcentinib blocks binding between α-syn fibrils and FAM171A2

With the predicted complex structure, we performed a virtual screening to identify potential interfering small molecules with the Drug-lib database in MTiOpenScreen (*26*). We reasoned that candidate molecules should show high affinity to the same binding site, thus blocking interaction between FAM171A2 and α-syn through competition. We screened a collection of 7173 previously approved drugs and found 7 compounds (bolazine, bemcentinib, dihydroergocristine, Mk3207, dihydroergotamine, OSU-03012, and abamectin-B1a) with high docking affinities to interacting residues from both FAM171A2 and α-syn (Fig. 5A). We measured six out of the seven molecules for their effects in inhibiting the interaction between FAM171A2 domain 1 and α-syn PFFs with our ELISA approach and found that bemcentinib, a drug developed for cancer treatment (*27*), showed a strong effect at micromolar concentrations (Fig. 5, B and C, and fig. S18A). To gain structural insights underlying the effects of bemcentinib, we conducted NMR spectroscopy experiments using titration of bemcentinib to the ^{15}N-labeled α-syn monomer solution. Bemcentinib caused a marked drop in the HSQC signal intensity and substantial CSDs in the C terminus of α-syn, with many affected residues matching those found to be the interaction sites to FAM171A2 domain 1 (Fig. 5, D and E).

These data suggest that bemcentinib might interfere with FAM171A2–α-syn interaction by competing overlapping residues.

We then examined whether bemcentinib could suppress the endocytosis of α-syn PFFs. We first measured the effect of bemcentinib in N2a cells with FAM171A2 overexpression. Pretreating N2a cells with 10-μM bemcentinib for 1 hour reduced the amount of α-syn binding to FAM171A2 and endocytosed into the cells (Fig. 5, F and G, and fig. S18B) but showed no effect in cells without FAM171A2 overexpression, indicating a potent effect in blocking FAM171A2-mediated endocytosis of α-syn PFFs. To test the effect of bemcentinib in vivo, we developed a liquid chromatography detection method for bemcentinib and found that bemcentinib could not cross the blood-brain barrier (*28*, *29*) (fig. S19). Therefore, we treated wild-type mice that previously received 2.5 μl of α-syn PFFs-488 (2 μg/ml) in the right striatum, with 5 μl of bemcentinib solution (2.5 mg/ml) injected in the right lateral ventricle for 7 consecutive days. Bemcentinib did not cause obvious toxicity to neurons (fig. S20) or abnormal behavior in treated mice. However, bemcentinib reduced the total amount of internalized α-syn PFFs-488 in the right SN (Fig. 5, H to J). Together, these findings suggest that bemcentinib might inhibit the binding between FAM171A2 and α-syn PFFs in vivo, thus representing a potential strategy to block the pathological spread of α-syn fibrils in the context of PD.

Discussion

Several membrane proteins, such as heparan sulfate proteoglycan (*12*), low-density lipoprotein receptor–related protein 1 (*11*), lymphocyte-activation gene 3 (*10*), Mer tyrosine kinase (*30*), and glycoprotein nonmetastatic melanoma protein B (*31*), have been proposed as potential mediators in the recognition of pathological α-syn. Despite the keen interest in identifying such a mediator, these proteins currently lack clear evidence for neuronal expression, selectivity for α-syn fibril over monomers, or in vivo efficacy (*11*, *12*, *32*). Our findings identify a binding site between FAM171A2 and α-syn and provide strong evidence suggesting that FAM171A2 has stronger binding affinity to α-syn fibrils compared with that of monomers. FAM171A2 is expressed on SN neurons in humans, with elevated expression and binding with α-syn fibrils detected in individuals with PD compared with controls. Altogether, our data suggest that FAM171A2 is a receptor that directly binds with α-syn fibrils and controls the neuronal uptake of them (fig. S21).

PD is predominantly marked by motor impairments due to the gradual degeneration of dopaminergic neurons in SN. The exact neural mechanisms responsible for the development of PD remain elusive, but the spread of pathological α-syn across different brain regions is closely linked to the disease's progression (*3*, *33*), suggesting a fundamental role in its pathogenesis. Currently, the specific molecular processes that facilitate the distribution of pathological α-syn are not fully understood. In this work, we identified a potential target for limiting the spread of α-syn fibrils between neurons. We pinpointed the specific subdomain of FAM171A2 and the corresponding interface on α-syn responsible for their direct interaction, identifying the key residues involved. Moreover, we identified bemcentinib, which interferes with the amino acids critical for the FAM171A2–α-syn interaction and demonstrated bemcentinib's ability to prevent the FAM171A2 and α-syn PFF binding and to block the uptake of α-syn PFFs in mice. Although bemcentinib may not be directly applicable in a clinical setting owing to its low efficacy in brain penetrance, our method of using structural analysis opens the possibility to discover effective drugs based on our findings. Altogether, we identified a pathway potentially involved in the spread of α-syn fibrils between brain areas and suggest a compelling strategy for impeding this process in individuals with PD.

REFERENCES AND NOTES

1. B. R. Bloem, M. S. Okun, C. Klein, *Lancet* **397**, 2284–2303 (2021).
2. H. R. Morris, M. G. Spillantini, C. M. Sue, C. H. Williams-Gray, *Lancet* **403**, 293–304 (2024).
3. M. Carceles-Cordon, D. Weintraub, A. S. Chen-Plotkin, *Neuron* **111**, 1531–1546 (2023).
4. M. X. Henderson *et al*., *Nat. Neurosci.* **22**, 1248–1257 (2019).
5. D. J. Surmeier, J. A. Obeso, G. M. Halliday, *Nat. Rev. Neurosci.* **18**, 101–113 (2017).
6. C. Peng, J. Q. Trojanowski, V. M. Y. Lee, *Nat. Rev. Neurol.* **16**, 199–212 (2020).
7. N. Uemura, M. T. Uemura, K. C. Luk, V. M. Y. Lee, J. Q. Trojanowski, *Trends Mol. Med.* **26**, 936–952 (2020).
8. Q. Zhang *et al*., *Proc. Natl. Acad. Sci. U.S.A.* **117**, 10865–10875 (2020).
9. S. H. Oh *et al*., *Cell Rep.* **14**, 835–849 (2016).
10. X. Mao *et al*., *Science* **353**, aah3374 (2016).
11. K. Chen *et al*., *Mol. Neurodegener.* **17**, 57 (2022).
12. B. B. Holmes *et al*., *Proc. Natl. Acad. Sci. U.S.A.* **110**, E3138–E3147 (2013).
13. W. Xu *et al*., *Sci. Adv.* **6**, eabb3063 (2020).
14. C. Xiang *et al*., *NPJ Parkinsons Dis.* **8**, 165 (2022).
15. K. C. Luk *et al*., *Science* **338**, 949–953 (2012).
16. L. A. Volpicelli-Daley *et al*., *Neuron* **72**, 57–71 (2011).
17. C. Quadalti *et al*., *Nat. Med.* **29**, 1964–1970 (2023).
18. N. Uemura *et al*., *Mol. Neurodegener.* **13**, 21 (2018).
19. J. Blesa, G. Foffani, B. Dehay, E. Bezard, J. A. Obeso, *Nat. Rev. Neurosci.* **23**, 115–128 (2022).
20. A. Tozzi *et al*., *Brain* **144**, 3477–3491 (2021).
21. I. Kawahata *et al*., *Biomedicines* **9**, 49 (2021).
22. T.-Y. Ha *et al*., *Mol. Brain* **14**, 122 (2021).
23. Z. Liu *et al*., *J. Biol. Chem.* **293**, 14880–14890 (2018).
24. S. Zhang *et al*., *Proc. Natl. Acad. Sci. U.S.A.* **118**, e2011196118 (2021).
25. Y. Li *et al*., *Cell Res.* **28**, 897–903 (2018).
26. C. M. Labbé *et al*., *Nucleic Acids Res.* **43**, W448-54 (2015).
27. S. J. Holland *et al*., *Cancer Res.* **70**, 1544–1554 (2010).
28. R. Cecchelli *et al*., *Nat. Rev. Drug Discov.* **6**, 650–661 (2007).
29. P. Jeffrey, S. Summerfield, *Neurobiol. Dis.* **37**, 33–37 (2010).
30. M.-F. Dorion *et al*., *Brain* **147**, 427–443 (2024).
31. M. E. Diaz-Ortiz *et al*., *Science* **377**, eabk0637 (2022).
32. M. Emmenegger *et al*., *EMBO Mol. Med.* **13**, e14745 (2021).
33. C. Smith *et al*., *J. Neurol. Neurosurg. Psychiatry* **90**, 1234–1243 (2019).
34. D. Chang *et al*., *Nat. Genet.* **49**, 1511–1516 (2017).

ACKNOWLEDGMENTS

We extend our heartfelt gratitude to the participants and researchers involved in the UK Biobank, the PDWBS study, the PDGene study, the FinnGen study, and the PPMI cohort databases. We extend our sincere gratitude to L. Ma for her valuable suggestions for this study. We also express our appreciation to J. Shen from Shimadzu Corporation for his invaluable experimental support. Special thanks are due to all members of Dr. Yu's laboratory for their unwavering support, assistance, and guidance. Lastly, we express our profound appreciation to all the patients who generously donated their brain, blood, or CSF samples for research purposes. **Funding:** STI2030-Major Projects (2022ZD0211600) (J.-T.Y.); National Natural Science Foundation of China (82071201, 82271471, and 92249305) (J.-T.Y.); Shanghai Municipal Science and Technology Major Project (2023SHZDZX02) (J.-T.Y.); Excellent Academic Research Leader Program of Shanghai (23XD1420400) (J.-T.Y.); Emerging Interdisciplinary Research Project of Shanghai (2022JC014) (J.-T.Y.); Research Start-up Fund of Huashan Hospital (2022QD002) (J.-T.Y.); National Natural Science Foundation of China (82188101, 22425704, and 32171236) (C.L.); the CAS Project for Young Scientists in Basic Research (YSBR-095) (C.L.); the Strategic Priority Research Program of the Chinese Academy of Sciences (XDB106000) (C.L.); STI2030-Major Project no. 2021ZD0201100 Task 4 no. 2021ZD0201104 (W.-S.L.); China Postdoctoral Science Foundation (2023M740682) (K.-M.W.); Postdoctoral Fellowship Program of CPSF (GZC20230506) (K.-M.W.); National Natural Science Foundation of China (82401676) (K.-M.W.); Shanghai Pilot Program for Basic Research – FuDan University 21TQ1400100 (22TQ019) (P.Y.); National Natural Science Foundation of China (32371036) (P.Y.). J.-T.Y. was additionally supported by ZHANGJIANG LAB; Tianqiao and Chrissy Chen Institute; and the State Key Laboratory of Neurobiology and Frontiers Center for Brain Science of Ministry of Education, Fudan University. C.L. was additionally supported by Shanghai Basic Research Pioneer Project and the Shanghai Pilot Program for Basic Research, Chinese Academy of Science, Shanghai Branch. C.L. is a SANS Exploration Scholar. **Author contributions:** Conceptualization: J.-T.Y., P.Y., K.-M.W.; Methodology: K.-M.W., Q.-H.X., Y.-Q.L., Y.-W.F., S.-D.H., Z.-F.Y., T.-T.W., M.C., L.Y., Y.-J.X., Y.-S.S., C.L., P.Y.; Data curation: K.-M.W., Y.-R.Z., S.-D.C., Y.G., B.-S.W., L.-Z.M.; Investigation: K.-M.W., Q.-H.X.; Visualization: K.-M.W., Y.Z., Y.-L.C., P.Y.; Resources: J.W., J.Z., S.-F.C., W.-D.L., W.-S.L., J.-T.Y., C.L., P.Y.; Funding acquisition: J.-T.Y., P.Y., C.L., K.-M.W., W.-S.L.; Project administration: J.-T.Y., P.Y.; Supervision: J.-T.Y.; Writing – original draft: K.-M.W., P.Y., J.-T.Y.; Writing – review and editing: B.-X.L., W.-D.L., K.Y., J.-Y.L. **Competing interests:** K.-M.W., P.Y., and J.-T.Y. are inventors on a patent application (PCT/CN2025/071237) submitted by Huashan Hospital, Fudan University, that covers potential strategies in suppressing FAM171A2 or blocking FAM171A2–α-syn interaction as potential treatment for neurodegenerative diseases. **Data and materials availability:** Individual-level genotype data described in this study are available to bona fide researchers per the UK Biobank data access protocol (https://www.ukbiobank.ac.uk/enable-your-research/apply-for-access). Summary statistics for the top 9830 variants from Chang *et al*. (2017) (*34*) is available at http://research-pub.gene.com/chang_et_al_2017/. FinnGen data are available at https://risteys.finngen.fi/. PPMI data are publicly available to bona fide researchers upon application at https://www.ppmi-info.org/. All data presented in the article are available in data S1.

SUPPLEMENTARY MATERIALS

science.org/doi/10.1126/science.adp3645
Materials and Methods
Figs. S1 to S21
Tables S1 to S4
References (*35*–*47*)
MDAR Reproducibility Checklist
Movies S1 and S2
Data S1

Submitted 22 March 2024; resubmitted 21 October 2024
Accepted 10 January 2025
10.1126/science.adp3645

Let *Science* Careers help advance your career.

- Register for a free online account on **ScienceCareers.org**.
- Search hundreds of job postings.
- Sign up to receive job alerts that match your criteria.
- Upload your resume into our database to connect with employers.
- Watch one of our many webinars on different career topics such as job searching, networking, and more.
- Download our career booklets, including Career Basics, Careers Beyond the Bench, and Developing Your Skills.
- Complete a personalized career plan at "my IDP."
- Read relevant career advice articles from our library of thousands.

Visit **ScienceCareers.org** today — all resources are free

Science Careers
FROM THE JOURNAL SCIENCE AAAS

SCIENCECAREERS.ORG

By **Avraneel Paul**

Comic relief

"Good afternoon, everyone. Glad you all could join me today. I am excited to share my research on ..." *Uh-oh*. "I am excited to share my research on ..." *Oh no! No! No!* "... my research on ..." *Why is this happening to me?* My knees were buckling; my throat felt drier with every second. It was the annual seminar at my department, where all Ph.D. students had to present their research progress. I looked around the lecture hall and saw 50 pairs of keen eyes staring at me, anticipating my next words. I was certainly not glad they had joined me, nor excited to be speaking.

Although I felt confident at my work bench and comfortable discussing my research with my mentor and lab mates, my introvert nature silenced me when I faced a larger, unfamiliar audience. Prior to graduate school, I had no experience in public speaking, and now the fear overwhelmed me. But with another seminar just a couple of months away and more public speaking ahead, I refused to let my nerves hold me back again.

I took a drastic step outside my comfort zone to sign up for an open mic event at a local stand-up comedy club in Bengaluru, India. I'd always admired the confidence of stand-up comedians, and I thought the jovial atmosphere might allow a bit more room for error.

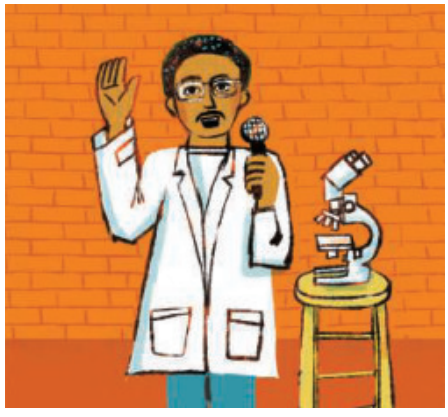

"I took a drastic step outside my comfort zone to sign up for an open mic event."

Although my jokes did not receive thunderous applause, I was surprised to find I enjoyed my time on stage. And I felt I could do better. I approached Sania, a brilliant comic whose wit and eloquence made her the highlight of the evening. Sania offered three invaluable tips.

"Attend more open mic events," she advised. "Watch more comics perform." Though she meant to help me succeed as a comedian, her suggestion helped me improve my upcoming research presentation. For the next few months, I attended numerous seminars at my institute, observing how skilled orators presented their stories and conveyed complex scientific data through easily digested takeaways.

Sania's next piece of advice was to write and rewrite a script. Although some speakers can improvise, I found value in preparation. The script was a bridge from my cluttered thoughts to spoken words. It helped me maintain a logical flow, avoid rambling, and refine my timing. Most important, having a clear road map reduced my anxiety.

Sania saved her most valuable advice for last: Practice! With my script in hand, I began to rehearse my research presentation tirelessly. Alone, with colleagues, and even with unsuspecting visitors—every audience counted. I practiced every pause and hand gesture. Initially, it felt forced and unnatural. However, with each iteration, my presentation became more fluid and organic. Slowly but surely, my words morphed into muscle memory.

When the time came for my next research presentation, the difference was clear. My confidence, eloquence, and presentation skills had improved dramatically. I finished to applause rather than an awkward silence.

Unexpectedly, this process benefited my research. I began to view science through a storyteller's lens. Instead of merely presenting the results of my experiments, I used my data set to tell a story. The genes and proteins I studied became enigmatic characters in an unfolding drama. I sought to identify gaps in the narrative of my research and design my experiments to advance the story.

I have continued to sharpen my public speaking skills on various stages and now share my research with confidence. But I'll always be grateful for that pivotal moment of stage paralysis—when I failed to convey my findings despite months of painstaking research. That experience taught me that generating data is only part of doing science. Effective communication is just as important.

After coming to the United States for a postdoc, I joined Toastmasters, a nonprofit that aims to help people master public speaking, and I'm now the president of my university's chapter. I share Sania's advice to prepare and practice with researchers who attend our meetings. I also tell them data points and graphs aren't just numbers and lines—they tell stories. Realizing that is the key to sharing them with the world. ■

Avraneel Paul is a postdoctoral fellow at the University of Alabama at Birmingham. Send your career story to SciCareerEditor@aaas.org.

ILLUSTRATION: ROBERT NEUBECKER

Cold Spring Harbor Laboratory 2025 Meetings & Courses

Meetings

meeting dates / abstracts due

Probabilistic Modeling in Genomics March 5 - 8

Network Biology March 11 - 15

Nucleic Acid Therapies March 19 - 22

Cancer Genetics: History & Consequences
March 26 - 29

Ubiquitins, Autophagy & Disease April 1 - 5

Brain Barriers April 8 - 12

Systems Immunology April 22 - 26

Telomeres & Telomerase April 29 - May 3

Biology of Genomes May 6 - 10

Mechanisms of Metabolic Signaling
May 13 - 17 / February 21

Retroviruses May 19 - 24 / February 28

89th Symposium: Senescence & Aging
May 28 - June 1 / March 7

Genomic Data Science and Beyond with *Galaxy & Bioconductor* June 23 - 26 / April 4

Advances in Brain Tumor Research & Therapy
July 17 - 20 / April 25

Genome Engineering: CRISPR Frontiers
August 12 - 16 / May 23

Eukaryotic mRNA Processing August 19 - 23 / May 30

Mechanisms of Eukaryotic Transcription
August 26 - 30 / June 6

Eukaryotic DNA Replication & Genome Maintenance
September 2 - 6 / June 13

Microbial Pathogenesis & Host Response
September 8 - 12 / June 20

Biology of Cancer: Microenvironment & Metastasis
September 16 - 20 / June 27

Cell Fate Conversions September 24 - 27 / July 7

Bioengineered Tissue Systems & Models
September 28 - October 1 / July 11

Neurobiology of *Drosophila* October 7 - 11 / July 21

Immune Engineering & Cellular Immunotherapy
October 28 - 31 / August 15

Genome Informatics November 5 - 8 / August 22

Single Cell Analyses November 12 - 15 / August 29

Zebrafish Neurobiology November 19 - 22 / September 5

Plant Genomes, Systems Biology & Engineering
December 3 - 6 / September 12

Assembloids & Complex Cell-Cell Interactions Across Tissues & Organs
December 8 - 11 / September 19

Courses

course dates / applications due

Tutorials in Genomics & Bioinformatics: RNA-Seq Analysis May 11 - 13 / no application, rolling admission

Advanced Bacterial Genetics June 2 - 22 / March 1

Ion Channels in Synaptic & Neural Circuit Physiology
June 2 - 22 / March 1

Mouse Development, Stem Cells & Cancer
June 2 - 22 / March 1

Pancreatic Cancer June 3 - 10 / March 1

Statistical Analysis of Genome Scale Data
June 6 - 20 / March 1

Metabolomics June 6 - 22 / March 1

Vision: A Platform for Linking Circuits, Behavior & Perception June 12 - 28 / March 1

Advanced Techniques in Molecular Neuroscience
June 26 - July 12 / March 15

Single Cell & Spatial Transcriptomics Analysis
June 26 - July 14 / March 15

***Drosophila* Neurobiology: Genes, Circuits & Behavior**
June 26 - July 17 / March 15

Frontiers & Techniques in Plant Science
June 26 - July 17 / March 15

Neural Data Science July 7 - 21 / March 15

Autism Spectrum Disorders July 22 - 29 / March 31

Synthetic Biology July 22 - August 5 / March 31

Chromatin, Epigenetics & Gene Expression
July 22 - August 10 / March 31

Imaging Structure & Function in the Nervous System July 22 - August 12 / March 31

Yeast Genetics & Genomics
July 22 - August 12 / March 31

Neuroscience of Addiction
July 29 - August 5 / March 31

Bench to Biotech August 5 - 12 / March 31

Proteomics August 5 - 19 / March 31

Macromolecular Crystallography
October 12 - 28 / July 15

Programming for Biology
October 12 - 28 / July 15

Antibody Engineering & Display Technologies
October 14 - 28 / July 15

High Throughput Neuroanatomy
October 16 - 28 / July 15

Tutorials in Genomics & Bioinformatics
November 9 - 11 / no application, rolling admission

Advanced Sequencing Technologies & Bioinformatics Analysis November 9 - 22 / August 15

Scientific Writing Retreat November 10 - 15 / August 15

Computational Genomics December 2 - 10 / August 15

Photo: The 2024 Chromatin, Epigenetics & Gene Expression Course taking a break on the Christeen off the Cold Spring Harbor Beach

meetings.cshl.edu

CALL FOR PAPERS

SPJ
SCIENCE PARTNER JOURNALS

THE KOREAN SOCIETY FOR BIOMATERIALS

spj.science.org/bmr

Biomaterials Research

OPEN ACCESS

Biomaterials Research is a Science Partner Journal published in affiliation with the **Korean Society for Biomaterials (KSBM)** and distributed by the **American Association for the Advancement of Science (AAAS)**. The journal serves the multidisciplinary community of biomaterials research by publishing original, breakthrough research in the interdisciplinary fields of novel biomaterials, cutting-edge technologies of biomaterials synthesis and fabrication, and biomedical applications in clinics and industry.

The Science Partner Journals (SPJ) program was established by the American Association for the Advancement of Science (AAAS), the nonprofit publisher of the *Science* family of journals. The SPJ program features high-quality, online-only, Open Access publications produced in collaboration with international research institutions, foundations, funders, and societies. Through these collaborations, AAAS furthers its mission to communicate science broadly and for the benefit of all people by providing top-tier international research organizations with the technology, visibility, and publishing expertise that AAAS is uniquely positioned to offer as the world's largest general science membership society.

Submit your research to *Biomaterials Research* today!
Learn more at: **spj.science.org/bmr**

@SPJournals **@SPJournals** **@SPJournals**